UNIVERSITY OF SOUTHAMPTON

Faculty of Physical Sciences and Engineering
Physics and Astronomy

Explosions in the Sky: The Physics of Type Ia Supernovae from Large Astrophysical Datasets

by

Robert Elliot Firth

A thesis submitted in partial fulfillment for the degree of Doctor of Philosophy

December 2016

UNIVERSITY OF SOUTHAMPTON

Abstract

Faculty of Physical Sciences and Engineering

Physics and Astronomy

Doctor of Philosophy

Explosions in the Sky: The Physics of Type Ia Supernovae from Large Astrophysical Datasets

by Robert Elliot Firth

This thesis studies type Ia supernovae (SNe Ia) discovered by the Palomar Transient Factory (PTF). We use this large, high–quality imaging and spectroscopic dataset to analyse the very earliest part of the SN Ia light curve, probing the ejecta structure, the postmaximum light curve, the ^{56}Ni distribution, and the utility of SNe Ia as standard candles at different wavelengths.

The high cadence of PTF makes it capable of studying SNe Ia at very early times, as they rise just after explosion. In this thesis we use 18 SNe Ia from PTF and the La Silla-QUEST variability survey (LSQ) to measure the time between first light, t_0, and maximum light (t_{rise}), and rise index (n), where $f = (t - t_0)^n$. We find that n shows significant variation ($1.48 \leq n \leq 3.70$), and has a mean value $\bar{n} = 2.44 \pm 0.13$, inconsistent with a simple fireball model ($n = 2$) at 3σ. We calculate an average $t_{\rm rise}$ of our sample $t_{\rm rise} = 18.98 \pm 0.54$ days, and find that the variation seen in $t_{\rm rise}$ and n is principally driven at the very earliest epochs.

We use a further sample of 31 PTF SNe Ia to explore the diversity of the post-maximum light curve in R–band, as the emission at these phases is linked to the same driver of variation – the distribution of ^{56}Ni through the ejecta. By modelling the shoulder on the light curve we quantify the strength and timing of this feature. We find that the timing of the additional emission is correlated with light curve width, but that the duration is not. We also find that the prominence of the gaussian, relative to its peak, is inversely correlated with the light–curve width. We interpret this as the impact of intermediate mass element spectral features dominating over those of iron peak elements.

Having explored the physics that governs these objects, we turn to the primary motivation for studying SNe Ia – their use as standardisable candles. We consider 60 SNe Ia in three filters, B, R and i, constructing hubble diagrams for each. We find that the magnitude of the corrections for light curve width and SN colour decreases as a function of wavelength, and that SNe Ia in i–band do not need correction for light curve width. We also find that the colour law observed for our sample is not consistent with the standard Milky–Way extinction law, with $R_V = 3.1$. Finally, we find that SNe Ia in i are superior standardisable candles to B–band, and that they are overall the best in R. This sample is well placed to anchor future high–redshift rest–frame i–band cosmological studies.

"In the beginning there was nothing, which exploded."

- Terry Pratchett, *Lords and Ladies*

Contents

List of Figures

List of Tables

Abbreviations

CCD	**C**harge **C**oupled **D**evice
CMB	**C**osmic **M**icrowave **B**ackground
CO	**C**arbon–**O**xygen
CSM	**C**ircum–**S**tellar **M**aterial
CSP	**C**arnegie **S**upernova **P**roject
DD	**D**ouble **D**egenerate
DDT	**D**eflagration-to-**D**etonation **T**ransition
ESO	**E**uropean **S**outhern **O**bservatory
EFOSC2	**E**SO **F**aint **O**bject **S**pectrograph and **C**amera V**2**
GRB	**G**amma **R**ay **B**urst
LOSS	**L**ick **O**bservatory **S**upernova **S**earch
LSQ	**L**a **S**illa **Q**UEST
MW	**M**ilky **W**ay
PTF	**P**alomar **T**ransient **F**actory
PESSTO	**P**ublic **E**SO **S**pectroscopic **S**urvey of **T**ransient **O**bjects
S/N	**S**ignal-to-**N**oise
SCP	**S**upernova **C**osmology **P**roject
SDSS	**S**loan **D**igital **S**ky **S**urvey
SD	**S**ingle **D**egenerate
SLSNe	**S**uper-**L**uminous **S**uper**N**ovae
SNLS	**S**uper**N**ova **L**egacy **S**urvey
WLR	**W**idth–**L**uminosity **R**elation
WD	**W**hite **D**warf

Declaration of Authorship

I, Robert Elliot Firth, declare that this thesis titled, 'The Physics of Type Ia Supernovae from Large Astrophysical Datasets' and the work presented in it are my own. I confirm that:

- This work was done wholly or mainly while in candidature for a research degree at this University.
- Where any part of this thesis has previously been submitted for a degree or any other qualification at this University or any other institution, this has been clearly stated.
- Where I have consulted the published work of others, this is always clearly attributed.
- Where I have quoted from the work of others, the source is always given. With the exception of such quotations, this thesis is entirely my own work.
- I have acknowledged all main sources of help.
- Where the thesis is based on work done by myself jointly with others, I have made clear exactly what was done by others and what I have contributed myself.

Notably, this thesis contains work that has already been published in the following works:

- R.E. Firth, et al. 2015, MNRAS, 446, 3895-3910, 'The rising light curves of Type Ia supernovae'

Signed: _____

Date: _____

Acknowledgements

Despite my best efforts, this is not a short list of thanks, but I owe so much to so many.

I am supremely grateful to my supervisor, Mark Sullivan for giving me first the opportunity, and then his support, guidance and seemingly endless patience over the last 4 years. Not once have I left a meeting without renewed purpose, or a chat without a sense of progress; you always seemed to know what to say, about science, or anything else. It's been a privilege to be your student.

My wife Katy; what a time we have had, four years after our big move; a proposal, a wedding and now this. Without you, none of what I have achieved would have been possible, you've been amazing. You're the love of my life, and I'm constantly in awe of you. Sorry you've been thesis widowed for the past few months, I promise it has all been worth it. I'll make it up to you.

Andy and Hannah, for letting me pretend I'm a grown up, but for never for too long. You mean a tremendous amount to both Katy and I, and have helped more than you know through stressful times. Having you so close by has been an absolute joy.

The Southampton Supernova Group; Mike, Chris, Natasha, Regis, Szymon, you've all taught me so much. Mat, thanks for the late nights at the office, and the weekend emails that helped me to get this over the line, we've laughed, we've cried – I wouldn't change it. Chris and Georgios, on top of everything else thanks for being the best travelling companions anyone could ask for, without you, I'd be many memories, and a few cracking stories poorer. I'm grateful to PESSTO, for the chance to twice observe at ESO La Silla in Chile, and the opportunity for adventures in a country I will always hold dear.

Aarran, James and Sam, for the early mornings in the gym and on the squash court, and the late nights in the pub; for the spilled drinks, the board games, the gigs, the beer, the stag, the wedding, the eye rolls, the sighs and for generally putting up with me. Thanks in no small part to you, the last four years have been the best of my life. I'm proud to count you amongst my closest friends, thanks for the memories, I hope we make many more.

Bigman, you helped me learn who I am; the anwers to the biggest questions distilled from blood, sweat and tears on the ice, scraped from the bottom of coffee cups wherever we could find them, and crystallised from the post game haze of many memorable road trips. We never did set the world fully to rights, but I'm sure we will keep trying. Additional thanks, to you and to Sarah, for de–mystifying academics in the best way

possible. And to Will, Jonah and Eva a special thanks for reminding me with evey question, just what a wonderful place the universe is and how lucky I am to study it.

Massive thanks to Keira, John, España, Andy, Amy, Fred, Cat and everyone else who was ever 'Occasionally Third', for making me look forward to Monday nights. To all the astrofootballers for keeping me sweaty but sane. To Boon, and to Maxi for helping to make the office somewhere I never wanted to be away from for long. To Sadie and our greatest team, for the chance to engage with so many people through the AstroDome, and letting me loose in a van.

To Stu, for always having time, for helping make sense of everything and for keeping the laughter. For the catch ups and your insight and your perspective - I have been, and always will be, able to trust you with anything. To you and the whole MCHS crew, you know who you are, thanks for always making it feel I've never been away. To Mike, for the visits and the long and winding chats over beers and coffees, and for your unshakable friendship and support - I always enjoyed your visits to Southampton. To Jill, Stu and Lauren thanks for the support you have given me and Katy, and for always showing an interest in my work.

To some memorable physicists and educators; My high school physics teachers, Saeed Saeed and Jon Grange without whom I may have ended up a historian, and Paul Crowther and Vik Dhillon at the University of Sheffield, who encouraged me to continue on this path.

Finally, to Mum, Dad and Katie, thank you for the last 26 years, and particularly in the last 4 over my PhD making home a place of (admittedly chaotic) sanctuary. It makes everything I do that much easier knowing that I always have you behind me.

I'm indebted to you all.

RF - Southampton, 2016

Felix, qui potest rerum cognoscere causas

– Virgil, *Georgios* #2, v490

For the little boy who wanted nothing more than to be a scientist.
We did it.

Chapter 1

Introduction

"Space is big. Really big. You just won't believe how vastly, hugely, mind-bogglingly big it is. I mean, you may think it's a long way down the road to the chemist, but that's just peanuts to space."

- Douglas Adams, *Hitchikers Guide to the Galaxy*

Type Ia Supernovae (SNe Ia) are bright stellar explosions that are luminous enough to be seen out across the Universe, far back into cosmic time. Their unique qualities, namely that by using measurements of their intrinsic colour and light–curve shape they can be used as cosmological standard candles, make them indispensible tools for understanding the Universe, and its expansion. Using SNe Ia, the expansion of our Universe was found to be accelerating, providing the most compelling evidence yet for the existence of dark energy.

SNe Ia are understood to be the thermonuclear explosion of a carbon–oxygen (CO) white dwarf (WD) star, which by some mechanism gains sufficient mass to reach high enough internal pressure and temperature to trigger runaway fusion. This burns the CO to heavier iron peak elements (IPEs), and releases huge amounts of energy. This unbinds the star and launches the material that formed the star out into the local environment, enriching its neighbourhood with heavy elements.

Despite our best understanding, open questions remain about the exact nature of SNe Ia, their progenitor configuration, explosion mechanisms and the underlying physical processes that underpin their diversity. Now, in the era of large astrophysical datasets we can use an unprecedented number of observations in unexplored ways, extracting and quantifying variation, giving us insight into the physics that governs these objects.

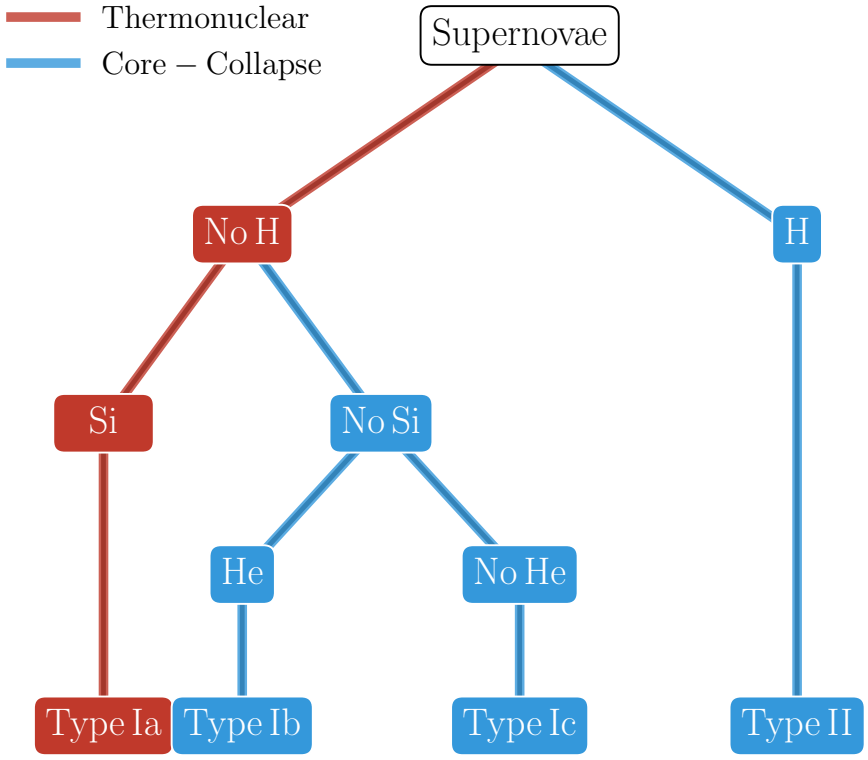

FIGURE 1.1: Classification schematic of Supernovae classes

1.1 Supernova Classification and Characteristics

Supernovae (SNe) are catastrophic stellar explosions that dramatically mark the final point of stellar evolution, first identified as distinct from novae by Baade & Zwicky (1934). SN classification is performed primarily using spectra, but the behaviour of the light curve is sometimes used as a secondary method of discrimination between classes. A simplified classification scheme is shown in Figure 1.1.

1.1.1 Supernova Classes

SNe have long been divided into two broad classes based on the presence of hydrogen lines in their spectra (Minkowski, 1941). As shown in Figure 1.1, those without hydrogen are classified as Type I, and those with hydrogen as Type II. Both types can be broken down into further subclasses.

Within SNe Type I, SNe Ia are identified by the presence of silicon in their spectra, particularly blueshifted Si II $\lambda 6347, 6371 (6355)$, often referred to as the 6150Å feature. This distinguishes normal SNe Ia from SNe Type Ib/Ic (SNe Ibc), which do not exhibit this feature (Filippenko, 1997). An example of a SN Ia spectrum can be seen in Figure 1.2.

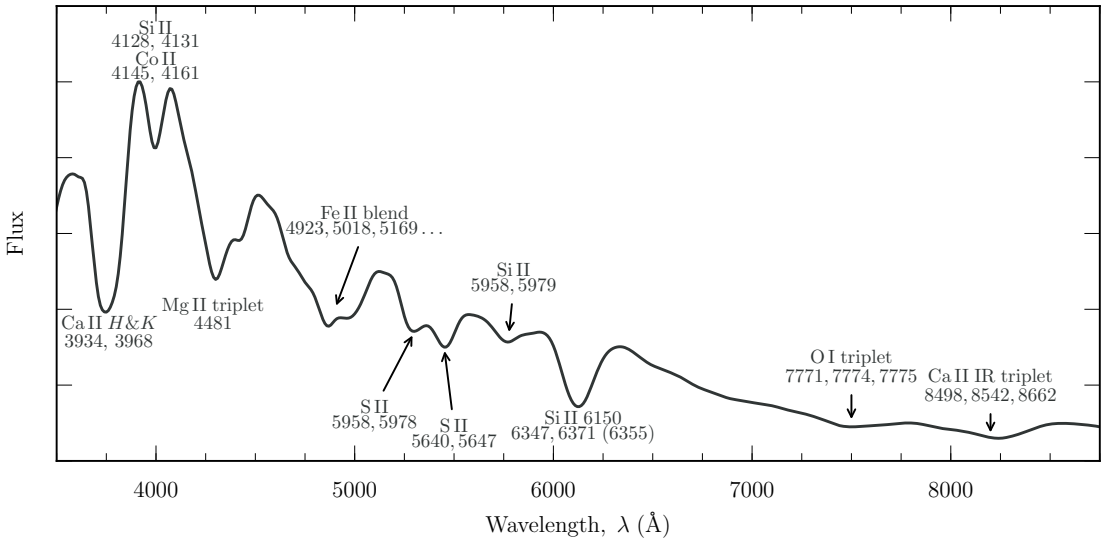

FIGURE 1.2: Rest–frame spectrum of a Supernova Type Ia at maximum light, showing the distinctive ionic species. The rest–frame wavelengths of the strongest lines are marked, but as a result of the rapid expansion velocities ($\sim 10,000$ km s^{-1}) the absorption features are significantly blueshifted.

To make a further distinction between Ib and Ic, optical He I lines (such as He I λ5876) appear in Ib, but are absent in Ic (Harkness et al., 1987). Normal SNe Ia peak at an absolute B-band magnitude of around $M \simeq -19.1$, ~ 1.5 mag brighter than SNe Ibc (Richardson et al., 2002, 2014). As well as being more luminous, SNe Ia are the most common subtype of SN (Li et al., 2011).

Recently, a new subclass of Type I SNe has been identified; Superluminous Supernovae Type I (SLSNe-I) (Quimby et al., 2011). While SLSNe-I are spectroscopically similar to SNe Ic but with an absolute magnitude brighter than -21, they are less common by a factor of ~ 1000 over a wide range of redshifts (Quimby et al., 2013; Prajs et al., 2016).

There are 4 'normal' (Turatto, 2003) subclasses of Type II SNe (SNe II) which span ~ 5 optical magnitudes (with the brightest objects ~ 1 mag fainter than a typical Ia; Anderson et al., 2014), and, like Type I's, a superluminous population (see Gal-Yam, 2012). Type IIL and IIP, which make up the majority of the total observed SNe II, are spectroscopically similar, differing in their post-maximum-light photometric behaviour. SNe IIP have a marked persistant 'plateau' phase, giving them their name, and lasting up to 100 days, while the behaviour of the type IIL subclass is a more rapid linear decay. SNe IIb, though rare, typically show a blue continuum and exhibit broad H and He I lines before transitioning to a Ib-like spectrum dominated by strong He I lines. SNe IIn exhibit narrow balmer emission lines, while the broad absorption lines, typical of other types, are absent.

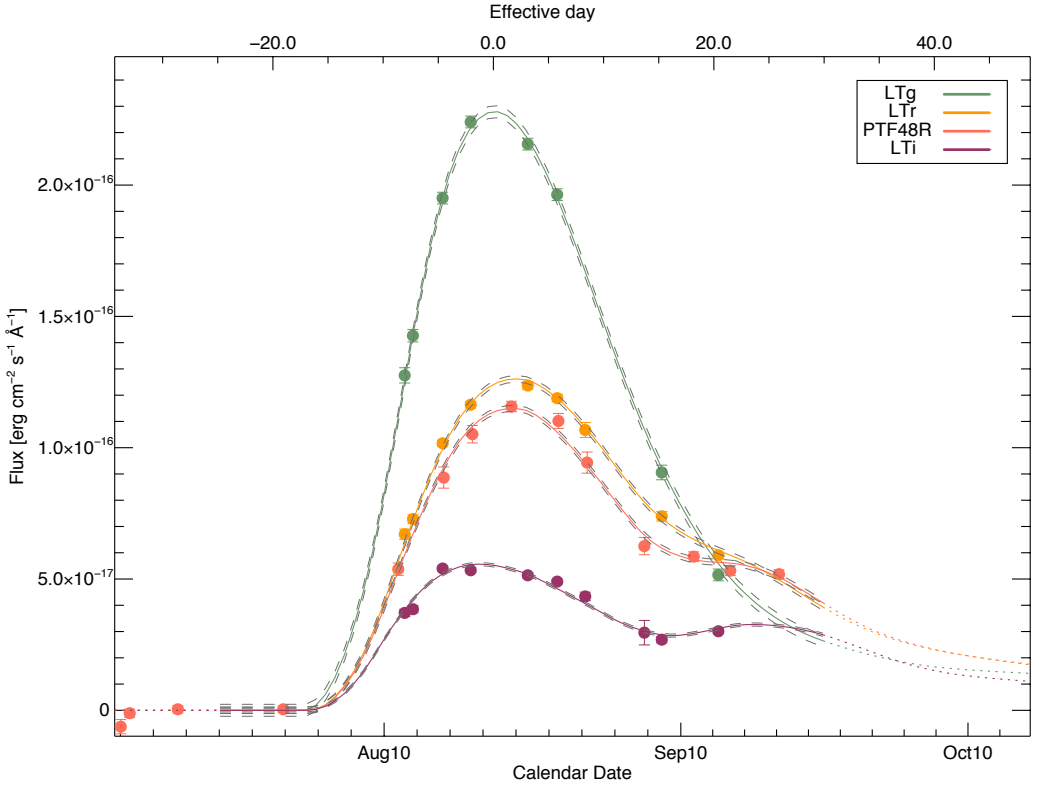

FIGURE 1.3: Multicolour SN Ia light curve; PTF10qky showing PTF48R (red points), LTg, LTR and LTi (as green, orange and purple filled points) bands. The solid lines show the SiFTO fit to the data.

1.2 Observations of SNe Ia

SNe Ia typically rise from first light to maximum brightness over a period of around 19 days (Firth et al., 2015), and initially fall $\sim$ 1 magnitude in the first two weeks after peak (depending on the wavelength of observations). When considering the time evolution of SNe Ia the rest–frame 'phase', τ (measured in days) is used, with $\tau = 0$ defined at B–band maximum. While the ultra–violet (UV) and blue–optical light curves fall uniformly after peak, the R–band light curve exhibits a shoulder or plateau for $\sim$ 10 days (Figure 1.3). While the luminosity still decreases monotonically, the rate of decline slows. At the same phases, redward of the i–band, through the infra-red (IR) there is a second light curve peak. Rising and falling on a similar characteristic timescale as the primary peak, in some IR bands it is comparably luminous. As a result of this additional red flux, there is a feature at the same position on the bolometric lightcurve of most SNe Ia. These rise, fall and secondary maximum timescales are for an average SNe Ia, but around maximum a range of light–curve widths are seen and the strength of the secondary varies from event to event. These features can be seen on the multicolour SNe Ia light curve shown in Figure 1.3.

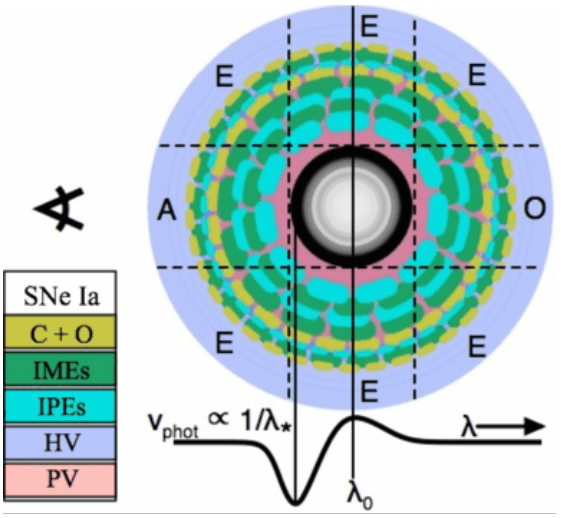

FIGURE 1.4: Schematic representation of a stratified ejecta, and how a spherically sharp and embedded photophere creates a P-Cygni profile. The high-velocity (HV) region is shown in purple, and the photospheric velocity (PV) material in pink. Regions visible to an observer in absorption (A) and emission (E) are labelled, as is the region that is occulted (O). Figure adapted from review of Parrent et al. (2014).

The typical optical spectral features of SNe Ia can be seen in Figure 1.2, which shows a template maximum light spectrum, with the dominant spectral features labelled. The near–ultraviolet (NUV) portion of the SED is heavily blanketed by iron peak elements (IPEs). At early phases, and around maximum light, the main features in SNe Ia spectra are due to IPEs such as Fe and Co and intermediate mass elements (IMEs) including O I, Mg II, Si II, and Ca II, the ashes of thermonuclear burning. As a result of being emitted by an expanding ejecta, the spectral features are seen as P Cygni line profiles (Figure 1.4).

The spectral behaviour of SNe Ia is typically quantified by line strength, via measurements of pseudo equivalent line widths (pEWs; Branch et al., 2006; Hachinger et al., 2008; Silverman et al., 2012a; Maguire et al., 2014) and velocities (Benetti et al., 2005; Wang et al., 2009) of the most distinctive features. The velocity evolution of these properties, as well as the value at maximum light is used to sub–divide the class into smaller subclasses. Most SNe Ia fall into the 'Branch–normal' spectroscopic sequence (Branch & Tammann, 1992; Branch et al., 1993), although a significant fraction (Li et al., 2011) are spectroscopically perculiar. These spectroscopic peculiarities are, broadly speaking, reflected in a corresponding photometric diversity, discussed in Section 1.3. Under–luminous SNe Ia with red colours, narrow light curves and no secondary maximum show spectroscopic similarity to SN 1991bg (Filippenko et al., 1992a), displaying lines of Ti II and extremely strong Si II absorption, while over–luminous SNe Ia are often spectroscopically well matched with SN 1991T (Filippenko et al., 1992b), do not show strong Ca II or Si II before maximum light and are often observed to have a prominent secondary

maximum. The divide between 'normal' and 'peculiar' SNe Ia has blurred in recent times, in part due to discoveries of individual SNe that defy immediate classification such as SN 1999aa (Garavini et al., 2004), SN 2002cx (Li et al., 2003),SN 2002ic (Hamuy et al., 2003), SN 2005gj (Prieto et al., 2005; Aldering et al., 2006), PTF 09dav (Sullivan et al., 2011a), PTF 10ops (Maguire et al., 2011), PTF 11kx (Dilday et al., 2012), SN 2012fr (Maund et al., 2013; Childress et al., 2013a).

While observations of the light curves and spectra of SNe enable us to classify events, without further analysis it is impossible to decipher the physical processes that make each of the subclasses distinct. And, as has been shown by the increasing observed diversity, it is difficult to classify objects based on observations alone. To understand the observations, we must consider the physics.

1.3 The Physics of SNe Ia

Minor variations aside, the observed emission from most Type Ia Supernovae is remarkable not only in its intensity, but also uniformity, both spectroscopic and photometric. This homogeneity is a product of a common power source, the radioactive decay of IPEs, the amount of which falls in a fairly narrow range, due in part to the Chandrasekhar Mass $M_{ch} \sim 1.4 M_{\odot}$, the limit at which electron degeneracy pressure can no longer hold up the star, providing a ceiling on the CO WD mass. Shortly after explosion the bulk of the optical light curve, in *normal* SNe Ia at least, is powered by the radioactive decay of ^{56}Ni to ^{56}Co, and at later times, after the peak in emission, the decay of ^{56}Co to ^{55}Fe in the following decay chain

$$^{56}\mathrm{Ni} \xrightarrow{\mathrm{t}_{1/2}=6.08\,\mathrm{d}} {}^{56}\mathrm{Co} \xrightarrow{\mathrm{t}_{1/2}=77.2\,\mathrm{d}} {}^{56}\mathrm{Fe} \tag{1.1}$$

(Hoyle & Fowler, 1960; Colgate & McKee, 1969; Arnett, 1982; Pinto & Eastman, 2000a). Following the explosion the ejecta expansion is homologous and adiabatic, which causes significant cooling, with the SN only becoming optically bright once heated by the gamma rays from ^{56}Ni decay diffusing through the young ejecta. The first photons that diffuse out of the ejecta result from energy deposition from the decay of the ^{56}Ni that is located furthest out in the ejecta (Piro & Nakar, 2013). This diffusion is not instantaneous, and as such, there may be a dark phase between explosion and t_0, as has recently been suggested by abundance tomography (Hachinger et al., 2013; Mazzali et al., 2014). The escape of the first photons starts the rise of the light curve, and as the ejecta expands, photons generated by energy deposited by deeper ^{56}Ni escape. The expanding ejecta become less opaque, increasing the amount of energy escaping, and the point at which the energy radiated is equal to the energy deposited by ^{56}Ni is identifiable as a

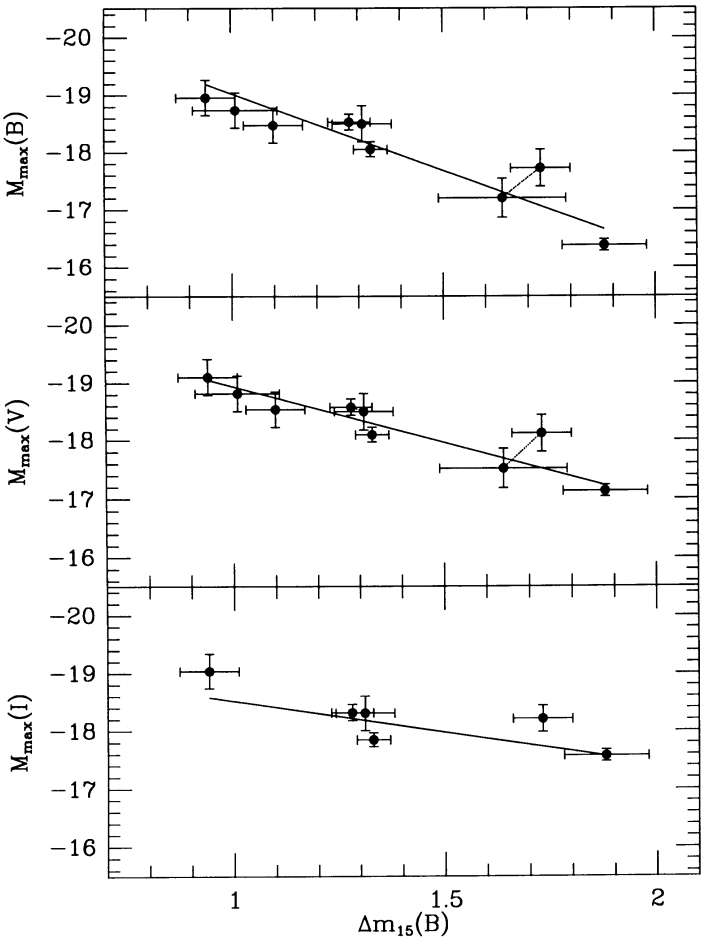

FIGURE 1.5: Decline rate–peak luminosity relation for the nine best–observed SNe Ia from Phillips (1993). Absolute magnitudes in B, V and I are plotted vs. $\Delta m_{15}(B)$, which measurese the amount in magnitudes that the B light curve drops during the first 15 days following maximum. Figure and caption from Phillips (1993)

point of inflection on the light curve (Pinto & Eastman, 2000a). The ejecta continue to radiate previously deposited energy as well as the energy instantaneously deposited by ongoing ^{56}Ni decays, and consequently the peak of the SN light curve occurs several days later. The time between the first photons escaping the ejecta (not necessarily the time of explosion) and this peak is the 'rise-time', $t_{\rm rise}$.

The peak bolometric luminosity reached is closely related to the mass of ^{56}Ni synthesised, known as Arnett's Rule (Arnett, 1979, 1982). The relatively narrow possible ranges of total ^{56}Ni mass gives rise to the relatively low dispersion in peak magnitudes. As well as a correlation with ^{56}Ni mass, the peak luminosity of SNe follow a tight relation with the light–curve width, the 'width–luminosity relation' (WLR), first formulated as the decline–rate luminosity relation (Figure 1.5 Phillips, 1993; Phillips et al., 1999). Previous efforts to extract such a relation from the data (Pskovskii, 1977, 1984) had

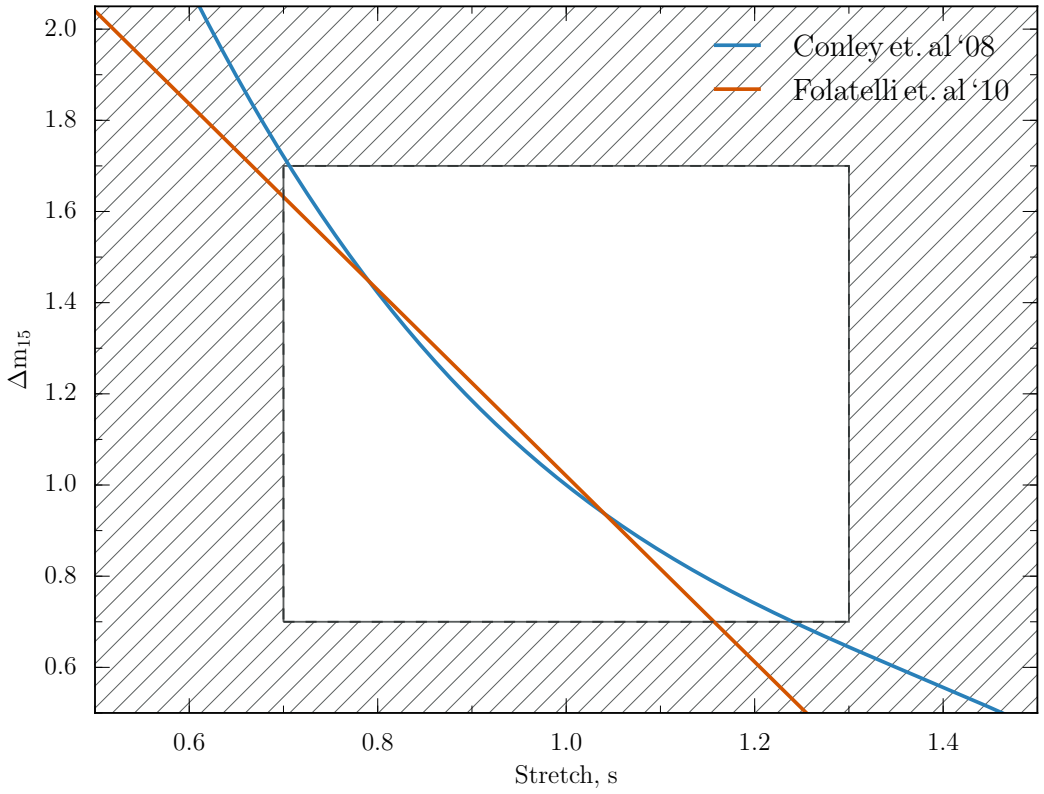

FIGURE 1.6: A comparison between the Δm_{15} to Stretch conversions used in the literature. Shown are those used by Folatelli et al. (2010) (orange) and Conley et al. (2008b) (blue)

proved contoversial, with initial results suggested to be driven by photometric contamination from the host galaxy (Boisseau & Wheeler, 1991). However, with the advent of CCD observations, and with two objects that were extreme examples of either ends of the distribution (SN 1991T and SN 1991bg), Phillips (1993) was able to confirm the relationship.

The light–curve width, and the degree of variation seen across the population of SNe Ia is commonly quantified through parameters such as stretch, x_1 or $\Delta m_{15}(B)$. Stretch (Conley et al., 2008a) and x_1 (Guy et al., 2007) are template based parameters taking into account the behaviour of the SN either side of maximum light, while $\Delta m_{15}(B)$ is simply the fall in B–band magnitudes 15 days post–peak (Hamuy et al., 1996b). While conversions between the different systems should not be used for precision work, a 'normal' SNe Ia has a stretch, $s = 1$, $x_1 = 0$ and $\Delta m_{15}(B) \simeq 1.1$. A figure showing approximate conversions, and the relative areas of the normal and peculiar SNe in stretch and $\Delta m_{15}(B)$, is shown as a rough guide in Figure 1.6.

Also present in Figure 1.5 is evidence of a colour dependence - the decline rate in B is most closely tied to the peak luminosity in B band, whereas in I it is only the most extreme outliers that drive the relationship. Not only are brighter SNe broader than

average, they are bluer as well, meaning as well as a broader–brighter, narrower–fainter WLR, there is a brighter–bluer, fainter–redder colour–luminiosity relationship (Riess et al., 1996).

The width of the bolometric light curve of a SN Ia is related to the photon diffusion time (Pinto & Eastman, 2000b; Woosley et al., 2007). A photon emitted in a ^{56}Ni decay will random walk out of the ejecta, depositing energy at each collision. A longer diffusion time means that the photon spends longer within the ejecta and as such deposits more energy in total, both increasing the peak brightness and stretching the light curve. The important parameters for determining the bolometric diffusion time are the mass of the ejecta, the kinetic energy, the radial distribution of ^{56}Ni and the effective opacity (Woosley et al., 2007). The opacity increases with the ionisation state of Fe-group elements, which blanket the blue, and, as this increases with temperature, links opacity to the ^{56}Ni mass - as hotter, brighter SNe Ia have more ^{56}Ni.

As the ejecta expands and cools, the photosphere moves deeper into the ejecta. As a result, the earliest spectra are imprinted with features from the material furthest out in the ejecta, which typically has the highest velocities. As the ejecta is stratified (Stehle et al., 2005) this outer material is made up of intermediate mass elements (Figure 1.4), however direct observations of gamma–rays from the nearby SNe Ia SN 2014J (Isern et al., 2016) and spectral modelling of the early absorption features (Tanaka et al., 2008a) suggest ^{56}Ni is also present.

1.3.1 Spectral Velocities

Measurement of spectral velocities and their evolution is a powerful tool for probing the underlying physics at play in the SN. Single epoch measurements of Si II λ4131 can be used as a first order estimation of the light–curve width (Chotard et al., 2011) suggesting a close relationship between velocity and ejecta conditions. Wang et al. (2009) divide SNe into two groups using the Si II 6355Å velocity at maximum light, $v_{si} = 12,000$ km s^{-1}, and find that high velocity SNe have a narrower range of both peak luminosity and light curve width. Benetti et al. (2005) used the photospheric velocity evolution of SNe to define high-velocity gradient (HVG) and low-velocity gradient (LVG) SNe using the rate of change of the Si II 6355Å feature, $\dot{v} = \Delta v/\Delta t$, from maximum light until the feature disappears. In their definition HVG have $\dot{v} > 70$km s^{-1}day^{-1} and LVG $\dot{v} > 60 - 70$km s^{-1}day^{-1}.

In addition to the ejecta stratification contributing to different velocities in different species, some features are decoupled into a high-velocity feature (HVF) and photospheric velocity (PV) feature at early times, notably in Ca II $H\&K$ and Si II 6150 Å (Figure 1.2)

(Wang et al., 2003; Gerardy et al., 2004; Mazzali et al., 2005a,b; Childress et al., 2014; Maguire et al., 2014). The origin of these HVFs is not yet fully understood, but current interpretations attribute them to either interaction with a circumstellar medium (CSM) very close to the SN, some abundance enhancement of IMEs above the photosphere (Mazzali et al., 2005a,b), or ionisation state variation in the IMEs (Blondin et al., 2013). Childress et al. (2014) find that there is a correlation between the strength of the observed HVFs and light curve width. In addition, the same study shows that objects with a low v_{si} have stronger HVFs.

1.3.2 Post Maximum

The behaviour post maximum is driven by a rapid release of energy due to an IPE ionisation state change, is seen (Kasen, 2006). In this formulation, as a region of ejecta cools to $\sim$ 7000K, the IPEs, particularly Fe and Co, relax from doubly ionised to singly ionised. This dumps a large amount of energy into the thinning ejecta, heating it back up and slowing the decline, or causing another peak depending on the wavelength.

Whether a secondary peak is displayed or not, the ejecta eventually become optically thin, allowing gamma rays to freely stream out of the ejecta, but still trapping positrons (Chan & Lingenfelter, 1993). The light curve eventually falls onto a linear ^{56}Co radioactive decay slope (Contardo et al., 2000; Lair et al., 2006), observed to be slightly steeper in the case of incomplete trapping. Extremely late time observations of some nearby SNe see the transition from a ^{56}Co slope onto one that is a combination of ^{57}Co and ^{55}Fe (Graur et al., 2016) as predicted by models (e.g. Seitenzahl et al., 2009).

As the SN ejecta becomes optically thin at $\tau > 50$ the spectrum becomes dominated by forbidden emission lines from IPEs at the center of the ejecta (Axelrod, 1980). In this nebular phase it is possible to measure ^{56}Ni masses, and constrain the mass of the progenitor (Childress et al., 2015).

1.3.3 Local Environment

The analysis of the spectra of SN 2006X by Patat et al. 2007 identified the Na I D doublet (5889.95, 5895.92 Å), and linked it to the SN. Finding not only a strong galactic component, but also four offset features blueshifted with respect to the galactic component, which were interpreted as narrow shells or clumps of material. Over four epochs the velocity and strength of these features was observed to change, indicating their close proximity to the SNe. Following this detection, Blondin et al. 2009 undertook a systematic study of the Harvard-Smithsonian Center for Astrophysics (CfA) SN sample and

found further evidence of blueshifted Na I D in one object of their final sample of 31 SNe - SN 1999cl. It was noted that both objects suffer from a high degree of reddening, raising the prospect that the presence of such lines bears some connection to the environment. More recent work indicates that as many as 20% of SNe Ia show blueshifted Na I D absorption (Sternberg et al., 2011; Maguire et al., 2013).

1.4 SN Ia Progenitors and Explosion Models

Unlike a number of the other SN classes, SNe Ia occur in a diverse range of environments, not only those with evidence of very recent star formation. As a result of this, and due to the absence of hydrogen and helium in their spectra (by definition), SNe Ia are thought to be the progeny of low–mass stars. These stars, with a zero–age main sequence mass ($M_{\rm ZAMS}$) of $M_{\rm ZAMS} \lesssim 8M_{\odot}$ evolve off the main sequence and become CO WDs (Chandrasekhar, 1957). Recent observational evidence placing constraints on the radius of the primary consistent with that of a WD (Nugent et al., 2011; Bloom et al., 2012b), based on an absence of shock emission from SN 2011fe, support this. Isolated, slowly contracting WDs were first suggested as progenitors Finzi & Wolf (1967), but ruled out due to unphysical evolution requirements.

However, the mass distribution of WDs peaks at around $0.6M_{\odot}$ (Liebert et al., 2005), which means that in some way the WD must grow in mass to ignite. The mechanism for triggering the explosion is thought to be accretion of matter from a companion in a close binary system, which has held as the dominant theory since being proved viable (Wheeler & Hansen, 1971). The precise configuration of the progenitor system however, is still unknown and is a topic of ongoing research. Broadly, the candidate scenarios fall into two categories, Single Degenerate (SD) systems (Whelan & Iben, 1973a) and Double Degenerate (DD) (Iben & Tutukov, 1984) systems. The SD configuration is made up of a CO WD and a less evolved secondary, and the DD is usually made up of two CO WDs.

The trigger for ignition, which is often simplified as approaching M_{ch} (Carbon ignition at the centre of a non-rotating WD has been calculated to occur when the WD mass reaches $\sim 1.38{\rm M}_{\odot}$ (Arnett & Truran, 1969; Nomoto, 1982)) is in fact more properly understood as a region of the progenitor reaching the threshold pressure needed for fusion to take place. This can be provided by the mass threshold being reached, but can be achieved at both higher and lower masses. Higher masses can be achieved in rapidly rotating WDs, and lower mass progenitors can reach the requisite pressure by experiencing a compression due to, for example, violent accretion, collision between two WDs, or a surface detonation.

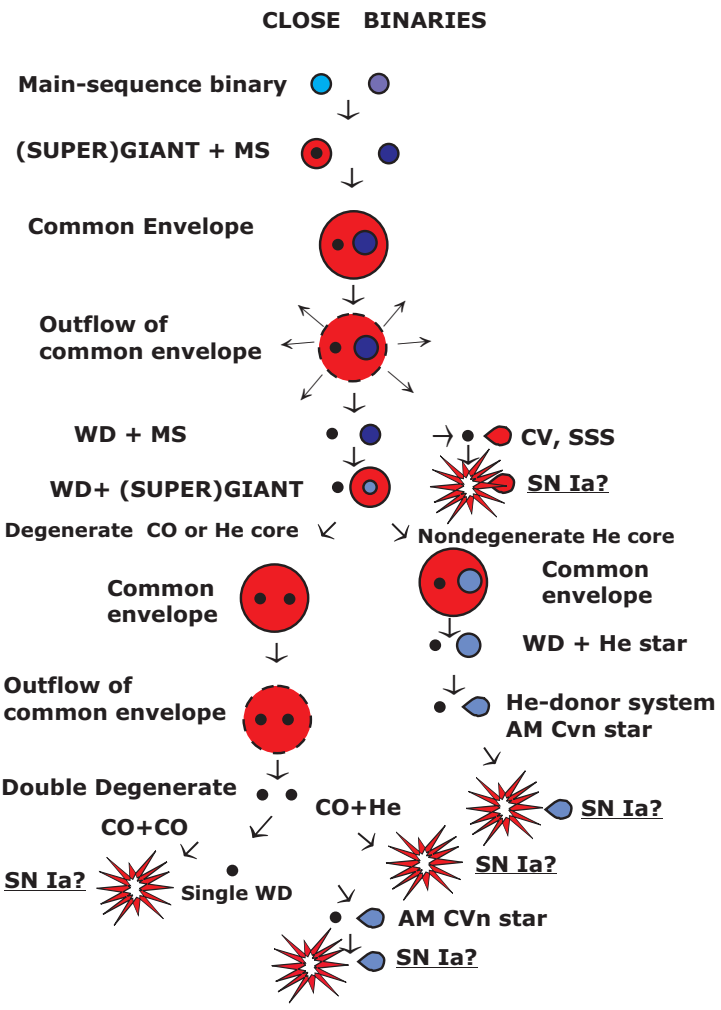

FIGURE 1.7: Formation of close dwarf binaries and their descendents scale and (color-coding are arbitrary). Figure and caption from Postnov & Yungelson (2014)

Figure 1.7 shows some of the many paths through close binary evolution, possibly ending in SNe Ia. It is likely that both of these channels occur in nature (see Section 1.4.3 and the review of Maoz et al., 2014), but the dominant mechanism is not yet clear. The likelihood of each outcome shown in Figure 1.7 depends on the specific treatment of the stellar evolution, and much is dependent on accretion rates and the intricacies of common–envelope evolution (see Ivanova et al., 2013; Postnov & Yungelson, 2014, for in–depth reviews). Models of SNe Ia must also attempt to match the observed delay–time distribution (DTD), the length of time between formation and the SN. The latest measurements of the delay time distribution find it takes the form of a powerlaw with an index ~ -1 (Maoz & Badenes, 2010; Graur et al., 2011; Maoz et al., 2012). Here we go into more detail about the most commonly discussed progenitor configurations.

1.4.1 Single Degenerate

As explained above, the SD scenario (Whelan & Iben, 1973b), consists of a massive WD gaining mass from a donor secondary, either a main sequence or more evolved (sub)giant star, and approaching M_{ch}. From formation, the binary evolves, with the more massive star (the primary) moving off the main sequence evolving into an asymptotic giant branch (AGB) star, containing a degenerate CO core. As the primary star expands, depending on separation, the primary either undergoes a period of Roche-lobe overflow (RLOF) or a common envelope forms without such a phase of mass exchange. In either circumstance, an envelope is thought to eventually envelop both stars before being stripped, stopping any mass transfer. This is the case until the secondary itself evolves and begins to transfer mass via RLOF (or via a strong wind in some models). This configuration predicts the presence of hydrogen in the spectrum of the SNe, either swept up at very late times, or at very early times, when the SN ejecta impacts and shocks the secondary star.

Most iincarnations of the SD model requires a fairly low and stable mass transfer rate, around $\sim 10^{-8} - 10^{-7} M_{\odot}$ year^{-1}. If it is too low then recurrent novae will remove more mass than was accreted (Nomoto, 1982; Livio & Truran, 1992) - if it is too high then rather than forming a static envelope, a wind is thought to remove the extra material (Hachisu et al., 1996). Accreting White dwarfs (AWDs) in this regime should be X–ray bright super–soft sources (SSS), capable of sustaining continuous hydrogen burning (van den Heuvel et al., 1992; Kahabka & van den Heuvel, 1997). However there is some debate as to whether X–ray observations support a large enough population of SSSs to contribute meaningfully to the overall SN Ia rate, with Gilfanov & Bogdán (2010) placing a limit of only $\sim 5\%$ of SNe Ia in early–type galaxies from such binaries. On the other hand, Hachisu et al. (2010) suggest that SSSs spend a factor of 10 less time in the SSSs phase than claimed by Gilfanov & Bogdán (2010), meaning the limit should be raised accordingly.

1.4.2 Double Degenerate

Proposed by Webbink (1984) and Iben & Tutukov (1984), the DD scenario involves the merger of two CO WDs, which together approach M_{ch} and trigger thermonuclear burning. The stars form in a binary, and undergo evolution including two common envelope phases. The end of the second common envelope phase is triggered by mass loss, with the envelope stripped away from the binary. The binary then loses orbital angular momentum through gravitational wave radiation, shrinking the separation between the two bodies, merging on a timescale of anywhere between 10^5 to 10^{10} years, depending

on initial orbital separation and period (Tutukov & Yungelson, 1979; Ruiz-Lapuente, 2014).

In most models, the less massive WD is disrupted and accreted onto the secondary, however a number of mechanisms have been put forward for the precise trigger for ignition following this accretion phase. If carbon burning is ignited on the surface (an 'off–center C flash' Saio & Nomoto, 1985), a non–explosive flame will travel through the ejecta, converting the CO primary into a oxygen, neon and magnesium WD. Subsequent electron captures by Ne and Mg would cause the WD to collapse into a neutron star (Nomoto & Iben, 1985) without a SN. Recent refinements have shown this collapse can be avoided if the accretion rate is low enough ($\dot{M} \lesssim 10^{-5} M_{\odot}$ year^{-1} ; Yoon et al., 2007). If, rather than a binary the progenitor system was a triple, a SN can be triggered by the collision of two WDs head on in a a 'violent merger' by invoking resonances to increase the eccentricity of the system (Katz & Dong, 2012; Kushnir et al., 2013). By colliding head on, it is possible to avoid the problems with the tidal disruption picture, namely the surface burning or the triggering of dynamical burning during the DD tidal disruption itself (Pakmor et al., 2012).

The rate of WD–WD mergers can account for the SNe Ia rate (Badenes & Maoz, 2012), however, the rate of super–Chandrasekhar pairs is only $\sim 1/14$. If sub–Chandrasekhar mergers can prove to be a viable source of SNe Ia, then the DD channel could produce the bulk of the observed SNe Ia. A number of 'Super–Chandrasekhar' events (Howell et al., 2006) that have inferred progenitor masses $M > M_{ch}$ have been observed, but are sufficiently unusual in their characteristics that it is unlikely they contribute to the overall normal population. Endeavours in this area are promising, with models consisting of a He WD and a CO WD able to broadly reproduce the characteristics of light curves and spectra (Sim et al., 2013). Such a configuration does not seem to be uncommon, with Napiwotzki et al. (2007) finding a much higher frequency of He WDs than CO WDs in a sample of over 1000 WDs.

1.4.3 Progenitor Signatures

The lack of hydrogen observed in the spectra of normal SNe Ia is evidence against the SD scenario. However, recent observations of Hα in SN 2011kx reported by Dilday et al. (2012) and in a further analysis of so–called SNe Ia CSM (circumstellar medium) by Silverman et al. (2013a) show that, counter to the definition of SNe Ia, hydrogen is sometimes detected.

If SNe Ia are the product of WD mergers, much in the same way as the prediction of hydrogen emission in SD, unburned C and O should be seen at high velocities. Folatelli

et al. (2012) see unburned carbon in the spectra of 30% of the SNe from the Carnegie Supernova Project (CSP). Significantly, high–velocity oxygen was observed in the very early spectra of SN 2011fe (Nugent et al., 2011), with analysis of a very early time series also showing significant amounts of unburned carbon (Parrent et al., 2012). Coupled with these observations, further evidence for a DD scenario is the lack of observations of a surviving companion star in supernova remnants (SNRs; Schaefer & Pagnotta, 2012).

An observational diagnostic of the SD progenitor channel is the interaction between the SN ejecta and a material from a non-degenerate secondary, both direct and indirect. Some models predict interaction with a companion to be visible as hydrogen and helium present in the late time spectra, depending on the type of companion (Marietta et al., 2000; Pakmor et al., 2008). Ongoing observational searches are increasingly placing limits on the amount of swept up material (Mattila et al., 2005; Lundqvist et al., 2013; Shappee et al., 2013; Lundqvist et al., 2015; Maguire et al., 2016). Interestingly, in their study of 11 SNe Ia Maguire et al. (2016) report a tentative detection of Hα emission in a late-time spectrum of SN 2013ct, corresponding to $\sim 0.007 M_{\odot}$ of stripped or ablated material from a companion star. No evidence of similar emission is found in the remaining 10 objects. Another tracer of indirect interaction, time varying blueshifted Na I D features of the kind seen in SN 2006X (Patat et al., 2007) are likely linked to outflows from the progenitor system, and have been likened to those seen in both classical and recurrent novae (Williams et al., 2008; Patat et al., 2011), hinting that the progenitors of these kinds of events are via the single degenerate channel.

Another mechanism for interaction is the violent direct collision between the expanding SN ejecta and the secondary itself (Kasen, 2010; Pan et al., 2012). Instead of the shocked material being part of the primary, as is the case with CC–SNe, collision between the ejecta and companion creates a strong reverse shock in the envelope of the companion. This mechanism predicts emission on two timescales; seconds and days, in two different energy regimes; X-ray and UV/optical.

The prompt emission from the collision is a result of the companion punching a hole in the ejecta, halting the expansion and allowing shock emission to stream away. The flux increase over longer timescales is powered by photons diffusing into the ejecta material, unable to escape before the cavity is filled in by the overrunning ejecta. Both channels for emission have a strong dependence on orientation, companion radius and separation, and perhaps only $\sim$ 10% of SD SNe will have favourable viewing angles for this to be seen (Kasen, 2010).

While initial observational efforts to search large samples for such emission did not find evidence of any contribution from progenitor interaction (Bianco et al., 2011; Hayden et al., 2010b), the non-detection enabled Bianco et al. (2011) to place a 3σ upper limit on

the RG-WD binary fraction at 20%. Additionally the analysis of Hayden et al. (2010b) strongly disfavours a RG companion, even if the SD channel dominates, in line with constraints from radio searches (Panagia et al., 2006).

However, in the case of iPTF14atg, UV and optical observations by the Swift Space Telescope triggered immediately after detection found strong but declining emission in all three UV bands and excess flux in u and b (Cao et al., 2015). The authors ruled out spherical emission mechanisms such as shock cooling and CSM interaction and found that companion interaction provided the best fit to the data, in case where the separation between the binary was less than $100R_{\odot}$. However Cao et al. (2015) show that iPTF14atg is spectroscopically similar to the under-luminous 91bg–like SN 2002es (González-Gaitán et al., 2014), implying that this may not be behaviour seen in normal SNe Ia.

Shock heated cooling from interaction with a sub stellar companion has been put forward to fit the light curve of SN 2015F (Im et al., 2015). While in SN 2012cg a companion of around $6M_{\odot}$, using the models of Kasen (2010) has been proposed (Marion et al., 2016). In the case of SN 2012cg, the lightcurve returns to normal power-law rise shape at phases later than $\tau > 14$, meaning that there is a window of ~ 4 days after the first light to catch such emission. Though the strongest emission is expected, and in the case of SN 2012cg, observed, in the UV, with a large enough companion the tail of the shock can appear in optical wavelengths.

The case for interaction in SN 2012cg is far from settled however, with Maguire et al. (2016) putting stringent limits on Hα emission from swept up material at late times (equivalent to a solar metallicity mass limit of $\mathrm{M}_{\mathrm{H}\alpha} < 0.005\mathrm{M}_{\odot}$ at 3σ). The Marion et al. (2016) result is also with tension with deep radio studies with the VLA (Chomiuk et al., 2012, 2016) and the early optical observations of Silverman et al. (2012b) (assuming certain viewing angles). The fits of (Marion et al., 2016) fit the U-band well, but overpredict the observed B- and V-band flux at early times by an order of magnitude (see e.g. Figure 6 of Silverman et al., 2012b). Supporting the result however, is the analysis of HST observations which Graur et al. (2016) find to be better matched to synthetic yields from SD models. Although the authors concede that their observations are also compatible with an additional contribution from a light echo. Obviously the matter is unresolved, and merits further study.

Though unusual, early Hα emission features have been detected in a number of SNe Ia, initially in the prominent cases of SN 2002ic (Hamuy et al., 2003) and SN 2005gj (Prieto et al., 2005; Aldering et al., 2006), however 'hybrid Ia/IIn' have been the subject of some debate (cf. Benetti et al., 2006; Trundle et al., 2008; Fox et al., 2015). The first '*unambiguous*' detection of CSM in emission in an otherwise normal SNe Ia was

made by Dilday et al. (2012) in the spectra of PTF 11kx, which showed strong narrow Hα and Ca emission around maximum light, with both features developing prominent broad components $\sim$ 40 days after maximum light. This emission is a signature of the SN ejecta interacting with the CSM, converting the kinetic energy of the ejecta into radiation via shock interaction. Not as broad or bright as SN 2002ic and SN 2005gj, and showing modest host extinction ($\sim$ 0.5 mag), the spectra of PTF 11kx demonstrate a striking similarity to not only SN 2002ic, but also the slightly overluminous (but otherwise normal) SNe Ia SN 1999aa (Garavini et al., 2004). PTF 11kx also demonstrated Na I D similar to that observed in SN 2006X and took place in a spiral galaxy with a mass and metallicity typical of SNe Ia hosts (Dilday et al., 2012) whereas SN 2002ic and SN 2005gj both occurred in low metallicity hosts with very high star formation (Aldering et al., 2006). In effect, PTF 11kx was to bridge the gap between photometrically normal SNe Ia, and the extreme broad/bright CSM objects. The presence of the lines, and the spectral evolution, are interpreted as swept up material from a recent nova, confined in the equatorial plane. The Hα emission persists until approximately a year later (Silverman et al., 2013c), when the emission ceases as a result of SN ejecta overtaking the CSM shells. Following the discovery of PTF 11kx, a number of studies have attempted to search for misidentified SNe Ia-CSM within existing samples, notably Silverman et al. (2013a) who found 16 SNe Ia-CSM.

An alternative model, which explains the absence of hydrogen in most SNe Ia is accretion from a helium secondary, which deposits a helium layer directly onto the WD. This leads in most models to a shell detonation on the surface, driving a shockwave into the core of the WD, compressing it and raising the density to levels where it ignites a second, carbon detonation (Woosley & Weaver, 1994; Livne & Arnett, 1995; Shen & Bildsten, 2014). However, this so-called 'double detonation' process has also been suggested to be possible in the case where a He WD donor secondary provides the He rich material, meaning signatures of helium are not necessarily diagnostic of either channel.

1.4.4 Deflagration–to–Detonation Transition

One important process that must be dealt with, whatever the progenitor arrangement, is the deflagration–to–detonation transition (DDT). In order to synthesise the observed abundances of elements, the thermonuclear burning front must transition from a subsonic deflagration, to an explosive, supersonic detonation. This is known as a delayed detonation (Khokhlov, 1991; Arnett & Livne, 1994a,b). If such a transition does not occur, the resulting explosion is subluminous, and such a subclass of SNe, similar to SN 2002cx fit this model well (Fink et al., 2014; Magee et al., 2016). Alternatively, undergoing a detonation without first having a deflagration phase results in extremely

efficient burning, converting the overwhelming majority of the carbon and oxygen into IPEs, which as can be seen in Figure 1.2, is not what is observed. Instead, More complete descriptions of the DDT are currently an active research topic, with turbulence and flame thickness being key, although a self–consistent model has not yet been constructed (Schmidt et al., 2010; Woosley et al., 2011; Seitenzahl et al., 2013).

1.5 Use in Cosmology: SNe Ia as Standardisable Candles

We now turn to our primary motivation for studying SNe Ia in this thesis – the accelerating universe. The strongest evidence for an accelerating universe is currently provided by observations of high–redshift SNe Ia (Schmidt et al., 1998; Riess et al., 1998; Perlmutter et al., 1999; Knop et al., 2003; Astier et al., 2006; Wood-Vasey et al., 2007; Sullivan et al., 2011b; Betoule et al., 2014). These observations combine with a raft of other evidence, such as analysis of the Cosmic Microwave Background (CMB) anisotropies from both WMAP (Hinshaw et al., 2013) and Planck (Planck Collaboration et al., 2015) and measurements of the baryon acoustic peak using large galaxy samples (Eisenstein et al., 2005; Cole et al., 2005; Percival et al., 2014), and point towards a contribution to the mass–energy density of the universe from dark energy. Though the scatter in the peak B–band magnitude of SNe Ia is intrinsically quite low ($\simeq 0.5$ mag) for those objects defined as cosmologically normal i.e. excluding objects that fall outside of the ranges $0.7 \leq s \leq 1.3$ for stretch, and $-0.25 \leq (B - V) \leq 0.25$ for colour (e.g. Sullivan et al., 2011b), improvements are possible. The empirical relationships between light–curve width, colour and absolute luminosity (Section 1.3) can be used to correct the observed brightness and standardise the candle. For each SNe Ia a corrected absolute magnitude, $\mathcal{M}_{\rm corr}$ can be calculated

$$\mathcal{M}_{\rm corr} = \mathcal{M} - \alpha(s-1) + \beta\mathcal{C} \tag{1.2}$$

where α is the light–curve width correction parameter and β is that for the SN colour, $\mathcal{C}$. m, s and $\mathcal{C}$ can be determined from fitting individual SN light curves using fitting packages like SiFTO (Conley et al., 2008a) and SALT/SALT2 (Guy et al., 2005, 2007). $\mathcal{M}$, α and β are constants determined from fitting a cosmological sample of SNe Ia, to minimise the peak dispersion. By making these corrections, modern cosmological analyses achieve a scatter of < 0.15 mag in B–band (Kessler et al., 2009; Sullivan et al., 2011b; Suzuki et al., 2012; Rest et al., 2014; Betoule et al., 2014). There has been

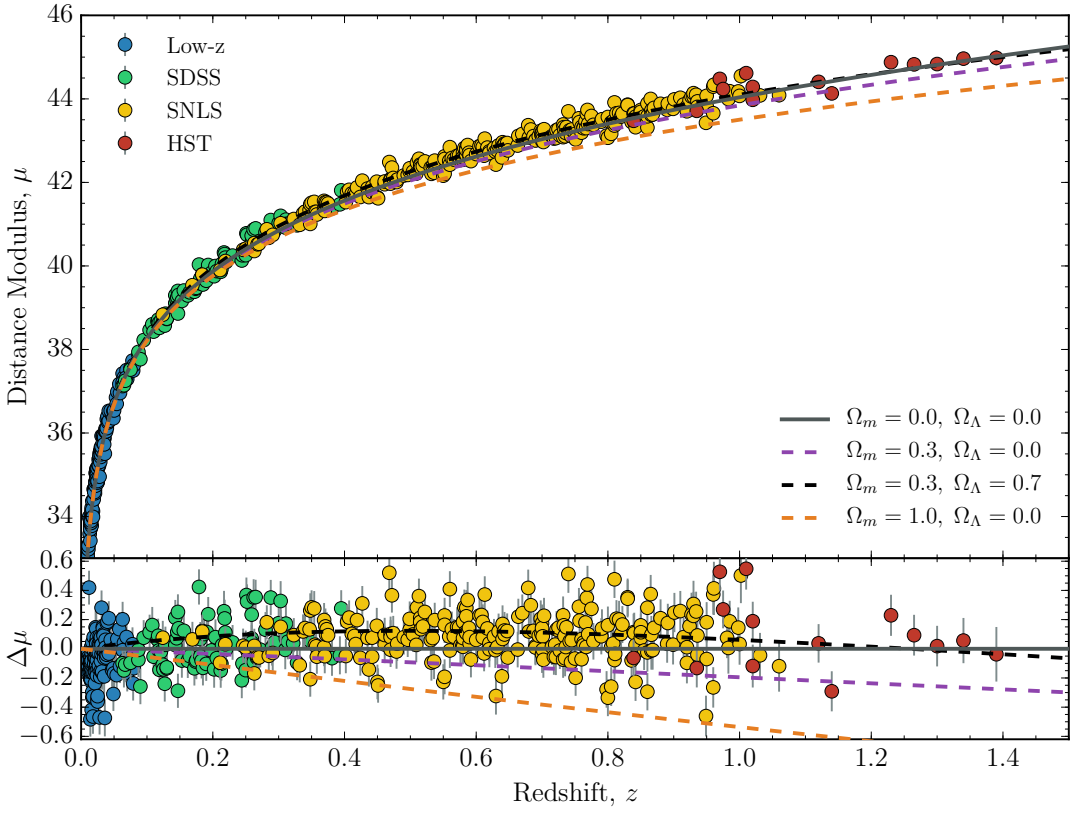

FIGURE 1.8: Hubble diagram of the combined sample of SNe Ia from Conley et al. (2011). The overplotted cosmological models are described in the text, and include Empty (grey solid), Einstein-de Sitter (purple dashed), a Lambda-CDM concordance model, black dashed), and a matter dominated case (orange dashed). The residuals from the predictions for an empty universe are shown in the bottom panel.

some evidence to suggest that in the NIR, SNe Ia are truly standard candles, without additional calibration (Barone-Nugent et al., 2012).

Subtracting the corrected absolute magnitudes from the observed apparent magnitude of the SNe gives the distance modulus, $\mu = m_{\rm obs} - \mathcal{M}_{\rm corr}$, which when plotted against redshift, z, forms the Hubble Diagram (Hubble, 1929), such as the one in Figure 1.8. These measurements provide a relative distance estimate to the SN, but by using both low- and high-redshift SNe, the diagram can be properly anchored, and cosmological parameters constrained. Figure 1.8 shows a hubble diagram for the combined sample of Conley et al. (2011). This is then compared against a cosmological model, with the difference being the 'Hubble Residual'. The theoretical distance modulus is:

$$\mu_{\rm model} = 5\log_{10}\mathcal{D}_{\mathcal{L}}(\mathrm{z_{hel}}, \mathrm{z_{cmb}}, \mathrm{w}, \Omega_{\rm m}, \Omega_{\rm DE}, \Omega_{\rm k}) + 25 \tag{1.3}$$

where $\mathcal{D}_{\mathcal{L}}$ is the c/H_0 reduced luminosity distance, Ω_m and Ω_{DE} are the fractional energy density of matter and dark energy respectively and z_{hel} and z_{cmb} are the heliocentric redshift and redshift relative to the CMB. w is the dark energy equation of state, the

ratio of its pressure to density $w = P/\rho c^2$. In a standard Λ + cold dark matter (ΛCDM) cosmology, a cosmological constant is assumed, and the dark energy equation of state, $w = -1$, meaning $\Omega_{DE} = \Omega_\Lambda$. Different model compositions of the fractional energy densities of dark energy and matter provide different predictions for the evolution of the distance modulus with redshift.

As well as the 472 SNe Ia, Figure 1.8 shows the predicted $\mu(z)$ for four cosmological models. Compared to an empty universe, the addition of non-zero (pressureless) matter density slows the expansion of the universe, decreases the predicted luminosity distance, meaning the SNe Ia are too faint. Introducing Ω_{Lambda} which exerts pressure, acts in the opposite sense, speeding up the expansion of the universe and increasing the predicted luminosity distance relative to an Ω_m dominated case. As we observe the Universe to be non empty, and as such, $\Omega_m > 0$ the models need the addition of the Ω_Λ component to match the data, increasing the predicted luminosity distance and implying cosmic acceleration.

In a combined joint light curve analysis (JLA) of two large SN surveys (the Supernova Legacy Survey, SNLS; Conley et al. 2011 and the Sloan Digital Sky Survey; SDSS-II Sako et al. (2014)) Betoule et al. (2014) measure $\Omega_m = 0.295 \pm 0.034$ for a flat, ΛCDM model, and for a flat wCDM model $w = -1.027 \pm 0.055$, consistent with a cosmological constant.

Additional corrections can also be made, to further improve the cosmological fits. It has long been noted that SNe Ia properties correlate with the properties of their host galaxies. In star forming galaxies, SNe Ia are brighter and broader than their counterparts in passive galaxies (Hamuy et al., 1995; Riess et al., 1999a; Sullivan et al., 2006). Sullivan et al. (2010) found evidence for a dependence on host galaxy stellar mass – finding SNe Ia of the same stretch and colour to be brighter on average by 0.08 mag in more massive (i.e. where the stellar mass of the galaxy satisfies $\log(M_{stellar}(M_\odot)) > 10$), low specific star formation rate (sSFR) hosts. This is usually interpreted as either a metallicity enhancement or a result of different progenitor ages - perhaps hinting at different progenitor paths. Decoding these variations in large samples, and in the best observed individual SNe from local surveys, is key to understanding these hugely important astrophysical objects.

1.6 Thesis Outline

In this thesis, we will leverage the unique properties of the large astrophysical dataset provided by the Palomar Transient Factory (PTF) to explore the physical processes

that underpin Type Ia supernovae (SNe Ia). In particular, we are concerned with discovering what physical insights about the SN Ia population we can determine from the large imaging and spectroscopic dataset that PTF has produced. This thesis will cover the very earliest part of the SN Ia light curve, probing the ejecta structure, the post–maximum light curve, probing the ^{56}Ni distribution, and finally assess the utility of SNe Ia as standard candles at different wavelengths. An outline of this work follows.

In Chapter 2 we present the sources of data used in this thesis, and define our main sample. The light curve fitting software and image reduction pipeline are introduced, and additonal calibration steps, including the removal of fringes from our images, detailed.

In Chapter 3 we explore the very early rising emission of SNe Ia, and lay out the physical framework used to understand these events at such epochs. A review of the literature follows, and the methods of parameterisation used are outlined. We define a sample of SNe Ia, a parameterisation and associated methodology to quantify the degree of diversity seen in SNe Ia at these phases. Finally, we use the nearby, well–observed SNe SN 2011fe and SN 2015F to verify our method.

In Chapter 4 the results of the fitting methodology outlined in Chapter 3 are presented. These results are compared to previous work, and to theoretical models.

In Chapter 5 we explore the post–maximum diversity of SNe Ia. In particular, we attempt to quantify the shoulder on the light curve in red optical bands. We are able to sucessfully model the emission, and quantify the diversity seen. We then use our results to explore the physical processes that drive the feature, and find that the assumption that the feature is driven in the same way as the secondary maximum in the near-IR is flawed.

In Chapter 6 we use a low–redshift multi–colour subsample of SNe Ia to construct a series of Hubble Diagrams. We compare the properties of SNe Ia as 'standardisable' candles in three filters: B, $R_{\rm P48}$ and $i_{\rm LT}$. We derive empirical corrections for each of the bands, to standardise our SN, and find that these corrections change drastically as a function of redshift, and that the rest-frame $R_{\rm P48}$ and $i_{\rm LT}$ are superior standard candles to B. In the case of $i_{\rm LT}$, we find this is the case even without correction for light curve width and colour.

In Chapter 7 we provide a summary of the work, and provide a future outlook discussing how the results from this thesis may be used in future surveys.

Chapter 2

Observations and Data

"My dear Kepler, what would you say of the learned here, who, replete with the pertinacity of the asp, have steadfastly refused to cast a glance through the telescope? What shall we make of this? Shall we laugh, or shall we cry?"

- Galileo Galilei, *Frammenti e lettere*, 1610

In the following chapter we describe the sources of data used in this work, the suveys and their data products. We also introduce the light curve fitting procedures used to establish observational parameters such as light curve width and SN optical colour. We also outline the selection criteria and resulting subsamples for each of the analyses in this work. Unless otherwise stated, the photometric data used was extracted by the author using a pre-existing photometric pipeline described in this chapter. The author was also responsible for performing additional calibration of photometric and spectroscopic data; notably de-fringing and extinction correction, which are also described in depth. The photometry produced was then fitted by the author using the SiFTO light curve fitting package. As a result, SN parameters for the described samples used in this thesis are a product of this combined procedure, unless otherwise specified.

2.1 Palomar Transient Factory - PTF

The Palomar Transient Factory (PTF; Law et al., 2009; Rau et al., 2009; Nugent et al., 2015), a three-and-a-half year, northern hemisphere, low-redshift sky survey is the main source of data for this work. The following is a description of its operation and the resulting SN sample.

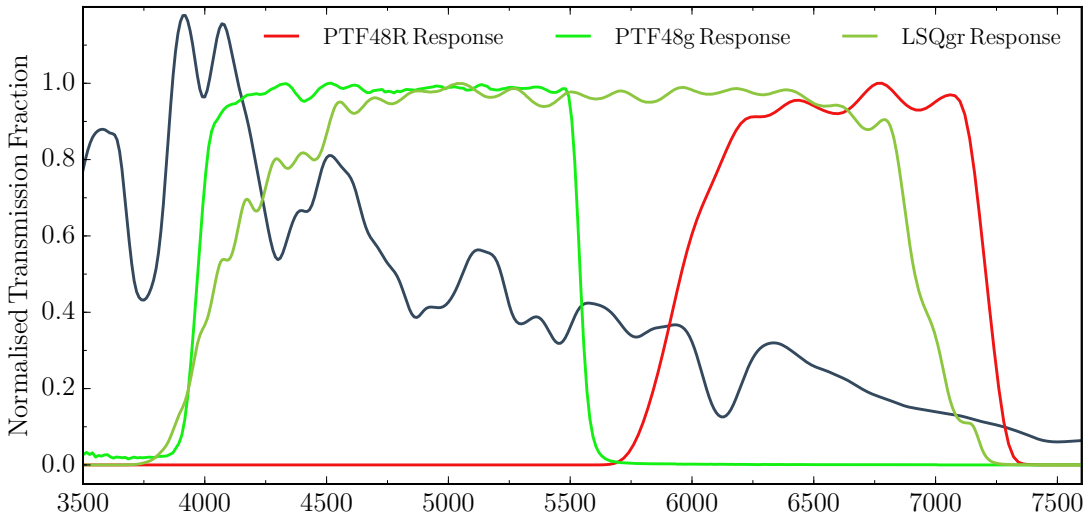

FIGURE 2.1: Filter transmission curves for PTF and LSQ, the main $R_{\rm P48}$ and secondary $g_{\rm P48}$ filters are shown, as well as $gr_{\rm LSQ}$, with a template maximum light SNe Ia spectrum to showing the dominant spectral features.

2.1.1 Survey Overview

PTF was a fully automated, wide-field, local rolling transient search that operated from 1st March 2009 to 31st December 2012, originally aiming to operate for around 290 nights yr^{-1}. PTF primarily used the CFH12k camera (Rahmer et al., 2008) mounted on the 48 inch Samuel Oschin telescope at Palomar Observatory (the P48 telescope). This combination gave a 3 deg^2 field of view and a plate scale of $1.01''$ pixel^{-1}, allowing a large survey footprint. The P48+CFH12k saw first light on 13th December 2008, and was used for routine scanning for initial photometric detection and subsequent folloup. The 60 inch Palomar telescope was then used for fast photometric followup of selected targets.

Followup selection was made on image subtraction data using a machine-learning algorithm (Bloom et al., 2012a), using a 'realbogus' score to downweight variable stars, asteroids and other artefacts, and flag up likely real transient cadidates. Following this, likely SN candidates were then visually inspected by collaboration members before being sent for spectroscopic confirmation. The survey operated primarily in a broad Mould R-band filter (hereafter R_{P48}), with occasional runs in a SDSSg filter (g_{P48}) around new moon. The transmission curves for these filters, and a template maximum light spectrum to highlight dominant spectral features, can be seen in Figure 2.1. A map of the on–sky locations of all 1258 of the spectroscopically confirmed PTF SNe Ia is shown in Figure 2.2.

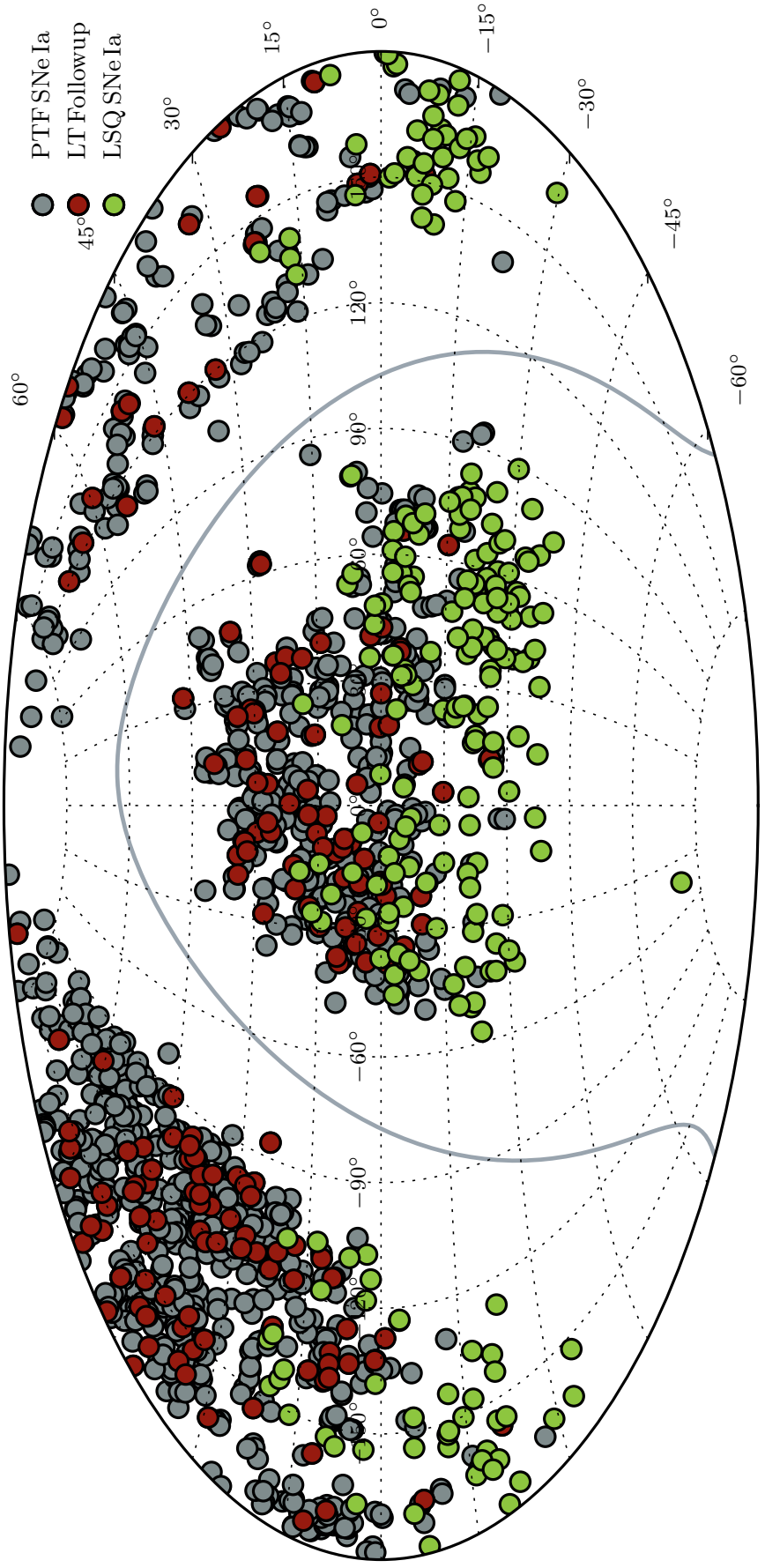

FIGURE 2.2: Spatial distribution of our SNe Ia, showing the PTF parent distribution, in light grey and the objects for which LT followup data was taken in red. Also shown, in green, are the 239 LSQ spectroscopically confirmed SNe Ia. Shown as a grey line is the Galactic plane.

2.1.2 Survey Cadence

One of the stated goals of PTF (Rau et al., 2009) was to fill in the gaps of the optical transient space. It therefore operated in two modes – the main 3-to-5-day cadence survey (5DC) and the dynamic cadence experiment (DyC).

The 5DC experiment ran yearly between 1st March and 31st October, using 65% of the available nights in all lunar phases. This covered approximately 8000 $\deg^2$, with galactic latitude $|b| > 30°$ and ecliptic latitude $|\beta| > 10°$, and with a median cadence of 4 days. Typically, the area active in a search was some 2700 $\deg^2$, with two 60s exposures being taken of an individual field, separated by an hour.

The DyC was run to detect events, such as extremely young local SNe Ia, on timescales of 60s to 3 days, with a continually updated targeting pattern. This approach proved successful, and a number of new classes of transients were identified and numerous objects added to existing rare sub-classes in the luminosity gap between novae and SNe (Kasliwal, 2012) as a direct result of PTF observations. Notably the faint-and-fast '.Ia' PTF bhp/SN2010X (Kasliwal et al., 2010), the faint-and-slow SNe Ia PTF 10ops (Maguire et al., 2011), Ca-rich halo transients PTF 09dav (Sullivan et al., 2011a), PTF 10iuv, PTF 11bij,(Kasliwal et al., 2012) and the Luminous Red Novae PTF 10fqs and PTF 10acbp (Kasliwal et al., 2011; Kasliwal, 2012).

2.1.3 Survey Redshift Distribution

Most of the volume sampled by PTF came as a result of its large area coverage rather than its depth, having a limiting magnitude of around $R_{\mathrm{P48}} \sim 20.5$, meaning PTF was a true low redshift survey. The redshift distribution for the parent sample of 1258 spectroscopically confirmed SNe Ia in PTF can be seen in Figure 2.3. This distribution has a median value $\hat{z} = 0.10$. The subsamples used in this work drawn from this parent dataset are used in the analysis in Chapters 3, 5, and 6.

2.1.4 Spectroscopic Followup

Spectroscopic followup was used to classify PTF transients using: the Palomar Observatory Hale 200-in and the double spectrograph, the William Herschel Telescope (WHT) and the Intermediate dispersion Spectrograph and Image System (ISIS), the Keck-I telescope and the Low Resolution Imaging Spectrometer (LRIS; Oke et al., 1995), the Keck-II telescope and the DEep Imaging Multi-Object Spectrograph (DEIMOS; Faber et al., 2003), the Lick Observatory 3m Shane telescope and the Kast Dual Channel

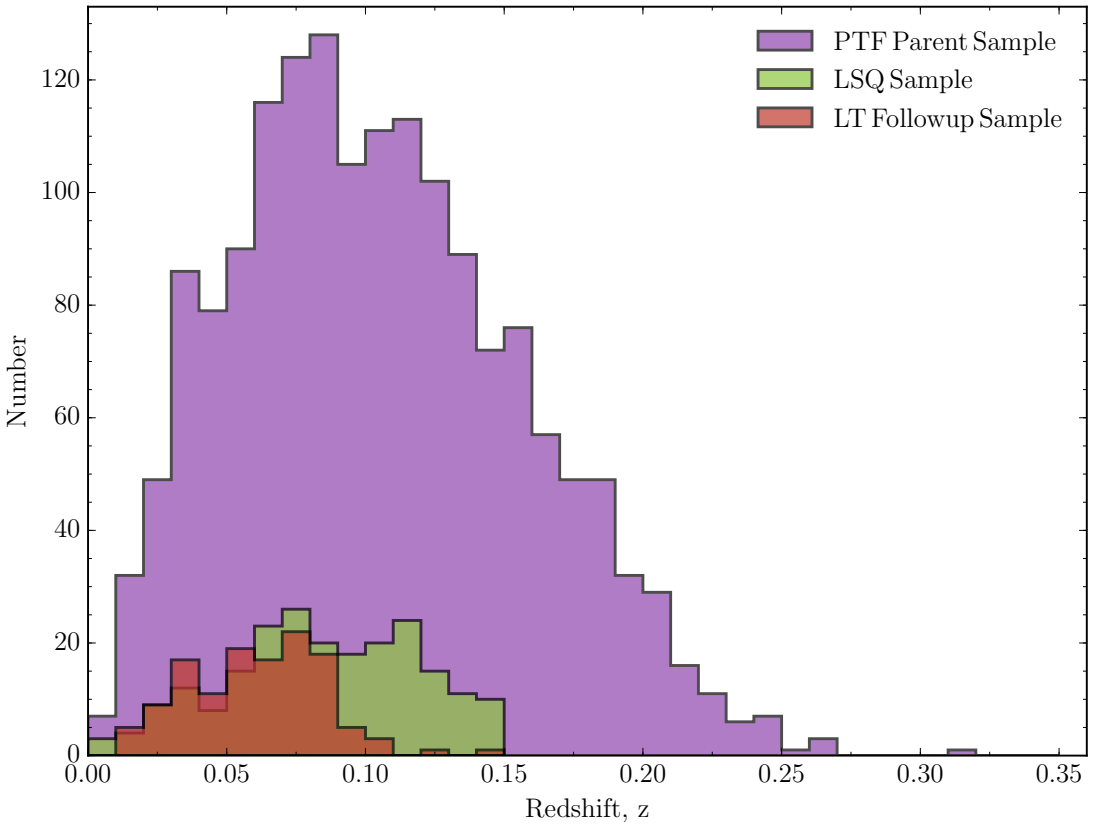

FIGURE 2.3: Histogram showing the redshift distribution for the 1258 spectroscopically confirmed SNe Ia PTF over the full survey period, 1st March 2009 to 31st December 2012 (purple). Also shown is that of the LSQ spectroscopically confirmed sample (green), comprising of 239 objects, and the LT subsample of 132 objects that passed our photometric pipeline.

Spectrograph (Miller & Stone, 1994), the Gemini-N telescope and the Gemini Multi-Object Spectrograph (GMOS; Hook et al., 2004), and the University of Hawaii 88-in and the Supernova Integral Field Spectrograph (SNIFS; Lantz et al., 2004). All of the classification spectra for SNe in this work are available via the WISeREP archive (`http://wiserep.weizmann.ac.il/`; Yaron & Gal-Yam, 2012), and are also presented in Maguire et al. (2014).

2.2 Other Sources of Data

In addition to the core PTF sample data, we use supplemental multicolour followup data on a subsample of the objects from the Liverpool Telescope. As well as PTF, the La Silla QUEST Transient Search provides us with a number of SNe of a comparable redshift, cadence and photometric quality to augment our sample. We also describe the data provided by the Public ESO Spectroscopic Survey of Transient Objects and Las Cumbres Observatory Global Telescope network, that enable us to study the nearby

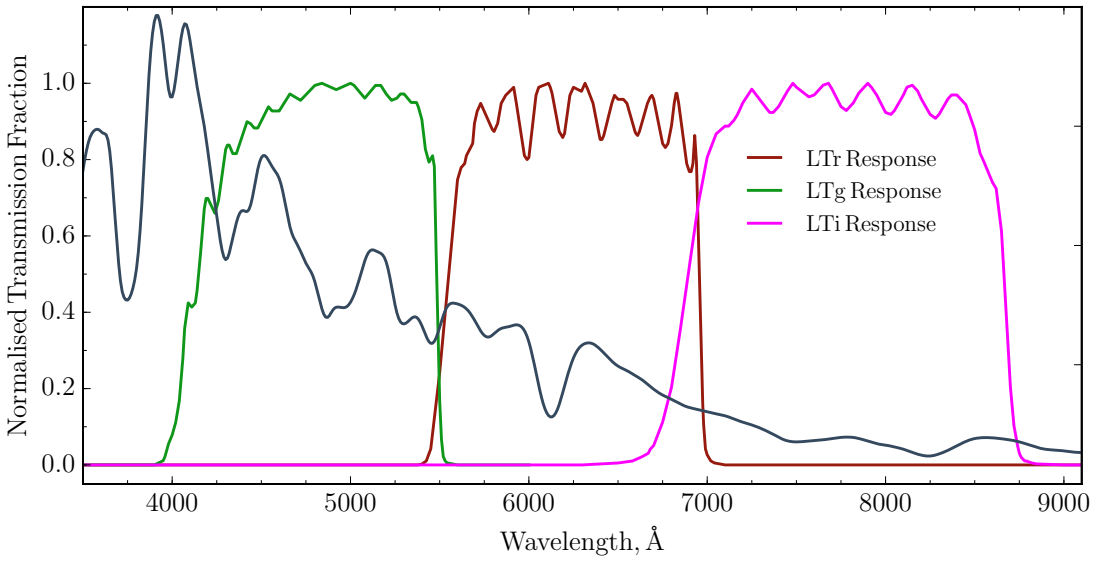

FIGURE 2.4: Filter transmission curves for the Liverpool 2m Telescope. $g_{\rm LT}$, $r_{\rm LT}$ and $i_{\rm LT}$ are shown, with a template maximum light spectrum to illustrate the dominant spectral features in each.

SN 2015F. This object, though not observed by PTF, provides a powerful check on our analysis methods.

2.2.1 Liverpool Telescope - LT

The 2m Liverpool Telescope (LT; Steele et al., 2004) is located at the Spanish Observatorio del Roque de los Muchachos, La Palma, and operated by Liverpool John Moores University. The dataset consists of followup observations of 181 supernovae from PTF under a number of programmes, from both the RATCAM and IO:O instruments. LT followup was generally triggered on SNe from PTF that were spectroscopically classified before maximum, and were below a threshold redshift of 0.09, when time was available. In addition, exceptionally luminous or otherwise interesting objects were also followed above this cut-off.

Observations were initially made with RATCam, the LT optical CCD imager, and following its replacement, the wider field-of-view imager IO:O (`http://telescope.livjm.ac.uk/Tellnst/Inst/IOO/`). The g and r filters used by LT (hereafter $g_{\rm LT}$ and $r_{\rm LT}$), cover a slightly narrower spectral range than the $g_{\rm P48}$ and $R_{\rm P48}$. The width of the $r_{\rm LT}$ in particular means that it often fails to show the characteristic shoulder on the light curve decay, seen in $R_{\rm P48}$. To account for this, we have coverage that extends into i-band, hereafter $i_{\rm LT}$. Due to the selection criteria the redshift distribution of this sample of 181 objects, which can be seen in Figure 2.3 is both narrower and lower on average; the mean redshift is $\hat{z} = 0.061$. The stretch distribution of this sample can be seen

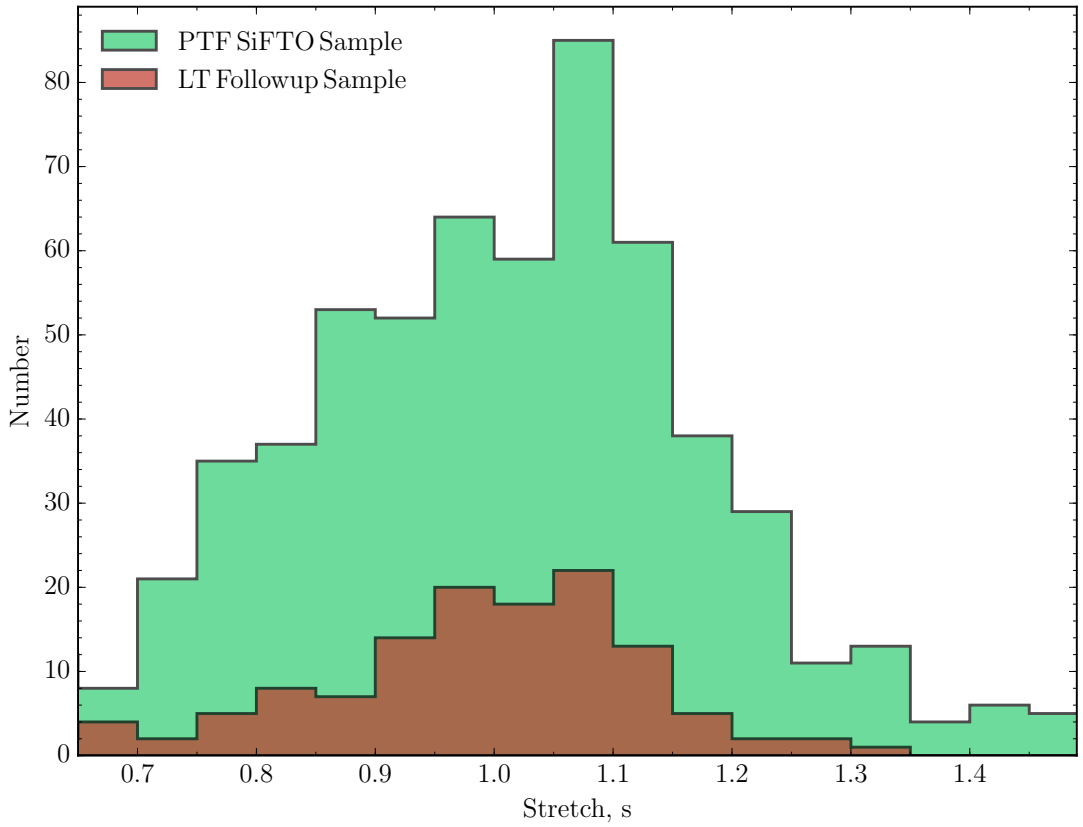

FIGURE 2.5: Histogram showing the stretch distribution of the parent sample (green) that passed the pipeline and fitter, and the stretch distribution of the LT followup sample (red)

in Figure 2.5 in red, compared to 702 PTF SNe with measured stretches (green). The mean $\bar{s} = 0.97$ and median $\hat{s} = 0.99$ of the subsample are both lower than the respective values for the PTF measured-stretch sample, $\bar{s} = 1.06$ and $\hat{s} = 1.01$. It is apparent from the distribution, and the discrepancy between the mean and median in the case of the larger sample, that it is distorted by SNe that are consistent with having very broad lightcurves. The decrease in the average light curve width is a result of imposing a redshift cut on the sample; SNe with broader lightcurves are brighter, meaning they are over-represented at higher redshifts, where the fainter objects are more difficult to detect.

2.2.2 La Silla QUEST - LSQ

The La Silla QUEST Transient search (LSQ; Baltay et al., 2013), part of the larger La Silla QUEST Southern Hemisphere Variability Survey (Hadjiyska et al., 2012), uses the 10deg^2 QUEST instrument (Baltay et al., 2007) on the 1.0m European Southern Observatory (ESO) Schmidt telescope at La Silla, Chile. LSQ operates with a cadence of

between two hours and two days, using a broad gr filter (hereafter $gr_{\rm LSQ}$). The $gr_{\rm LSQ}$ filter, the transmission function of which can be seen in Figure 2.1, has approximately the same spectral coverage as $g_{\rm P48}$ and $R_{\rm P48}$ combined. LSQ is a complementary survey to PTF in that it covers the southern hemisphere with some overlap in the PTF search field, has a similar cadence, redshift coverage and limiting magnitude. The redshift distribution compared with that of the PTF sample is shown in Figure 2.3.

2.2.3 PESSTO and LCOGT

The Public ESO Spectroscopic Survey of Transient Objects (PESSTO; Smartt et al., 2015) is a public spectroscopic followup survey that began in Aprl 2012, using the 3.58m New Technology Telescope (NTT) to classify transients supplied by feeder surveys and public sources, as well as selecting a subset for detailed photometric and spectroscopic followup. PESSTO operates 9 months a year over the southern hemisphere winter, August-April. In the first spectroscopic data release (SSDR1; Smartt et al., 2015), 221 SNe were classified.

We use PESSTO data on one object in particular: SN 2015F. SN 2015F was discovered by Monard et al. (2015) and subsequently classified by PESSTO (Fraser et al., 2015) using the European Southern Observatory (ESO) Faint Object Spectrograph and Camera V2 (EFOSC2; Buzzoni et al., 1984) on the NTT. SN 2015F was selected as a science folloup target by PESSTO and a comprehensive spectral and photometric campaign followed. The data that we use in this work is presented in detail in Cartier et al. (2016, *submitted.*). As well as EFOSC2/NTT, the spectroscopic data we use comes from WiFeS on the Australian National University (ANU) 2.3m Telescope (Dopita et al., 2010), and the FLOYDS spectrograph on the 2m Faulkes Telescope South (FTS) at the Siding Spring Observatory. The multi-band photometric data for SN 2015F was collected using Las Cumbres Observatory Global Telescope network (LCOGT).

2.2.4 Carnegie Supernova Project - CSP

The Carnegie Supernova Project (CSP; Hamuy et al., 2006) was a 5-year, Low redshift supernova survey, commencing in September 2004 that aimed to obtain well sampled optical and near infra-red light curves and spectra for up to 250 SNe of all types. The observing campaign consisted on 300 nights spread between the Swope 1m and Du Pont 2.5m telescopes, located at Las Campanas Observatory (LCO) in Chile.

CSP was a targeted survey, following up SNe identified by The Lick Observatory Supernova Search (LOSS; Li et al., 2000) and amateur astronomers, selecting objects discovered before maximum light, with $\delta \lesssim +20^{\circ}$ and $z \lesssim 0.07$.

The data products of CSP are comprised of two photometric (Data release 1 (DR1), Contreras et al. 2010; Data release 2 (DR2), Stritzinger et al. 2011) and one spectroscopic data release (Folatelli et al. 2013). These well studied datasets will be used as a consistency check on our own data and methods in later chapters.

2.3 SiFTO

We determine the light curve parameters for each SN Ia in our sample using the SiFTO light curve fitter (Conley et al., 2008b). SiFTO manipulates the properties of a time-series SN Ia spectral energy distribution (SED) in order to best fit an observed light curve in flux space, returning the SN stretch (s), the time of maximum light in the rest-frame B-band ($t_{\max}$), a peak magnitude, and a colour parameter $\mathcal{C}$ for SNe with data in more than one observed filter. An example of such a fit is shown in Figure 2.6. For a comprehensive description of SiFTO, see Conley et al. (2008b), however due to the relevance to this work, a brief outline of the operations of the package follows.

2.3.1 Fitting SNe With SiFTO

To fit the observed photometry, model lightcurves are generated by integrating a model SED (ϕ), which is dependent on B-Band stretch s_B, time of maximum light in B, t_0, a factor related to flux calibration for each filter, n_i, the integrated flux of a SN in filter j at a heliospheric redshift of $z_{\rm hel}$, F_j is given by

$$F_j = \frac{\int_0^{\infty} \phi(\frac{\lambda}{1+z_{\rm hel}}, t, t_0, n_i, s_B) T_j(\lambda) \lambda \mathrm{d}\lambda}{(1+z_{\rm hel}) \int_0^{\infty} T_j(\lambda) \lambda \mathrm{d}\lambda}, \tag{2.1}$$

where $T_j(\lambda)$ is the total transmission function of the system i.e. with contributions from the atmosphere, optics, filter and CCD.

2.3.2 Constructing an Initial Model Spectral Energy Distribution - ϕ_0

The SED used in Equation 2.1, ϕ, is derived from an initial SED, ϕ_0. ϕ_0 is constructed using a time series of spectral templates based on those of Hsiao et al. (2007), combined

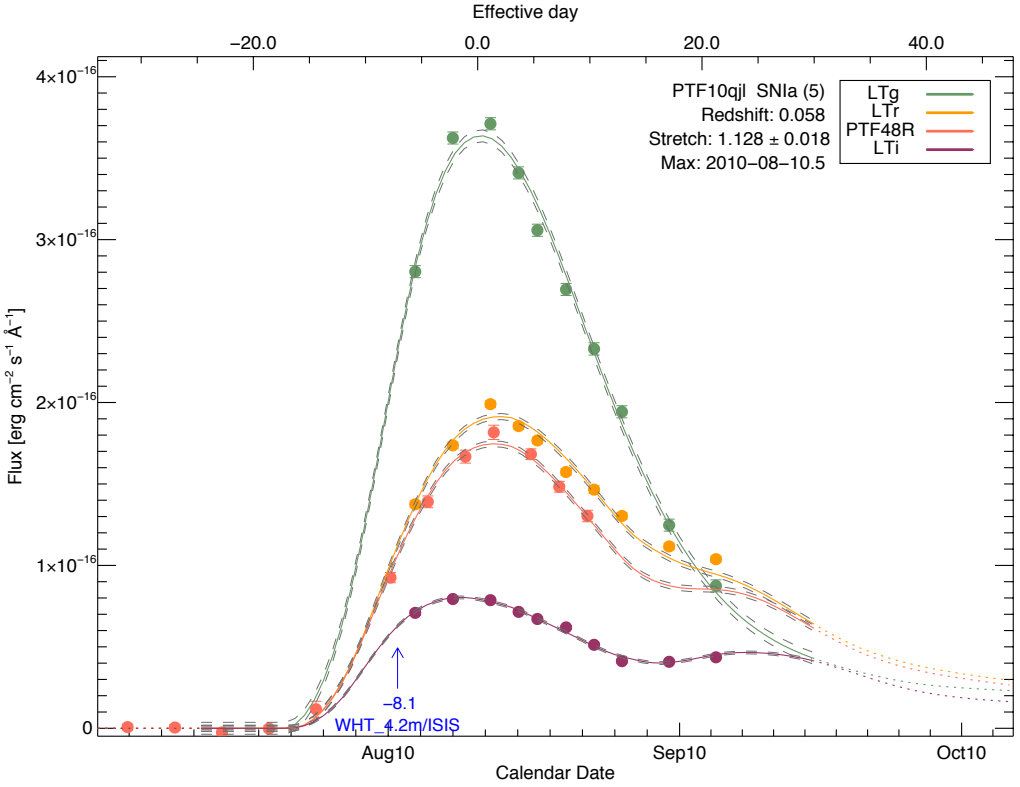

FIGURE 2.6: Typical SiFTO fit of a normal SN Ia, PTF10qjl. The solid lines show the best fit to the data, the dashed lines outline the 1σ uncertainties on the fit. In this case, four bands were fit: $R_{\rm P48}$, $g_{\rm LT}$, $r_{\rm LT}$and $i_{\rm LT}$. The blue marker indicates the point at which a spectrum was taken, in this case a classification spectrum from WHT/ISIS at a phase of $\tau \simeq -8$.

with additional data from Matheson et al. (2008). By design, these templates do not follow a well defined broadband flux or colour evolution. To control the luminosity evolution of the models that SiFTO fits to the data, a number of template lightcurves covering the Near-UV to Near-IR are used. The SED time series is mangled so that the flux evolution of the series matches that of the input template lightcurves. Shown in Figure 2.7 are the light curve templates and associated bandpasses used by default throughout this thesis. Where different behaviour is explored, for example in the post-maximum evolution, the light curve templates are explicitly presented.

ϕ_0 also incorporates an error snake, based on the uncertainties from the modelling and and additional component accounting for the variability of SNe Ia. For a full discussion of this, see §3.3 in Conley et al. (2008b).

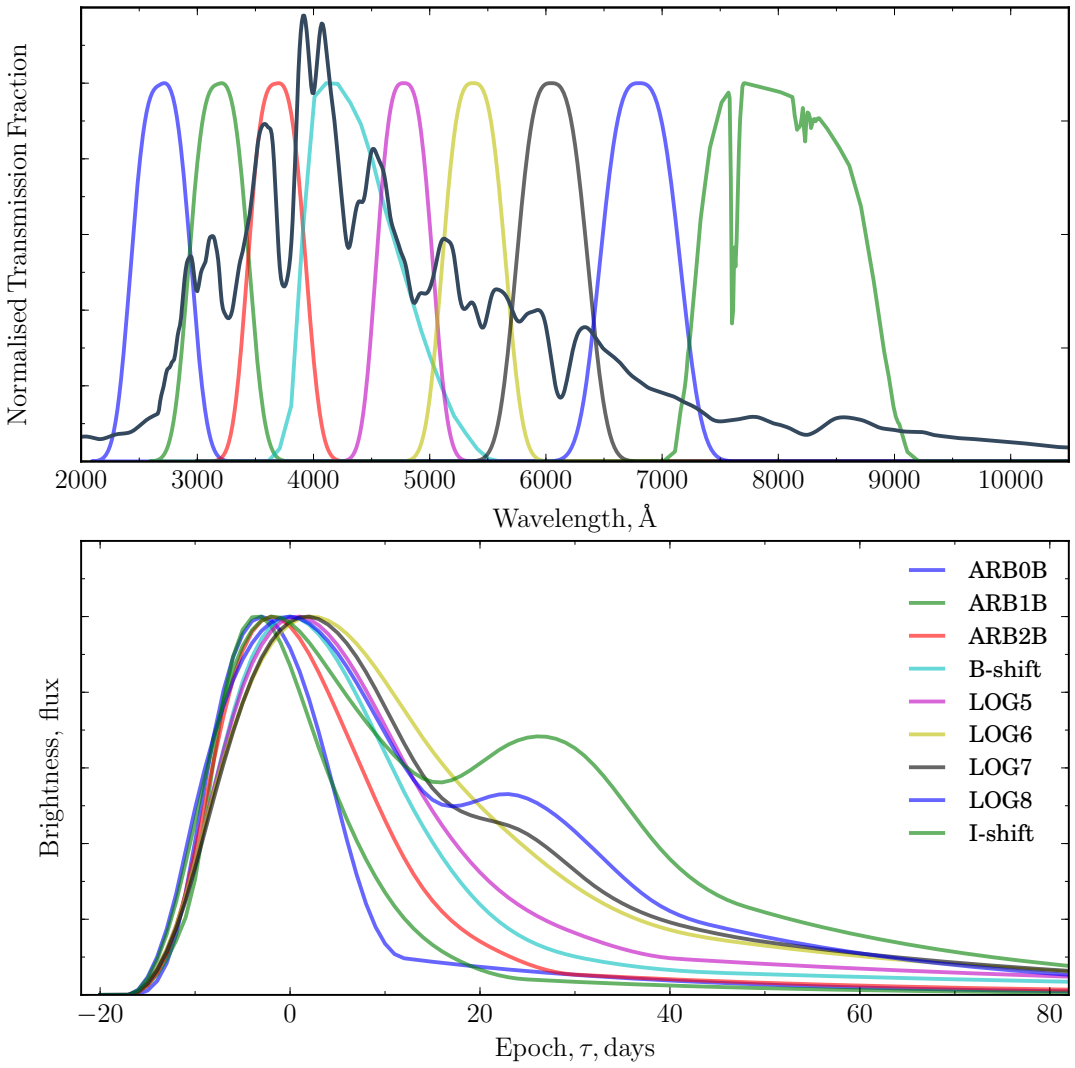

FIGURE 2.7: *Top Panel*: The SiFTO template filters used to mangle template spectra to fit obsered light curves. *Bottom Panel*: The light curve templates, shown in flux space, used by SiFTO to fit the SNe Ia photometry.

2.3.3 Details of the Fit

The manipulation of the SED uses a spline, $\mathcal{S}$ to scale ϕ_0 to ϕ

$$\phi(\lambda, t, t_0, n_i, s_B) = \phi_0(\lambda \frac{t - t_0}{1 + z_{\text{hel}}}) \times \mathcal{S}(\lambda; t, t_0, n_i, s_B, s_j, z_{\text{hel}}), \tag{2.2}$$

where, in addition to the terms defined abover, s_j is the light curve stretch in a given filter, j. During the fit, the normalisation in each filter is an independent free parameter. Once these are fit, the model SED is mangled to match the colours, this process is demonstrated in Figure 2.8. The use of a spline rather than a single parameter relation (such as those used by SALT/SALT2) is to better reproduce the full spectrum of observed colours across multiple observed bands.

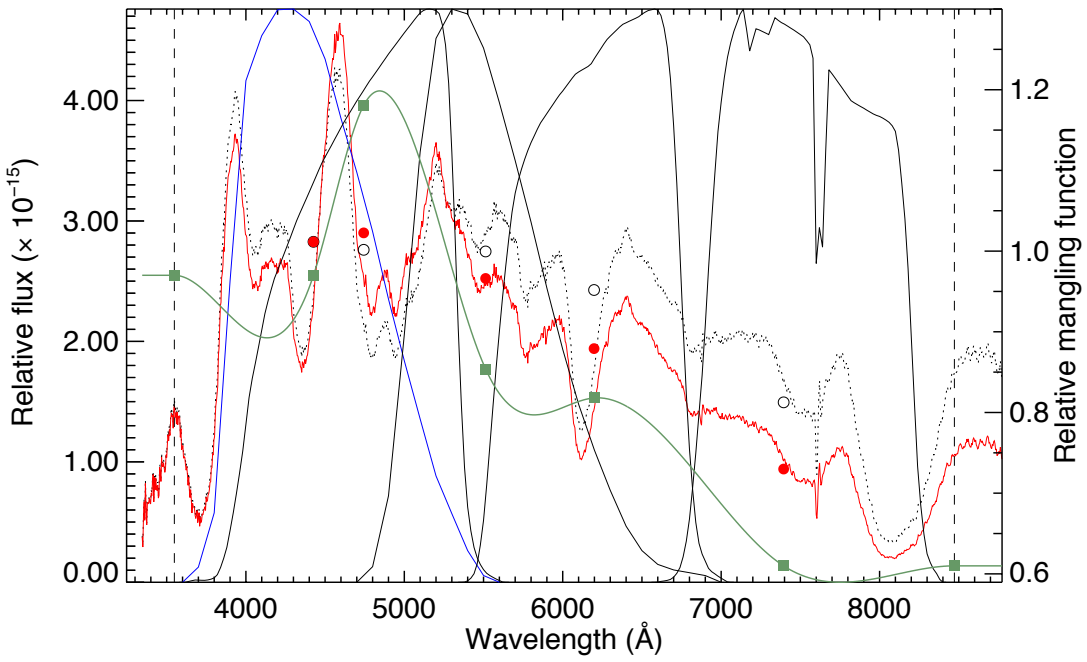

FIGURE 2.8: Mangled SN 2015F spectrum before (dotted) and after (red) mangling to the colours of observed photometry, using the spline $\mathcal{S}$, shown in green. The dashed lines show the upper and lower extent of the fit, the solid black and blue lines are the filters used in the mangle. The hollow points are the original in-band flux for each of the filters at the effective wavelength, the red filled points are the equivalent fluxes from the photometry, and the green points show the locations of the spline knots on the mangling function (green line) used to manipulate the SED from one to the other.

Ultimately, the light curve fit minimises the χ^2 statistic,

$$\chi^2 = \sum_{j=1}^{N_f} \sum_{i=1}^{N_j} \frac{(F_j(z_{t,t_0,n_i,s_B,\mathrm{hel}}) - f_{ij})^2}{\sigma_{ij}^2 + \sigma_F^2(z_{t,t_0,n_i,s_B,\mathrm{hel}}, \lambda_{\mathrm{eff}}^j)} \tag{2.3}$$

where the number of photometric points in a given band j is N_j, σ_F is the template error, λ_{eff}^j is the effective wavelength of finter j, and f_{ij} are the observed photometric datapoints, with associated uncertainties σ_{ij}.

To calculate the SiFTO colour parameter $\mathcal{C}$, if more than one band is observed, the colours at maximum are combined. Combining the colours is weighted to the values in bluer restframe bands, particularly $B - V$. Since we are working in the low redshift regime and with mainly g and r data, $\mathcal{C}$ is effectively equivalent to a standard $B - V$ colour term.

After performing the fit we define all phases (τ) in the SN light curve as days relative (in the rest-frame) to maximum-light, i.e. $\tau = (t - t_{\mathrm{max}})/(1 + z)$; thus epochs prior to maximum light have negative phases. The spectral time-series template used by SiFTO

assumes a t^2 photometric evolution in the B-band at phases $\tau \leq -10$ (equivalently 8-10 days post explosion for a normal SN Ia) due to a lack of accurate early SN Ia photometric data at the time the SiFTO package was written.

2.4 Data Quality

Having outlined the sources of our data, we now discuss additional steps taken to ensure that the data is of the highest possible quality. This includes a description of our photometric reduction pipeline (Section 2.4.3) and a discussion of corrections made after the initial reduction, e.g. extinction and fringe frame subtraction (Sections 2.4.2)

2.4.1 Spectroscopic Data

The spectroscopic data used in this work are primarily those from the usual operation of PTF, the reduction of these spectra were performed by members of the collaboration. In addition to PTF, we make use of the spectral time series of SN 2015F, detailed extensively in Cartier et al. (2016) and outlined previously, in Section 2.2.3. Where possible these spectra, as well as being corrected for telluric features and cosmic rays as standard, are corrected for extinction and matched to the observed photometric colour.

2.4.1.1 Mangling

As outlined in Section 2.3 (and in the literature c.f. Hsiao et al., 2007), mangling is the process of manipulating an SED to match observed colours. This helps to remove the systematic uncertainties in flux calibrating the spectrum, and through processes such as slit losses. However, this approach rests on the assumption that the photometry is less affected by uncertainties than the spectra. For SN 2015F, we have extensive photometric coverage, meaning that we can mangle the spectral series to match the observed colours, enabling us not only to consider the integrated spectra as an optical pseudo-bolometric, but also to measure the evolution of spectral lines with more confidence.

2.4.2 Extinction Correction

As extragalactic objects, SNe Ia are subject to extinction along the line of sight from the host galaxy, intergalactic medium (IGM) and the Milky Way. Extinction correction is of particular importance to SNe Ia as it affects the observed colour of the object, and while intrinsic colour is corellated with brightness, extinction colour excess is not. Extinction

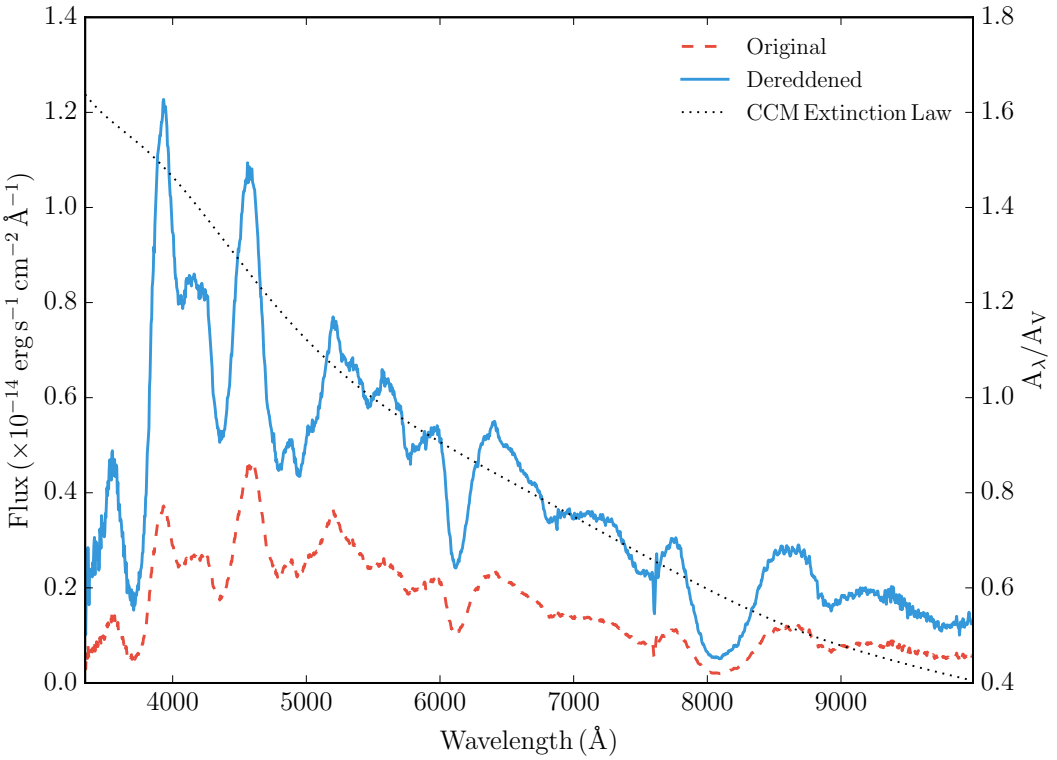

FIGURE 2.9: Correcting for the reddening due to dust in the spectrum of SN 2015F

is charecterised using the total-to-selective absorption ratio R_V (Rieke & Lebofsky, 1985; Cardelli et al., 1989; Fitzpatrick, 1999; Fitzpatrick & Massa, 2007) defined as

$$R_V = \frac{A_V}{E(B-V)} \tag{2.4}$$

where A_V is the V band reddening in magnitudes, and $E(B-V)$ is the colour excess. The relationship between extinction at a given wavelength and that in V is given by

$$\frac{A(\lambda)}{A_V} = a(x) + \frac{b(x)}{R_V}, \tag{2.5}$$

where a and b are polynomials wih empirically derived coefficients (see Cardelli et al., 1989; Fitzpatrick, 1999). R_V has been found to take a range of values, with a MW ISM mean value ~ 3.1 (Fitzpatrick, 1999). In this work we choose to use a MW-like extinction law, $R_V = 3.1$ unless otherwise specified, though the overall ratio is fairly resistant to the choice of R_V, particularly redward of 8000 Å. The effect of de-reddening a SN spectrum can be see in Figure 2.9, where an early spectrum of SN 2015F is corrected for a modest colour excess of $E(B-V)_{MW} = 0.175$ and $E(B-V)_{\rm host} = 0.085$. The shape of the extinction curve defined in Equation 2.5 can be seen as the dotted line in Figure 2.9.

2.4.3 Photometric Reduction and Calibration

To reduce the photometric data, we use a single pipeline used extensively in earlier PTF papers (e.g., Maguire et al., 2012; Ofek et al., 2013, 2014a; Pan et al., 2014; Firth et al., 2015) and we summarise the main details here.

The photometric pipeline runs on image subtraction, constructing a deep reference image from data prior to the SN explosion, registering this reference to each image containing the SN light, matching the point spread functions (PSFs), performing image subtraction, and then measuring the SN flux using PSF photometry on the difference images. The PSF is determined using isolated stars in the unsubtracted images, and the image subtraction uses a pixelized kernel (similar to that in Bramich 2008). The SN position is measured from epochs when the SN is present with the highest S/N (typically the position is determined to better than 0.05-0.1 pixels), and then the PSF photometry is performed in all images with this position fixed, avoiding biases in the low S/N regime (see Appendix B of Guy et al. (2007) for a discussion).

The flux calibration is to the Sloan Digital Sky Survey (SDSS; York et al., 2000) Data Release 10 (DR10; Ahn et al., 2014) if the SN lies within that survey's footprint, or otherwise to the photometric catalogue of Ofek et al. (2012) for $R_{\rm P48}$, or the AAVSO Photometric All-Sky Survey, APASS, (Henden et al., 2009), for the other filters.

2.4.4 LT i-band Fringe Correction

The initial reduction of the LT data that we will use in this work was performed by the standard LT pipeline, for both RATCam and IO:O. In both cases standard bias subtraction, flat fielding and overscan trimming were done, but cosmic ray and bad pixel masking were not, to ensure more control. Additionally, CCD fringing was not corrected for by default. The $i_{\rm LT}$ images obtained with RATCAM suffer from heavy fringe contamination which must be removed prior to the images entering our pipeline. The later data, from IO:O, does not suffer from significant fringing in $i_{\rm LT}$. Fringing is a form of pattern noise, or additive spatial systematic error, arising as a result of an interference pattern due to variations in the thickness of a CCD (Gullixson, 1992). This is particularly bad in narrow band images or sky line dominated images, meaning that the red end of the spectrum is more severely effected. Primarily, this is because for wavelengths of $>$ 700nm the absorption depth of silicon becomes comparable to the thickness of the CCD. This means that in a similar way to a Fabry-Perot interferometer, the light is internally reflected several times, amplifying the fringes through constructive and destructive interference, before being absorbed.

Fringing resembles an abstract pattern of large scale 'wavy' variation across an entire affected image, as shown in the upper panel of Figure 2.10. Fortunately, the fringe pattern of a CCD in a given band, arising as a direct result of the physical qualities of the detector, is typically very stable. This stability allows for subtraction once it has been characterised. Unfortunately, standard dome flats or twilight sky flat fields will not contain fringes – as the illumination in these cases is polychromatic and as such, any internal reflection will not undergo strong interference (Howell, 2012). Though the sky lines that cause the fringes in dark-time are still present in bright sky conditions, they are overpowered by the flat spectrum of the bright sky which does not intefere in the same way.

This effect is of particular concern to us, as fringing is present in the science and reference images but not necessarily aligned or the same magnitude. As a result, subtracting a reference image from a science frame is likely to result in large residual values just because of the differences in the degree and orientation of the fringing. The approach to removing fringes is to utilise a super-sky flat, either archival, or by using clipped science images, as dithering does not affect the position of the fringes on the chip.

The i_{LT} fringe subtraction super-sky flat was compiled from 107 individual background-subtracted archival frames. The images are stacked and the median value per pixel is used in the final flat. A bad pixel mask was then used to identify gaps in the image, before using a cubic spline function to interpolate over the pixels. This is to ensure that bad pixels are not introduced unintentionally into images as a result of the fringe subtraction process. After this had been done, the image was smoothed using a 5x5 boxcar moving average, to further reduce small scale variations. The resulting fringe frame can be seen in Figure 2.11.

The fringe frame not only has a complex spatial distribution, but also a double-peaked counts distribution, as can be seen in the left panel of Figure 2.12, showing that over the entire chip, more 'troughs' than peaks are present. The median and mean of the fringe count values are $\bar{F} = 0.17$ and $\hat{F} = -0.21$, with a standard deviation $\sigma = 7.76$.

2.4.5 Scaling the Fringe Frame

Because fringing is a function of sky line emission, the strength of the fringes in a given image are a result of the sky brightness, as a result, attempting to scale the subtraction using the exposure time gives an sub-optimal result. Equally, the individual sky flats were taken at different airmasses, with different exposure times and moon illumination, making it non-trivial to know a priori what the scaling would be. The approach used was to minimise the RMS background in the science images, after subtracting the fringe

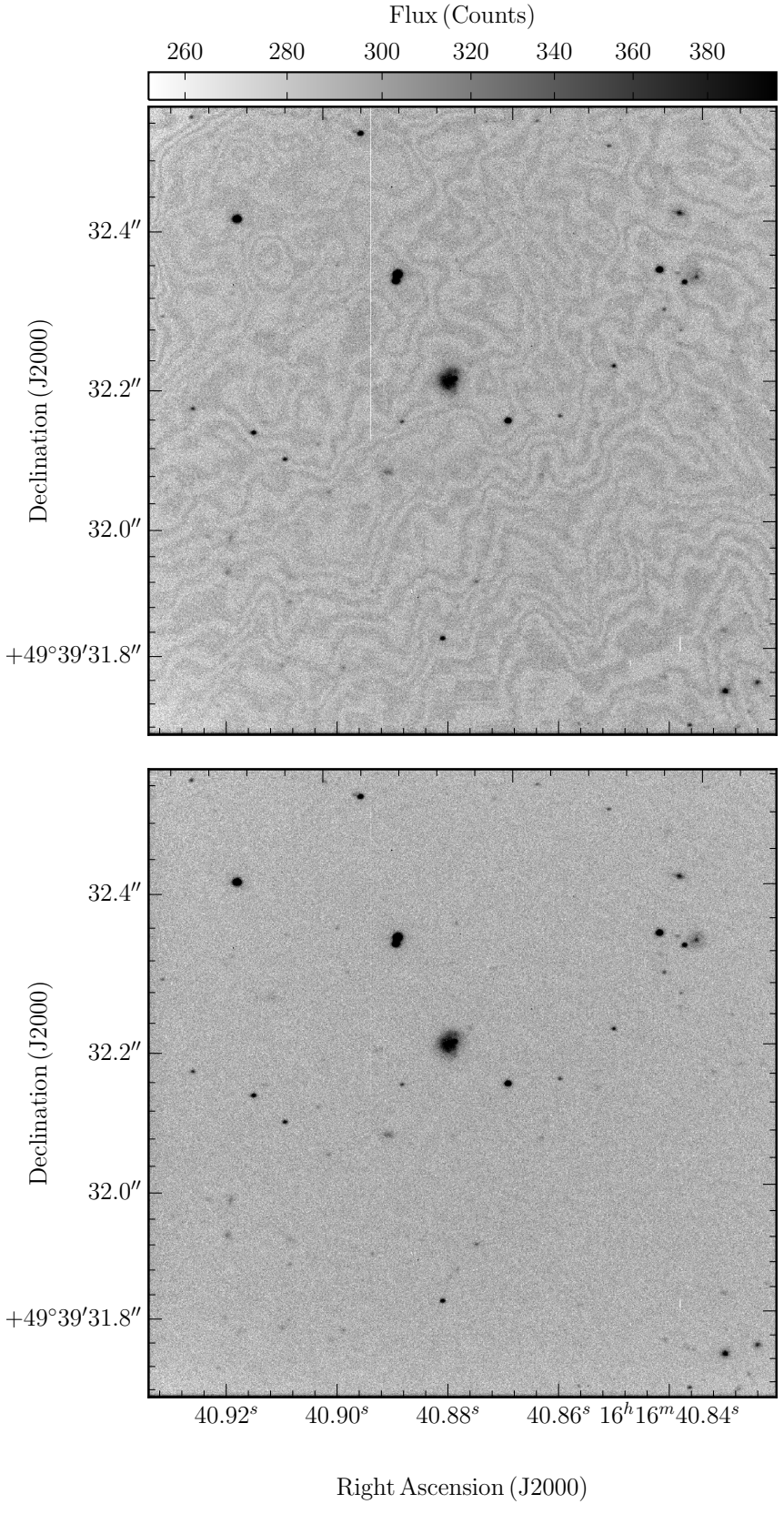

FIGURE 2.10: The effect of fringe subtraction on an $i_{\rm LT}$ band image. *Top*: frame showing extensive fringing over the entire image frame. *Bottom*: frame with fringes subtracted following the scaling and subtraction process outlined in Section 2.4.5. Also note the effective removal of bad pixels.

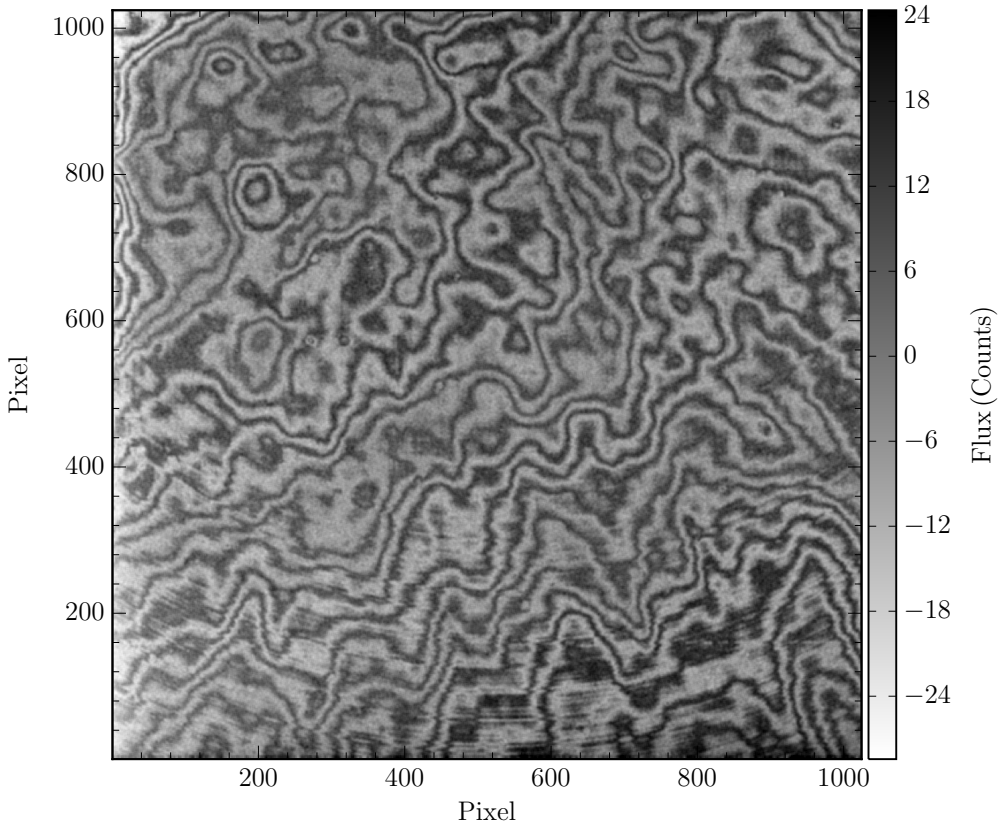

FIGURE 2.11: Final LT RATCam fringe frame, made up of a median-combined stack of 107 images. The median and mean of the fringe count values are $\bar{F} = 0.17$ and $\hat{F} = -0.21$, with a standard deviation $\sigma = 7.76$.

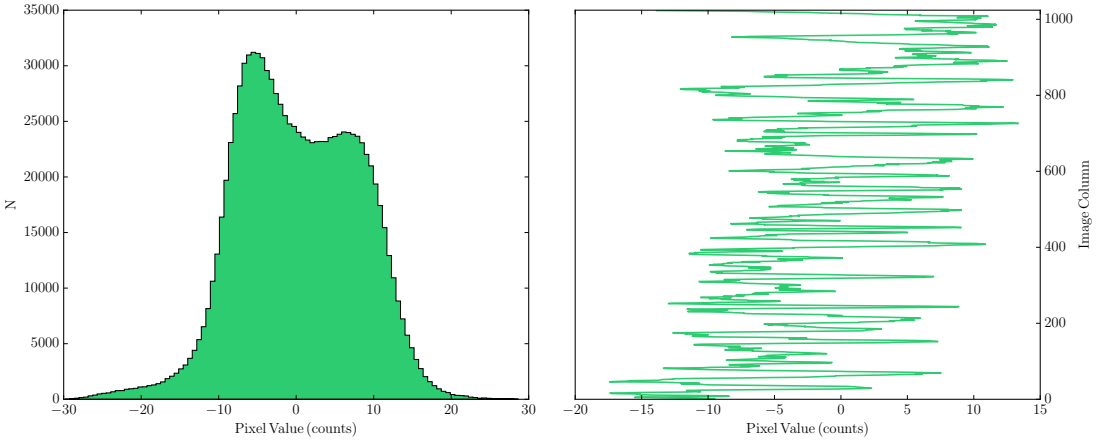

FIGURE 2.12: *left panel*: Histogram of pixel values for our entire fringe fringe frame. The median and mean of the counts per pixel are $\bar{F} = 0.17$ and $\hat{F} = -0.21$, with a standard deviation $\sigma = 7.76$ *right panel:* The counts per pixel of the central row of the fringe frame in Figure 2.11 showing the typical degree and scale of variation.

frame, i.e. x_{RMS}, multiplied by a scaling coefficient γ

$$x_{\mathrm{RMS}} = \left(\frac{1}{n} \sum_{i=1}^{n} (I_i - \gamma F_i) \right)^{\frac{1}{2}} \tag{2.6}$$

where the sum runs over all of our image pixels in the science image (I) and fringe frame (F). This approach proved successful in removing the fringing, as can be seen in Figures 2.10.

2.5 Summary

In this Chapter we have given an overview of the sources of our data, both photometric and spectroscopic. We introduced our primary light curve fitting tool, SiFTO, and summarised its outputs, and how we would use them in the following analyses. We also described the reduction processes, both for difference imaging and calibration for the photometry, as well as additional steps taken to increase the final data quality. This included a detailed explanation of the fringing effects in the LT dataset, and a demonstration of the effectiveness of the fringe subtraction, and a discussion of extinction correction.

In the next chapter, we explore how, by leveraging the unique properties of the PTF and LSQ samples, we can explore the early phases of SNe Ia emission hours to days after explosion. Previous work, existing parameterisations and their derivations will be discussed, and using two well studied SNe, SN 2011fe and SN 2015F, we test the veracity of our chosen methods.

Chapter 3

Rising Lightcurves

"I've never seen a supernova blow up, but if it's anything like my old Chevy Nova, it'll light up the night sky."

- Philip J. Fry, *Futurama; 'Roswell that Ends Well'*

In this chapter we explore what we can learn from studying SNe Ia at the earliest possible times, as they rise up to their peak brightness. Given the link between lightcurve width and luminosity, measuring the duration of the rise is an appealing initial measurement to make. This 'rise time' is usually defined as the time from explosion to the peak of the emission. However, both the definitions and parameterisations of the 'rise time' are nuanced, and as such we consider methods of parameterisation that have been used in the literature and their theoretical justifications, and outline the framework with which we will study our sample. As well as following the method outlined in this Chapter, the photometric data reductions and light curve fits were performed by the author using the pipeline and fitting package described in Chapter 2. The spectra used in this Chapter were obtained and reduced by the PTF collaboration (SN 2011fe) and R. Cartier (SN 2015F), for more detail see Section 2.4.1.

Prior to the era of large, cadenced surveys, the early time coverage of SNe Ia was sparse and the reliance on serendipitous discoveries meant that the precise nature of the first phase of the SN were not well observationally constrained. We leverage the unique qualities of the PTF dataset, its cadence and large size, to analyse a statistically meaningful number of objects by measuring not only the duration of the rise, but also the shape. Additionally, to better understand our sample, given our limitations, we consider two SNe with extraordinarily well measured early photometry and spectra, SN 2011fe and SN 2015F which enable us to test the robustness of our methodology.

TABLE 3.1: Ensemble mean rise-time results from the literature, assuming a 'fireball model' (See Section 3.2.1), with the main survey source of data shown, where possible.

Data Source	Rise Time (days)	
SCP[1]	17.6 ± 0.4	Groom (1998)
	19.5 ± 0.2	Riess et al. (1999b)
	20.08 ± 0.19	Aldering et al. (2000)
SCP[1]	18.3 ± 1.2	Goldhaber et al. (2001)
SNLS[2]	$19.10^{+0.18}_{-0.17} \pm 0.2$(syst)	Conley et al. (2006a)
SDSS-II[3]	17.38 ± 0.17	Hayden et al. (2010a)
LOSS[4]	18.03 ± 0.24	Ganeshalingam et al. (2011a)
SNLS[5]	$16.85^{+0.54}_{-0.81}$	González-Gaitán et al. (2012)

[1]Supernova Cosmology Project, Perlmutter et al. (1997a)
[2]Supernova Legacy Survey, Guy et al. (2010)
[3]Sloan Digital Sky Survey - II, Frieman et al. (2008)
[4]Lick Observatory Supernova Search, Li et al. (2000)
[5]Supernova Legacy Survey, González-Gaitán et al. (2011)

3.1 SNe Ia Rise Times

3.1.1 Importance of rise time measurement

By measuring the rise time of supernovae, it is possible to discern between different theoretical models (Leibundgut & Pinto, 1992) as the time since explosion directly influences nucleosynthesis, abundances and opacity as well as the overall luminosity. As can be seen in Table 3.1, a number of different approaches; stacking lightcurves, template fitting and hybrid models, have yielded a range of rise times, over a range of redshifts and sample sizes. A firm grasp of the early time emission from SNe Ia can also help to distinguish between power sources above and beyond ^{56}Ni.

3.1.2 Limitations of Stacked Light-curves

Previous attempts to characterise the earliest-time light curve shapes of SNe Ia have used stretch corrected and stacked lightcurves of many events from large surveys (Hayden et al., 2010a; Ganeshalingam et al., 2011a; González-Gaitán et al., 2012). While leveraging the statistical power of so many events to look at the average 'template' SNe, the arguably more useful SN to SN variation is smoothed out. This is particularly true if only a small percentage of these objects show deviations, due to asymmetries or other intrinsic qualities. We therefore consider events on an object by object basis.

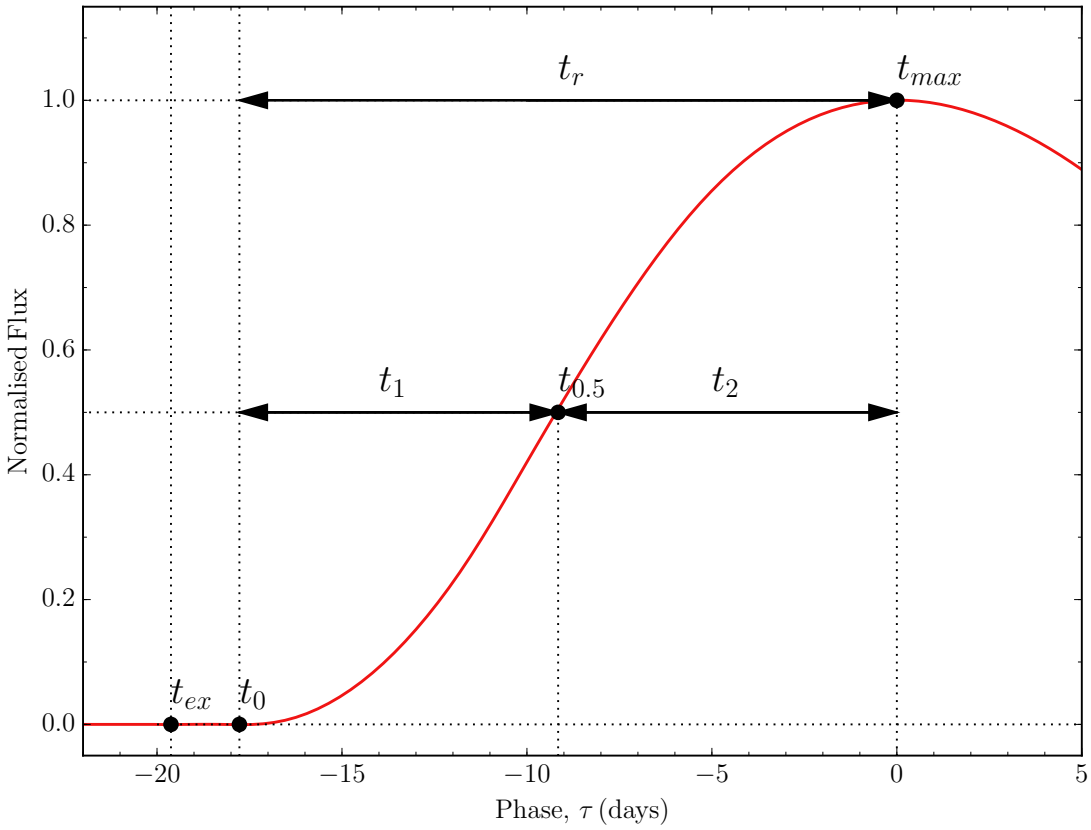

FIGURE 3.1: Schematic diagram of a SNe Ia lightcurve, showing important timescales and points of phase.

3.2 Parameterisation

To add context to the diversity shown in the literature, we set out the parameterisation of the early emission from SNe Ia, highlighting the assumptions that may lead us to expect some divergence from the most naive descriptions. To aid in this, our toy light curve, Figure 3.1 shows the typical evolution of flux as a function of time relative to B–band maximum, or 'phase', τ (where $\tau = t - t_{\rm max}(\rm b)$). Also shown are number of important points pre-maximum light, that are referred to in subsequent sections.

3.2.1 Canonical 'Fireball' Model

The most widely used model parameterisation (e.g., Riess et al., 1999b; Conley et al., 2006b; Strovink, 2007; Hayden et al., 2010a; Ganeshalingam et al., 2011a; González-Gaitán et al., 2012) for the early-time optical SN Ia luminosity, $L_{\rm model}$, as a function of time, t, is the so-called 'fireball model':

$$L_{\rm model}(t) = \alpha(t - t_0)^2, \tag{3.1}$$

for $t > t_0$, and $L_{\rm model}(t) = 0$, otherwise. Here, α is a normalising coefficient, and t_0 is usually interpreted as the time of explosion.

As well as being a good fit to data, the fireball model can be justified by making straightforward assumptions about both the ejecta velocity (v) and temperature (T), namely that they both remain constant over the period being fit (Riess et al., 1999b). At low redshift, assuming the spectral energy distribution (SED) is an approximate blackbody and that the emitting region of the SN is hot enough, the standard optical passbands lie to the red side of the peak in the Rayleigh-Jeans tail of the emitted SED. This means that the SED can be assumed to be flat, and the optical luminosity, $L_{\rm opt}$ is given by:

$$L_{\rm opt} \propto r^2 T \propto v^2 (t - t_{\rm ex})^2 T. \tag{3.2}$$

If we *do* make the assumption that v changes slowly, and T remains constant, then this simplifies to:

$$L_{\rm opt} \propto (t - t_{\rm ex})^2. \tag{3.3}$$

These assumptions, are however, unrealistic over any timescales longer than a few hours, as both the photospheric velocity and colour of the SN are predicted (eg. Piro & Nakar, 2013), and observed (eg. Patat et al., 1996; Altavilla et al., 2007; Hsiao et al., 2007), to change most rapidly at very early times. A more in depth justification in Nugent et al. (2011), shows that t^2 behaviour can be derived without relying upon the same simple assumptions, by following the Arnett (1982) one-zone model. Starting from the change in internal energy, E_i, as described by the first law of thermodynamics is equal to the energy injected by ^{56}Ni decay, less the radiated energy and work done expanding the ejecta;

$$\frac{\partial E_i}{\partial t} = -P\frac{\partial V}{\partial t} + L_{\rm Ni}(t) - L_{\rm e}(t). \tag{3.4}$$

Where V is the ejecta volume, P the internal pressure and $L_{\rm Ni}$ and $L_{\rm e}$ are the energy injected by ^{56}Ni decay and radiated luminosity respectively. If we rely on the assumptions that the expansion is homologous (the ejecta is 'coasting'), such that the volume, V, increases as $V \propto t^3$ and that radiation pressure is dominant so that $P = E_i/3V$, we can substitute into Equation 3.4, removing the term for expansion losses:

$$\frac{1}{t}\frac{\partial}{\partial t}\left[E_i t\right] = L_{\rm Ni}(t) - L_{\rm e}(t). \tag{3.5}$$

Assuming uniform spherical emission, the diffusion equation gives:

$$\frac{L_{\rm e}}{4\pi R^2} = \frac{c}{3\kappa\rho}\frac{\partial E_i/V}{\partial r} \approx \frac{c}{3\kappa\rho}\frac{E_i/V}{R}, \tag{3.6}$$

where κ is the opacity, and ρ the density of the one-zone ejecta. Returning to the assumption of homologous expansion, $R = v_{\rm f}t$; where $v_{\rm f}$ is the characteristic final ejecta velocity defined as

$$v_{\rm f} = \left(\frac{E_{\rm sn}}{2M_{\rm ej}}\right)^{1/2}, \tag{3.7}$$

where $M_{\rm ej}$ is the total ejecta mass, and assuming 100% efficient conversion of SN explosion energy $E_{\rm sn}$ to ejecta kinetic energy. We can re-write Equation 3.6 as

$$L_{\rm e} = \frac{E_i t}{t_d^2}. \tag{3.8}$$

$t_{\rm d}$ is the effective diffusion time given by:

$$t_{\rm d} = \left[\frac{3}{4\pi}\frac{M_{\rm ej}\kappa}{v_f c}\right]^{1/2}. \tag{3.9}$$

In the regime where the time since explosion is less than the ^{56}Ni decay time of $\tau_{\rm ni} = 8.8$ days, we can take $E_{\rm Ni}$ to be constant with time, and in this limit Equation 3.7 has the solution:

$$L_{\rm e}(t) \approx \frac{E_{\rm Ni}}{\tau_{\rm Ni}}\left[1 - e^{\frac{-t^2}{2t_{\rm d}^2}}\right] \qquad t \ll \tau_{\rm Ni}, \tag{3.10}$$

Assuming that the internal energy is dominated by ^{56}Ni decay, and the contributions from other sources, such as shock-heated cooling and CSM interaction (Section 3.3) are negligible, we can simplify this using a Taylor Expansion, leaving

$$L_{\rm e}(t) \approx \frac{E_{\rm Ni}}{\tau_{\rm Ni}}\frac{t^2}{2t_{\rm d}^2} \qquad t \ll t_{\rm d}, t \ll \tau_{\rm Ni}. \tag{3.11}$$

3.2.2 More general cases

Despite being a more thorough treatment of the early phases, the justification of a parabolic rise still rests on some key assumptions, namely that of homologous expansion, fully efficient SN explosion energy to ejecta kinetic energy conversion, and the power source being entirely ^{56}Ni decay. As a more general case, and to test departures from the 'fireball model', we consider an index that may take values other than 2, and model

TABLE 3.2: Rise-time results from the literature, where n is measured

Survey	n	Rise Time (days)	
SNLS	1.8 ± 0.2	$18.50^{+0.18}_{-0.17} \pm 0.2$(syst)	Conley et al. (2006a)
SDSS	$1.8^{+0.23}_{-0.18}$	17.38 ± 0.17	Hayden et al. (2010a)
LOSS	$2.2^{+0.27}_{-0.19}$	18.03 ± 0.24	Ganeshalingam et al. (2011a)
SNLS	$1.92^{+0.31}_{-0.37}$	$16.85^{+0.54}_{-0.81}$	González-Gaitán et al. (2012)

the SN flux as:

$$f_{\rm model}(t) = \alpha(t - t_0)^n, \tag{3.12}$$

again for $t > t_0$, and with $f_{\rm model} = 0$ otherwise; n will be known as the 'rise index'. This parameterisation was introduced initially in the analysis of stacked light curves (Table 3.2), and then further applied to individual SNe with well enough sampled early-time data to constrain all three parameters (Table 3.3). Rather than interpret t_0 as the time of explosion, we refer to t_0 as the time of first light, that is, when the first photons are observed to diffuse out of the ejecta and refer to the time of explosion as t_{ex}; this distinction can be seen in our schematic light curve, Figure 3.1.

TABLE 3.3: Rise-time results from the study of individual SNe

SN	n	Rise Time (days)	Band	
SN 1994D	N/A*	17.8 ± 1.7	'optical-bolometric'	Vacca & Leibundgut (1996)
SN 2002bo	2†	17.9 ± 0.5	R	Benetti et al. (2004)
SN 2009ig	2†	17.13 ± 0.07	B	Foley et al. (2012)
SN 2011fe	2.01 ± 0.01		$g_{\rm P48}$	Nugent et al. (2011)
SN 2011fe	2.05 ± 0.025		$g_{\rm P48}$, R & scaled unfiltered	Vinkó et al. (2012)
SN 2010jn	2.3 ± 0.6	19.1 ± 1.2	$R_{\rm P48}$	Hachinger et al. (2013)
SN 2012ht	2†	17.62 ± 0.52	R	Yamanaka et al. (2014)
SN 2013dy	2.24 ± 0.08	17.7 ± 1.2	Unfiltered	Zheng et al. (2013)
SN 2014j	2.89 ± 0.27		Unfiltered	Zheng et al. (2014)
ASASSN-14lp	$1.57 - 2.4$	$16.94 \pm 0.11(V)$	u, V, g, r, i	Shappee et al. (2015)
SN 2012cg	3.2 ± 0.1 , 2.19 ± 0.05 , 2.05 ± 0.04		U, B, V	Marion et al. (2016)
SN 2015F	2.195 ± 0.033	18.06 ± 0.08	V	Cartier et al. (2016)

*Rise time defined as Δt_{30}, time taken to rise 30 magnitudes to maximum

†Only fitted with the fireball model, not the best fit value of n

3.2.3 Combined Rise Model and Template Fitting

Aldering et al. (2000) used the fireball model with a simple modification to ensure that it could be used as part of a fit using a whole lightcurve, by introducing a parameter, $t_{\rm join}$, defined as a point at which the rise time fit should flow continuously onto a template. In the case of Aldering et al. (2000) this was the a modified Leibundgut (1988) standard template, as used by the Supernova Cosmology Project (SCP; Perlmutter et al., 1997b).

Whilst this approach ensures that the number of free parameters in the model does not increase, we avoid this approach as the derivation of $t_{\rm join}$ in effect fixes our parameter α, the normalisation. As can be seen in Figure 3.2, our parameters show degeneracy, and fixing one of them constrains the other.

3.2.4 Time dependent index - '$\dot{n}$'

Another method to probe both the structure of the ejecta and the assumptions is to investigate how the fit deviates from a $n = 2$ fireball model over time. To this end, we also consider a modified, time dependent, power law.

$$f_{model}(t) = \alpha(t - t_0)^{n_0 + \dot{n}(t - t0)}, \tag{3.13}$$

where n_0 is the rise index at time t_0 and $\dot{n}$ is a variable measuring the rate of change of n. By setting $n_0 = 2$, we can test deviation from the fireball model as time progresses.

3.2.5 Broken Powerlaw

For the local and well observed SNe Ia SN 2013dy, SN 2014J and SN 2015F (Zheng et al., 2013, 2014; Goobar et al., 2014; Im et al., 2015), a broken powerlaw was used to fit the early emission:

$$f(t) = \beta \left(\frac{t - t_0}{t_b}\right)^{\alpha 1} \left[1 + \left(\frac{t - t_0}{t_b}\right)^{s(n_1 - n_2)}\right]^{-1/s}, \tag{3.14}$$

where β is a normalisation constant, t_0 is the time of first light, t_b is the time of the 'break', n_1 and n_2 are the two rise indices before and after t_b, while s is a smoothing parameter. This broken powerlaw model is commonly used to fit gamma-ray burst (GRB) afterglows (e.g. Urata et al., 2009; Zheng et al., 2012). As this model has so many free parameters, it is only possible to use it with reliability on the most well sampled early light curves.

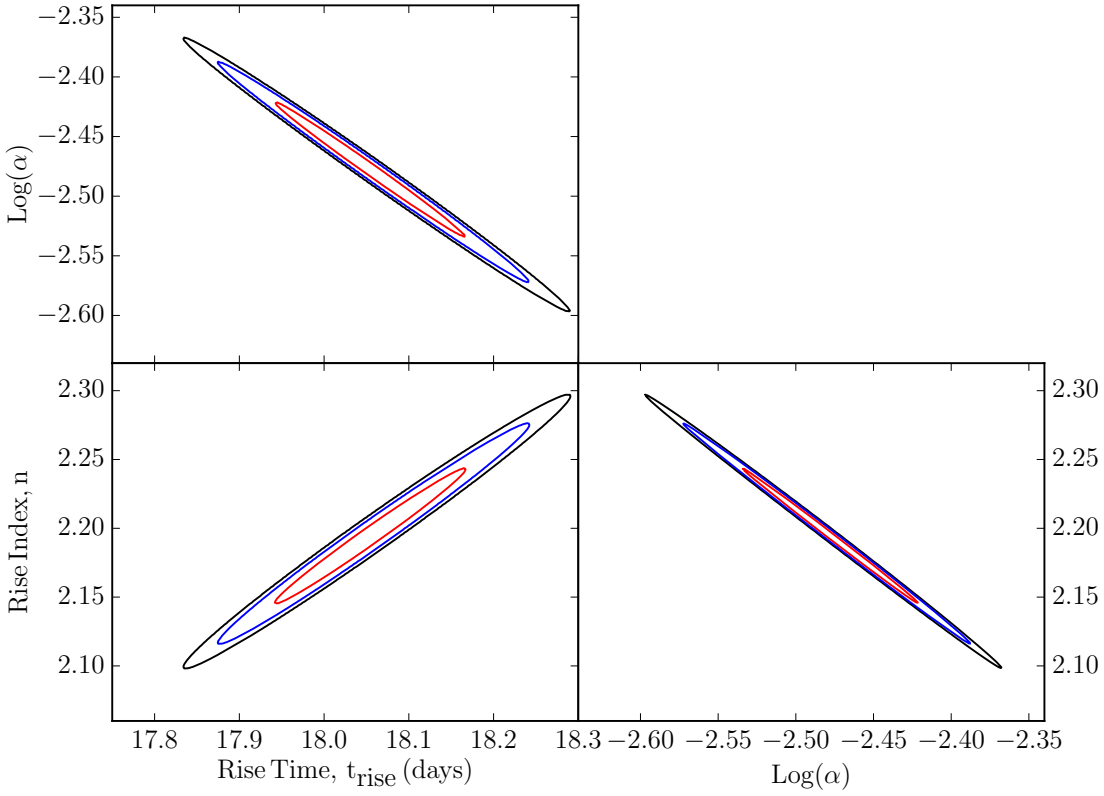

FIGURE 3.2: Fit contours from SN 2015F LCOGTV fitting. The contours are at 1σ, 2σ and 3σ and contain 68%, 95%, 99% of the probability respectively. The ellipticity of the contours indicates degeneracies between our parameters.

The rise times computed using this method tend to be shorter than those inferred by a single power law fit, as n_1 tends to take a greater value than n in a single powerlaw fit, and as such direct comparisons are difficult.

3.2.6 Shape Independent Measurements

Other methods for measuring the time of explosion, independent of the shape of the lightcurve have recently been developed. Abundance tomography has been used to explain the spectral evolution of a number of objects (Mazzali, 2000; Stehle et al., 2005), but most notably for this work, SN 2010jn, SN 2011fe and SN 2014J (Hachinger et al., 2013; Mazzali et al., 2014; Ashall et al., 2014, respectively), which all have photometrically measured rise times. This method models the spectra as the photosphere recedes (in mass coordinates) into the ejecta, revealing more of the mass as time goes on. This approach can yield the time of explosion, $t_{\rm ex}$, by fitting the spectra and relative abundances (i.e. Hachinger et al., 2013), but is more often estimated from the earliest spectrum (Mazzali & Schmidt, 2005), in order to remove a free parameter from the modelling. Following Piro & Nakar (2013), the minimum explosion time, $t_{\rm min}$, can be

estimated from the bolometric luminosity, the colour temperature, T_c and the photospheric velocity, v_{ph}, using

$$t_{min} = 3.4 \left(\frac{L}{10^{42}\,erg\,s^{-1}} \right)^{1/2} \left(\frac{T_c}{10^4\,K} \right)^{-2} \left(\frac{v_{ph}}{10^4\,km\,s^{-1}} \right)^{-1} days. \quad (3.15)$$

Even more simply, the time of explosion can be derived using linear fits to the photospheric velocity evolution, which have been proposed to evolve uniformly (Piro & Nakar, 2014), with a prediction of $v_{ph} \propto t^{-0.22}$. This method has been applied to several SNe; SN 2009ig, SN 2011fe, SN 2012cg (Piro & Nakar, 2014) and ASASSN-14lp (Shappee et al., 2015), however it drastically simplifies the observed diversity in velocity gradients (cf. Benetti et al., 2005).

3.2.7 Dark Phase

Tension has appeared between these independent measures of rise time and light curve fitting, as the spectral fitting methods; either abundance tomography or velocity fitting uniformly require longer rises. However, this is not entirely unexpected, and can be explained by considering the way the light curve is powered post-explosion. The first photons that diffuse out of the ejecta result from energy deposition from the decay of the ^{56}Ni that is located furthest out in the ejecta (Piro & Nakar, 2013), this amount may be small, depending on the level of mixing. This diffusion process is not instantaneous, particularly for deeper deposits, and as such, there may be a 'dark phase' between the explosion and first light.

The escape of the first photons starts the rise of the light curve, and as the ejecta expands, photons generated by energy deposited by deeper ^{56}Ni escape. As such, fitting the subsequent rise only places an upper limit on the true time of explosion, and is the reason we consider t_0 distinct from t_{ex} (see Section 3.2.2).

3.3 Additional Sources of Luminosity

As well as the emission due to the radioactive decay of ^{56}Ni, several other mechanisms are expected to shape the early time light curve of a reasonable fraction of SNe Ia, and in a number of notable cases, have been used to explain deviations from expected behaviour. Broadly, there are two families: interaction with a shell of circumstellar material (CSM), or interaction with a binary companion. These processes occur over a range of timescales, some of which are comparable to the rising portion of the lightcurve

that is under consideration. An example of the effect that these additional sources of flux can have can be seen in Figure 3.3.

3.3.1 Circumstellar Material

Attempts to find direct evidence of interaction of SNe Ia with their immediate circumstellar environment proved challenging, with searches providing only upper limits on masses (Cumming et al., 1996), but more recently, interaction in the form of local Na I D absorption and Hα emission have both been observed.

As detailed in Section 1.4.3, interaction with CSM expressed as Na I D absorption is thought to occur in $\sim 20\%$ of SNe (Sternberg et al., 2011; Maguire et al., 2013). The effect of these Na I D lines are of interest to this work as they sit within the rest frame band pass of $R_{\rm P48}$ and almost centrally with respect to the $gr_{\rm LSQ}$. Therefore any variation in these lines is likely to change the duration of the rise and the shape of light curve evolution. If any effect is seen, it would likely act to shorten the length of the rise. However, we estimate that the magnitude of this effect will be small. Inspection of the spectra of our sample shows we find evidence of Na I D absorption in only two SNe (PTF 11gdh and PTF 12gdq) around maximum light.

While apparently less common than CSM in absorption, a growing number SNe Ia-CSM are being newly discovered (Fox et al., 2015) and misidentified objects are being classified in existing samples, notably Silverman et al. (2013a) who found 16 SNe Ia-CSM, including 7 from our parent PTF sample, as well as PTF 11kx. It has long been suggested that one cause of an 'anomalous' rise would be an energy contribution from interaction with CSM material (Falk & Arnett, 1977). Silverman et al. (2013a) noted that the rise of these SNe tends to be significantly longer than a typical SNe Ia, following a simple photon diffusion argument - not only does a photon have to diffuse through the ejecta, but also significant amounts of CSM as well. In that respect, Ofek et al. (2014b) showed that in the related SNe Type IIn there is a possible correlation between rise time and peak luminosity, and as such an anomalously long rise in an otherwise ordinary SNe may be an indication of CSM interaction.

We will fit PTF 11kx using Equation 3.12 along with the rest of our sample following the method outlined in Section 3.7, as well as two other PTF SNe Ia CSM objects identified by Silverman et al. (2013a), that have sufficiently good data for us to fit a simple fireball model.

3.3.2 Shock Breakout

As discussed in Section 1.4, in explosions that undergo a deflagration-to-detonation transition (DDT), immediately following the explosion a shock travels through the envelope, causing it to become unbound from the star. The length of the sub-sonic deflagration phase and the speed of the burning front governs the radius of the pre-shocked ejecta, due to thermal expansion. In the case where the shock is radiation-dominated, the shock travels outwards until the optical depth falls to a level at which the radiation driving the shock can escape as a UV/X-ray flash, as seen in some core collapse supernovae (Soderberg et al., 2008).

However, as the strength of the shock breakout of the explosion is closely related to the radius of the progenitor at the time of the DDT, the shock breakout itself is likely too dim and fast to be detectable for extragalactic events (Rabinak et al., 2012; Nakar & Sari, 2012), due to the small size of the C+O WD progenitor (Hoyle & Fowler, 1960; Bloom et al., 2012b).

3.3.3 Shock-heated Cooling

Whilst detection of the shock breakout directly from a SNe Ia is impossible for all but the closest events, emission from the cooling ejecta heated by the shock could be detected. This shock-heated cooling is predicted to be faint but should be best observed in UV and blue optical bands (Piro & Nakar, 2013). Adding to the difficulty in detection, the timescale for this faint emission is very short given the small size of the progenitor star (Piro et al., 2010; Nugent et al., 2011; Bloom et al., 2012b).

3.3.4 Signatures of Interaction with Companion

A source of emission that is a diagnostic of the SD progenitor channel is the interaction between the SN ejecta and a non-degenerate secondary. This interaction has been theoretically predicted to be seen as contamination in the late-time spectra by material stripped from the secondary, with both Hydrogen and Helium contributing, depending on the type of companion (Marietta et al., 2000; Pakmor et al., 2008), with observational searches ongoing placing limits on the amount of swept up meterial (Mattila et al., 2005; Lundqvist et al., 2013; Shappee et al., 2013; Lundqvist et al., 2015; Maguire et al., 2016). Another mechanism for interaction is similar to the shock breakout and shock heating described above, wherein the violent collision between the young ejecta and the secondary is the source of strong flux (Kasen, 2010; Pan et al., 2012). Instead of the

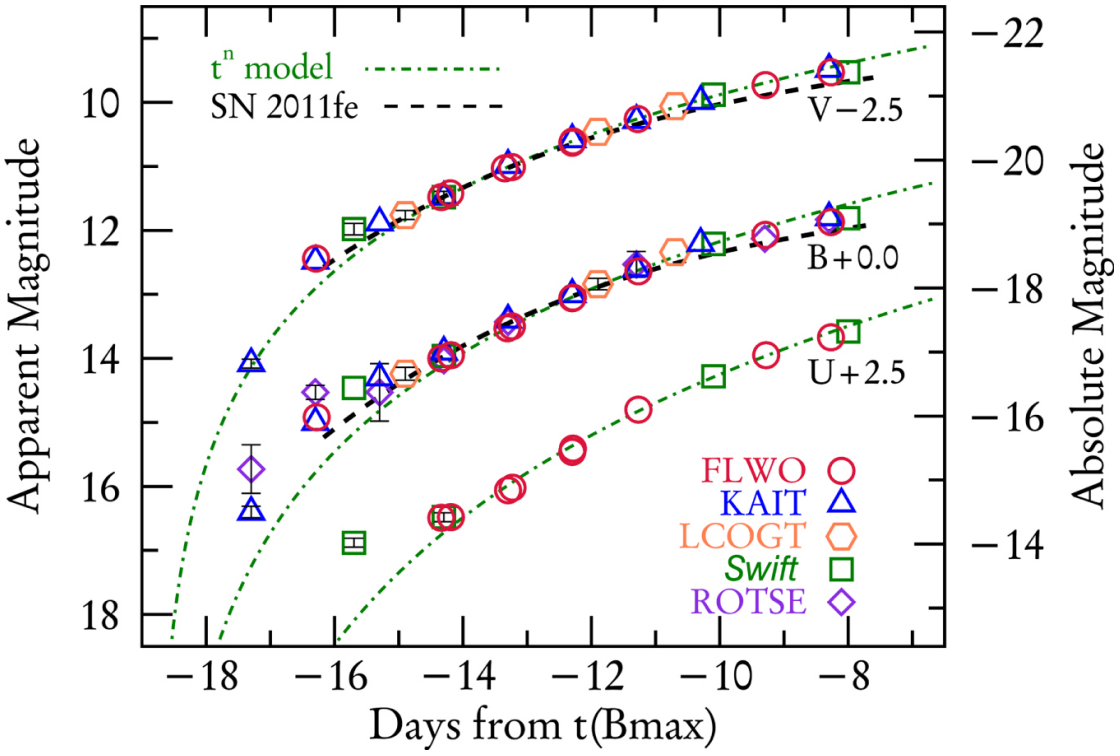

FIGURE 3.3: V-, B-, and U-band photometry (top to bottom) of SN 2012cg from multiple sources. The data have been corrected for extinction. The LC of SN 2011fe (Vinkó et al. 2012, dashed black lines) stretched to yield a rise time of 18.8 days equivalent to SN 2012cg (see the text) and tn model LCs (dotteddashed, green) are plotted as templates for a normal SN Ia. The power-law indices used for different bands are 3.4 (U), 2.4 (B), and 2.2 (V), see Marion et al. 2016 for details. In all bands, the SN 2012cg data display excess flux at phases earlier than 14 days. From 14 days toward maximum light, the data from SN 2012cg and SN 2011fe fit the templates well. Uncertainties are marked only where they approach the size of the symbols. Figure and caption from Marion et al. 2016

shocked material being part of the primary, collision between the ejecta and companion creates a strong reverse shock in the envelope of the companion. This mechanism predicts emission on two timescales; seconds and days, in two different energy regimes; X-ray and UV/optical. The prompt emission is a result of the companion punching a hole in the ejecta, halting the expansion and creating a 'cone' where the shock emission can stream away almost unimpeded. The flux increase over longer timescales is powered by those photons not radiated before the cavity is filled in by the overrunning ejecta, which diffuse into the bulk material. Both channels for emission have a strong dependence on orientation, companion radius and separation, and perhaps only $\sim 10\%$ of SD SNe will have favourable viewing angles for this to be seen (Kasen, 2010). Initial observational efforts to search large samples for such emission were unable to find evidence of any contribution from progenitor interaction (Bianco et al., 2011; Hayden et al., 2010b). However, the non-detection enabled Bianco et al. (2011) to place a 3σ upper limit on the RG-WD binary configuration fraction at 20%, while the analysis of Hayden et al.

(2010b) strongly disfavours a RG companion, even if the SD channel dominates, in line with constraints from radio searches (Panagia et al., 2006).

However, in the case of iPTF14atg, UV observations by the Swift Space Telescope triggered immediately after detection found strong but declining emission in all three UV bands ($uvw2$, $uvm2$, $uvw1$) and flux excesses in u and b (Cao et al., 2015). The authors explored and ruled out spherical emission mechanisms such as shock cooling and CSM interaction and found that companion interaction was the most likely candidate, where the separation between the binary was less than $100R_{\odot}$. It should be noted however, that iPTF14atg does not appear to be part of the 'spectroscopically normal' population of SNe Ia; showing most similarity to the SN 2002es (Ganeshalingam et al., 2012), an underluminous object known to be photometrically (González-Gaitán et al., 2014) and spectroscopically (Foley et al., 2016) perculiar, sitting between SNe Iax and 91bg-like SNe. Ganeshalingam et al. (2012) estimate that such objects make up no more than 2.5% of all SN Ia events.

3.3.4.1 Limits on the Progenitor of SN2015F

As well as UV emission, Im et al. (2015) have suggested shock heated cooling from interaction with a sub stellar companion to fit the optical light curve SN 2015F. While in SN 2012cg (Marion et al., 2016), the early time lightcurve of which can be seen in Figure 3.3, interaction with a companion of around $6M_{\odot}$ is the favoured best fit, using the models of Kasen (2010). In the case of SN 2012cg, the lightcurve returns to normal power-law rise shape at phases later than $\tau > 14$, meaning that there is a window of ~ 4 days after the first light to catch such emission. As the strongest emission is expected (and in the case of SN 2012cg, seen) in the UV, observing this effect in our rise time sample of predominantly $R_{\rm P48}$ data is unlikely for all but the most extreme configurations.

Data from Cartier et. al. (sub.)for SN 2015F have two non-detections approximately 12 hours before the first detection of Im et al. (2015), and in the bluer V filter. This means that we should be able to place more stringent limits on the progenitor radius, by fitting the same series of models (Kasen, 2010; Pan et al., 2012).

3.4 Light Curve Fitting

To obtain SNe parameters such as stretch, time of maximum light and peak brightness, we will use the light curve fitter SiFTO (Conley et al., 2008b), described in Section 2.3.

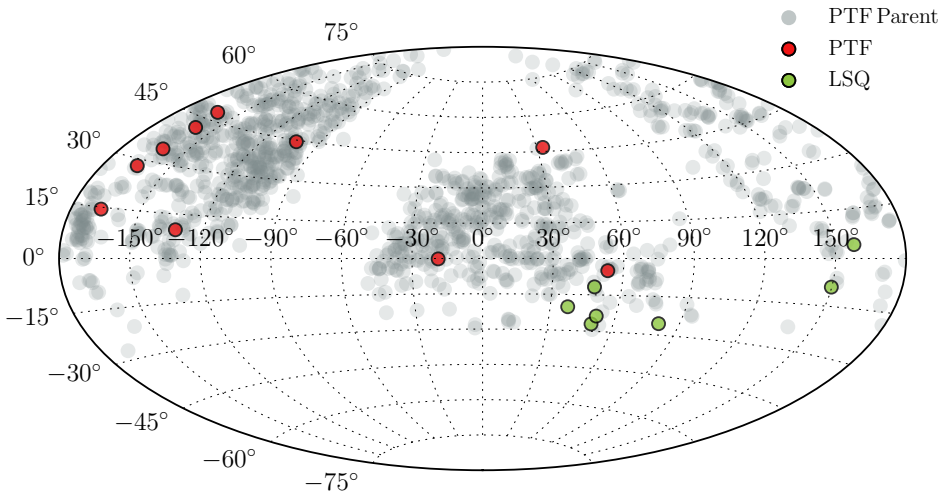

FIGURE 3.4: Spatial distribution of the SNe Ia rise time sample

SiFTO operates by manipulating a template time series SED to best fit the observed SN photometry. We define the time of maximum for a given SN as the one returned by SiFTO, $t_{\max}(B)$, such that phase, $\tau = t - t_{max}$, and use the single-colour stretch, S, as our measure of light curve width.

3.5 Rise-time Sample Selection

This sample utilised both PTF (Section 2.1) and LSQ (Section 2.2.2) photometry. The spatial distribution of this sample can be seen in Figure 3.4.

3.5.1 Selection Cuts

As our study requires well-sampled and relatively high signal-to-noise (S/N) data, there are several selection criteria that we make. We only allow SNe with both more than three epochs of data and more than 4 photometric points within the calculated fitting region (Section 3.2, Figure 3.1), as fewer would be insufficient to constrain the free parameters in the model. Light curves with more than four days between any two consecutive points are also excluded.

3.6 Testing

We have outlined the lightcurve models and other methods used to measure and parameterise the rise to maximum brightness of SNe Ia. To best use our dataset, we will fit

our lightcurves with Equation 3.12, allowing n to vary as a free parameter rather than constrain it to $n = 2$, and with Equation 3.13, holding $n_0 = 2$ to test the time dependence of the variation from the canonical fireball model. We will do this on an object by object basis, to avoid the pitfalls of stacking the lightcurve. For SN 2011fe we will also fit Equation 3.14 to search for evidence of a break, and Equation 3.13 with n_0 as an additional free parameter. As we have a combined data sample including a number of filters, we must perform a series of tests to check the validity of our conclusions. The nature of our sample means that we do not have simultaneous multi-band observations at the epochs we are investigating. As a result we cannot reliably construct bolometric luminosities or calculate accurate k-corrections for our objects, other for the exceptional SNe SN 2011fe and SN 2015F. In order to draw meaningful conclusions from our data, we need to investigate how the filtered data compares to other bands and the bolometric shape of the light curve, and ensure that we are measuring a consistently well-defined rise time region. To achive this, we consider two well observed SNe, SN 2011fe and SN 2015F, and measure how the parameters we measure, in particular $t_{\rm rise}$ and n change under a series of tests. While the variation between SNe is expected to be significant, we must also check for systematic offsets in our photometry. As we are fitting in flux space, we are forcing $f_{\rm model} = 0$ for $t < t_0$, but if there is an offset, the measured flux may not be centered around 0 in the absence of SN flux.

3.6.1 Flux before t_0

As our method is sensitive to variation in the data at very early times, i.e. very low flux levels, it is important to test for systematic effects from the data reduction, for example in the image subtractions. This was performed by averaging the points before the SN first light. Prior to the explosion, the flux level is consistent with 0, with no evidence of a systematic offset, as shown in Figure 3.5. We find for the above, the mean value, $\bar{\sigma} = -0.015 \pm 0.08$, median $\hat{\sigma} = -0.127$ and standard deviation $s = 1.22$. The mean of the raw counts is $\bar{N}_{\rm counts} = 15.8 \pm 18.3$, median $\hat{N}_{\rm counts} = -5.8$ and standard deviation $s = 76.0$. This means that both the counts, and the flux taking into account the associated uncertainty are consistent with 0.

3.6.2 The Rise Time Region

As detailed in Section 3.2.1, the assumptions on which the 'Fireball' model (Equation 3.1) are based only hold for the first few days after explosion. More fundamentally, the rise of the SN must slow and peak. All of our parameterisations only deal with the period before the light curve inflects, and eventually turns over to peak. We must

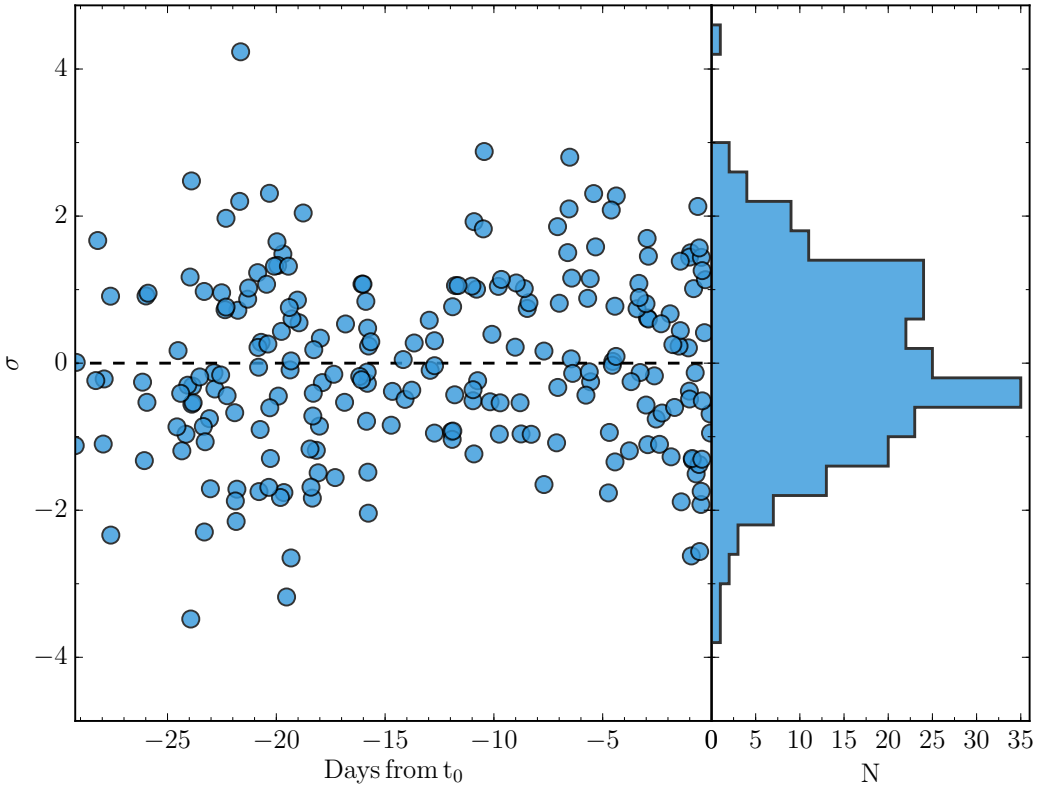

FIGURE 3.5: Flux prior to first light for our entire sample, where $\sigma = F/\sigma_F$. No evidence of a systematic offset is found. We find a mean of $\bar{\sigma} = -0.015 \pm 0.08$, median of $\hat{\sigma} = -0.127$ and standard deviation $s = 1.22$.

therefore determine over which range the model holds, and thus over which range we can fit the data.

Both Conley et al. (2006b) and Ganeshalingam et al. (2011a) define their rise-time region as earlier than 10 days before B-band maximum light, (i.e., $\tau < -10$). This may occur at a different number of days post-explosion for different SNe Ia due to the stretching of the SN light curves. As we are not stretch-correcting the raw data in this study, prior to fitting, we instead prefer a definition relative to t_0.

The choice of the fitting region must balance two competing constraints: there must be sufficient data to allow a meaningful rise-time fit, yet the fitting region must not reach too far into the photometric evolution where the rise-time parameterisation does not hold. Balancing these requirements across the sample, as well as taking into account the stability of the result, is challenging.

In many cases, the cut-off time that best satisfied these constraints was nearly coincident with $t_{0.5}$, the time at which the SiFTO light curve was at half of its maximum value (see Figure 3.1). $t_{0.5}$ is not reliant on either the stretch or a fixed number of days, so is an ideal choice as a limit of the fitting region. It is also broadly consistent with

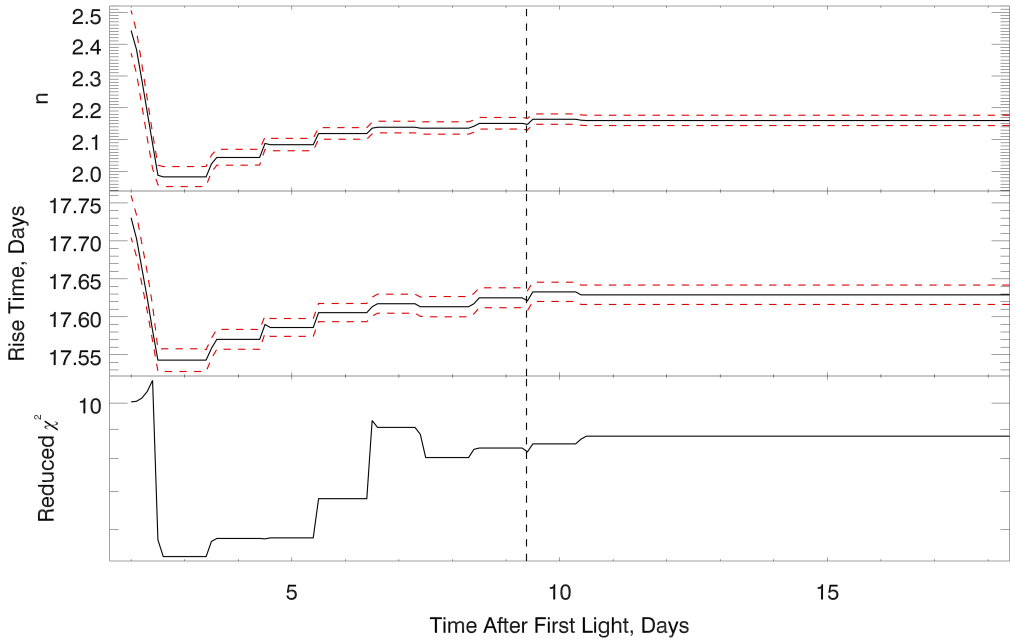

FIGURE 3.6: The fit parameters for SN 2011fe as a function of the epoch range over which the fit is performed, from 2 to 18 days after first light. *Top panel*: The change in n, *Middle panel*: The variation in rise time, *Bottom panel*: The evolution of the goodness of fit statistic, χ^2 per degree of freedom, as defined in Equation 3.16. The vertical dashed line shows the time at which the lightcurve reaches half of its maximum value ($t_{0.5}$)

$\tau < -10$ if the light curve was stretch corrected. To ensure a consistent definition of $t_{0.5}$, after fitting, the value of $t_{0.5}$ is re-calculated using the best fit to the data. This is in most cases almost indistinguishable from that calculated from SiFTO, indicating a good match, but is free of any reliance on the later time data. We also find it useful to split the rise time into two components, t_1 and t_2 at t_0 (See Figure 3.1).

This approach is similar to that used in González-Gaitán et al. (2012), where they define their limiting epoch as the 'transition phase', $\tau_{\rm t}$, where the light curve transitions from the rise to the main body, and they find $-10 \leq \tau_t \leq -8$.

TABLE 3.4: Results for the SN 2011fe synthetic light curves. Δn is the difference between n in a given filter and that of the pseudo-bolometric, i.e. $n(\text{filter}) - n(\text{pseudo-bol})$. Similarly, Δt is the difference between $t_{\rm rise}$. Note: results in $g_{\rm P48}$ differ from Nugent et al. (2011) as a result of fitting a longer segment of the light curve.

Filter	n	Δ n	$t_{\rm rise}$, days	$\Delta t_{\rm rise}$ days
Pseudo-bol	2.23	0.0	17.75	0.0
B	2.05	−0.18	17.13	−0.62
V	2.33	0.1	18.54	0.79
$g_{\rm P48}$	2.15	−0.08	17.62	−0.13
$R_{\rm P48}$	2.15	−0.08	18.14	0.39
$gr_{\rm LSQ}$	2.20	−0.03	17.94	0.19

3.6.3 Filtered data versus 'bolometric'

Our next task is to establish the validity of comparing fits obtained in different filters and at different redshifts, both for comparison to earlier work, and for comparison between the different surveys in our sample. Ideally we would measure the rise-time on the bolometric output of the SN, but obviously such data are not available, and hence we need to examine any biases that might result; essentially, we are testing the effect of k-corrections. We test this by using the very well-observed nearby SNe Ia SN 2011fe and SN 2015F, which have significant spectroscopic and photometric early time data.

3.6.3.1 SN 2011fe

We use 15 available pre-maximum spectra from the literature of SN 2011fe (Nugent et al., 2011; Parrent et al., 2012; Pereira et al., 2013; Mazzali et al., 2014). We measure synthetic light curves from these spectra in the B, V, $g_{\rm P48}$, $R_{\rm P48}$, and $gr_{\rm LSQ}$ filters, as well as a 'pseudo-bolometric' band with a wavelength range $3500 - 9000$Å, with each spectrum scaled so that its synthetic $g_{\rm P48}$ magnitude matched that measured from the real $g_{\rm P48}$ photometry. Using the spectral templates of Hsiao et al. (2007), this pseudo-bolometric filter contains $\simeq 70\%$ of the bolometric flux at $t_{0.5}$ (corresponding to $\tau = -8.9$), and $\simeq 72\%$ of the flux at maximum light. The wavelength range of the pseudo-bolometric filter was chosen as it is covered by most of our available spectra.

The uncertainties in our synthetic light curves come from the $g_{\rm P48}$ photometric uncertainties, with an additional systematic uncertainty added in quadrature arising from relative flux calibration errors (e.g, differential slit losses). We estimate this to be 1%. These synthetic light curves were then fit as described in Section 3.7, and the results are in Table 3.4.

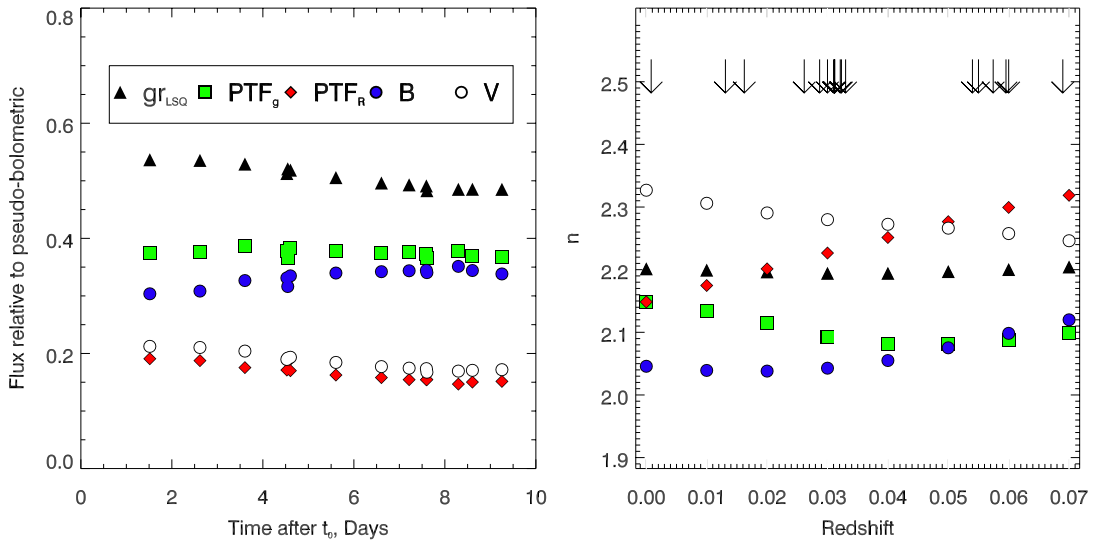

FIGURE 3.7: *Left Panel*:The flux of SN 2011fe through various filters relative to a pseudo-bolometric flux (see Section 3.6.3 for details) as a function of epoch. The filters are (top to bottom) $gr_{\rm LSQ}$, $g_{\rm P48}$, B, V, and $R_{\rm P48}$ filters. *Right Panel*: The fits to the redshifted spectra of SN2011fe, over the range of redshifts covered by our sample. The scatter around the mean redshift is consistent with the values found in the neighbouring panel. The arrows at the top of the figure show where our supernovae lie.

The results show some differences between different filters, due to rapid evolution in the spectral features in each band. Figure 3.7 shows how the flux in each filter, relative to pseudo-bolometric flux at that epoch, changes with time. The $g_{\rm P48}$ band shows an almost constant flux ratio, but $R_{\rm P48}$ decreases with time, while the B-band increases. The pseudo-bolometric value, 2.23 is greater than that in $g_{\rm P48}$, and greater than 2, in agreement with the findings of Piro & Nakar (2014). The broadest filter, $gr_{\rm LSQ}$, is obviously the closest to bolometric, but also shows a decreasing flux ratio. Note that earlier work has predominantly used data either in, or corrected to, the B-band. Table 3.4 shows that this fit has an n closest to 2; however, it is significantly lower than the values in the other filters, and is not consistent with the pseudo-bolometric value.

In an attempt to further understand the colour evolution and its effect on n, templates from both SALT2 (Guy et al., 2007) and Hsiao et al. (2007)/SiFTO were analysed. however, our investigation probes the very earliest epochs, where there have been few spectral observations. For example, the earliest Hsiao et al. (2007) templates pre-maximum are based on 6 spectra with an average epoch of $\tau = -11.6$ days. Because of this, and despite being a single example, the data from SN 2011fe are the best resource available

at very early times. Comparing with SN 2013dy (Zheng et al., 2013), the colour evolution is similar, although SN 2011fe exhibits a stronger Ca II IR triplet compared with SN 2013dy within the first 2 days. This does not fall within any of our filters, but falls within the pseudo-bolometric range. In summary, by considering the different fits to our simulated photometry, we estimate the systematic effect of using different filters to be $n \pm 0.1$.

3.6.3.2 Redshift

As our sample lies across a range of redshifts, we also need to ascertain the impact that this has on the colour evolution. To do this, we performed the same procedure as in Section 3.6.3.1, redshifting the spectra each time, up to our maximum redshift of $z = 0.07$ before fitting. The results of these tests can be seen in the right-hand panel of Figure 3.7.

We find that the broad $gr_{\rm LSQ}$ filter provides data that is very stable with redshift, withthe value of n remaining almost constant. Leaving the rest-frame, the measured n in $R_{\rm P48}$ and $g_{\rm P48}$ diverges, with the $R_{\rm P48}$ increasing and the $g_{\rm P48}$ decreasing more steadily. The scatter around the mean redshift ($z = 0.036$) is consistent with the dispersion between filters in Table 3.4.

In summary, we estimate the systematic effect of redshift to be reflective of that from using different filters, since the low redshifts do not shift the spectra by more than the width of our filters, that is, a systematic effect of at most $n \pm 0.1$.

3.6.3.3 Extinction

We also performed these checks after reddening the spectra by $E(B-V) = 1$, using the inverse of the process described in Section 2.4.2, and found no significant deviation in results. Additionally, inspecting the spectra at maximum light of each PTF object in our sample, we find evidence of Na I D absorption in only two SNe (PTF 11gdh and PTF 12gdq). These are discussed in more detail in the next chapter but do not appear to be unusual events.

3.6.4 SN2015F

To use SN 2015F as a test case, we avoid the need to create synthetic multi-band photometry from spectra as we have access to multicolour photometry, enabling us to directly measure the rise in a number of bands. Having this data in hand means that we can also

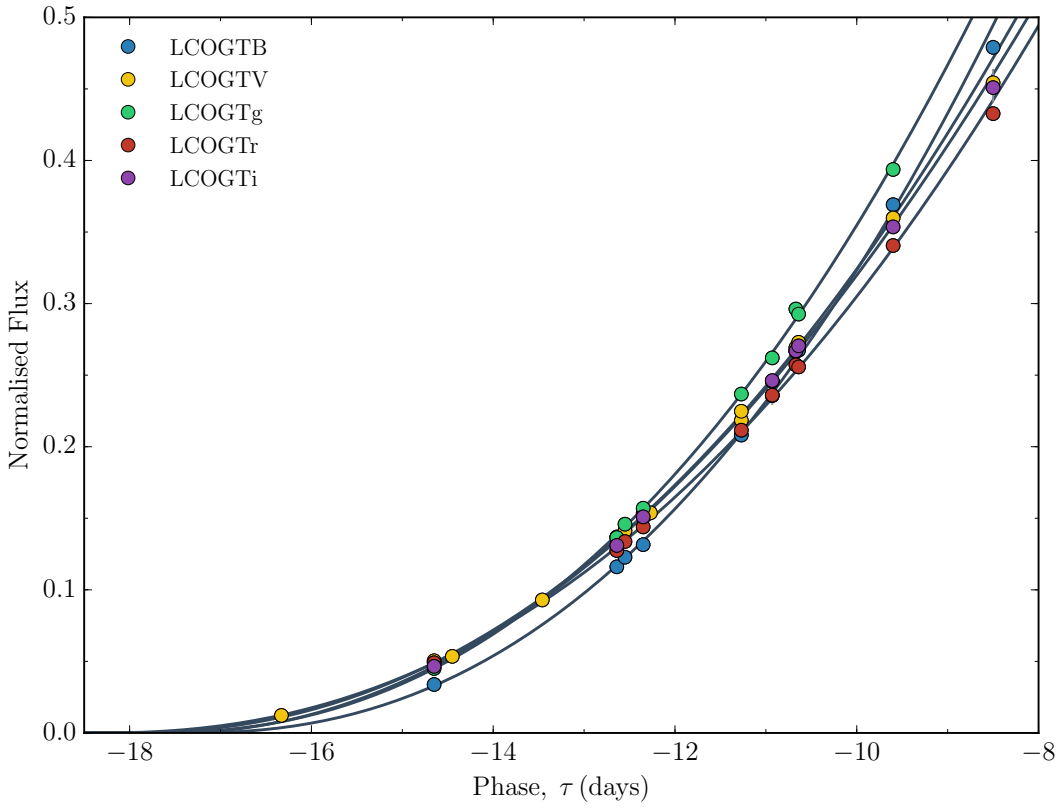

FIGURE 3.8: Multicolour Rise Time Observations of SN2015F

mangle the available spectra to the colour of the SN photometry. To construct a pseudo-bolometric in this case we corrected the fits to the photometry, shown in Figure 3.8, for dust extinction following Section 2.4.2. We then summed the model fluxes and barring LCOGTg (to avoid excessive overlap), before renormalising. Summing the fluxes in this way is relatively rudimentary as it neglects gaps and overlaps in the bandpasses, but has been found to reasonably approximate the bolometric luminosity (Contardo et al., 2000; Stritzinger et al., 2006). This 'BVri' bolometric model is then sampled at the same epochs as the LCOGTV-band, and fit with representative uncertainties of 1% of the peak normalised flux. The numerical results are presented in Table 3.5 and plotted against the effective wavelength of each filter in Figure 3.9.

As can be seen in Figure 3.9, the LCOGTg and LCOGTr values are consistent with the psuedo bolometric, and like in the case of $g_{\rm P48}$and $R_{\rm P48}$ in SN 2011fe, are approximately equal. As a result, combining the two should not be problematic. Again, if anything LCOGTr is a slight underestimate of the bolometric, however this to a lesser extent than in SN 2011fe. Notably, V, which was seen to exceed the pseudo-bolometric in the previous case by a large amount (0.1), now trails the 'bolometric' value. B, which in 11fe most closely approximated the fireball model, is in this instance the highest single measurement, instead being replaced by the reddest band, LCOGTi as the closest

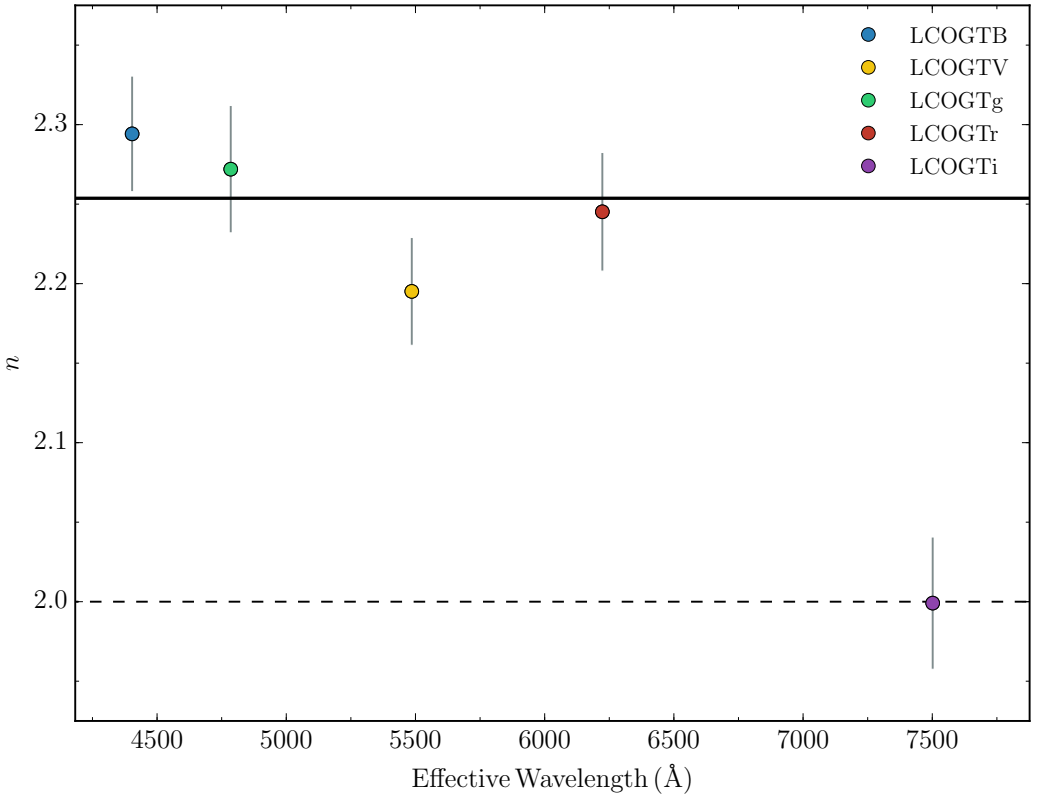

FIGURE 3.9: SN 2015F n vs effective wavelength of filter. The dotted line shows the 'fireball model' $n = 2$, and the solid line shows the 'bolometric' value (see Section 3.6.4)

TABLE 3.5: Results for the SN 2015F. Δn is the difference between n in a given filter and that of the pseudo-bolometric, i.e. n(filter) − n(pseudo-bol). Similarly, Δt is the difference between $t_{\rm rise}$, filtered and pseudo-bolometric.

Filter	n	Δ n	$t_{\rm rise}$, days	$\Delta t_{\rm rise}$ days
Pseudo-bol	2.254 ± 0.002	-	17.83 ± 0.01	-
B	2.294 ± 0.035	0.040	17.38 ± 0.08	0.46
V	2.195 ± 0.033	−0.059	18.06 ± 0.08	-0.22
g	2.272 ± 0.039	0.018	17.79 ± 0.08	0.04
r	2.245 ± 0.036	−0.009	18.34 ± 0.09	-0.51
i	1.999 ± 0.040	−0.255	17.51 ± 0.09	0.32

approximation of $n = 2$. The departure from the other filters may be in part due to the presence of the strong Ca II IR triplet within the bandpass, dominating the evolution.

3.7 Description of Fitting Method

We perform fits of Equation 3.12 to our data, correcting for $1 + z$ time dilation, using a grid-search minimisation of the χ^2 statistic over our three free parameters; α, t_0 and n,

i.e.,

$$\chi^2 = \sum_{i=1}^{n} \left(\frac{F_i - f_{model}}{\sigma_{F_i}} \right)^2 \tag{3.16}$$

where F and $\sigma_{\rm F}$ are the SN flux measurements and uncertainties, $f_{\rm model}$ is the model SN flux from Equation (3.12), and the sum runs over all the data points. We compute probabilities over a grid and report the mean value of the marginalised parameters as the best-fits, with our quoted uncertainties enclosing 68.3% of the probability. The conversion from χ^2 to probability, P, is $P \propto e^{-\frac{\chi^2}{2}}$.

The grid size is chosen to enclose as close to 100% of the probability as is measurable. Specifically, we chose ranges of: $-15 < t_{max} - t_0(n = 2) < 10$, where $0.0 < n < 8.0$ and $-9 < \log(\alpha) < 0$. An example of the range covered, and probability distribution, can be seen in Fig. 3.2. We sample $\log(\alpha)$ rather than α to better sample low values of α, while maintaining dynamic range.

This is a different, and slightly more direct approach to that used in Conley et al. (2006b) and Ganeshalingam et al. (2011a), in which Monte Carlo simulations are used to estimate the parameter uncertainties. However those analyses were performed on stacked light-curve data (rather than fitting individual objects), which requires a careful correction of the light curve shape and SN flux normalisation. This can introduce covariances between stacked data points, which demands a more sophisticated Monte Carlo like approach to handle these covariances.

The ellipticity of the contours in Figure 3.2 demonstrate the covariance between the parameters in a typical fit, and is representative of that seen in other SNe in the sample. The strongest is found between n and $\log(\alpha)$ but is present in significant strength between all of the variables.

3.8 Summary

In this Chapter we have introduced the theoretical underpinning of the rising portion of a SN Ia lightcurve, and outlined what we can hope to learn by studying these objects at these epochs. In addition, we have:

- defined a sample of 18 SNe Ia from PTF and LSQ
- constructed a fitting methodology, following a review of the literature, to measure the rise time and rise index n of a light curve, that follows a power law evolution, $F \propto t^n$

- tested this method on two nearby, well observed SNe, SN 2011fe and SN 2015F and considered the impact of dust extinction, redshift and inter–filter variation
- using the variation between filters seen in SN 2011fe, shown the consistency of our values using R_{P48} and gr_{LSQ}, and estimated a bolometric correction for n

In the next chapter, we present the results of the fitting methodology outlined here. We will compare our results to those in the literature and against theoretical predictions. From our results, we aim to draw conclusions about the physical processes and power sources that dominate at very early times.

Chapter 4

Rising Light Curves Results

"Astronomers ... deserve our awe and respect, because their everyday job consists of dealing with concepts so intense and overwhelming that it's a wonder their skulls don't implode through sheer vertigo. Generally speaking, it's best not to contemplate the full scope of the universe on a day-to-day basis because it makes a mockery of basic chores. It's Tuesday night and the rubbish van comes first thing Wednesday morning, so you really ought to put the bin bags out, but hey if our sun were the size of a grain of sand, the stars in our galaxy would fill an Olympic-sized swimming pool, and if our entire galaxy were a grain of sand, the galaxies in our universe would fill several Olympic-sized swimming pools. You and your bin bags. Pfff!"

- Charlie Brooker, *Guardian G2*, September 2009

In this chapter, we present the results of of applying our fitting methods (Section 3.7) to our data sample (Section 3.5) outlined in the previous chapter. Firstly we consider the 'normal' SNe Ia, we then go on to discuss three supernovae showing evidence of interaction with circum-stellar material (SNe Ia CSM).

In the discussion that follows, we consider the underlying physics in an attempt to describe the distribution of parameters.

4.1 Results

The diversity of the early-time light curves in our sample can be seen in Figure 4.1. The light curves have been stretch corrected and normalised, and shifted to have a coincident $t_{0.5}$. Whilst when stretch corrected, in the t_2 distribution the scatter is reduced, the data in t_1 still show a large amount of variation (Figure 4.1). This variation, even after stretch

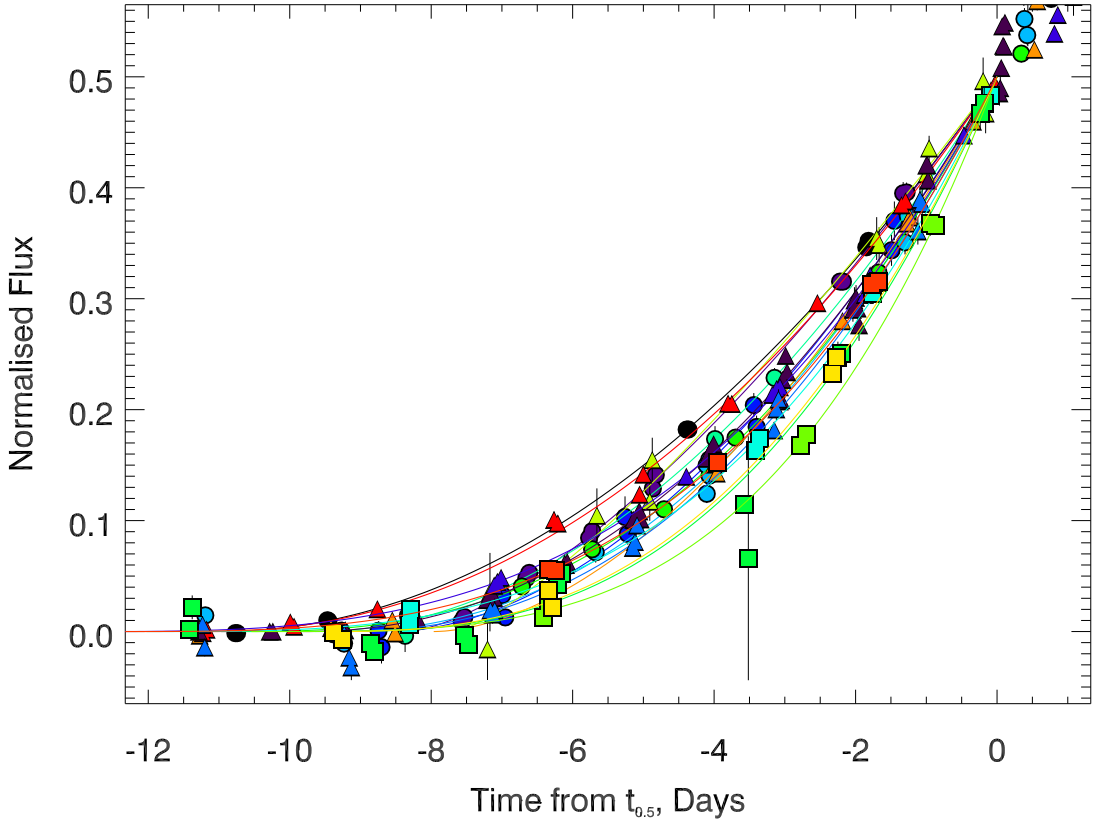

FIGURE 4.1: Our sample of SNe Ia Normalised, stretch corrected and shifted to have coincident $t_{0.5}$. Note the diversity in the early SNe Ia light curves even after stretch correction

correction, may have been lost within instrumental noise in previous surveys. To avoid introducing additional systematics due to misinterpreting this scatter, care must be taken when using SNe Ia data in this region for cosmology as the variation is significant.

In this section we first discuss the rise-time , followed by the rise index. Our results can be found in Table 4.1.2.3.

4.1.1 The SN Ia rise time

The average rise-time of the 18 SNe Ia in our sample with n a free parameter in the fit,

$$f_{\text{model}}(t) = \alpha(t - t_0)^n, \tag{3.12}$$

is $t_{\text{rise}} = 18.89 \pm 0.54\,\text{days}$, or $t_{\text{rise}} = 18.87 \pm 0.44\,\text{days}$ if the rise-times are stretch-corrected, where the uncertainties in both cases are the standard error on the mean. We exclude one SN, PTF12emp, from this latter calculation as there is insufficient data to reliably estimate a stretch. For the stretch correction, we use SIFTO to measure the stretch based on photometry later than $\tau = -10$, and so it is independent of the

TABLE 4.1: Rise-time results from the literature, where n is measured. Also shown is the difference between the measured values of n and t_{rise} in each work, and this analysis.

Survey	n	Rise Time (days)	Δn	σ	Δt_{rise} (days)	σ	
SNLS	1.8 ± 0.2	$18.50^{+0.18}_{-0.17} \pm 0.2$(syst)	0.64	2.7σ	0.39	0.7σ	Conley et al. (2006a)
SDSS	$1.8^{+0.23}_{-0.18}$	17.38 ± 0.17	0.64	2.7σ	1.51	2.7σ	Hayden et al. (2010a)
LOSS	$2.2^{+0.27}_{-0.19}$	18.03 ± 0.24	0.24	0.8σ	0.86	1.5σ	Ganeshalingam et al. (2011a)
SNLS	$1.92^{+0.31}_{-0.37}$	$16.85^{+0.54}_{-0.81}$	0.52	1.6σ	2.04	2.7σ	González-Gaitán et al. (2012)

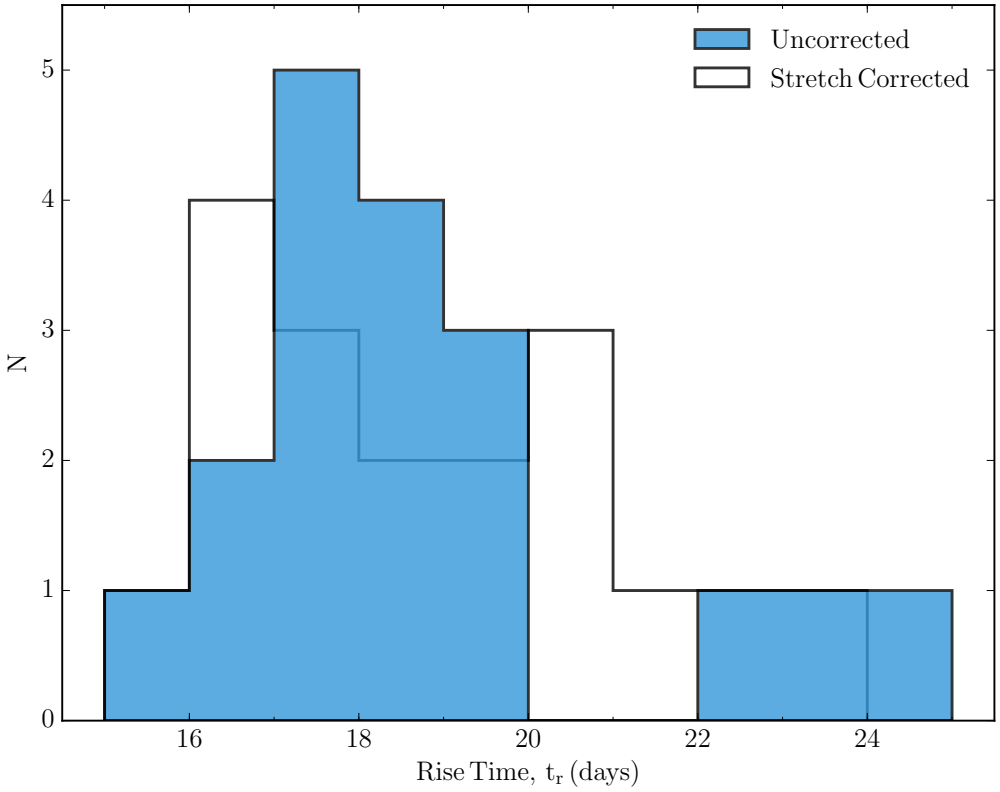

FIGURE 4.2: Histogram showing the distribution of rise times in our sample after fitting Equation 3.12. The rest-frame rise-time distribution is shown in blue, and the result of correcting this for the width of the lightcurves is shown as black outline.

shape of the early light curve. These values are longer than those found in previous work. Assuming $n = 2$, the mean rise-times are $t_{\rm rise} = 17.86 \pm 0.42$ days uncorrected and $t_{\rm rise} = 17.90 \pm 0.33$ days, after stretch correction. The $n = 2$ rise times are shorter in both cases. These values are consistent with Ganeshalingam et al. (2011b), but lower than Conley et al. (2006b) and higher than those found in both Hayden et al. (2010a) and González-Gaitán et al. (2012) by 3σ. The histogram of the rise-time distributions can be found in Figure 4.2. Strovink (2007) previously suggested that there may be two rise time modes, once the rise times have been corrected for the overall shape of the

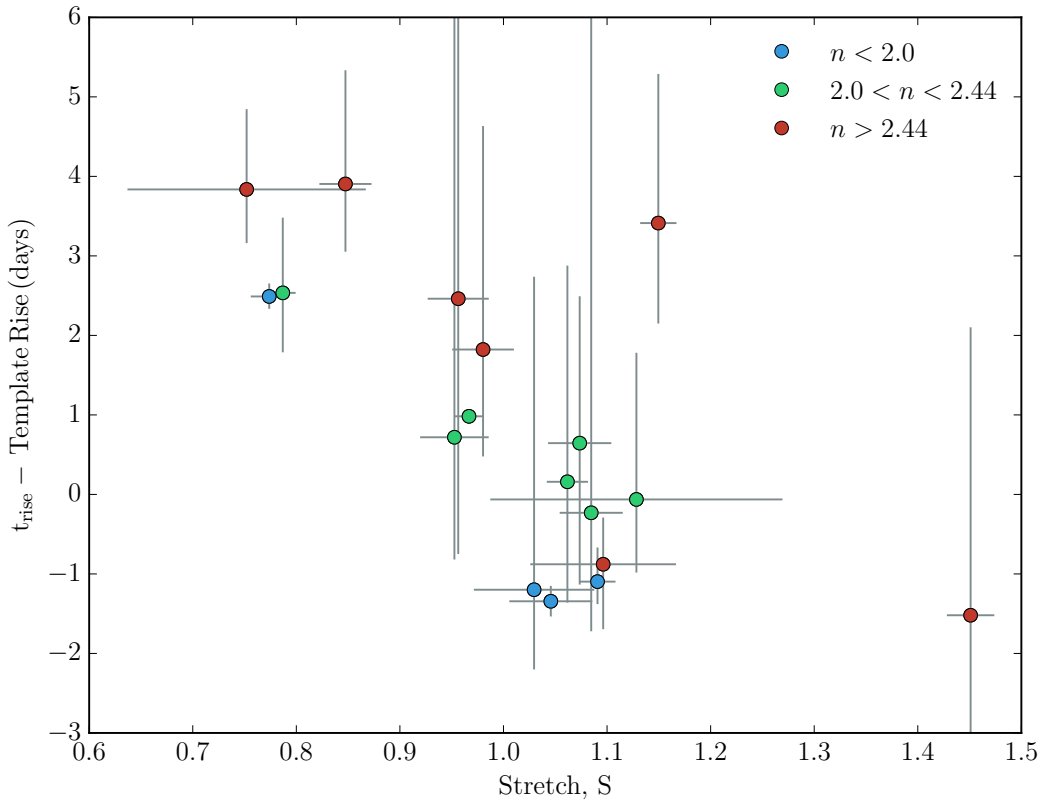

FIGURE 4.3: The difference between the measured $t_{\rm rise}$ and the $t_{\rm rise}$ expected from our SN template based on the stretch, plotted against the stretch. The coloured points denotes a binning by the rise index. Red circles are $n > 2.44$, green triangles $2.0 < n < 2.44$, and blue squares $n < 2.0$. Higher stretch SNe Ia have a $t_{\rm rise}$ that is faster than that implied by the stretch-corrected template $t_{\rm rise}$.

light curve (using the fall time). We do not find any evidence for this using either $n = 2$ or n-free.

Hayden et al. (2010a) and Ganeshalingam et al. (2011b) both find that the fraction of their sample that are slowest to decline after peak are amongst the fastest to rise. Both studies therefore parameterise the width of the light curve using two stretch parameters, one pre- and one post-maximum. Ganeshalingam et al. (2011b) also find that the luminous SNe Ia have a faster rise than expected based on a single stretch value. We see a similar trend in Figure 4.3, also lower stretch SNe appear to have slower light curves than would be expected from a single stretch. In Figure 4.4, we show the relation between stretch (again calculated without the very early photometric data) and $t_{\rm rise}$. A correlation is expected and observed in the data. The results are also shown for $n = 2$ showing, on average, shorter rise times.

The rise-time can be decoupled into two components: t_1, the time between first light (t_0) and the time of half maximum ($t_{0.5}$), and t_2, the time between $t_{0.5}$ and $t_{\rm max}$(shown in Figure 3.1). As can be seen in Figure 4.6, surprisingly, these two timescales do not show a

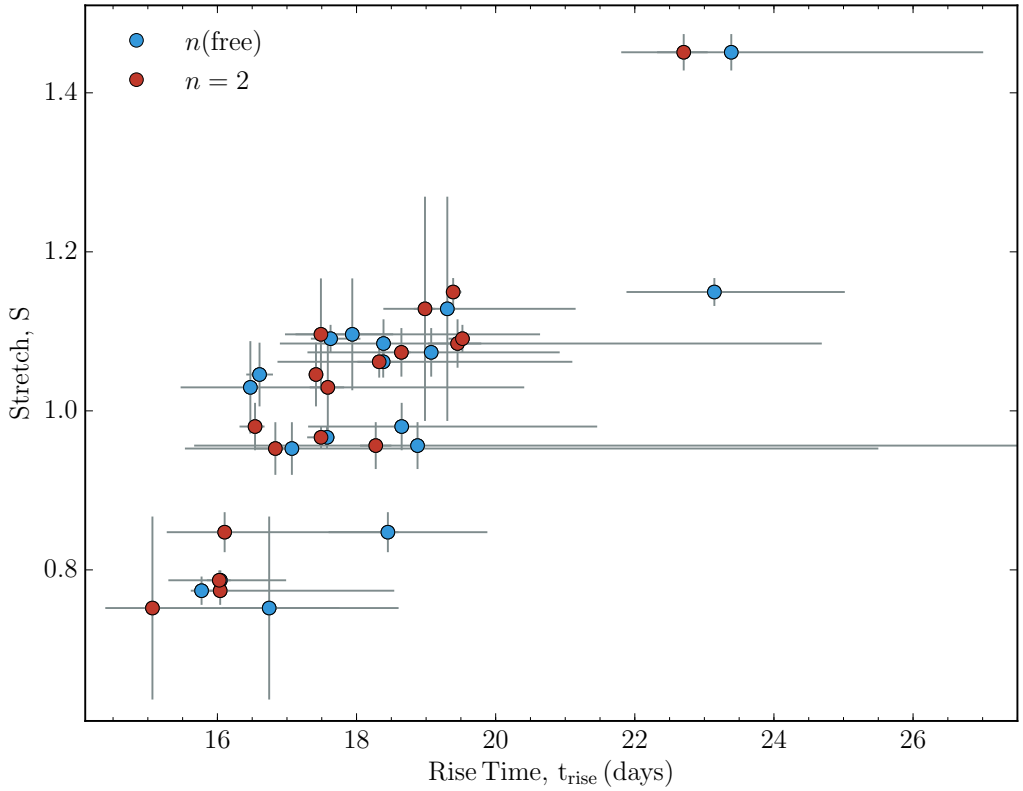

FIGURE 4.4: $t_{\rm rise}$ vs stretch for $n = 2$ and n(free)

particularly strong dependence, having a Pearsons correlation coefficient (Francis, 1895) $R = 0.61$, and when imposing a stretch cut commonly used in cosmology, $0.7 \leq s \leq 1.3$ (Conley et al., 2011), which excludes LSQ12gpw, this drops to 0.43. As the SiFTO fit includes data from $\tau > 10$, which is roughly consistent with $t_{0.5}$, it is unsurprising that Figure 4.7 shows a strong correlation between t_2 and stretch, with $R = 0.89$. However, there is also no strong relationship between stretch and t_1 (Figure 4.7) ($R = 0.57$, which weakens to $R = 0.34$ when imposing a stretch cut).

4.1.2 The Rise Index - 'n'

The distribution of the n parameter, which can be seen in Figure 4.8, has a mean of $n = 2.44 \pm 0.13$ and a tail in the distribution towards higher n. When corrected to a pseudo-bolometric value, as discussed in Section 3.6.3, this becomes $n = 2.50 \pm 0.13$. Neither of these values are consistent with the $n = 2$ fireball model, although individual SNe Ia within the sample are consistent with $n = 2$ (Table 4.1.2.3); the n values broken by SN name are shown in Figure 4.9. To compare with previous work (Table 3.1,3.3), our n value is consistent with Ganeshalingam et al. (2011b), who use the low-redshift LOSS sample and find $n = 2.2^{+0.27}_{-0.19}$. Our result is inconsistent with more recent higher

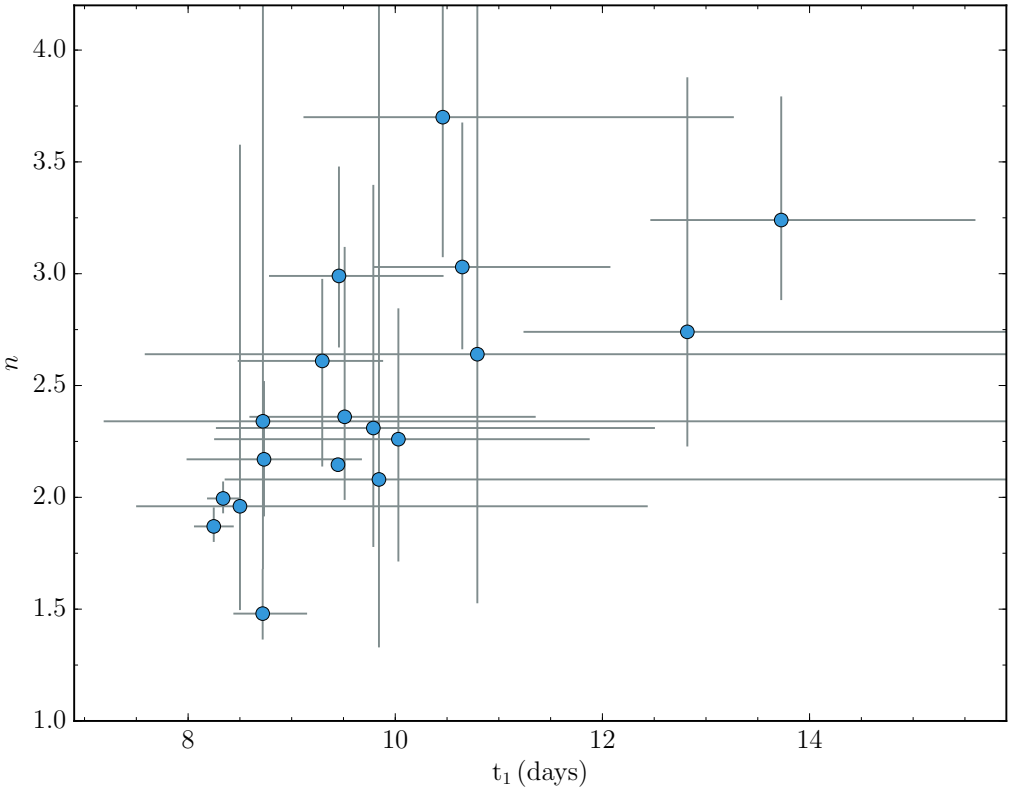

FIGURE 4.5: Plot showing n vs t_1. In the fitted region, n correlates with the length of time from t_0 to $t_{0.5}$. Note that the the values of n and t_1 for individual SNe are covariant, meaning that the uncertainties plotted here are conservative. A representative example of the ellipticity of the probability distribution marginalised to calculate the uncertainties can be seen in Figure 3.2

redshift studies, Hayden et al. (2010a) or González-Gaitán et al. (2012). Furthermore, the recent study of SN 2014J found a rise index of $n = 2.94 \pm 0.20$ (Zheng et al., 2014). This lends further evidence that there is not only a range of n, but that the centre of the distribution is located at values $n > 2$. This result supports the finding of Piro & Nakar (2014) that a t^2 rise is not a generic property of SNe Ia.

As mentioned in Section 3.6.3.3, we see non-zero Na I D absorption lines at the position of the host galaxy in the low-resolution spectra, in two SNe: PTF 11gdh and PTF 12gdq (Figure 4.10). However, we cannot tell whether this is from the host or from CSM interaction, but the measurements of n and $t_{\rm rise}$ are not different from to bulk of the sample and the line centres do not move over time. We do not find these SNe to occupy any unusual position in any of the parameter space we investigate. Both have a value of n that is consistent with the mean value within the calculated uncertainties.

We find no evidence of a correlation between n and stretch (Figure 4.11, left panel). González-Gaitán et al. (2012) found a weak trend, with larger stretches corresponding with higher n. While both $t_{\rm rise}$ and stretch do not correlate strongly with n, as can

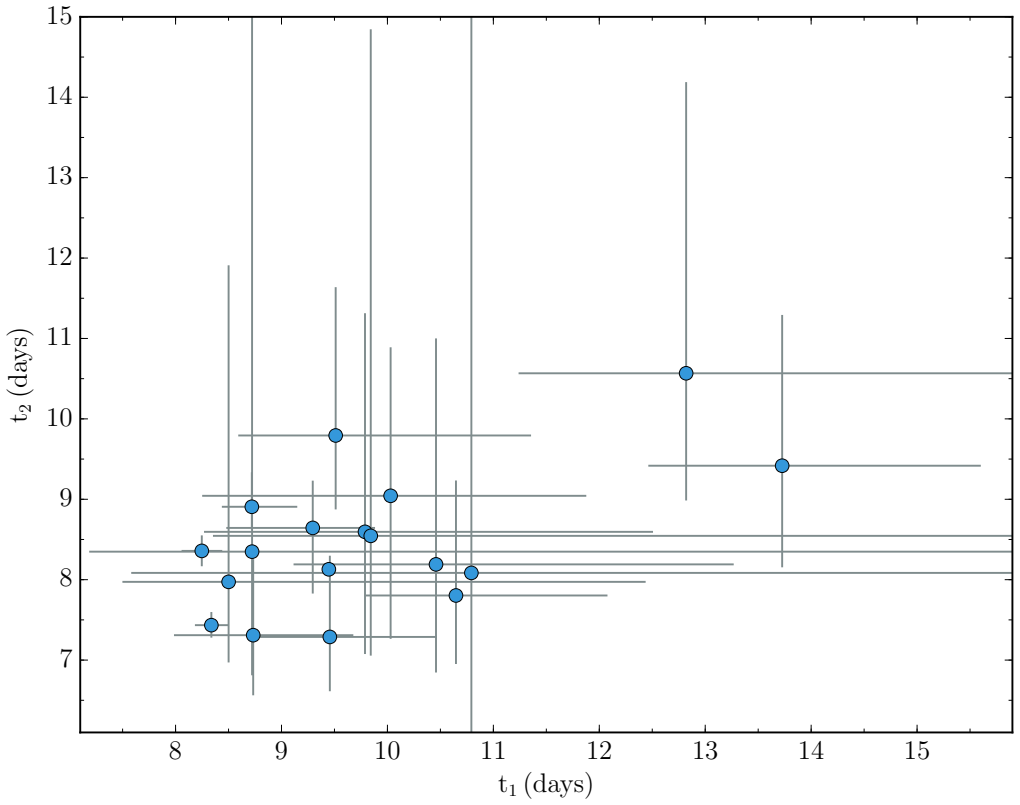

FIGURE 4.6: t_2 vs t_1

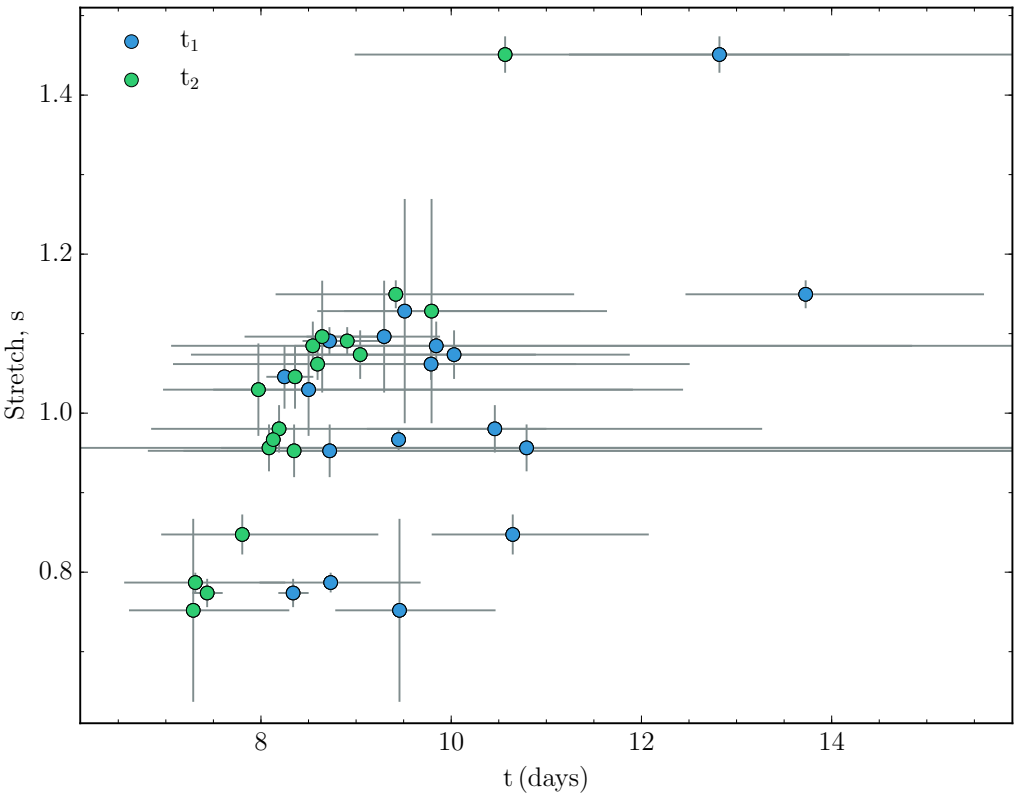

FIGURE 4.7: Stretch vs t_1 and t_2

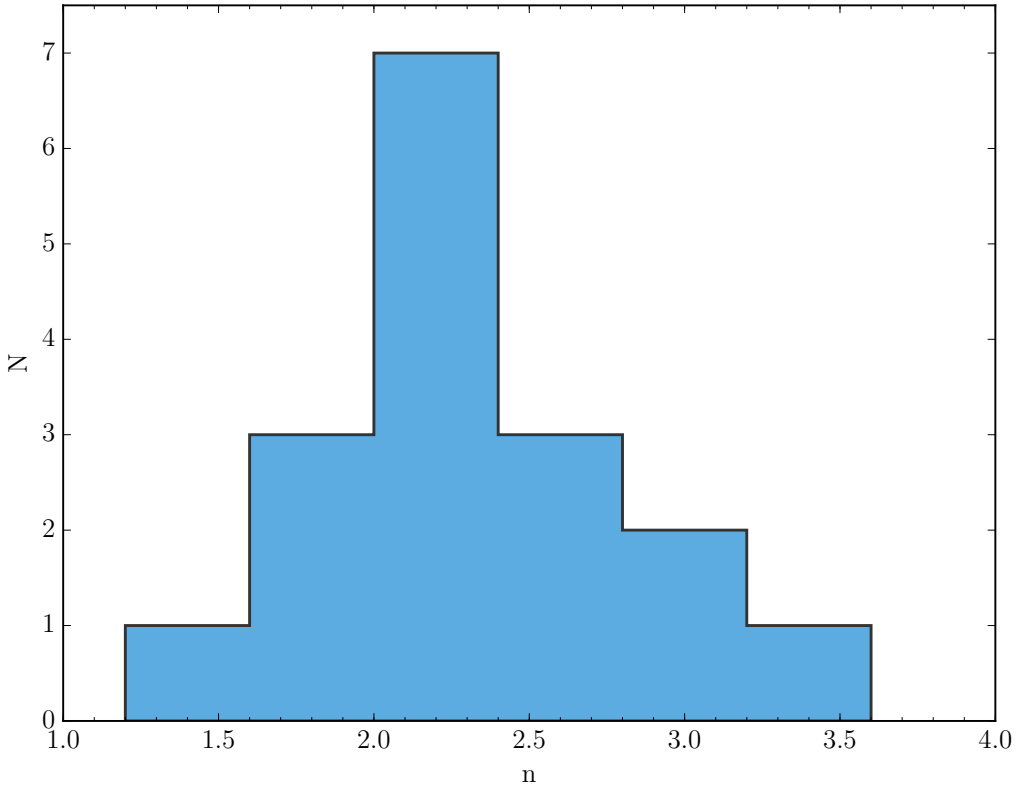

FIGURE 4.8: Histogram showing the distribution of n in our sample after fitting Equation 3.12.

be seen in Figure 4.11, there is a clear correlation between t_1 and n (Figure 4.5), with the lowest rise indices corresponding to the shortest initial time spans. A distribution of n values centred above 2 agrees well with previous work on individually fitted SNe (Nugent et al., 2011; Hachinger et al., 2013; Zheng et al., 2013, 2014). However, these fits were done on rise time regions of varying sizes, it is for this reason that our value of n for SN 2011fe differs from that of Nugent et al. (2011). In Figure 3.6, when the data range fitted is the same, the values are fully consistent. Thus direct comparisons between studies are difficult, as a shorter, earlier fitting region probes a shallower ejecta region, raising the prospect of a time dependent index.

4.1.2.1 Testing the Value of n

To confirm our finding that the mean value of n in our sample is inconsistent with a simple fireball model, we utilise two statistical techniques: 'Monte-Carlo' analysis, and 'Bootstrapping with replacement'. In our Monte-Carlo, we simulate new samples of data by drawing a value of n from the probablity distribution used to find the value in the grid search, once it has been marginalised down to one dimension. The value randomly drawn from the distribution, which may be larger or smaller than the original, is then

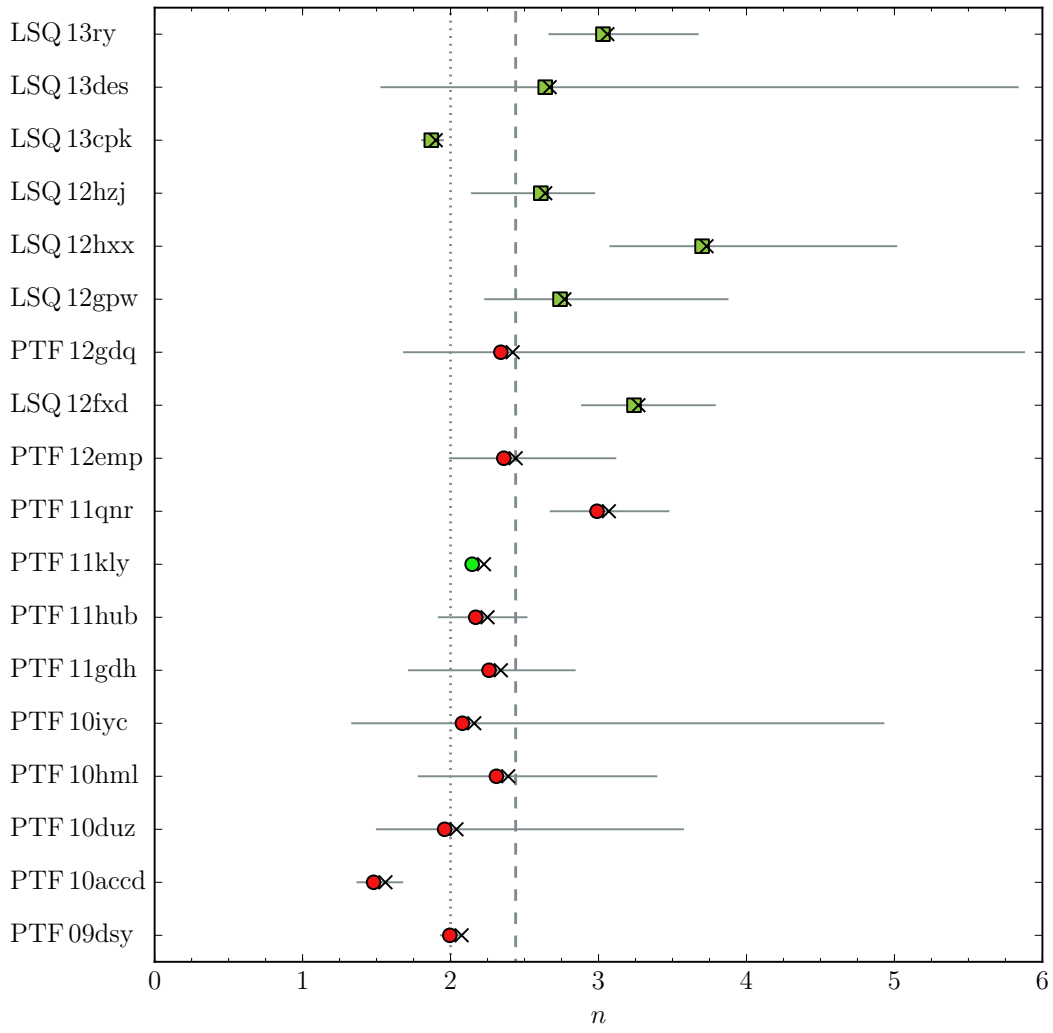

FIGURE 4.9: The best-fit 'n' and uncertainty for each SN in the sample. Hollow squares are $gr_{\rm LSQ}$observations, solid circles are $R_{\rm P48}$and hollow circles are $g_{\rm P48}$. The dotted line indicates $n = 2$ and the dashed shows the mean of the sample, $n_{mean} = 2.44 \pm 0.13$. The crosses show the location of the points corrected to the 'bolometric' value of n, if the SN 2011fe correction (Table 3.4) holds for other SNe

used in a new, resampled dataset. The mean of this new dataset is then calculated, and the resulting histogram for 1,000,000 iterations is shown in the left panel of Figure 4.12. The peak of this distribution is $n = 2.440$ and 99.993% of the probability in the distribution lies at values of $n > 2$.

In the Bootstrap with replacement, we resample our sample data by randomly drawing values of n from the sample (without removing the values from the pool once selected), until we have a resampled dataset with the same number of values as our original one. The mean of this resampled data is then taken and recorded. This process is repeated a number of times; in our analysis, we draw 1,000,000 resampled datasets. The histogram

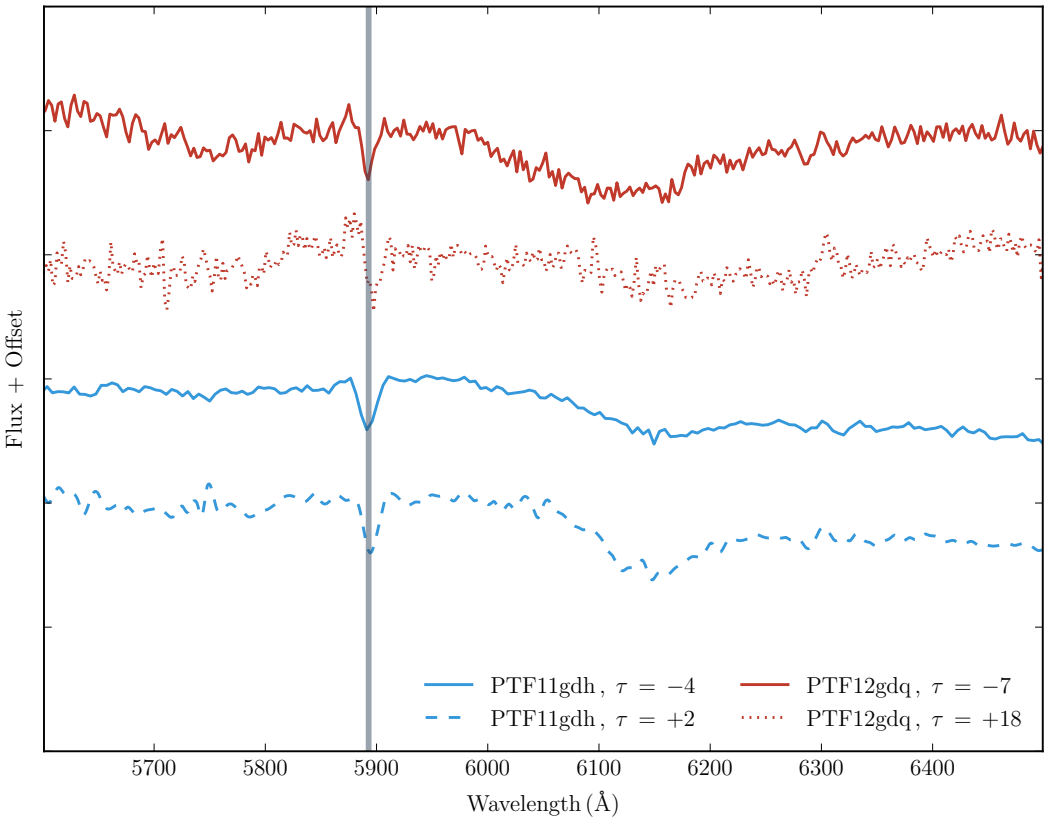

FIGURE 4.10: Na I D Lines Present in two phases PTF 11gdh (blue) and PTF 12gdq (red). These are the only objects in our sample to show significant Na I D absorption. Neither object occupies an unusual area of parameter space, and both have n and $t_{\rm rise}$ values consistent with the mean.

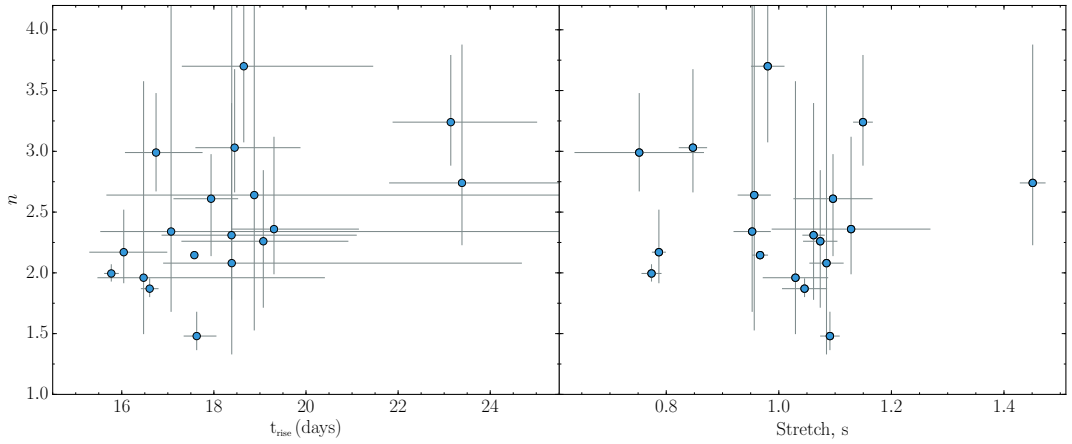

FIGURE 4.11: *Left Panel:* n and $t_{\rm rise}$ do show some evidence of a relationship, but with low significance. Note that the the values of n and $t_{\rm rise}$ for individual SNe are covariant, meaning that the uncertainties plotted here are conservative. A representative example of the ellipticity of the probability distribution marginalised to calculate the uncertainties can be seen in Figure 3.2. *Right Panel:* n vs Stretch for our sample, no evidence of a correlation is found.

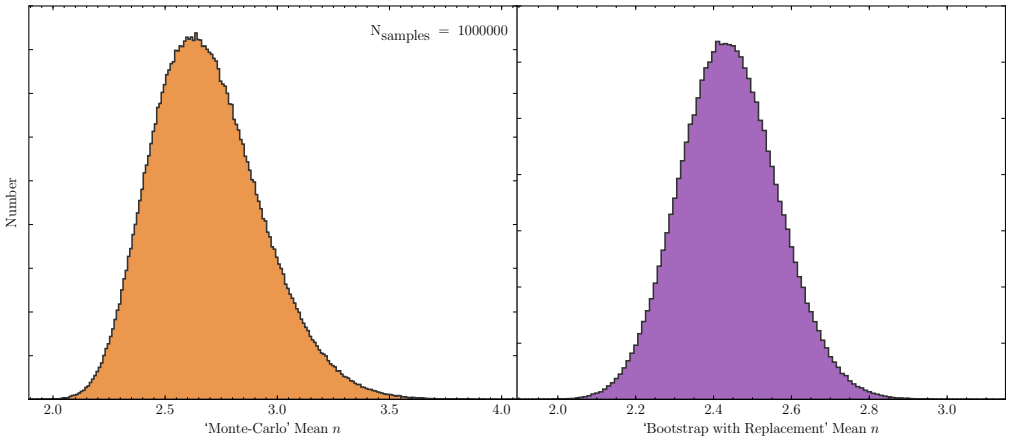

FIGURE 4.12: *Left Panel*: The distribution of mean n values from resampled data using a 'Monte-Carlo' method with 1,000,000 iterations, as described in Section 4.1.2.1. *Right Panel*: The distribution of mean n values from resampled data using a Bootstrap method, as described in Section 4.1.2.1, using the same number of iterations as for the Monte-Carlo.

of the mean values of the resampled data is shown in the left hand panel of Figure 4.12. The peak of this distribution is $n = 2.69$ and 99.997% of the probability in the distribution lies at values of $n > 2$. The higher mean value and tail of this distribution is a result of the asymmetrical errorbars on the individual values, with the tails towards higher n values.

4.1.2.2 A Time Dependent Index - '$\dot{n}$'

Figure 3.6 shows that the n measured changes with epoch, as more data is added the behaviour of n in Figure 3.6, is evidence that this is occurring. This effect explains the difference in n measured in this work ($n = 2.15 \pm 0.02$, for $t_0 \leq t \leq t_{0.5}$) and Nugent et al. (2011) (2.01 ± 0.01 for $t_0 \leq t \leq t_0 + 3$) procedure as outlined in Section 3.7, substituting Equation 3.13 for Equation 3.12.

We find evidence for a positive $\dot{n}$ in most SNe in our sample, with a mean value of $\dot{n} = 0.011 \pm 0.004\,\mathrm{d}^{-1}$ (where the uncertainty is the standard error on the mean) and a weighted mean value of $\dot{n} = 0.011 \pm 0.001\,\mathrm{d}^{-1}$. Specifically, in the case of SN 2011fe with n_0 as a free parameter, we find $n_0 = 2.02 \pm 0.02$, consistent with Nugent et al. (2011), and an $\dot{n} = 0.011 \pm 0.001\,\mathrm{d}^{-1}$. This positive $\dot{n}$ (in both cases) reflects that fitting Equation 3.12 we find the mean n greater than 2. We find some evidence that the SNe that have observations longest after explosion are those which, in general, have the largest $\dot{n}$; that is, the largest rate of deviation away from the fireball model. This may be driven physically by the later time data being driven by deeper ejecta layers.

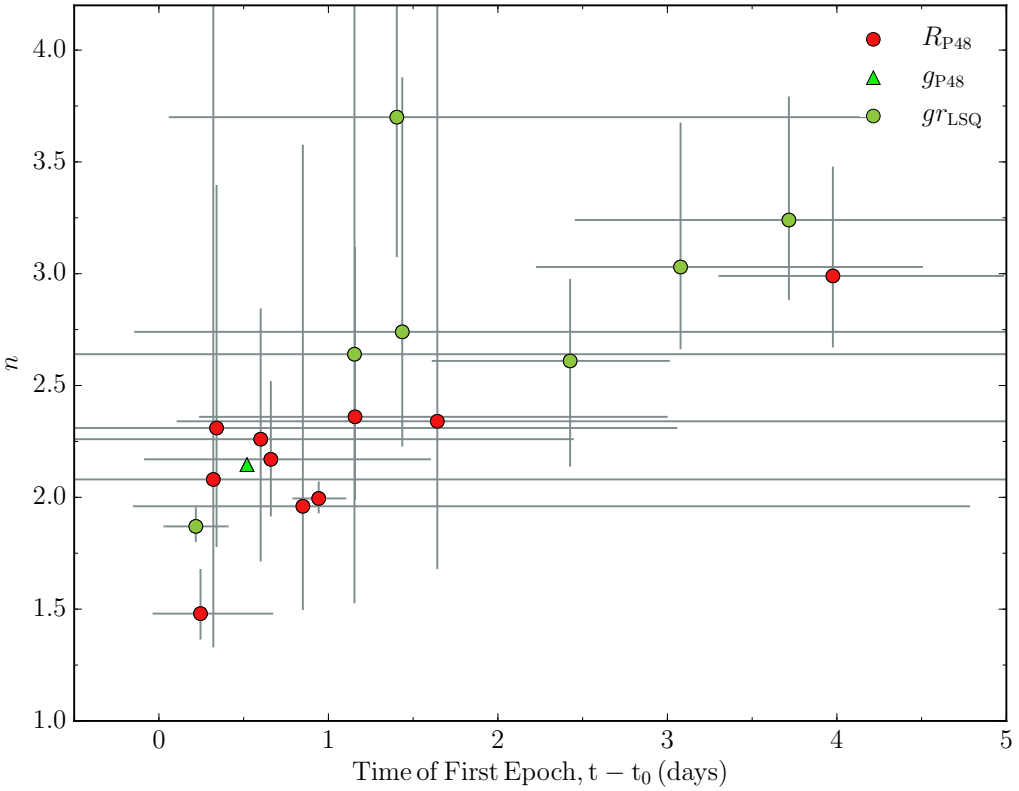

FIGURE 4.13: The fitted n plotted against the time of the first observation, relative to t_0 corrected for redshift. LSQ SNe are shown as green circles, PTF R_{P48}observations are shown in red, and g_{P48}(SN 2011fe) as a green triangle. Note that the the values of n and t_0 for individual SNe are covariant, meaning that the uncertainties plotted here are conservative. A representative example of the ellipticity of the probability distribution marginalised to calculate the uncertainties can be seen in Figure 3.2

This time dependence of n can also be seen in Figure 4.13. When the first observation of a SN is made earlier, the n is lower, due to the different ejecta conditions. Applying a linear fit, an intercept of $n = 1.8 \pm 0.2$ is found, and a slope of $m = 0.39 \pm 0.15$, making the trend significant to 2.6σ. When the observations begin at a later epoch, there is a smaller contribution from the ^{56}Ni in the upper most layers, changing the measured n.

4.1.2.3 Broken Powerlaw

We also performed a fit to SN 2011fe using Equation 3.14. Unlike Zheng et al. (2013) and Zheng et al. (2014) we find no evidence for a break in the light curve. The data from SN 2011fe contains 6 data points within the first three days after the explosion (i.e. before a 'break time'; $t_b^{2013dy} = 3.14 \pm 0.30\,d$ and $t_b^{2014J} = 2.61 \pm 0.20\,d$), however these are clustered in three epochs, and it may be that sub-day cadence is needed in this early time to be sensitive to broken power laws.

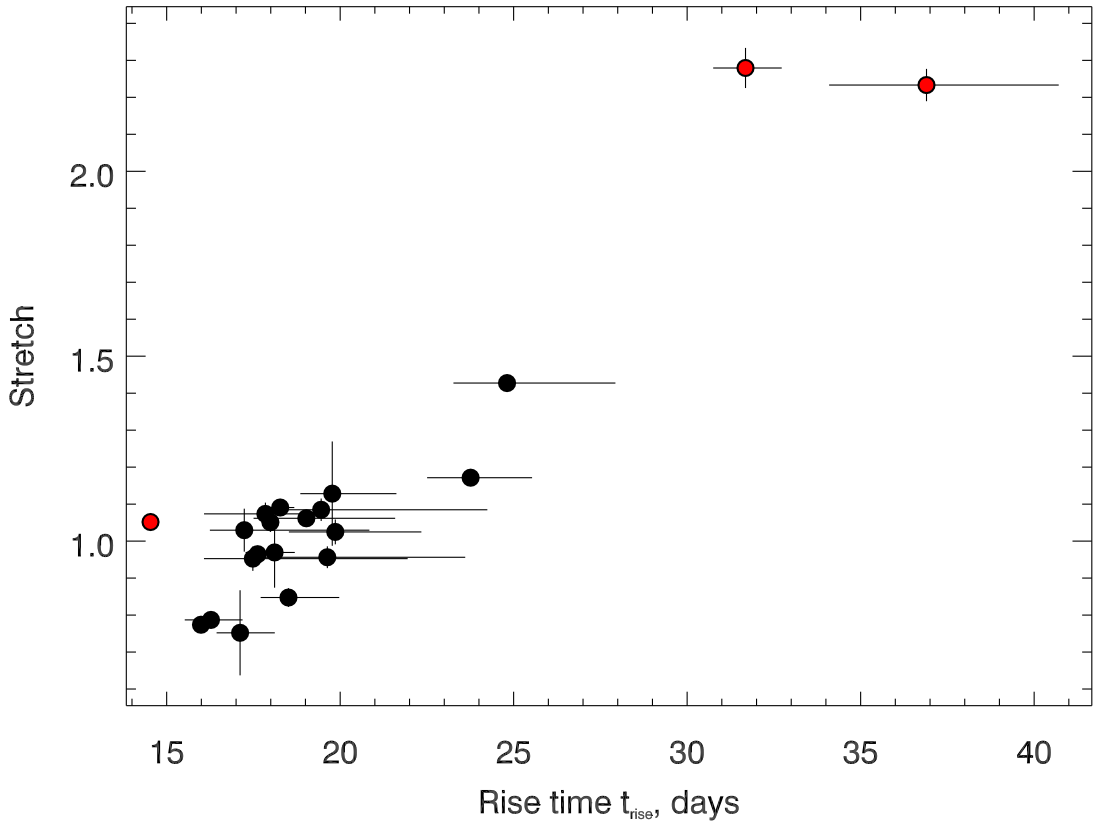

FIGURE 4.14: Stretch vs Rise time with 3 SNe Ia identified as CSM by Silverman et al. (2013b) plotted in red

4.1.3 Type Ia 'CSM' Supernovae

One reason for a SN to have an 'anomalous' rise would be an energy contribution from interaction with CSM material (Falk & Arnett, 1977). Silverman et al. (2013b) noted that the rise of SNe Ia-CSM tends to be significantly longer than a typical SNe Ia, following a simple photon diffusion argument - not only does a photon have to diffuse through the ejecta, but also significant amounts of CSM as well. In that respect, Ofek et al. (2014b) showed that in SNe Type IIn there is a possible correlation between rise time and peak luminosity.

Of the sample of Silverman et al. (2013b) (7 SNe) only 3 have sufficiently good photometry to provide acceptable fits, even after introducing constraints on the fitting. These fits assumed the fireball model, ($n = 2$), and the results of measuring the rise time can be seen in Figure 4.14.

One of these SNe, PTF12efc is a 'typical' broad and bright SNe-CSM, although having an extreme rise time and stretch, and seems to lie in agreement with the best fit to the

TABLE 4.2: Table of Results

SN	t_{max}, MJD	$t_{\rm rise}$, days	n	Stretch	$\chi^2_{\rm DOF}$	R.A	Dec. (J2000)	Filter (J2000)
PTF09dsy	55070.4 ± 0.1	15.98 ± 0.20	$2.00^{+0.08}_{-0.07}$	0.80 ± 0.01	0.58	3:33:22.1	-04:59:55.2	PTF48R
PTF10accd	55556.0 ± 0.2	$18.17^{+0.46}_{-0.32}$	$1.48^{+0.19}_{-0.12}$	1.11 ± 0.02	0.78	02:13:30.4	46:41:37.2	PTF48R
PTF10duz	55285.0 ± 0.2	$17.5^{+3.7}_{-1.0}$	$1.96^{+1.5}_{-0.46}$	1.00 ± 0.03	1.88	12:51:39.5	14:26:18.7	PTF48R
PTF10hml	55352.3 ± 0.1	$19.4^{+2.7}_{-1.5}$	$2.31^{+1.08}_{-0.53}$	1.07 ± 0.02	1.50	13:19:49.7	41:59:1.6	PTF48R
PTF10iyc	55361.5 ± 0.1	$19.4^{+4.4}_{-1.4}$	$2.08^{+2.00}_{-0.70}$	1.10 ± 0.02	1.04	17:09:21.8	44:23:35.9	PTF48R
PTF11gdh	55744.1 ± 0.1	19.57 ± 1.8	$2.26^{+0.58}_{-0.55}$	1.07 ± 0.03	1.25	13:00:38.1	28:03:24.1	PTF48R
PTF11hub	55770.0 ± 0.2	$16.50^{+0.96}_{-0.76}$	$2.17^{+0.35}_{-0.26}$	0.80 ± 0.01	1.17	13:12:59.5	47:27:40.3	PTF48R
PTF11kly/SN2011fe	55814.3 ± 0.1	17.59 ± 0.1	2.15 ± 0.02	0.965 ± 0.009	8.06	14:30:5.8	54:16:25.2	PTF48g
PTF11qnr	55902.3 ± 0.1	$17.01^{+1.0}_{-0.7}$	$2.99^{+0.49}_{-0.32}$	0.79 ± 0.04	1.57	22:44:25.4	-00:10:2.0	PTF48R
PTF12emp	56080.9 ± 0.4	$19.9^{+1.9}_{-1.0}$	$2.36^{+0.76}_{-0.37}$	1.13 ± 0.14	3.52	13:13:53.7	34:06:59.7	PTF48R
LSQ12fxd	56246.4 ± 0.1	$23.8^{+1.8}_{-1.3}$	$3.24^{+0.53}_{-0.36}$	1.17 ± 0.01	2.77	05:22:17.0	-25:35:47.0	LSQgr
PTF12gdq	56116.3 ± 1.8	$17.6^{+4.7}_{-2.3}$	$2.34^{+1.86}_{-0.61}$	0.94 ± 0.02	2.06	15:11:35.3	09:42:34.0	PTF48R
LSQ12gpw	56268.4 ± 0.1	$24.7^{+3.2}_{-1.6}$	$2.74^{+1.00}_{-0.50}$	1.42 ± 0.02	5.79	03:12:58.2	-11:42:40.0	LSQgr
LSQ12hxx	56289.8 ± 0.1	$19.9^{+2.3}_{-1.3}$	$3.70^{+1.08}_{-0.61}$	1.00 ± 0.03	2.00	03:19:44.2	-27:00:25.6	LSQgr
LSQ12hzj	56300.8 ± 0.2	$18.5^{+0.6}_{-0.8}$	$2.61^{+0.37}_{-0.47}$	0.97 ± 0.05	20.19	09:59:12.4	-09:0:8.30	LSQgr
LSQ13ry	56394.9 ± 0.1	$19.0^{+1.5}_{-0.8}$	$3.03^{+0.64}_{-0.37}$	0.86 ± 0.02	1.81	10:32:48.0	04:11:51.4	LSQgr
LSQ13cpk	56590.0 ± 0.1	$17.01^{+0.15}_{-0.25}$	$1.87^{+0.07}_{-0.13}$	1.05 ± 0.03	1.77	02:31:3.8	-20:08:49.6	LSQgr
LSQ13des	56638.9 ± 0.1	$20.0^{+3.9}_{-2.3}$	$2.64^{+1.37}_{-0.8}$	0.96 ± 0.03	2.79	03:25:18.9	-23:42:3.5	LSQgr

distribution of normal SNe Ia. PTF10iuf also has a long rise and large stretch but a higher stretch than would be predicted from the measured rise time. Despite lying on or near the correlation of 'normal' SNe Ia, there seems to be no reason for this to be the case - the rise is shaped by different physical processes over different timescales.

To make an estimate of the ejecta mass for PTF 11kx, Dilday et al. (2012) measure the equivalent width, W_λ, given by

$$W_\lambda = \left(N \frac{\lambda_0^4}{2\pi c} \frac{g_u}{g_l} A_{ul} \gamma_u \right)^{1/2}, \tag{4.1}$$

where N is the column density, λ_0 is the rest wavelength of the transition, A_{ul} is the Einstein spontaneous emission coefficient, γ_u is the radiation damping constant, and g_u and g_l are the statistical weights of the upper and lower states, respectively. When rearranged, the column density can be calculated: For the Ca II K line, with $\lambda_0 = 3933.6$Å, giving a Ca II column denisity of $\sim 5 \times 10^{18} \mathrm{cm}^{-2}$. To convert to total mass, a shell around the source is considered, $M_{ca} = k \times 4\pi r^2$, where k is the covering fraction, and r is the radius of the shell.

$$M_{Ca} = 3.43 \times 10^{-4} k \left(\frac{v}{25,000 \mathrm{km\,s^{-1}}} \frac{t}{59 \mathrm{days}} \right)^2 \left(\frac{N}{5 \times 10^{18} \mathrm{cm}^{-2}} \right) M_\odot, \tag{4.2}$$

PTF 11kx has a rise time of only $t_r^{n=2} = 14.5 \pm 0.2$ (Figure 4.15), but a measured stretch of $s = 1.05$. In Dilday et al. (2012), a rise time of ~ 20 days is assumed; note that a shorter rise time means that the ejecta will be smaller at a given phase. Consequently, the ejecta mass calculated using the previous estimate ($\sim 5.3 \mathrm{M}_\odot$) is too large, and should be $\sim 80\%$ of that value, $\sim 4.3 \mathrm{M}_\odot$, making the same assumptions as in the supplemental information of Dilday et al. (2012).

As well as performing a fit whilst holding $n = 2$, a grid-search was done to find the best fit where $t_r = 20$ days (Figure 4.15). With a fixed rise time, the best fit index was $n = 6.2 \pm 0.5$, this result is not physical for a 'normal' SN Ia, but SNe Ia-CSM have an additional contribution to their light from the collision of their ejecta with the CSM; this converts the kinetic energy in the ejecta into hard X-ray photons, which in the presence of sufficient optical depth can be converted into optical light (e.g. Chevalier & Irwin, 2012; Svirski et al., 2012; Ofek et al., 2014b). With this in mind, it may be expected for SNe Ia-CSM to have abnormal rise properties. Until a confirmed SN Ia-CSM is observed with enough precision to enable a relaxing of n, few constraints can be placed on the effect of CSM on a rising light curve.

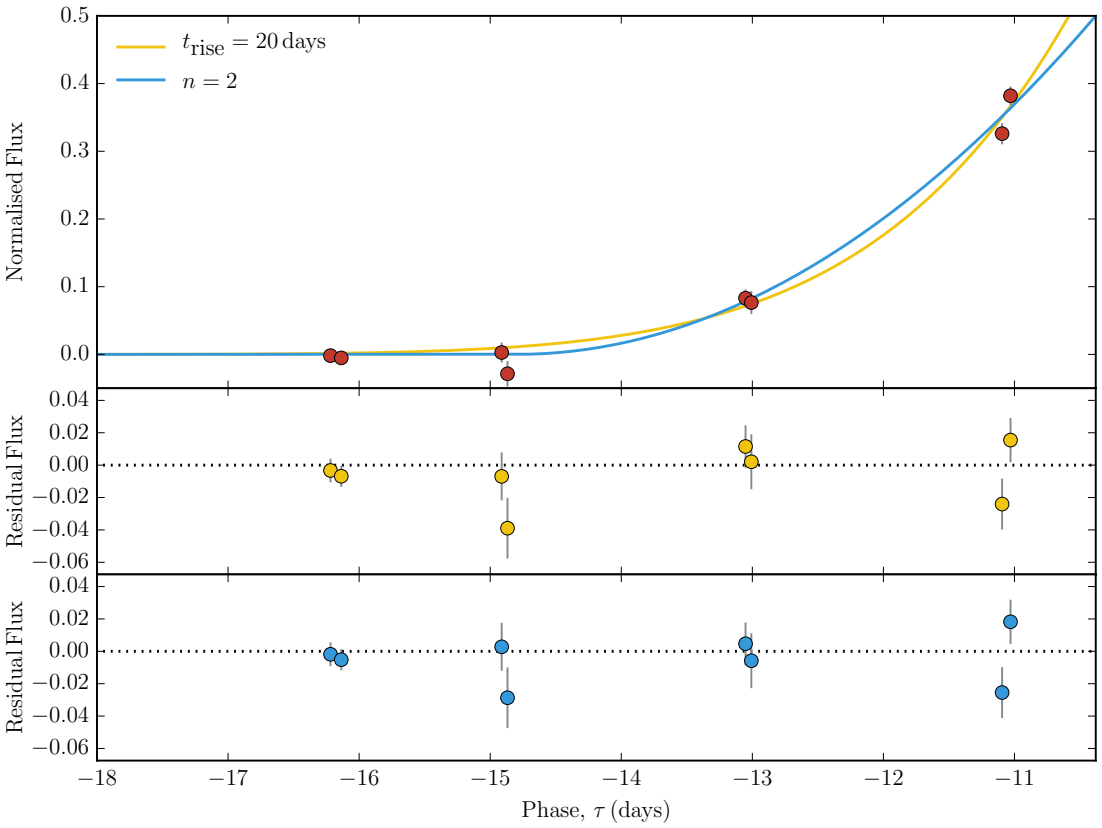

FIGURE 4.15: *Top Panel*: PTF11kx lightcurve and two fits to the data. A fit with a fixed rise of $t_{\rm rise} = 20.0$ days is shown in yellow, and a fit with fixed $n = 2$ is shown in blue. *Middle Panel*: Residual of the $t_{\rm rise} = 20$ fit to the data. *Bottom Panel*: Residual of the $n = 2$ fit to the data.

4.2 Discussion

In the following section, we discuss possible physical mechanisms for the diversity that we see in both $t_{\rm rise}$ and n. We condsider the effect of nickel distribution, rapid spectral evolution and the assumptions made in the derivation of a power-law rise.

4.2.1 Ejecta Mixing

In Piro (2012), the first four days of data from SN 2011fe were analysed and the implications of a power-law dependence explored, considering the dynamics and thermodynamics of the expanding ejecta bolometric luminosity goes as

$$L(t) \propto t^{2(1+1/\gamma+\chi)/(1+1/\gamma+\beta)} \tag{4.3}$$

for $t \lesssim t_{56}$, where t_{56} is the mean lifetime of ^{56}Ni ~ 8.8 days. The polytropic index, $\gamma = 3/2$ for non-relativistic electrons ($\gamma = 3$ for relativistic electrons Sakurai, 1960), and for a radiation pressure dominated shock, $\beta = 0.19$ which controls the rate of change of the shock velocity, while χ characterises the ^{56}Ni distribution in the ejecta shell. To change the n value, either χ or β must change. Simplifying the expression by setting $\chi = 0$ results in $n \simeq 1.8$. This value is consistent with Conley et al. (2006b), despite the fitting region being twice the size of the 4 days for SN 2011fe. If we treat the region from t_0 to $t_{0.5}$ as one shell, as in this parameterisation, increasing n is possible by increasing χ, and having deeper ^{56}Ni dominating the rise. However smaller n are more problematic to explain.

Note that, in Figure 4.13, the intercept of the best fit, at $n = 1.8$, is consistant with the above case from Piro (2012). This value is in tension with the findings of higher n values in SN 2013dy and SN 2014J and the justification that the value of n found was due to the unprecedented early discovery and followup. Clearly, data on further SNe collected very soon after first light are needed.

Only one of the SNe in our sample has $n < 1.8$: PTF10accd ($n = 1.48^{+0.19}_{-0.12}$). The small uncertainties make it inconsistent with both $n = 2$ and the lower limit of Piro (2012) ($n = 1.8$). It should be reiterated that the bolometric value is expected to be larger than the values in $R_{\rm P48}$ or $g_{\rm P48}$; however, from our tests in Section 3.6.3 this would not make PTF10accd consistent with $n = 1.8$.

This result has two possible implications depending on χ. If $\chi < 0$, either ^{56}Ni dominates the makeup of the outer ejecta, or the flux originates from elsewhere; potentially from some CSM interaction. Alternatively, the optical luminosity of the shock-heated cooling light curve may be dominant as this is expected to have $n = 1.5$. If $\chi \geq 0$, then the shock is not radiation pressure dominated and β may vary, or the delayed detonation transition (DDT) model, from which the velocity gradient is calculated (Piro et al., 2010) is an incomplete description of this process. Other models, such as He double-detonation (Fink et al., 2010) or the collision model (Kushnir et al., 2013; Dong et al., 2014) present different treatments of the velocity gradient.

More recent work (Piro & Nakar, 2013) investigates the contribution of ^{56}Ni heating, both directly and from the diffusive tail, throughout the ejecta. In the appendices of Piro & Nakar (2013), rather than treating shells of material individually, integrals are evaluated over the entire ejecta. This leads to a more complex picture of the energy generation, which depends on the relative fraction of ^{56}Ni throughout the ejecta, as given by

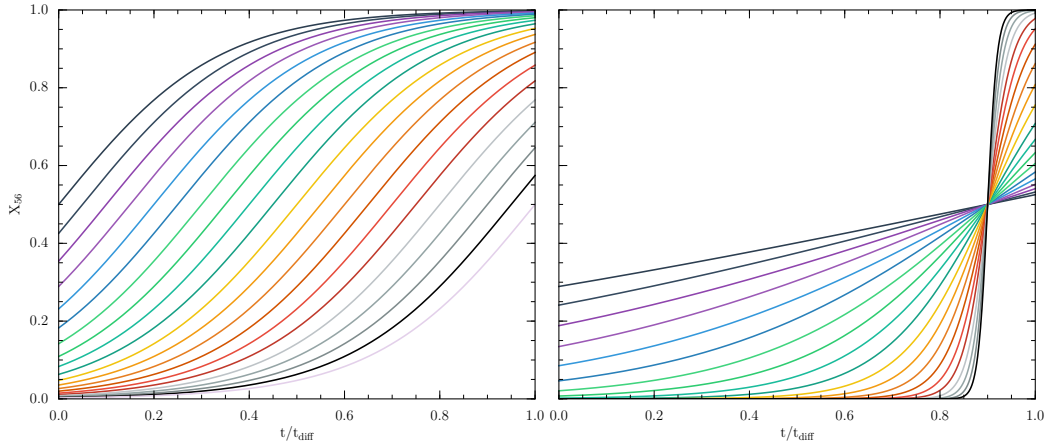

FIGURE 4.16: ^{56}Ni fraction X_{56} (Equation 4.4) as a function of diffusion time t/t_{diff} for varying values of $x_{1/2}$ and β. *Left panel*: Changes in X_{56} for $\beta = 6$ and varying $x_{1/2}$ from 0.0 to 1.0 in steps of 0.05. *Right panel*: Changes in X_{56} for $x_{1/2} = 0.9$ and varying $\beta = 6$ from 0.0 to 20.0 in steps of 2.0

$$X_{56}(x) = \frac{1}{1 + \exp[-\beta(x - x_{1/2})]}, \tag{4.4}$$

Figure 4.16 where x is a measure of normalised depth within the ejecta, $x_{1/2}$ is the point at which the ^{56}Ni fraction is half at that of its value at peak, and β is the steepness of the rise in the distribution. Generating a bolometric luminosity using this parameterisation, it is possible to attain a large range of n values, when fitting a power-law (Figure 4.18). The physical limits of this parameter space are uncertain, and fitting a number of SNe directly with this has yielded values in the ranges $6 \leq \beta \leq 8$ and $x_{1/2} \simeq 0.9$. The mean value of our study indicates that on average the envelope is less well mixed and there is an abrupt change within the ^{56}Ni distribution in most cases in the sample. This is the kind of ejecta stratification seen in the commonly used 'W7' (Nomoto et al., 1984), the sharp IPE drop off corresponding to a high value of β

However, at very early times, fitting with a simple power law, the fit is poor, as the light curve is better described as an exponential (Piro & Nakar, 2014). The timescales for this discrepancy are short, and beyond the scope of this work. However, this may be the apparent 'break' in the power law seen in 2013dy and 2014J (Zheng et al., 2013, 2014) – an exponential rise turning into a power law at later times. Our finding that $\dot{n}$ is, in general, positive, supports this.

In Figure 3.6 as the cutoff drops below ~ 3.5 days, n is consistent with 2, in agreement with Nugent et al. (2011). This value differs from our final result for SN 2011fe because the shorter time period used only probes a shallow region of the ejecta. At very early

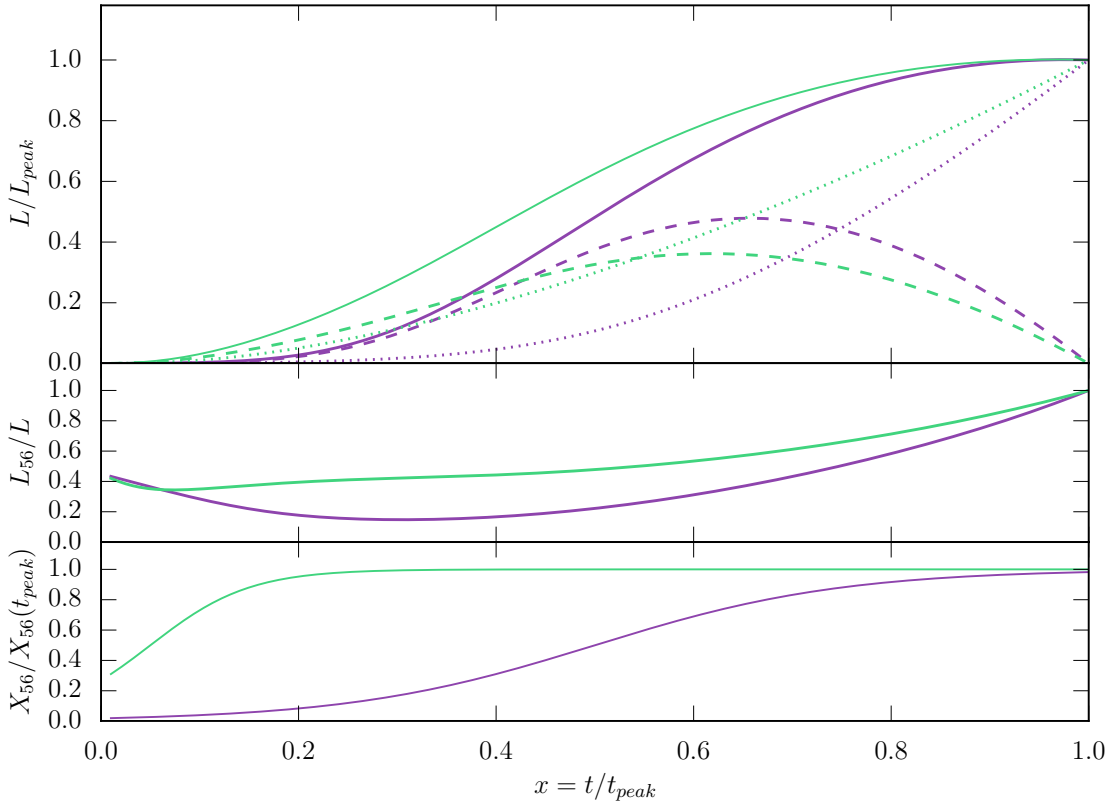

FIGURE 4.17: *Top panel*: Lightcurves Generated by Varying ^{56}Ni Fraction X_{56}, through Equation 4.4. The green lines show a model using $x_{1/2} = 0.05$ and $\beta = 20$. The purple lines show a model using $x_{1/2} = 0.5$ and $\beta = 8$. Dotted lines show the direct heating component from ^{56}Ni, while the dashed lines show the contribution from the diffusive tail of ^{56}Ni below the diffusion depth (Piro & Nakar, 2013). *Middle panel*: The ratio of luminosity from local ^{56}Ni heating to total luminosity. *Bottom panel*: The ^{56}Ni abundance fraction compared throughout the ejecta.

times, the rise index jumps to higher values. This difference could be hinting towards a broken power-law as outlined in Section 3.2.5, Equation 3.14, or something that resembles one (Piro & Nakar, 2014); however, attempting to fit this model to SN 2011fe is unsuccessful; as there is not enough data at very early times to constrain the 7 free parameters.

At present, none of these various models make any predictions that would explain the decoupling of the early and late part of the rise seen in our data. However, a scatter in the measured photometric rise time can be explained by invoking a 'dark phase', between explosion and first light (Figure 3.1), due to deep ^{56}Ni deposits. More work is needed to further understand this phenomena, using the methods previously applied to SN 2011fe and SN 2010jn (Mazzali et al., 2014; Hachinger et al., 2013), on future samples of well observed SNe. The dark time for SN 2010jn was estimated to be 1.4 days, and that of SN 2011fe to be 1 day. As we expect that, for a given value of $x_{1/2}$, higher n values are consistent with a steeper gradient, β, higher n values should be consistent with a longer

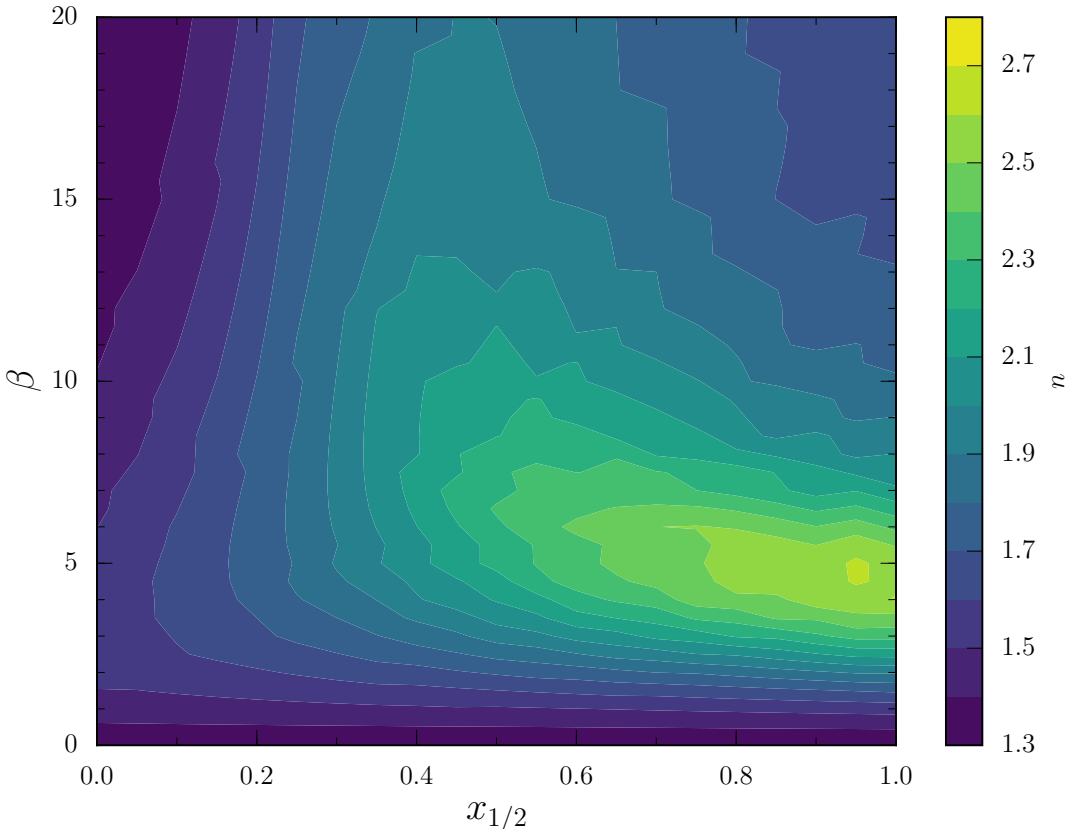

FIGURE 4.18: Contours showing the fitted n parameter of a bolometric light curve generated by using different values of β and $x_{1/2}$ in Equation 4.4. A large range of n values are recovered, but extreme values of β and $x_{1/2}$ may not be physical.

dark time. This effect is seen in these two SNe; SN 2011fe has an $n = 2.15 \pm 0.02$ (our value is used over that of Nugent et al. (2011) as the fitted regions are more comparable) and SN 2010jn $n = 2.3 \pm 0.6$.

As the available light curves can be well fit by using a simple power law, more high quality photometric and spectroscopic data is needed to distinguish between the models, and to see expected deviations from power laws (Zheng et al., 2013; Goobar et al., 2014). Ideally, future work would be able to concentrate on bolometric data, which is now becoming possible (Scalzo et al., 2014).

Tanaka et al. (2008b) find a significant range of ^{56}Ni abundances in the outer ejecta of a sample of SNe Ia, which is taken as one of the causes of early time spectral variation in SNe Ia; they also suggest this could have photometric consequences. Our work clearly demonstrates that there is indeed a photometric shape variation, and that a cause of this is in ^{56}Ni deposition between SNe Ia, as suspected.

4.2.2 Rapid Spectral Evolution

At early times, SNe Ia spectra are dominated by intermediate mass elements and remnant unburned material from the progenitor. Depending on the level of mixing, iron-peak elements can also present early. As the photosphere recedes into the ejecta, the spectral absorption features change, as the material above the photosphere changes in overall makeup.

The speed of recession of the photosphere is linked, through temperature evolution, to the ^{56}Ni distribution. However, the presence of high-velocity features (HVFs) and the velocity gradient is not so obviously physically linked. If the strength and velocity changes over time are significant enough to strongly affect the colour of the SN, then departures from expected rise behaviour would occur. This has been seen in the rapid evolution of HVFs in the unusual SN Ia SN 2000cx, where changes in the velocity contribute to the asymmetric light curve peak Branch et al. (2004).

Benetti et al. (2005) used the velocity evoution of SNe to define high-velocity gradient (HVG) and low-velocity gradient (LVG) SNe using the rate of change of the Si II 6355 Å feature, $\dot{v} = \Delta v/\Delta t$, from maximum light until the feature disappears. In the definition HVG have $\dot{v} > 70$ km s^{-1}day^{-1} and LVG $\dot{v} > 60 - 70$ km s^{-1}day^{-1}. While this definition does not link to the early time behaviour, and uses the post maximum behaviour (which, as we have shown in earlier sections does not neccessarily correlate) Pignata et al. (2008) suggest that HVG SNe should have shorter rise times, slower fall and higher maximum brightnedd brightness. Cartier et al. (2016) conclude that SN 2015F is a LVG SNe, and while the measured rise times (Table 3.5) are shorter than the mean value in our sample in all bands, they are greater than would be expected by stretch correcting our mean value by the $s = 0.9$ measurement of the SN.

HVFs are present in the early spectra of SN 2015F (Cartier et al., 2016). The early evolution of a number of lines can be seen in Figure 4.19. Unlike the gradient defined by Benetti et al. (2005), this method of fitting uses the time of explosion, t_{ex}, as it's zeropoint. This means that any length of time between explosion and t_0 will change the fits. The fits are described by

$$v(t) = t^{\epsilon} + v_i. \tag{4.5}$$

Where t is the time since explosion, and v_i is the initial velocity. However, to get the evolution to match the $t^{-0.22}$ predicted by Piro & Nakar (2014) (see Section 3.2.6), for SN 2015F the dark phase must be long (Table 4.3).

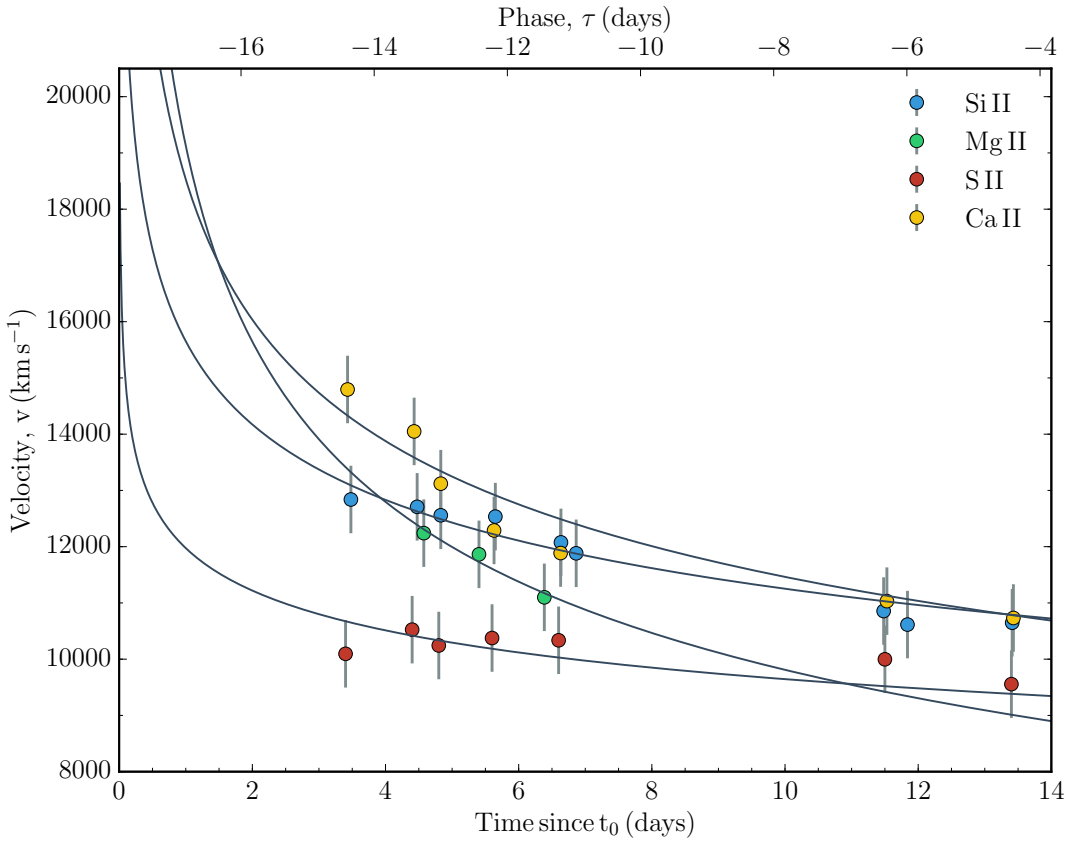

FIGURE 4.19: Spectral velocity evolution of SN 2015F, showing four lines Si II, Mg II, S II and Ca II. The parameters for the fits shown can be seen in Table 4.3

TABLE 4.3: Spectral velocity evolution of SN 2015F (see Equation 4.5)

Line	ϵ	$log_{10}(v_i)$	Line ID
Si II	−0.14	4.19	λ6150
Mg II	−0.29	4.28	λ4481
S II	−0.09	4.08	λ5958, 5978; λ5640, 5647
Ca II	−0.21	4.26	IR Triplet

As such, the very early spectroscopic evolution of SN 2015F does not seem to be as 'normal' as that of SN 2011fe, and it is difficult to accurately quantify a dark–phase using this method.

4.2.3 Weak Assumptions - Coasting

One of the main assumptions in the derivation of the 'fireball' t^2 model (see Section 3.2), is that of homologous expansion. This approximation that the ejecta is coasting, and the radius expands as t^2, is, as mentioned in previous sections, not reliable. However, Arnett et al. (2016) suggests that relaxing this assumption naturally increases the rise index, to

a value between 2 and 4. By assuming constant initial flux, radiative acceleration gives $L \propto t^4$, and relaxing this the luminosity evolution asymptotically approaches $L \propto t^2$, explaining the range of n observed.

However, in this scheme, values of $n < 2$ cannot be explained by ejecta dynamics alone. Additionally, Arnett et al. (2016) note that this dynamical argument predicts $dn/dt < 0$ ($\dot{n} < 0$). However, as can be seen in Figure 4.13, we find clear evidence for higher n at later times. When fitting for a time dependence i.e. $t^{2+\dot{n}}$ (see Section 4.1.2.2), we find for the sample $\dot{n} = 0.011 \pm 0.004\,\mathrm{d}^{-1}$. Even when relaxing the condition that $n_0 = 2$, in the case of SN 2011fe, we find a positive $\dot{n}$; $\dot{n} = 0.011 \pm 0.001\,\mathrm{d}^{-1}$ and $n_0 = 2.02 \pm 0.02$. As such, this dynamical assumption is clearly not the dominant driver for the behaviour we observe.

4.3 Summary

In this Chapter we have used 18 type Ia supernovae (SNe Ia) from the Palomar Transient Factory (PTF) and the La Silla-QUEST variability survey (LSQ) to measure the rise time (t_{rise}) (the time between first light t_0, and maximum light t_{max}) and rise index (n), where $f = (t - t_0)^n$. Our main conclusions are:

1. The rise index, n, of our sample shows significant variation ($1.48 \leq n \leq 3.70$), with the mean of the distribution $n = 2.44 \pm 0.13$, and $n = 2.5 \pm 0.13$ when correcting to a pseudo-bolometric value (Section 3.6.3.1), both inconsistent with a simple fireball model ($n = 2$) at a 3σ level. This implies that current understanding of the ^{56}Ni distribution or shock velocity through the ejecta is incomplete, and that more complex physically motivated parameterisations may be needed in future.

2. We find that when the rise index is allowed to vary with time from $n = 2$, $\dot{n}$ is in general positive, with an average value of $\dot{n} = 0.011 \pm 0.004$ day^{-1}. Supporting a time dependant n, is the finding that SN discovered later after first light have, in general a larger value of n, whereas those discovered soonest after t_0 have lower values.

3. The average t_{rise} of our sample is $t_{\mathrm{rise}} = 18.98 \pm 0.54$ days, and $t_{\mathrm{rise}} = 18.97 \pm 0.43$ days, when correcting for light curve width. We find no evidence for two rise time modes in our sample. These are longer than would ordinarily be found by enforcing $n = 2$.

4. The broadest light curves have a $t_{\rm rise}$ that is faster than that of our stretch-corrected light curve template, which enforces $n = 2$ in its construction. In agreement with previous studies, we find that a 'two stretch' model fits the data better. In contrast to current two-stretch fitting methods, which separate the light curve into the pre- and post-maximum sections ($t < t_{max}$ and $t > t_{max}$ respectively), the most significant variation occurs at the very earliest epochs ($t < t_{0.5}$, where $t_{0.5}$ is the time at which the SNe reaches half of its maximum, or phases $\tau < -10$ days).

5. We therefore decouple the rise time into two components: t_1 (where $t_1 = t_{0.5} - t_0$) and t_2 (where $t_2 = t_{max} - t_{0.5}$). These time-scales are not correlated with each other (Figure 4.6); furthermore t_2 is strongly correlated with stretch, whereas t_1 is not. As a result, stretch correcting using a single stretch is ineffective in reducing the dispersion in the earliest portion of the light curve (Figure 4.1).

6. These two regions are separated by the approximate location of the point at which energy deposition and radiation are equal, meaning that the physical conditions are distinct.

7. Using models from Piro & Nakar (2013), we show that potential variation in the shape of the ^{56}Ni distribution within the SN ejecta can explain the measured range of n and $t_{\rm rise}$.

8. Considering the prediction of Arnett et al. (2016) that $\dot{n}$ should be negative for early time variation as a result of non-homologous expansion, we conclude that this is not the main source of diversity in our observations, as we find $\dot{n}$ is positive.

9. SNe Ia showing evidence of strong interaction with circumstellar material (CSM) have long rise times. However a notable member of this subclass, PTF11kx, has an extremely short rise, $t_{\rm rise} = 14.5 \pm 0.5$ days, when fitted with a fireball model ($n = 2$).

Further work should concentrate on further understanding the variation, and on which other observable quantities it depends. For this, a large sample of SNe Ia with high quality photometric and spectroscopic data must be assembled. The presence of high velocity features, Si II velocities and colour evolution may hold valuable information, particularly if the variation at very early times is misunderstood when used for cosmology.

Chapter 5

The Post-Maximum Light Curve Diversity in SNe Ia from PTF

"I'm sciencing as fast as I can!"

- Prof. Hubert J. Farnsworth, *Futurama: Bender's Big Score*

In this chapter, we move from the early time emission of SNe Ia, to consider the diversity that may be found after maximum light, and the implications for our understanding of the physical processes that underpin their time evolution. As has been well established, the light curves of SNe Ia are remarkably uniform near maximum, in particular in the blue and visual optical bands. In redder observations, the transition onto the radioactive decay tail is delayed by a rebrightening, appearing as a shoulder or short plateau in R and i, and a second peak comparable in brightness to the first in the near-IR. The mechanism for this rebrightening was poorly understood until relatively recently, and the advent of more sophisticated treatment of emissivities and opacity within radiative transfer simulations. As well as following the method outlined in this Chapter, the photometric data reductions and light curve fits were performed by the author using the pipeline and fitting package described in Chapter 2. The fits to CSP objects are also the work of the author, but no re-reduction of raw data was performed.

5.1 Secondary Maximum

The secondary maximum in SNe Ia in the near-IR (J, H, K, L) was first highlighted by Elias et al. (1981, 1985), while its appearance in the i-band was first discussed by Ford et al. (1993). The typical optical behaviour of SNe Ia is a monotonic decline from peak,

onto a linear radioactive decay slope. In contrast, the NIR rebrightens, in some bands to a peak comparably bright to the first. Despite repeated observations after the advent of CCD photometry (cf. Suntzeff, 1996; Riess et al., 1996; Lira et al., 1998; Milne et al., 2001) and analysis of larger samples of archival data (Meikle, 2000) the interpretation of the feature was still unsettled, and coverage too sparse to make strong conclusions. Interest in such observations has renewed, as the apparent uncorrected uniformity of the peak brightnesses, which has a scatter of ~ 0.2 mag (Elias et al., 1981; Meikle, 2000; Krisciunas et al., 2004a; Barone-Nugent et al., 2012; Dhawan et al., 2015), make the near-IR an attractive standardisable candle. Furthermore, the reduced sensitivity of the NIR to dust extinction (Section 2.4.2; Cardelli et al., 1989; Fitzpatrick & Massa, 2007) have enabled not only accurate measurements of H_0 (Cartier et al., 2014) but have also lead to the construction of rest-frame NIR Hubble Diagrams (Krisciunas et al., 2004b; Freedman et al., 2009; Barone-Nugent et al., 2012).

In the both the bolometric light curve and R_{P48}, rather than a pronounced peak, the NIR secondary maximum appears as a shoulder on the lightcurve (Contardo et al., 2000), a schematic template of which can be seen in Figure 5.1. The decline is still monatonic, but slows significantly. It has been assumed that the behaviour of this feature is closely linked to the NIR secondary maximum, but the SED that falls into the r and i bands is complex, with the Si II and Ca II features dominant respectively, and the evolution equally complicated. In this chapter, we aim to observationally test this behaviour.

5.1.1 Post-maximum Diversity

Not all SNe Ia exhibit a secondary maximum, Riess et al. (1996) showed, but did not quantify, that in their sample, broader, brighter SNe Ia have a stronger secondary in i-band, and a more prominent shoulder in r (see also: Hamuy et al., 1996b; Nobili et al., 2005). This effect can be seen throughout the NIR, for example in YJH in Figure 5.2. In this era of large, systematic surveys, proper characterisation of statisistically meaningful NIR samples has been made possible (Folatelli et al., 2010; Stritzinger et al., 2011; Dhawan et al., 2015) and reinforce these earlier results.

As can be seen in the left hand panel of Figure 5.3 from Dhawan et al. (2015), the timing of the secondary maximum is strongly correlated with decline rate (and therefore light curve width). The relationship between decline rate and the brightness of the secondary is not as strong, but a correlation is found in all three bands. An earlier analysis by Biscardi et al. (2012) found that while the strength of the secondary maximum is related to decline rate only when the strength is measured relative to the local minimum beforehand (following the nomenclature of Kasen (2006)), no clear relationship is seen

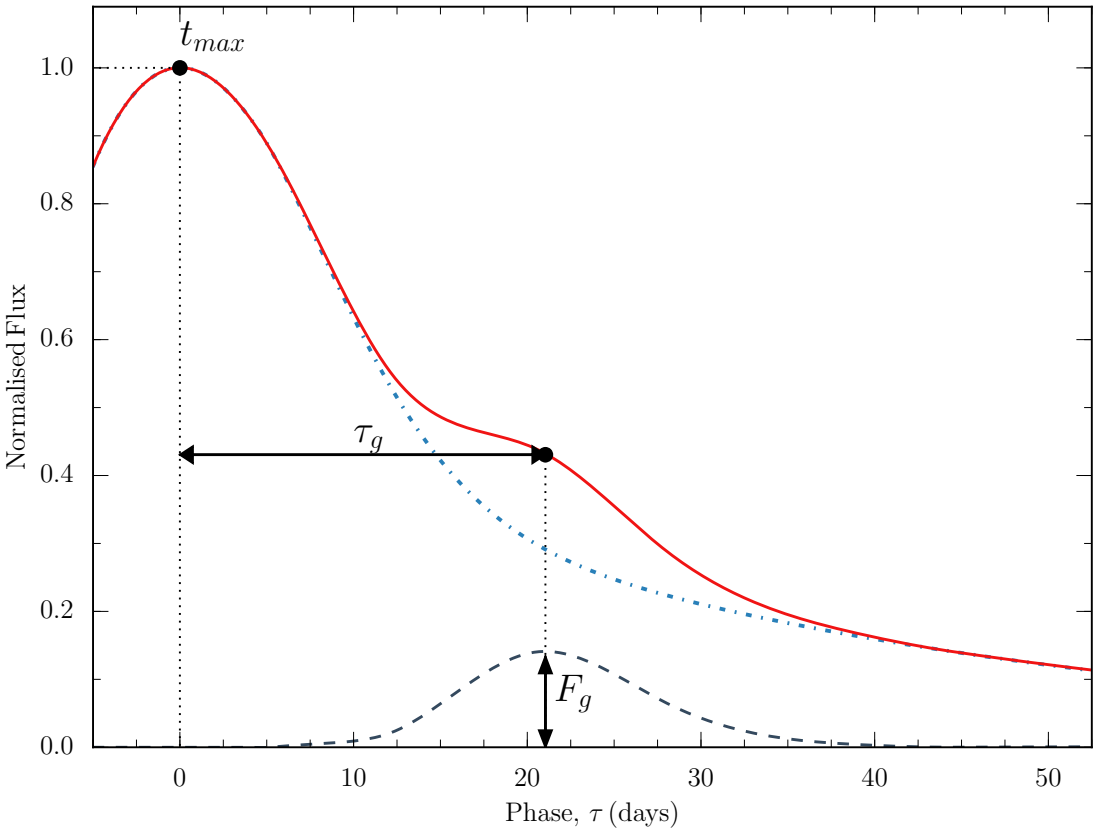

FIGURE 5.1: Schematic Post-Maximum $R_{\rm P48}$ SNe Ia Light Curve. Shown are a light curve exhibiting a secondary 'shoulder' (red), and one with the shoulder subtracted off in dot–dashed blue. The residual between the two is the gaussian shown as a dashed line, centered at time τ_g, with a peak normalised flux of F_g.

when measured relative to the magnitude of the main peak. Understanding the diversity within this feature can have far reaching implications; recent suggestions that the time when the feature is most prominent τ_g (see Figure 5.1), can be used to standardise SNe Ia for cosmological use (Dhawan et al., 2015, 2016; Shariff et al., 2016).

What is less clear is how this precisely relates to the shoulder seen in the r-band, as little has been done since the assertion of Riess et al. (1996) that a broader light curve corresponds to a more prominent feature. Helpfully for this work, the $R_{\rm P48}$ being a larger, redder band than standard means the feature should be stronger in our sample than for a normal r. However, the width of the filter means that it includes strong spectral features, (e.g. Si II 6150), and as such any commonality with the NIR, where the SED is more uniform, should not necessarily be expected.

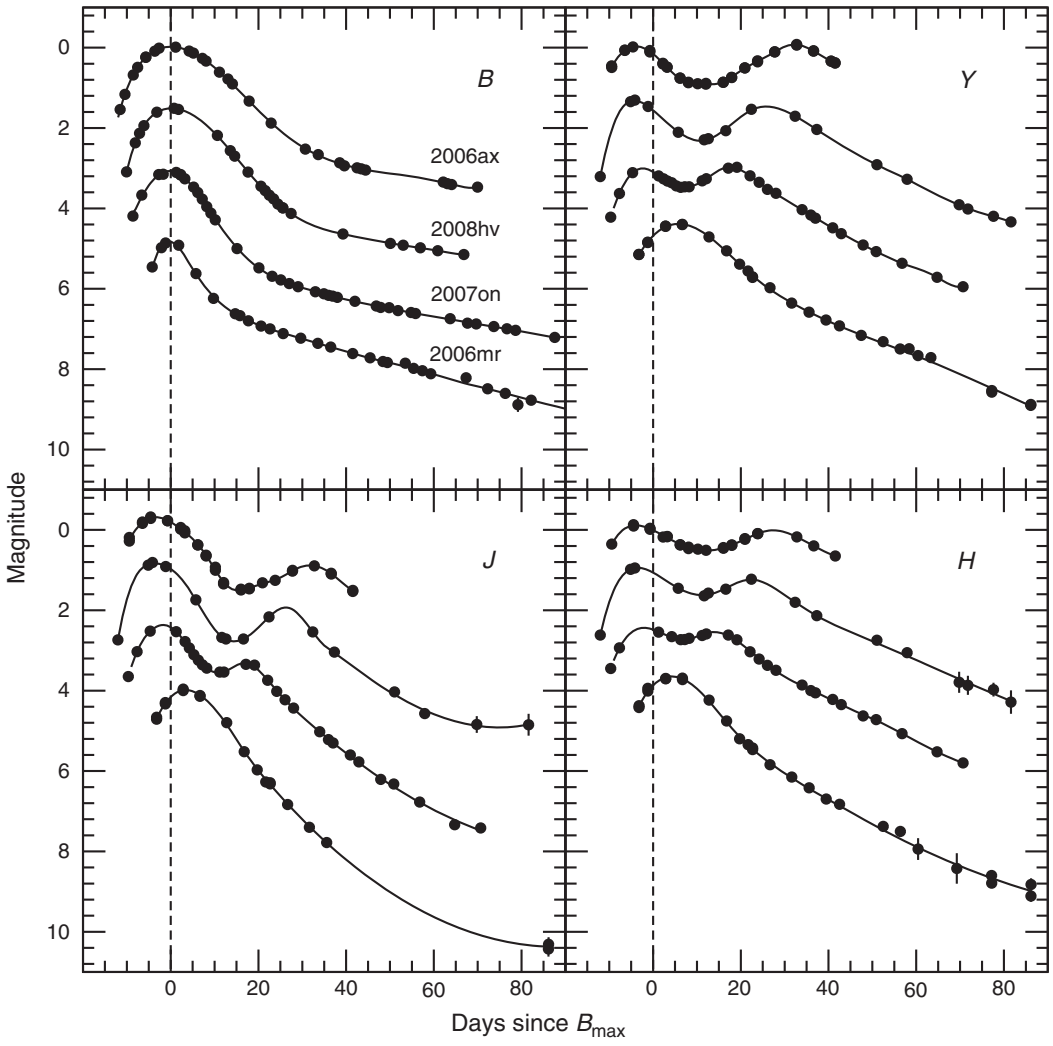

FIGURE 5.2: CSP light curves in B, Y, J and H, of four SNe Ia covering a wide range of decline rates: SN 2006ax ($\Delta m_{15} = 0.97$), SN 2008hv ($\Delta m_{15} = 1.25$), SN 2007on ($\Delta m_{15} = 1.62$), and SN 2006mr ($\Delta m_{15} = 1.71$). Arbitrary offsets in magnitude have been subtracted from the data to facilitate comparison. Broader light curves show a later and more prominent secondary. Figure from review of Phillips (2012).

5.2 Physics of the Secondary Maximum

In order to interpret any analysis of the post-maximum morphology of SNe Ia, we must first consider the physical processes thought to drive them where they are better understood. A number of explanations have been suggested, with all implicitly assuming that the shoulder in r is driven by the same mechanism. Hoeflich et al. (1995) generated optical and NIR light curves, and were able to produce a secondary maximum for a range of delayed detonation models. The interpretation of the secondary in these models is that it is a result of the photosphere continuing to expand after maximum light. This overcomes the cooling of the ejecta and causes the rebrightening. Hoeflich et al. (1995)

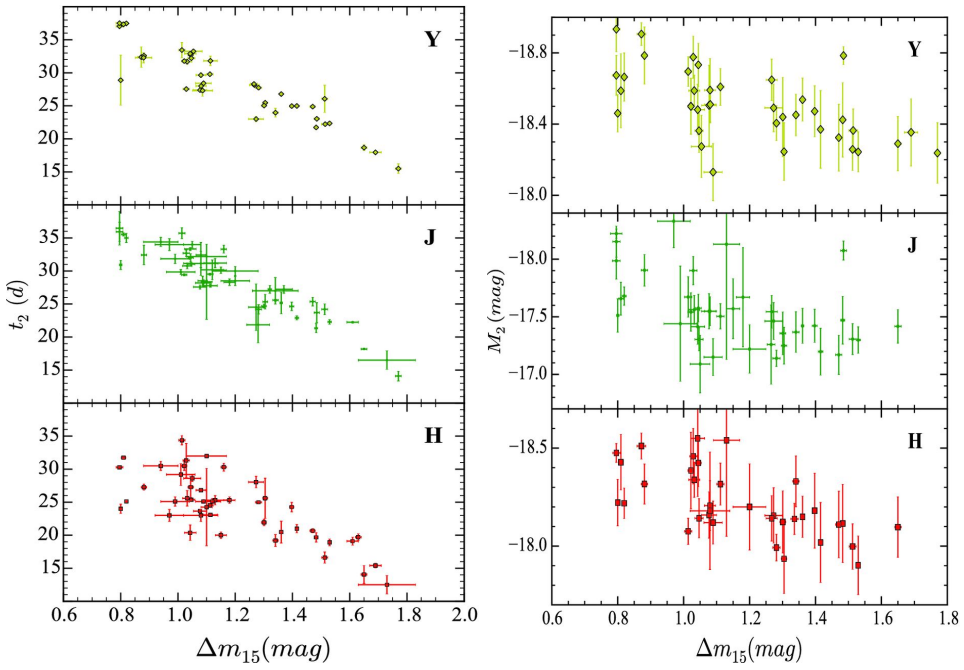

FIGURE 5.3: *Left Panel:* Comparison of the timing of the secondary maximum (here denoted t_2) in the NIR Y, J and K bands, with light curve width $\Delta m_{15}(B)$. *Right Panel:* Comparison of the absolute magnitude of the secondary maximum (M_2) in the NIR Y, J and K bands, with light curve width $\Delta m_{15}(B)$ Figures taken from Dhawan et al. (2015).

also draw the conclusion that the secondaries appear later for models with moderate expansion velocities and radioactive Iron Peak Elements (IPEs) close to the surface.

Alternatively, Pinto & Eastman (2000b) suggested that the emission was due to a sudden drop in the flux mean opacity, and that driving this was an ionisation change in the IPEs buried within the ejecta. If significant heating from these elements occurs, the recession of the photosphere will stall, causing the plateau in r, and secondary in NIR. IPEs are highlighted as the driver behind this process, being the domininant mass component, but also because the emissivity of singly ionised rather than doubly ionisied iron group elements is greatly increased.

The current consensus favours the latter theory, with a number of sophiticated radiative transfer simulations and subsequent analysis by Kasen (2006) using the multidimensional time-dependent Monte Carlo code, SEDONA (Kasen et al., 2006). Tracing the ionisation evolution of a Fe/Co gas, when the temperature falls to $T_{21} \simeq 7000$K, the transition temperature between singly and doubly ionised states, the emissivity sharply rises. The outer ejecta, being optically thin at longer wavelengths, does not trap the NIR emission, but as the ejecta remain optically thick at bluer wavelengths, most emission is reprocessed and re-emitted via NIR flourescence lines. Jack et al. (2015) claim to have identified Fe II as the driving spectral feature behind the I band secondary. The recombination of IPEs also serves to increase the opacity as a result of broad blended

Fe II and Co II features developing between $4500 - 5000$Å, further line-blanketing the spectrum. As a result, this process efficiently transports radiation from blue-optical to NIR.

This interpretation means the behaviour of the light curve post maximum is dependent on a number of physical parameters: the ^{56}Ni mass and its destribution through the ejecta, the mass of electron capture elements (such as stable ^{54}Fe and ^{58}Ni), the total IME mass, and the progenitor mass were all highlighted by Kasen (2006). As the jump in emissivity follows the diffusion of the $\simeq$ 7000K temperature front as it recedes into the ejecta, in SNe with ^{56}Ni located further out in the ejecta (in mass coordinates), this will be reached sooner. This triggers the ionisation change that goes on to cause a secondary; however, for sufficiently mixed ejecta, the secondary may be indistinguishable from the main peak as the emission will be spread out, as in the case of the perculiar low-luminosity, low-spectral-velocity SNe Ia SN 2002cx (Li et al., 2003). If the IPEs are centrally located, with a low degree of ejecta mixing, the diffusion wave will take a longer time to reach them, causing a later peak. Aside from the ^{56}Ni mass, the total ejecta mass also has an impact: a larger mass means a bigger ejecta, and a larger ejecta takes longer for the ionisation front to traverse it. The hotter the ejecta, the longer it will take to cool, delaying the secondary.

Additionally, Kasen (2006) finds that increasing the amount of stable IPEs, such as ^{54}Fe and ^{58}Ni, can shift the timing of the secondary, moving it up to 10 days earlier, and significantly narrower. Late time [Fe II] line profiles suggest a stable Fe core (Höflich et al., 2004) does exist in at least some SNe Ia. A similar effect can be seen in the model lightcurves when changing the progenitor metallicity from 1-3 times that of solar.

Kasen (2006) acknowledges that uncertainty around the Ca II IR triplet makes the i band evolution more complex than the other NIR bands. The Si 6150 feature is similarly dominant in r-band, and the proximity of the effective wavelength to the division between optically thin and optically thick regimes combine to make it uniquely difficult to model.

5.2.1 Links to Rise Time

As discussed in Chapter 4, the degree of mixing in the ejecta can profoundly effect not only the delay between the time of explosion, t_{ex} and the time of first light, t_0, but also the shape and speed of the rise to maximum light, t_{max}. More importantly, we have seen that early time behaviour does not correlate well with the light curve width, as previously expected. As the characteristics of the secondary are underpinned by many of the same physical parameters, similar departures from expected behaviour may be expected, and indeed correlated.

5.3 Fitting

A number of methods have been used to parameterise the secondary maximum, both for bolometric lightcurves and NIR. They range from the simple mean i-band flux over the phases 20 to 40, $\langle i \rangle_{20-40}$ (Krisciunas et al., 2001), to multi-parameter fits of the whole lightcurve (e.g. Vacca & Leibundgut, 1996; Contardo et al., 2000). In this section, we detail these models, and introduce our own hybrid fitting method.

5.3.1 Vacca and Leibundgut Model

An early attempt to parameterise the full light curve of SNe Ia was made by Vacca & Leibundgut (1996) (applied to a much larger sample of data by Contardo et al., 2000). This model described the evolution of the SN apparent magnitude over time as two gaussians, superimposed on a linear tail, supressed by an exponential at very early times. Mathematically, this model is expressed as

$$m(t) = \frac{f_0 + \gamma(t - t_0) + g_0 e^{\frac{-(t-t_0)^2}{2{\sigma_0}^2}} + g_1 e^{\frac{-(t-\tau_g)^2}{2{\sigma_1}^2}}}{1 - e^{\frac{\tau_r - t}{\theta}}} \tag{5.1}$$

where t_0 is the time the first gaussian peaks, τ_g the second, γ is the slope of the underlying linear decay, g_0 and g_1 are the strength of the first and second gaussians respectively, and σ_0 and σ_1 their widths. The denominator, which is responsible for the rising portion of the light curve, is governed by the characteristic rise time τ_r, and its phase, θ.

As shown in Figure 5.4, for uniformly sampled, high signal-to-noise data, this model provides outstanding fits to the data. However, the large numbers of free parameters means that it is difficult to constrain all of them. In order to stablise the fits, we considered all of the objects in the CSP DR1 and DR2 with $N_{obs} > 5$ at phases later than $\tau > 40$. By fitting just the linear component of the fit, $m(t) = f_0 + \gamma(t - t_0)$, we can test the variation in the late light curve, and its impact at earlier times. The resulting fits are shown in Figure 5.5 and the distribution of the slope of the fits can be seen in Figure 5.6. Considering the assumed uniformity at these phases, the distribution shows a remarkable degree of diversity. All bar one of the slopes are steeper than that predicted for ^{56}Co decay (~ 0.022 mag day^{-1}, Appendix A). This is expected as while the bolometric behaviour should follow this rate, after $\tau \sim 10$, flux is increasingly transported out of the UV-optical, and into the IR (Pereira et al., 2013). Some variation in the tail is expected due to different isotope ratios (Dimitriadis & Sullivan, 2016), but the driving force for this effect at these phases is likely opacity and ^{56}Co distribution.

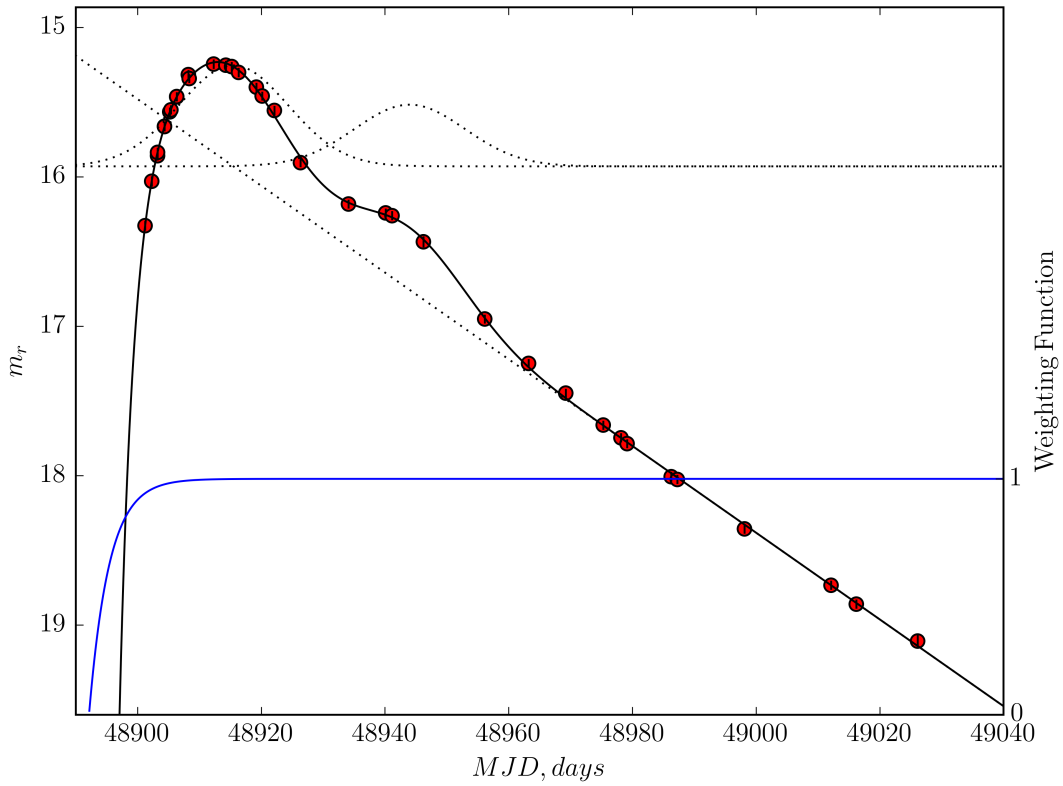

FIGURE 5.4: Light curve of SN 1992bc in r, showing the fit to the data using Equation 5.1. Photometry is from the Calán-Tololo sample presented in Hamuy et al. (1996a). The components of the fit are plotted individually, with the linear decline and both gaussians appearing as dotted lines, and the exponential in the denominator plotted as a weighting function in blue.

5.3.2 Template Fitting

An alternative approach from a purely parametric model is to utilise the homogeneity of SNe Ia and apply a template fitting package. To this end, we will use the light curve fitter SiFTO (Conley et al., 2008b, see Section 2.3).

The fitting algorithm used by SiFTO does not allow for the properties of the secondary maximum to change as a function of stretch, as is the case in other fitters, such as SNooPy (Burns et al., 2015). As such, the presence of a mean template value of the secondary is built into the templates, and in order to test the variation of the feature, we must remove it, and add it on after the template fitting. As the secondary maximum does not occur in all filters (Figure 5.7; lower panel), it does not appear in all of the templates – only the three reddest, 'LOG-7', 'LOG-8' and 'I-shift', the transmission functions of which can be seen in the top panel of Figure **??**.

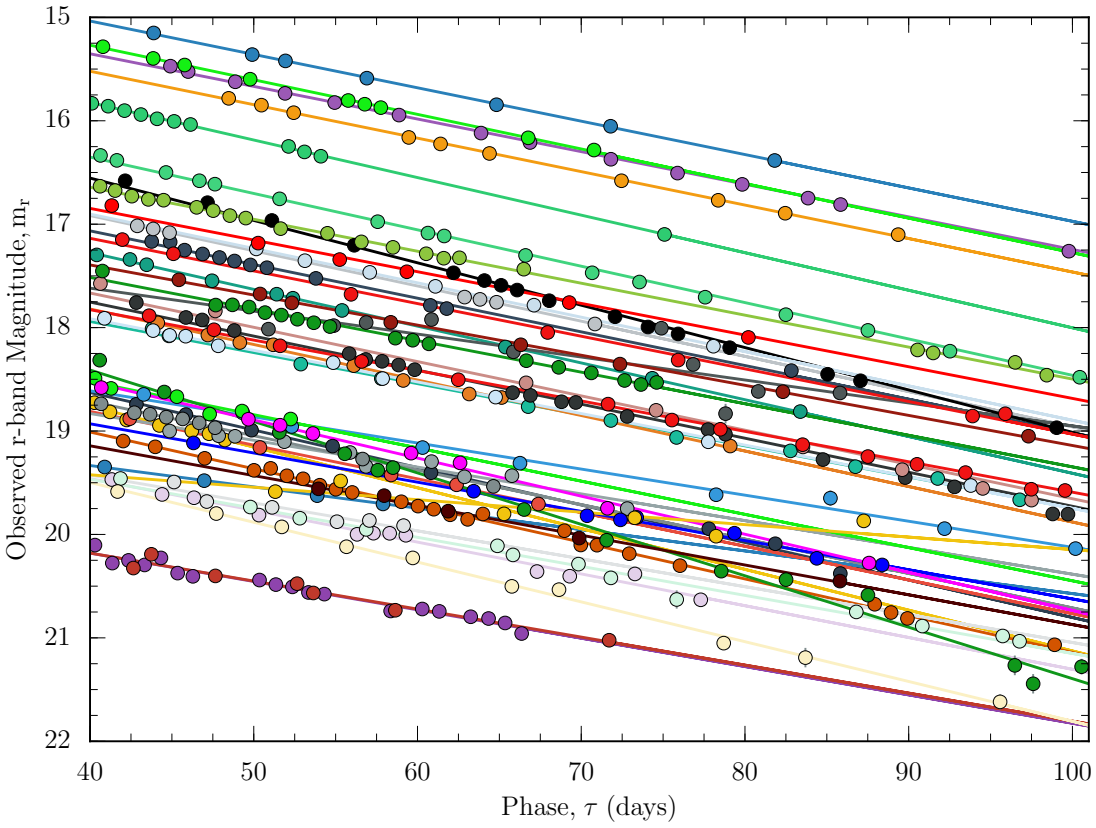

FIGURE 5.5: Linear fits to the apparent r band magnitude of CSP DR1 and DR2 SNe Ia at phases of $\tau > 40$ days. A histogram of the gradients of these lines is shown in Figure 5.6

5.3.2.1 Constructing a New Template

To construct a set of new 'bumpless' templates, to which we can control the size of the secondary, we fit each of the three templates with the model given by Equation 5.1. Such is the flexibility of the model, it fits the templates well, for example Figure 5.8. Simply subtracting the second gaussian from the template resulted in some residual variation, due to the construction of the initial templates using splines (Conley et al., 2008a). Instead, for the entire post-maximum light curve, the other components of the model were used, with the transition smoothed over.

5.3.2.2 Final Fitting Method

The final fitting method we will use consists of two steps: firstly a SiFTO template fit using the 'bumpless' templates as described in Section 5.3.2.1, secondly, a χ^2 minimisation will then be performed to find the best fitting gaussian to the residual of the

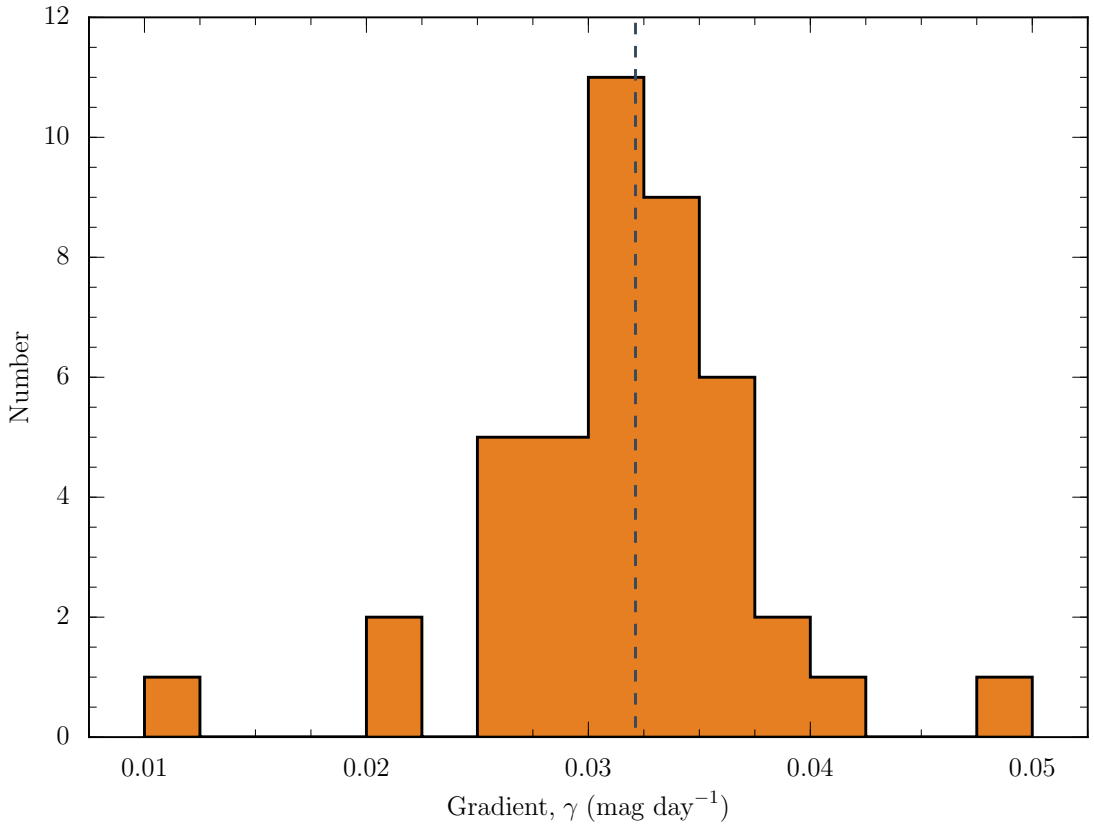

FIGURE 5.6: Distribution of linear decay slopes from CSP, as described in Section 5.3.1. The median of the distribution, $\hat{\gamma} = 0.032$ is shown as a dashed line.

template fit. The flux contributed by the gaussian as a function of time follows:

$$f(t) = F_g e^{-\frac{(\tau-\tau_g)^2}{\sigma_g^2}} \tag{5.2}$$

where the F_g is the prominence or strength of the gaussian, σ_g parameterises its width, and τ_g the phase of maximum. The area under the gaussian A_g can be computed using $A_g = F_g\sigma_g\sqrt{\pi}$ to measure the overall contribution of the shoulder. The initial SiFTO fit will only include data up to $\tau > 10$ days in order not to fit parts of the lightcurve where a secondary is present before fitting the additional component. The subsequent gaussian fitting only has two conditions; that the peak is after the time of maximum light in the B–band, t_{max}, and that $F_g > 0$ (see Figure 5.1).

5.3.3 Alternative Measurements of Secondary Strength

To measure the strength of the secondary in i-band, Krisciunas et al. (2001) (and later Folatelli et al., 2010) used the mean integrated flux, normalised to maximum light, for phases $20 \leq \tau \leq 40$, '$\langle i \rangle_{20-40}$' after fitting the data with a high-order polynomial (or with templates for a small subsample in the case of (Folatelli et al., 2010)). Both works

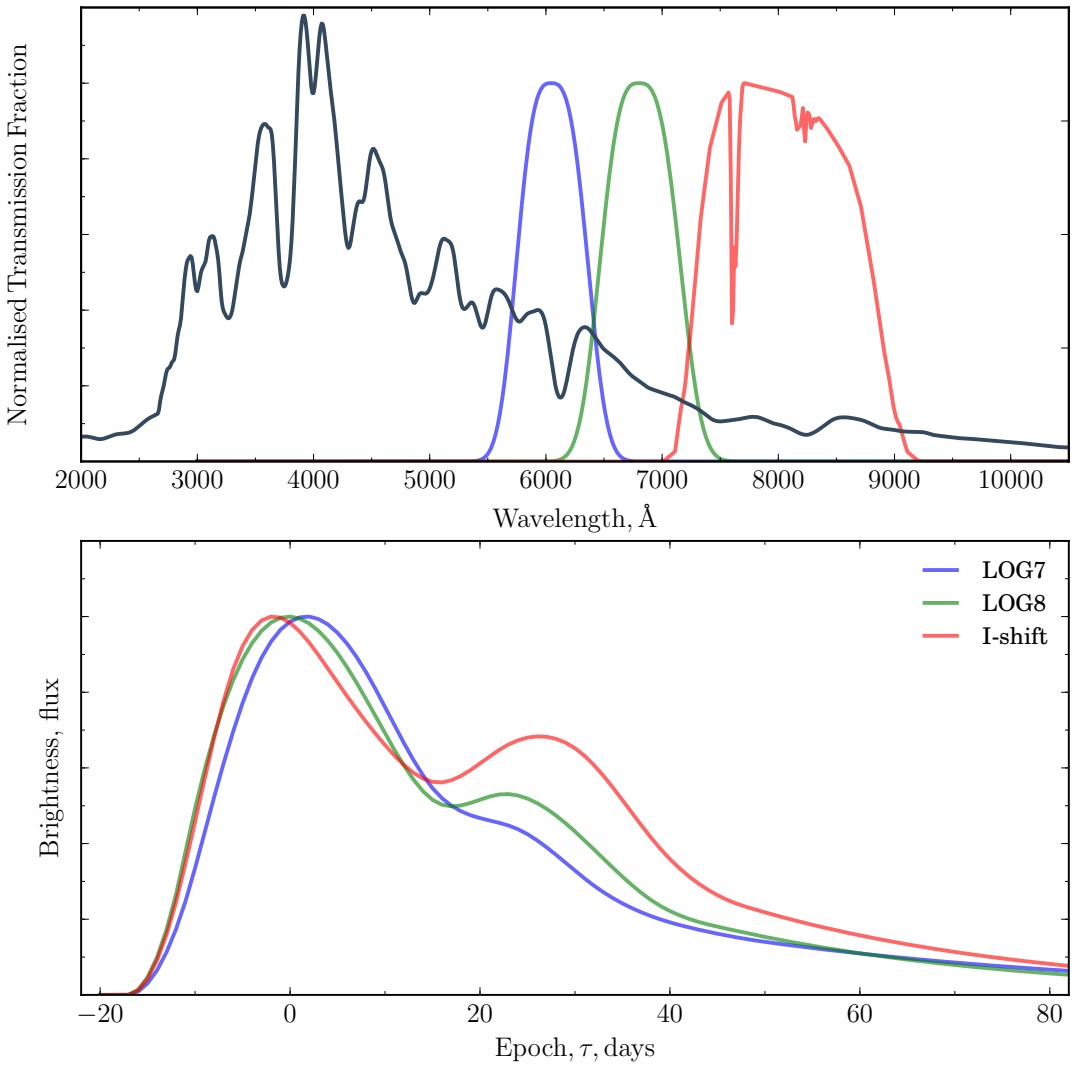

FIGURE 5.7: *Top Panel*: The SiFTO 'LOG-7', 'LOG-8' and 'I-shift' template filters used to mangle template spectra to fit obsered light curves. These are the three light curve templates that exhibit a 'shoulder' or secondary maximum, as shown in the lower panel. *Bottom Panel*: The light curve templates, shown in flux space, used by SiFTO to fit the SNe Ia photometry.

find that there is a strong correlation between $\langle i \rangle_{20-40}$ and Δm_{15}, finding the expected result that broader lightcurves have stronger secondary maxima.

We can test our light curves in a similar way, by defining the parameters $\langle R_{\rm P48} \rangle_{20-40}$ and $\langle R_{\rm P48} \rangle_{15-35}$, which are the mean integrated flux in $R_{\rm P48}$ between the phases $20 \leq \tau \leq 40$ and $15 \leq \tau \leq 35$ respectively. We use the former to directly test the difference between the i and r strength in the same phase, and the latter to adjust for the observation that the shoulder in r seems to appear earlier than that in i. Rather than fitting a high order polynomial, as in the literature examples, we use the integrated flux under our combined template and gaussian fit.

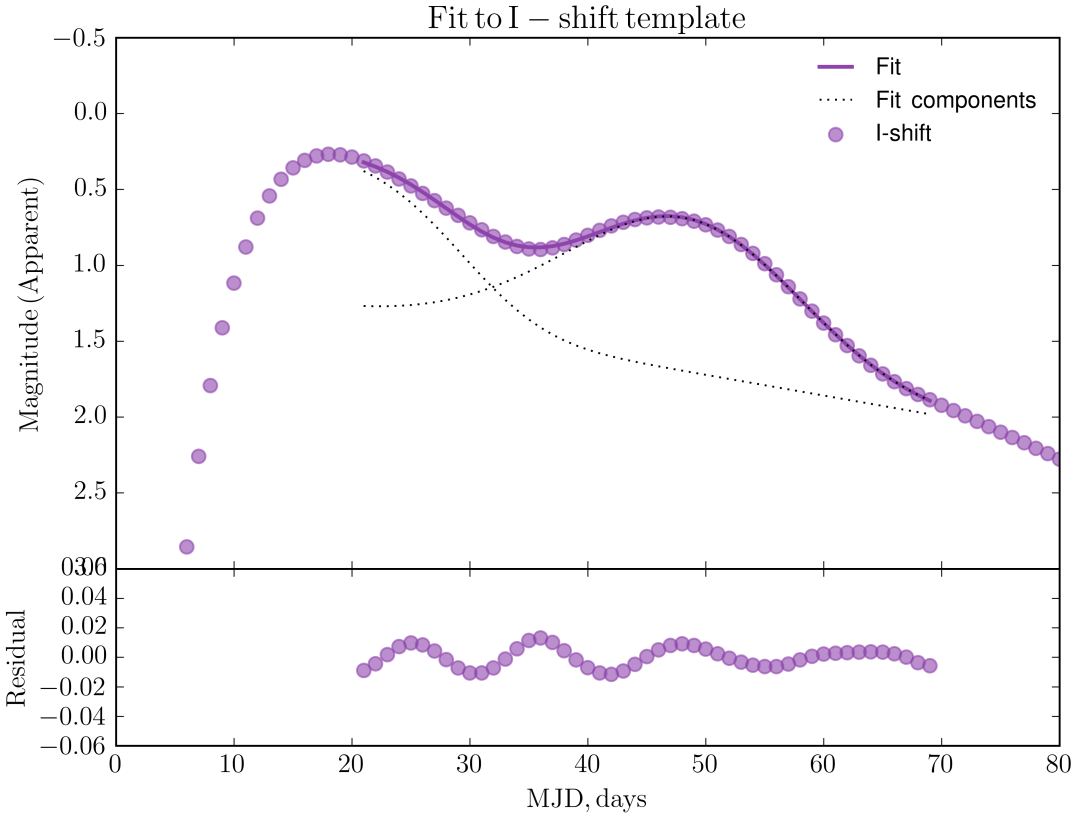

FIGURE 5.8: Fit to the SiFTO I–Shift template, the reddest template SiFTO uses internally to mangle spectra in order to fit lightcurves. The filter bandpass is shown in the top panel of Figure 5.7. *Top Panel*: Solid line shows the light–curve template, the dotted lines show the Gaussian components of the fit used in the fit to the template (see Equation 5.1). *Bottom Panel*: the residual of the fit, the higher–order variation observed is due to the use of a cubic spline in the constuction of the templates, and is the reason we use the model fit, rather than subtract the best fitting second Gaussian.

Other notable attempts to measure the morphology have been made by Hamuy et al. (1996b) and Contardo et al. (2000) which focus on using the time derivative of the flux to determine points of inflection on the light curve. This measurement is straightforward and is the likely subject of further work.

5.4 Post-maximum Sample

We draw our initial sample from the PTF parent sample. As we are investigating the diversity of post-maximum behaviours, it is important to ensure good coverage up until the lightcurve evolves onto the radioactive decay tail. Additionally, good coverage is needed around peak, to constrain the main observational parameters, peak flux and stretch. We also use a sample from CSP (Section 2.2.4) as a consistency check, and to show that our results do not sit within an unusal region of parameter space. Additionally,

TABLE 5.1: The effect of selection cuts on our parent sample, showing the number of SNe lost when imposing each cut, resulting in our sample. The cuts were done sequentially, from top to bottom as shown in the table; as a result, some SNe would have failed multiple criteria.

	Discarded	Remaining
PTF Parent	-	1258
SiFTO fit success	298	960
$z \leq 0.1$	438	523
$N_{\rm r}(\tau \leq 0) \geq 4$	156	367
$N_{\rm r}(0 \leq \tau \leq 15) \geq 4$	254	113
$N_{\rm r}(15 \leq \tau \leq 35) \geq 5$	57	56
$\widehat{\rm SNR}(15 \leq \tau \leq 35) \geq 12.0$	25	31

as the NIR behaviour of the CSP objects has been studied, we can link our $R_{\rm P48}$ analysis to longer wavelengths, and ensure the validity of our method.

5.4.1 Selection Cuts

We apply a redshift cut at $z = 0.1$, which as well as acting as a rough proxy for a signal-to-noise ratio (SNR) estimate, means that the dominant spectral feature in the bandpass over this phase, the Si II λ6355 P-Cygni feature, remains within the filter. In order to probe the behaviour of all SNe Ia, rather than those deemed cosmologically normal, we choose not to make a stretch cut. As we are not including phases $\tau > 10$ in the initial SiFTO fit, two cuts to ensure good coverage around maximum light, to reduce uncertainties in the measurement of stretch and peak magnitude, are made. We exclude objects that have $N_{\rm obs}(\tau \leq 0) \leq 4$ and $N_{\rm obs}(0 \leq \tau \leq 15) \leq 4$. We next ensure a sufficient number of epochs on the shoulder by requiring more than 5 separate epochs within $N_{\rm r}(15 \leq \tau \leq 35) \geq 5$. Finally, we test the SNR in this region, and require the median SNR, $\widehat{\rm SNR}(15 \leq \tau \leq 35) \geq 12.0$.

5.5 Results

We apply the fitting method described in Section 5.3.2.2 to our sample of 36 SNe Ia, outlined in Section 5.4. In this section, we present the results of our fits, which can be seen in Table C.1 (Appendix C) and compare the outcomes to those in the literature, and predictions from theory. The overall fit quality is excellent and the model reproduces the range of features seen well; an example fit to one of our SNe, PTF 10kdg, can be seen in Figure 5.10.

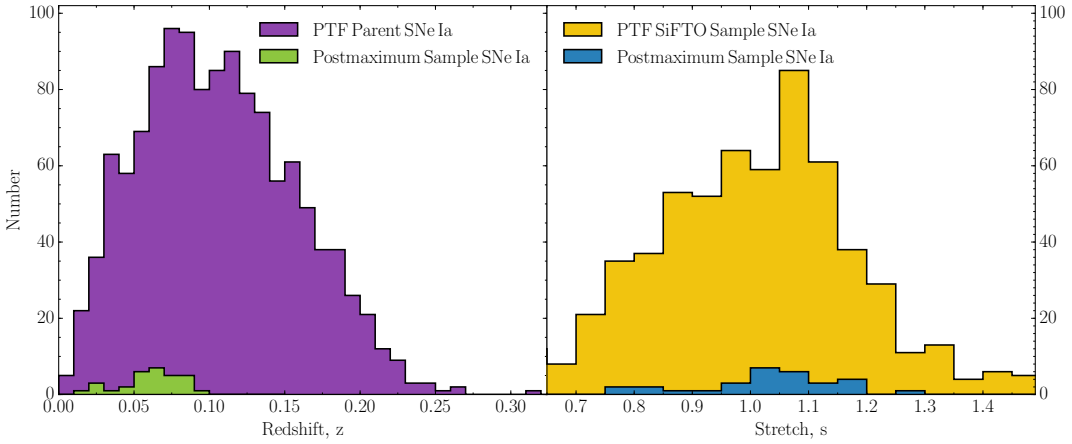

FIGURE 5.9: *Left Panel*: Histogram showing the redshift distribution of the entire PTF parent sample (purple), and in red, the redshift distribution of the final sample after applying the remaining cuts outlined in Table 5.1 and Section 5.4.1. *Right Panel*: Histogram showing the stretch distribution of the entire PTF parent sample that passed the pipeline and SiFTO light curve fit (yellow), after applying the same cuts.

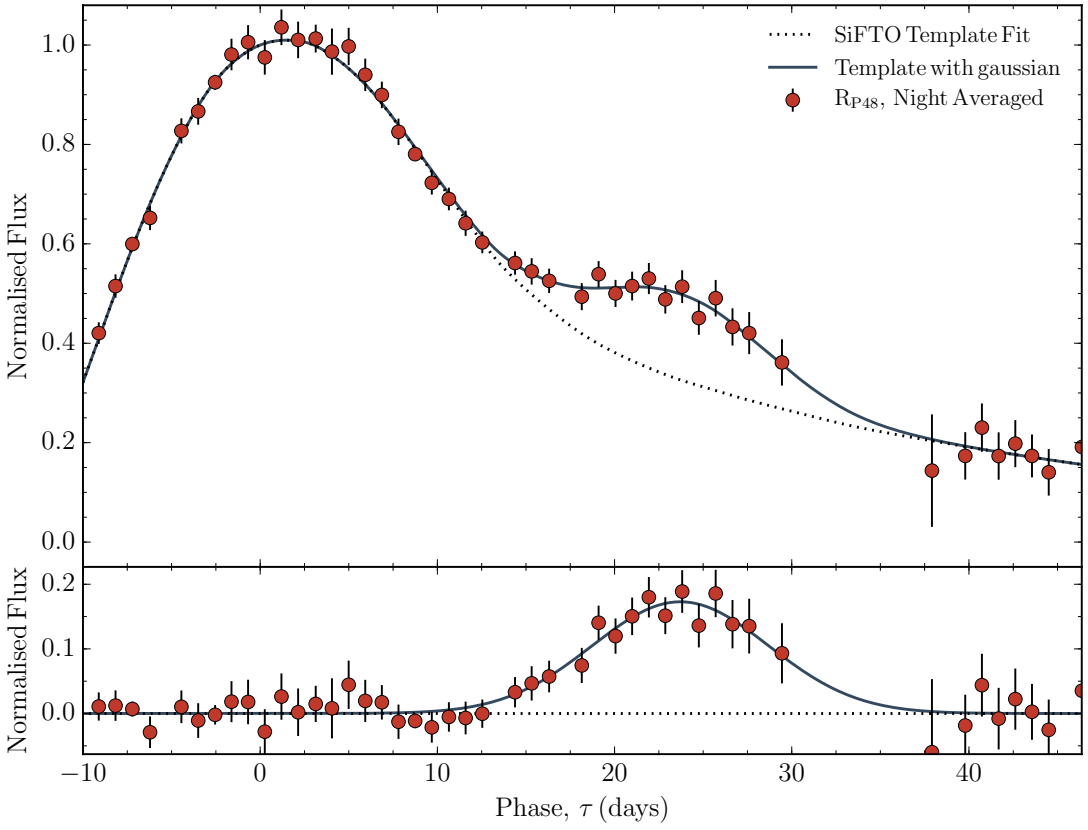

FIGURE 5.10: PTF 10kdg showing the best fit to the data, and components of the fit. *Top Panel*: Night-averaged R_{P48}light curve of PTF 10kdg (red points), the SiFTO template fit to data $-20 \leq \tau \leq 10$ (dotted line), and the total template plus gaussian (solid line) is shown. *Bottom Panel*: The residual from the initial template fit, with the gaussian fit shown as the solid line.

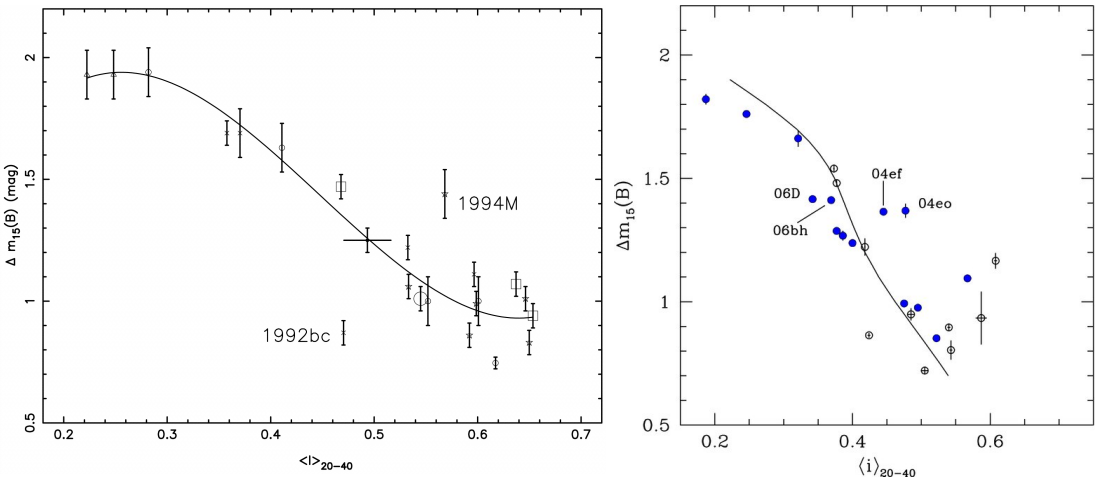

FIGURE 5.11: Decline rate parameter $\Delta m_{15}(B)$ vs. the mean I-band flux 20 to 40 days after the time of B-band maximum ($\langle R_{\rm P48}\rangle_{20-40}$). *Left Panel*: Taken from (Krisciunas et al., 2001), the labelled SNe are those that are the furthest from the overplotted third-order regression line. *Right Panel*: Taken from (Folatelli et al., 2010), the solid points are those measured using spline interpolation and the hollow points are those fitted using SNooPy templates (Burns et al., 2011).

5.5.1 Mean Secondary Flux – $\langle R_{\rm P48}\rangle_{15-35}$ and $\langle R_{\rm P48}\rangle_{20-40}$

The first measurement we make is the mean integrated flux of the lightcurve during the secondary (See Section 5.3.3). Figure 5.12 shows the relationship between light curve width and both $\langle R_{\rm P48}\rangle_{15-35}$ (left panel), and $\langle R_{\rm P48}\rangle_{20-40}$ (right panel), which act as a proxy for strength of the secondary. In both cases, the claimed correlation between lightcurve width and strength (Krisciunas et al., 2001; Folatelli et al., 2010), which can be seen in Figure 5.11 is recovered; the Pearsons correlation coefficent, R, is $R = 0.89$ for $\langle R_{\rm P48}\rangle_{15-35}$, and $R = 0.87$ for $\langle R_{\rm P48}\rangle_{20-40}$. However, when accounting for the lightcurve width, by stretch correcting the phase cutoffs, the relationship disappears. This indicates that the measured dependence is driven not by the increase of the relative strength of the secondary with light curve width, but is reflecting the underlying width luminosity relation. The presence of the correlation in both phase bins is reflective of this.

When the stretch is taken into account, the correlation coefficients not only decrease in magnitude, but become negative; $R = -0.53$ for $\langle R_{\rm P48}\rangle_{15-35}$ and $R = -0.56$ for $\langle R_{\rm P48}\rangle_{20-40}$. This, while a weaker correlation, suggests that in fact the lower the stretch, and therefore the lower the intrinsic brightness, the stronger the secondary is relative to the main peak.

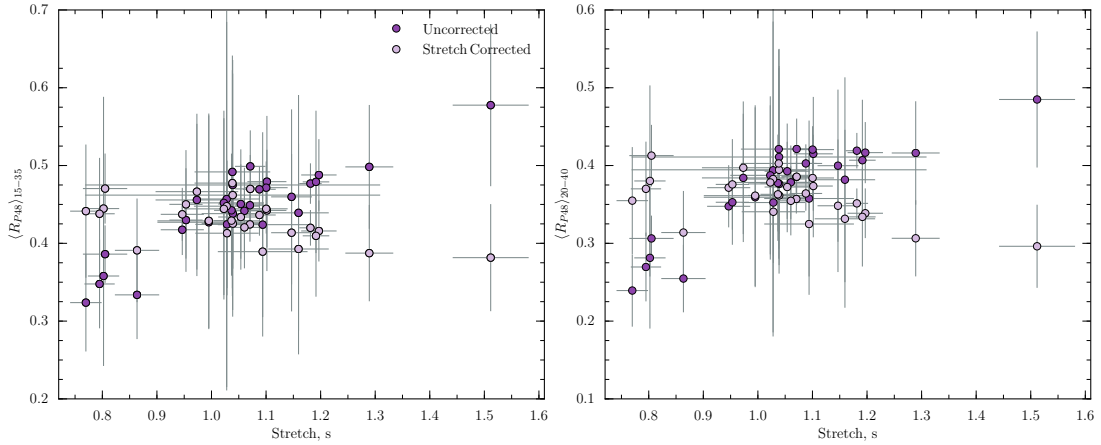

FIGURE 5.12: Mean $R_{\rm P48}$ flux in the shoulder as a function of stretch. *Left Panel*: $\langle R_{\rm P48}\rangle_{15-35}$ as a function of stretch. The mean integrated flux (dark) is well correlated with light curve width. When the value is corrected for lightcurve width (light), no relationship is seen. *Right Panel* $\langle R_{\rm P48}\rangle_{20-40}$ as a function of stretch. The mean integrated flux (dark) is well correlated with light curve width. When the value is corrected for lightcurve width (light), no relationship is seen.

5.5.2 Gaussian Parameters – F_g, σ_g, τ_g, A_g

We now move on to the specific parameters of the gaussians fitted onto our templates, in order to better quantify the morphological diversity seen. As discussed in Section 5.2, the strength (F_g), duration (σ_g) and timing (τ_g) of the secondary is key to understanding the underlying physics, and an important diagnostic tool for identifying differences between the post-maximum behaviours seen in the NIR and optical. We also combine the F_g and σ_g to consider the area under the gaussian, defined as $A_g = F_g\sigma_g\sqrt{\pi}$, to measure the total contribution of the 'secondary'.

5.5.2.1 Peak Time – τ_g

Firstly we consider the phase difference in days between t_{max} and the peak of the fitted gaussian, τ_g. Figure 5.13 shows the expected relationship between the light curve width and the time of maximum gaussian emission, τ_g in our sample (dark green points) and for CSP (light green points), that is broader, brighter objects have a larger τ_g. After correcting for stretch, the mean value became $\bar{\tau_g} = 25.16$ days, with a relatively low dispersion, with the standard deviation $S = 2.4$ days. This indicates that any variation in the peak timing is small, once light curve width has been accounted for.

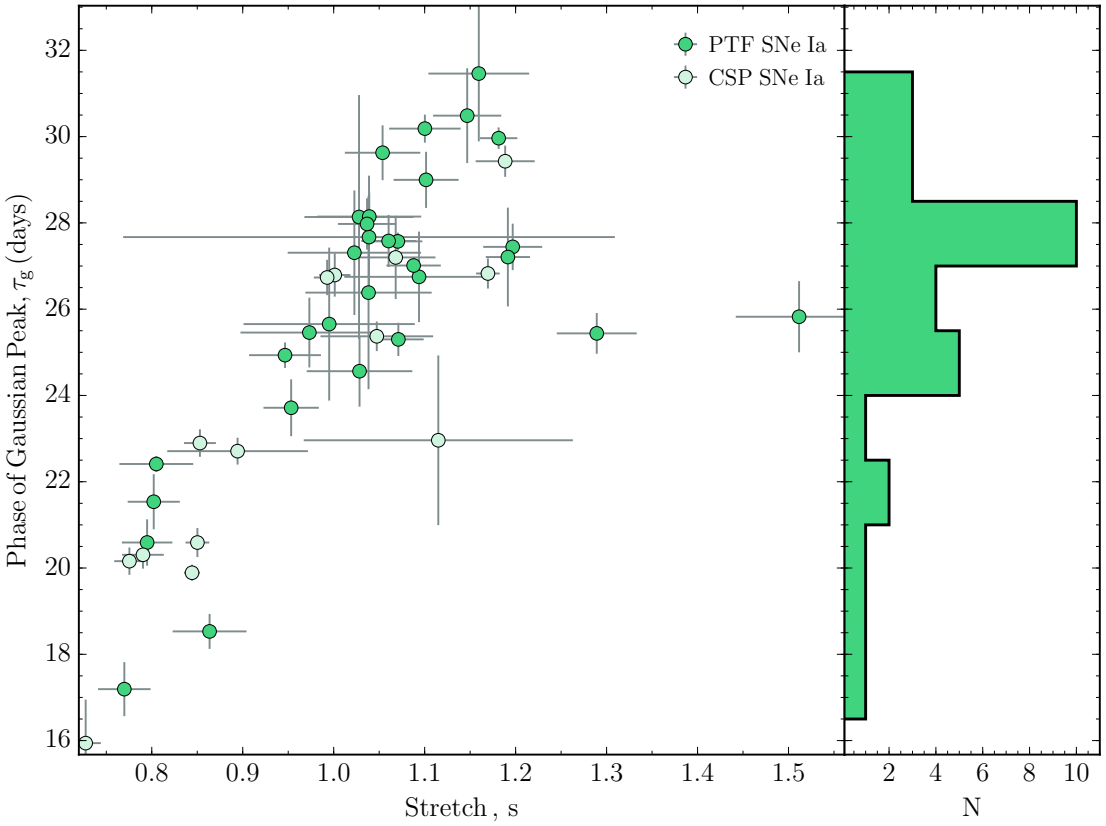

FIGURE 5.13: τ_g vs stretch. *Main Panel*: Dark green plots are PTF SNe Ia, light green points are CSP SNe. *Right Panel*: Histogram showing the distribution of τ_g.

5.5.2.2 Peak Duration – σ_g

Figure 5.14 shows the distributions of σ_g, the parameter that governs the width of the gaussian, and is our measure of the duration of the secondary. σ_g has a large range, with a median value $\widehat{\sigma_g} = 5.32$ days and standard deviation $S = 1.13$ days. There is a only weak dependence on stretch; the lack of a strong relationship with strength is somewhat surprising, especially given that seen between F_g and stretch. It might be expected from a photon diffusion argument similar to that made for the main peak width-luminosity relationship: broader, brighter SNe Ia have larger ejecta, and the photons released deep within undergo more collisions, taking longer to escape than their analogs in fainter, less massive SNe. It is important to note that the CSP and PTF datapoints have a similar distribution, despite the difference in range of stretch, that the effect persists indicates it is not a peculiarity of the PTF sample or the $R_{\rm P48}$ filter.

5.5.2.3 Peak Strength – F_g

A histogram showing the distribution of the fitted gaussian strength, F_g, and its relationship with stretch is shown in Figure 5.15. The distribution has a median value

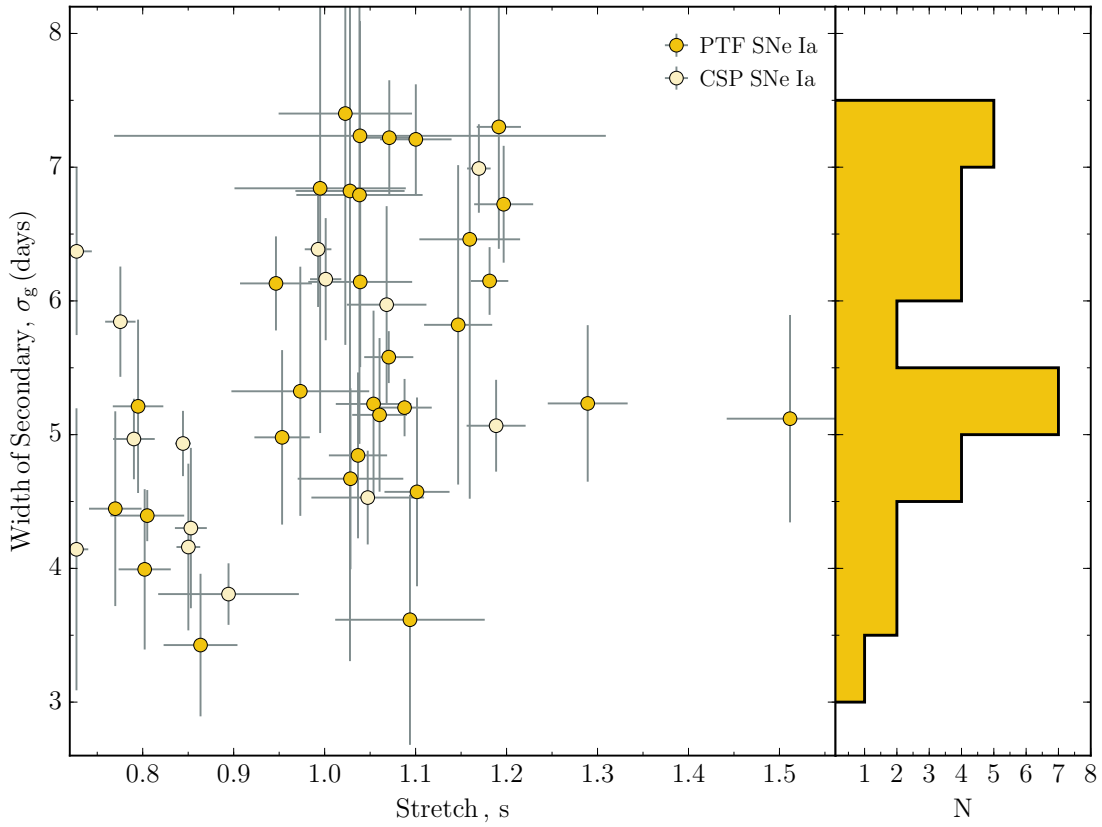

FIGURE 5.14: *Main Panel*: Duration of Secondary, σ_g vs Stretch, filled plots are PTF SNe Ia, light points are CSP SNe. *Right Panel*: Histogram showing the distribution of the σ_g parameter, which has a median value $\widehat{\sigma_g} = 5.32$ days and standard deviation $S = 1.13$ days.

$\hat{F}_g = 0.134$ and a standard deviation $S = 0.031$. There is a moderate correlation between F_g and stretch, $P = -0.48$; this implies that the lower the stretch of the object, the more powerful the secondary will be. This is the opposite result to that seen in the NIR, where broader lightcurves have more prominent secondary maxima. This may indicate a different physical mechanism. This corresponds well to the finding in Section 5.5.1.

The same trend can be seen in the CSP r-band data, which is on average lower, probably due to the fact it is bluer than $R_{\rm P48}$.

5.5.2.4 Area Under the Gaussian - A_g

A histogram showing the distribution of the area under the fitted gaussian, A_g, and its relationship with stretch is shown in Figure 5.16. A_g which has a median value $\hat{A}_g = 1.35$ and standard deviation $S = 0.39$. No strong correlation is seen, however, this is perhaps unsurprising, given that this measurement is a very similar one to that shown in Figure 5.12 when $\langle R_{\rm P48} \rangle$ is corrected for stretch. This follows when considering that

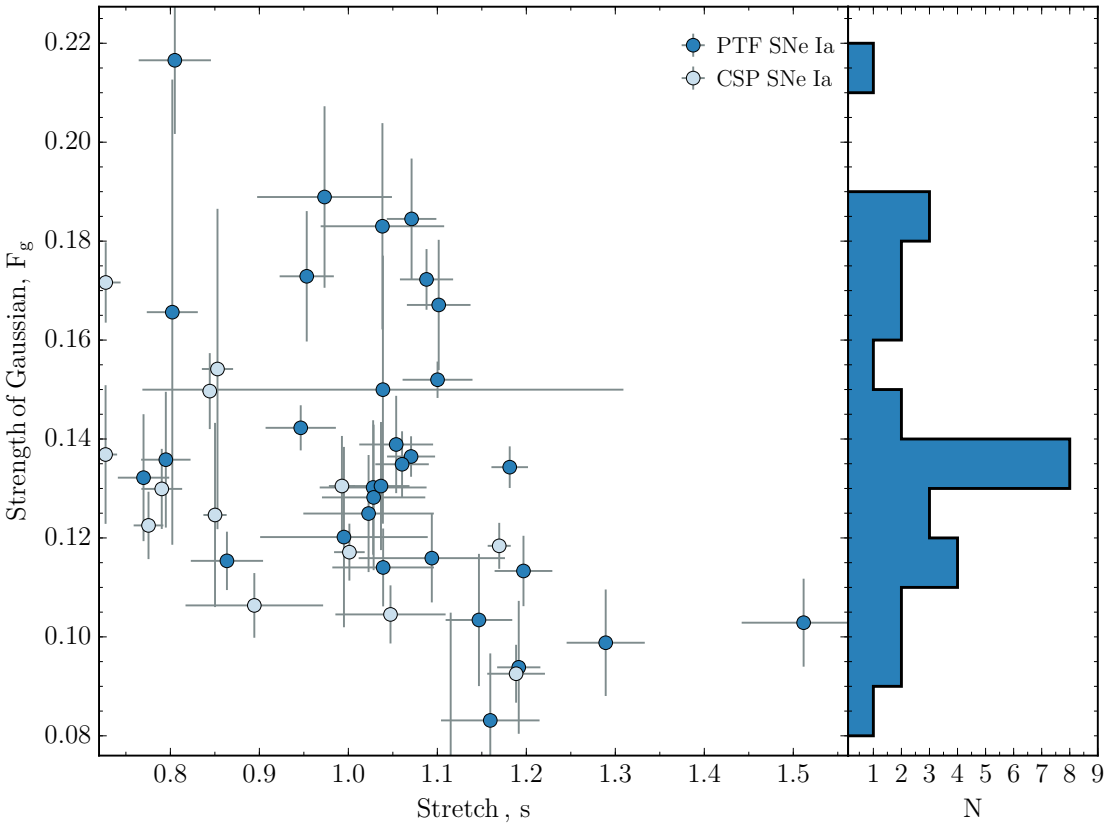

FIGURE 5.15: *Main Panel*: Strength of Secondary, F_g, vs Stretch. Dark blue plots are PTF SNe Ia, light blue points are CSP SNe. *Right Panel*: Histogram showing the distribution of F_g, which has a median value $\hat{F}_g = 0.134$ and a standard deviation $S = 0.031$.

the two parameters used to calculate A_g; F_g and σ_g correlate (even weakly) with light curve width in opposite sense.

5.6 Discussion

We find that the broadest light curves do have secondaries that have the peak in their emission later, this is consistent with both previous observations (e.g. Riess et al., 1996; Hamuy et al., 1996b; Nobili et al., 2005) and results from radiative transfer models (Kasen, 2006). However, we have shown that when accounting for overall light curve width, the value of τ_g shows only small dispersion from its mean value of $\bar{\tau}_g = 25.16$ days, with no residual correlation. This is also consistent with the broader-brighter higher ^{56}Ni mass description. It is somewhat surprising that σ_g does not show a similarly strong relationship with stretch, as following the same arguement, we would expect this to be the case.

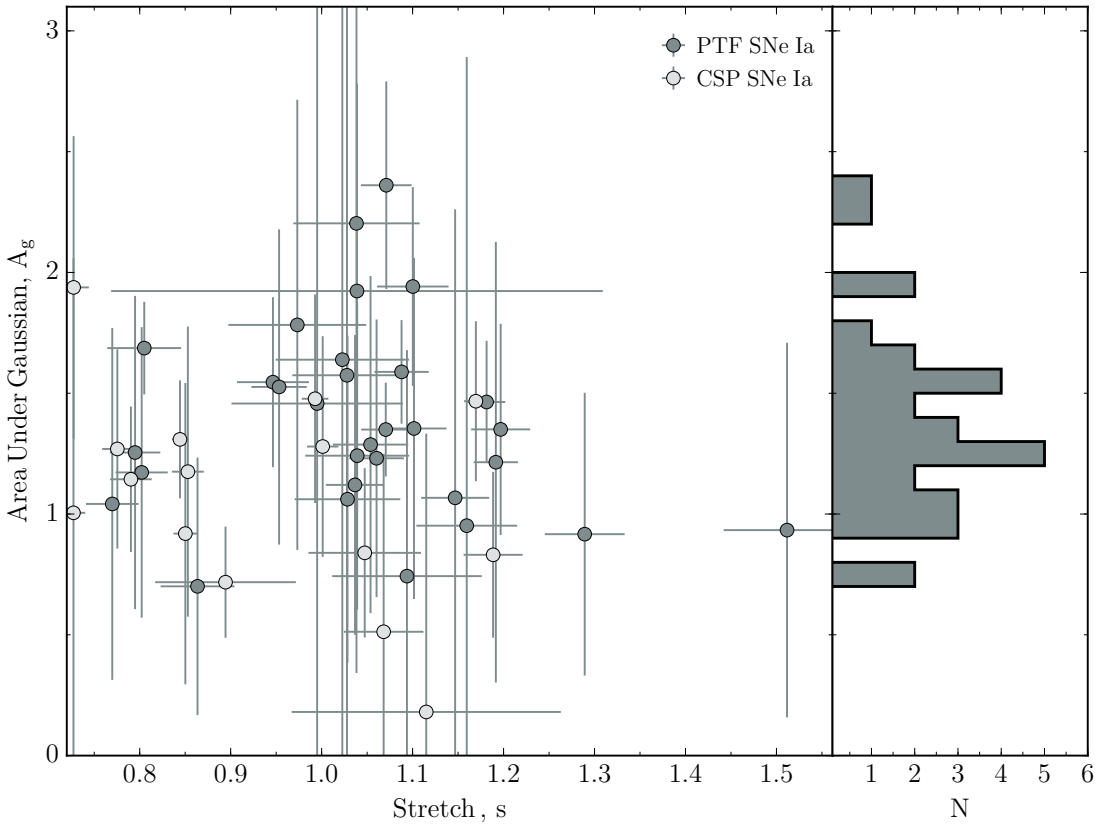

FIGURE 5.16: *Main Panel*: Strength of Secondary, A_g, vs Stretch. Dark grey plots are PTF SNe Ia, light grey points are CSP SNe. *Right Panel*: Histogram showing the distribution of A_g, which has a median value $\hat{A}_g = 1.35$ and standard deviation $S = 0.39$.

However, most unexpected is our finding that the strength of the secondary is not correlated with the light curve width, and therefore peak brightness. This behaviour is the opposite of that seen in NIR which intially seems to imply the physical mechanism powering the emission is distinct to that in the NIR. Another possibility is that the underlying process is the same, but the evolution is modified by changes in the spectral features, which if not dominant over the continuum, are comparable in strength. Kasen (2006) was able to mimic this behaviour by changing the progenitor metallicity. If this is the case, there may be some relationship between the secondary and evolution of later time features of for example [CoIII] λ5893 (Childress et al., 2015).

It would remain unusual however, that the r-band was the only place this was seen, if driven by metallicity. The interpretation of this finding hinges on whether the light curve shape is driven by line emission from IPEs, as is the case for the NIR, continuum reheating, or by evolution of spectral features caused by IMEs. Aside from changes in bulk ejecta properties, some simulations have been able to change the strength, duration and timing of a secondary feature by invoking orientation effects (Foley et al.,

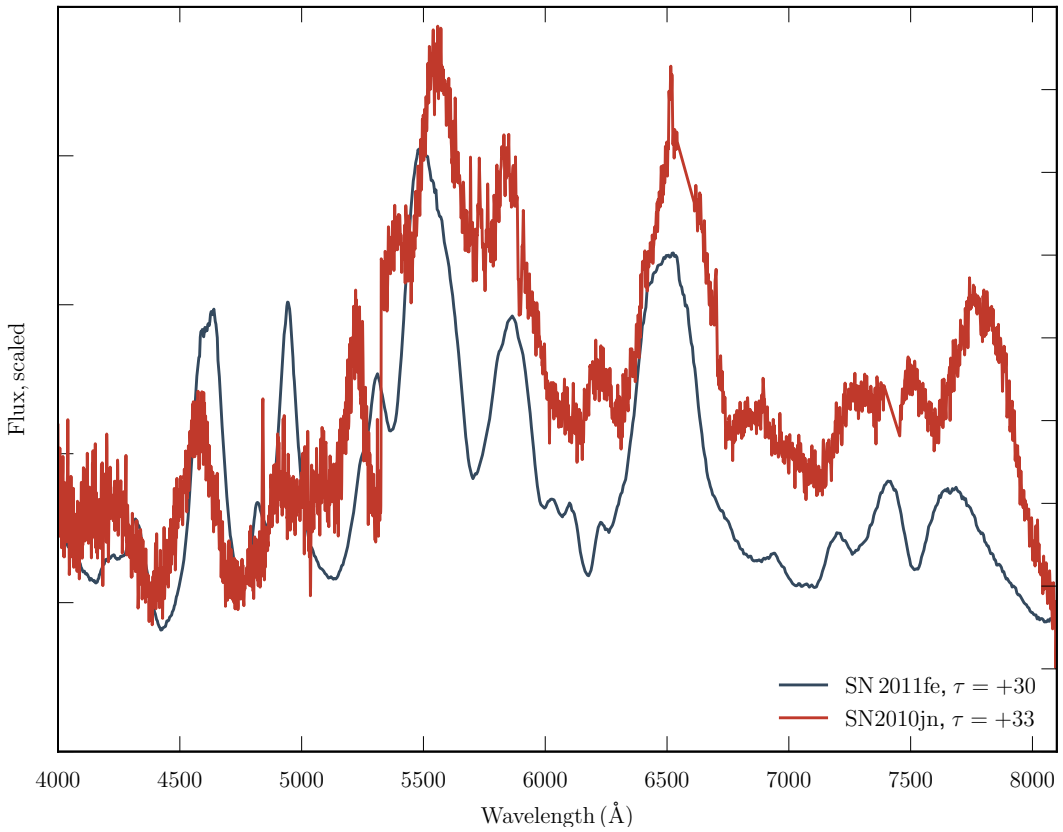

FIGURE 5.17: Spectra of SNe Ia SN 2011fe and 2010jn at $\tau = +30$ and $\tau = +33$, towards the end of the secondary phase.

2014). Whatever the explanation, the evolution of the lightcurve at these wavelengths is significantly more complex than the NIR.

Figure 5.17 shows clearly the spectral feature at $\sim$ 6500Å, the appearance of which coincides with the onset of the secondary. Unfortunately in our sample we do not have any SNe that have good spectral coverage over the phases $15 \leq \tau \leq 40$ days, so it is not possible to compare the evolution of the feature to the strength and duration of the secondary.

The nature of this feature is somewhat unclear, being identified as being the product of a number of species in the literature. Maurer et al. (2011) identify the dominant spectral feature as a blend dominated by Fe II while Jack et al. (2015) note Co II emission nearby but cannot unambiguously identify the feature. However, it may yet prove important that collisional data for Co II and III is incomplete (Kasen, 2006; Maurer et al., 2011).

If it is the result of an Fe-group element, the brighter-narrower relationship in the r-band is difficult to reconcile with the opposite behaviour in redder bands. One explanation is that efficiency of the re-absorption of IPE emission stimulated by $2 \rightarrow 1$ recombination, rather than the line emission itself may be the driver. This depends on the physical

conditions of the ejecta and the location of the photosphere. By regulating how much radiation is permitted to free stream out of the ejecta as *gamma*-rays and x-rays, it can drastically effect the secondary maximum (Pinto & Eastman, 2000b). Additionally, the decay of ^{56}Co releases not only γ-rays, but also positrons (Chan & Lingenfelter, 1993). These positrons are the dominant source of heating epochs $\tau > 200$, but are also significant at early times, as the ejecta is transitioning into a nebular state.

In addition to highlighting the role that high-excitation Fe II transitions play in driving the i-band secondary maximum, Jack et al. (2015) conclude that Co II blends present in the $6500 - 7000$ Å region do not contribute enough flux to explain the r-band secondary in the well observed nearby SN Ia SN 2014J. Pointing out that the Fe II blend around 7500 Å does not fall entirely within the bandpass, as it does for i-band, the blue wing of the feature could be a significant contributor. In their models, Jack et al. (2015) see a strengthening of the Si II P-Cygni profile between $6000 - 6500$ Å, but conclude the feature cannot provide a sufficient contribution to the overall luminosity to explain the plateau.

In contrast, van Rossum (2012) and Miles et al. (2016) use so-called 'knock-out' spectral models to identify spectral features withing SNe Ia spectra. The technique involves using a radiative transfer code (PHOENIX) to simulate SNe Ia ejecta, and removing a sub-sample of atomic transistion lines from the opacity. This is done while holding temperature, density, and atomic level population numbers fixed. Both authors suggest that over the phases where the secondary is most prominent, the Si II P-Cyg emission feature grows significantly in strength, something also discussed by Jack et al. (2015).

Given the unexpected behaviour of F_g with stretch, it seems likely that as well as contributions from IPE, which are synthesised in smaller amounts in cooler, fainter events, this Si II emission is providing a boost to the emission, causing a shoulder. In a similar vein, Kasen (2006) investigates Ca II IR triplet and concludes that the evolution of the feature in general supresses the overall flux when treated as either pure scattering (the emission wing of the P Cygni profile almost exactly cancels the absorpiton) or completely absorbing, but admits that the source function of the triplet still has sufficient uncertainties to draw strong conclusions.

5.7 Summary

In this chapter we used 31 SNe Ia from the Palomar Transient Factory to explore the diversity of the post-maximum phases in $R_{\rm P48}$. Using a modified SiFTO template fit, the secondary 'shoulder' present was fitted as an additional gaussian component. To compare

to previous work, the mean integrated model flux over two phase ranges $\langle R_{\rm P48}\rangle_{15-35}$ and $\langle R_{\rm P48}\rangle_{20-40}$ was calculated. The fitted parameters for the strength F_g, timing τ_g, and duration σ_g can be found in Table C.1. Our main findings are:

- The correlation between light curve width and mean integrated flux in i-band, $\langle i\rangle_{20-40}$, first found by Krisciunas et al. (2001) was seen in the equivalent parameters $\langle R_{\rm P48}\rangle_{15-35}$ and $\langle R_{\rm P48}\rangle_{20-40}$. However, this is found to be a reflection of the width luminosity relationship.
- After taking light curve width into account, by dividing by Stretch, s, there is a moderate anticorrelation between lightcurve width and secondary strength.
- F_g, which has a median value $\hat{F_g} = 0.134$ and a standard deviation $S = 0.031$. Like the stretch corrected $\langle R_{\rm P48}\rangle$ parameters is shown to be stronger for narrower, less luminous SNe Ia. Opposite to the observed behaviour of the NIR secondary maximum.
- σ_g parameter, which has a median value $\widehat{\sigma_g} = 5.32$ days and standard deviation $S = 1.13$ days is not found to depend strongly on light curve width.
- τ_g is found to have a strong correlation ($R = 0.87$) with stretch, and once corrected for light curve width has a narrow range, with a $\bar{\tau_g} = 25.16$ days, and a standard deviation $S = 2.4$ days. This is consistent with previous observations and the same as the NIR secondary maximum.
- Measuring the strength of the feature using the area under the gaussian, A_g gives a median value $\hat{A_g} = 1.35$ and standard deviation $S = 0.39$. As with the mean integrated flux, $\langle R_{\rm P48}\rangle$ this does not correlate with light curve shape.

Based on these findings, we suggest Si II evolution is just as important for the characteristics of the R-band light curve shoulder as the contribution from Fe-peak elements undergoing a ionisation change, particularly for low-stretch objects. However, significant changes to post-maximum morphology can be simulated by changing the metallicity, or the viewing angle. This may be tested by studying supernovae with good very early time coverage, polarimetry, $r - i$ colour evolution and analysis of nebular spectra.

Chapter 6

Multi–Colour Low-Redshift Hubble Diagrams From PTF

"There is a theory which states that if ever anyone discovers exactly what the Universe is for and why it is here, it will instantly disappear and be replaced by something even more bizarre and inexplicable.
There is another theory which states that this has already happened."

- Preface, *The Restaurant at the End of the Universe*, Douglas Adams, 1980

In this final chapter, we use our multicolour sub-sample of SNe Ia to further probe the diversity of these objects and to investigate claims of the cosmological utility of these events, and the uniformity of their peak magnitudes in R and i. By constructing a series of Hubble diagrams, we investigate the applicability of the empirical relationships used to correct these 'standardisable candles' to a uniform brightness. The properties of the Hubble residuals at different wavelengths are investigated, in an attempt to identify the most homogenous sample possible. We do not fit for cosmological parameters, and simply take residuals from a standard cosmology; instead our focus is on relative change in corrections within our own consistent sample. As well as following the method outlined in this Chapter to derive best fit standardisation parameters for the SNe sample, the photometric data reductions and light curve fits were performed by the author using the pipeline and fitting package described in Chapter 2. Of particular importance for this work was the additional fringe subtraction procedure on the $i_{\rm LT}$ images described in Section 2.4.4.

The use of i–band data is particularly interesting, as in this regime supernova light is less extincted by dust, the peak magnitude has previously been suggested to be more

uniform than elsewhere in optical wavelengths, and this study can act as an anchor for higher redshift surveys operating in the infra-red. With a raft of both ground–based and space–based campaigns planned to construct such samples, this is of some importance. We also explore the potential benefits of using an $R - i$ colour correction, rather than the archetypal $B - V$.

6.1 Motivation

In the era of large survey cosmology, the statistical uncertainties are becoming subdominant to systematic uncertainties (Betoule et al., 2014), one of the greatest challenges for SNe Ia cosmology is accounting for known systematics and testing for those that are, as yet, unknown. One of the most well known systematics, is extinction and reddening due to dust. Cosmological studies historically concentrate on the rest–frame U, B and V–bands, where the bulk of the SN emission is concentrated, observed at redder wavelengths to account for the effects of redshift. However, these observations are susceptible to extinction in both the host galaxy and our own Milky–Way.

The magnitude of this dust extinction and reddening, which may be catastrophic in the near-UV and optical, becomes increasingly manageable towards the near-IR (Cardelli et al., 1989). The difference between the size of the reddening corrections between B– and H–band is demonstrated in Figure 6.1 (taken from Mandel et al., 2011). This shows that in some cases, observations (red) being corrected by up to 3.5 magnitudes in B, while only a small fraction of this is needed in H. Such a dramatic reduction in the scale of the correction translates into a smaller uncertainty in the final cosmological measurements. Given the inherent assumptions in making such corrections, such as taking the extinction behaviour to be uniformly MW–like (while observationally, great diversity is seen e.g. Krisciunas et al., 2006; Elias-Rosa et al., 2008; Amanullah et al., 2014, 2015), any reduction is significant.

As well as being less susceptible to the effects of extinction, it has long been noted that the uniformity of the NIR peak brightnesses, which has a scatter of ~ 0.2 mag (Elias et al., 1981; Meikle, 2000; Krisciunas et al., 2004a; Barone-Nugent et al., 2012; Dhawan et al., 2015), makes SNe Ia a more 'standard' candle in NIR than optical. This combination of factors has recently led to a number of studies constructing rest-frame i–band, observer-frame NIR Hubble Diagrams (Krisciunas et al., 2004b; Nobili et al., 2005; Freedman et al., 2009; Barone-Nugent et al., 2012).

Our multicolour SN sample lightcurves enable us to quantify the corrections needed for each waveband, and for a consistent sample, investigate the change in intrinsic dispersion.

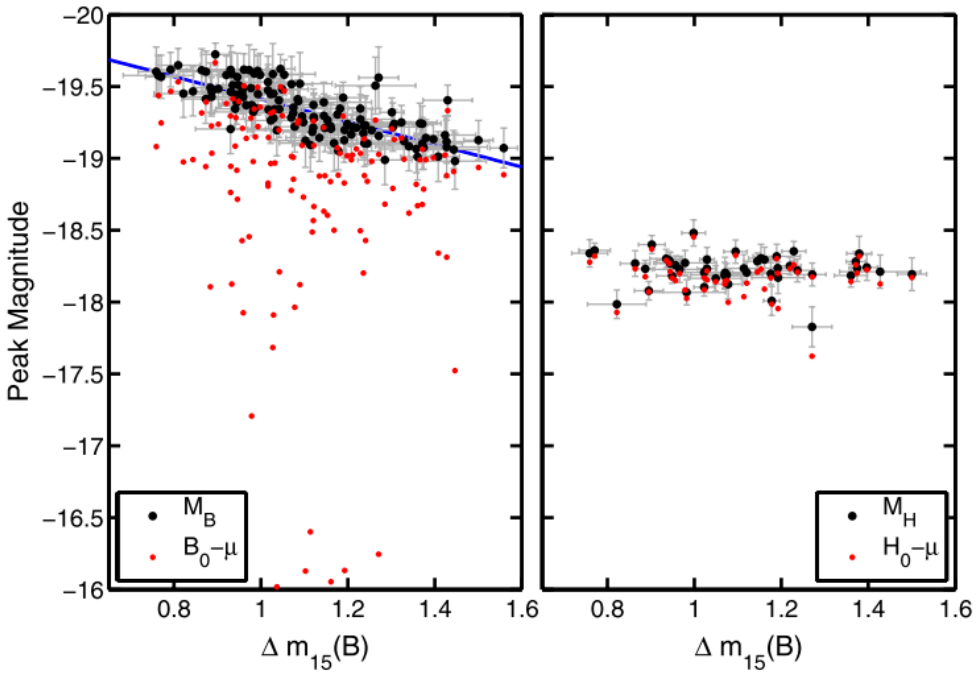

FIGURE 6.1: *Left Panel*: post-maximum optical decline rate Δm_{15}(B) vs. posterior estimates of the inferred optical absolute magnitudes (black points) and the uncorrected magnitudes (red points). Each black point maps to a red point through optical dust extinction in the host galaxy. The intrinsic light-curve- widthluminosity Phillips relation is reflected in the trend of the black points, indicating that SNe brighter in B have slower decline rates. The blue line is the linear trend of Phillips et al. (1999). *Right*: inferred absolute magnitudes and extinguished magnitudes in the near-infrared H-band. The extinction correction, depicted by the difference between red and black points, is much smaller in H than in B. The absolute magnitudes $\mathcal{M}_H$ have no correlation with Δm_{15}(B). The standard deviation of peak absolute magnitudes is also much smaller for $\mathcal{M}_H$ compared to $\mathcal{M}_B$.
Figure and caption from Mandel et al. (2011).

In addition, ongoing and upcoming high-redshift programs such as the Dark Energy Survey (DES; Flaugher et al., 2015) supernova program (DES-SN)/VISTA Extragalactic IR Legacy Survey (VEILS) and the Wide–Field IR Survey Telescope (WFIRST), will observe IR bands for SNe at $z \sim 0.5 - 1.2$ that correspond to rest–frame i–band, e.g in Y and J with VISTA (Figure 6.2). Constructing a low-redshift i–band hubble diagram will allow these future, high–redshift restframe i–band observations to be anchored at low redshift.

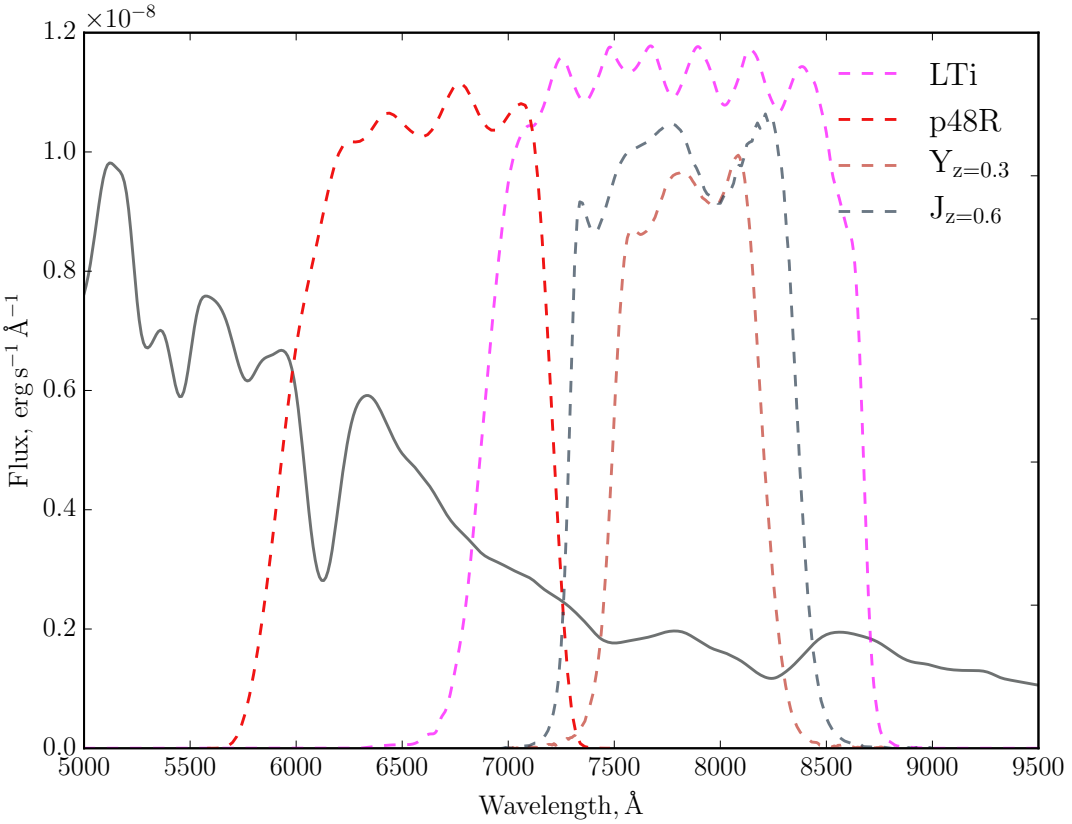

FIGURE 6.2: $R_{\rm P48}$and $i_{\rm LT}$filters on template spectrum, showing the restframe i–band overlap with high–redshift NIR

6.2 Methods

As in previous chapters we fit and parameterise our lightcurves using SiFTO. From this fit we obtain the light curve width, parameterised by stretch, s and a colour parameter, $\mathcal{C}$, an estimator of $B-V$ at maximum light (see Section 2.3 for details). In addition, we extract estimates of peak magnitude in B, $R_{\rm P48}$ and $i_{\rm LT}$, corrected for Milky–Way dust extinction using dust maps (Schlegel et al., 1998; Schlafly & Finkbeiner, 2011).

The light curve fits are set up to include all available photometric data in the light curve fit, but exclude $R_{\rm P48}$ and $g_{\rm P48}$ from the mangling used to modify the spectral templates (Conley et al., 2011). This is to avoid potential systematic offsets between LT and P48 data, in the event that the photometric calibration is imperfect.

For each of our three chosen filters, we calculate the model rest-frame maximum light apparent magnitude, m^{mod}, using

$$m_j^{mod} = 5\log_{10}\mathcal{D}_{\mathcal{L}}(\mathrm{z_{hel}}, \mathrm{z_{cmb}}, \mathrm{w}, \Omega_{\rm m}, \Omega_{\rm DE}, \Omega_{\rm k}) - \alpha_{\rm j}(\mathrm{s}-1) + \beta_{\rm j}\mathcal{C} + \mathcal{M}_{\rm j}, \tag{6.1}$$

for $j = (B, R_{\rm P48}, i_{\rm LT})$. $\mathcal{D}_{\mathcal{L}}$ is the c/H_0 reduced luminosity distance, Ω_m and Ω_{DE} are the fractional energy density of matter and dark energy respectively; as we use a standard cosmology thoughout, $\Omega_m = 0.3$, $\Omega_\Lambda = 0.7$, $k = 0$ and $H_0 = 70.0\text{km s}^{-1}\ Mpc^{-1}$, and a dark energy equation of state, $w = -1$, meaning $\Omega_{DE} = \Omega_\Lambda$. $\mathcal{M}_j$ is the absolute magnitude of the SN in the given band, j, α_j and β_j parameterise the stretch– and colour–luminosity relationships. These parameters are global for a given band, and apply to all of the SNe within our sample. z_{hel} and z_{cmb} are the heliocentric redshift and redshift relative to the CMB. We determine our free parameters, $\mathcal{M}_j$, α_j and β_j by minimising the χ^2

$$\chi^2 = \sum_{\rm SNe} \frac{(m_j^{obs} - m_j^{mod})^2}{\sigma_{total}^2}, \tag{6.2}$$

where m_j^{obs} is the observed apparent peak magnitude as determined by SiFTO, and $\sigma_{total}^2 = \sigma_{stat}^2 + \sigma_{int}^2$.

$$\sigma_{stat}^2 = \sigma_{\mathcal{M}_j}^2 + \sigma_z^2 + \alpha_j\sigma_s^2 + \beta_j\sigma_{\mathcal{C}}^2 + 2\alpha_j\sigma(\mathcal{M}_j, s) - \beta_j\sigma(s, \mathcal{C}) - 2\beta_j\sigma(\mathcal{M}_j, \mathcal{C})^2 + \sigma_{\rm vpec}^2 \tag{6.3}$$

where σ_x^2 is the variance in parameter 'x', and $\sigma(x, y)$ is the covariance between parameters x and y. We assume a peculiar velocity uncertainty of $v_{pec} = 300\text{km s}^{-1}$, which translates to a redshift uncertainty of $\Delta z = 0.001$.

$\sigma_{\rm int}$ parameterises the intrinsic dispersion of the sample, but also absorbs unknown systematics, selection effects and additional experimental uncertainties. $\sigma_{\rm int}$ is adjusted in our final fits to provide a value of χ^2 per degree of freedom of unity, and though our SNe share uncertainties across bands, we do not require that $\sigma_{\rm int}$ is the same in all bands, to account for any wavelength dependent effects.

The observed distance modulus, μ, for each SN is defined as

$$\mu_j = m_j^{obs} - \mathcal{M}_j. \tag{6.4}$$

Deviations from the theoretical value gives us a 'Hubble residual', $\Delta\mu_j = \mu_j^{obs} - \mu_j^{mod}$.

6.2.1 Hubble diagram sample

We draw our sample from the population of PTF SNe that were followed up by the LT, as described in Section 2.2.1. A number of SNe with followup observations failed our photometric pipeline, as in some cases we were unable to construct an appropriate reference image with which to perform difference imaging. Further to this, we applied a

number of cuts, both on the lightcurve parameters, and cadence, which we describe in the following Section.

6.2.1.1 Selection Cuts

We apply a redshift cut at $z = 0.09$ as used in other PTF analyses (e.g. Pan et al., 2015; Firth et al., 2015), which aligns this analysis with other 'nearby' programs such as the Calán/Tololo Supernova Survey (Hamuy et al., 1996a), Harvard-Smithsonian Center for Astrophysics (CfA) DR1, 2, 3 and 4 (Riess et al., 1999a; Jha et al., 2006; Hicken et al., 2009, 2012), the nearby Supernova Factory (SNFactory; Aldering et al., 2002), CSP1 and CSP2 (Hicken et al., 2009; Stritzinger et al., 2011) and the Lick Observatory Supernova Search (LOSS; Ganeshalingam et al., 2013). As PTF is an untargeted survey, the use of a redshift cut helps with the completeness, limiting the effect of Malmquist Bias. Helpfully, this also acts as an early check on the signal to noise of our data.

To properly calibrate SNe Ia, a maximum light colour is required. As PTF was principally a monochromatic $R_{\rm P48}$ survey, only the smaller number of the parent sample that were followed up with LT observations in $g_{\rm LT}$, $r_{\rm LT}$ and $i_{\rm LT}$ are used. We also employ cuts on the light curve width and SN colour as commonly used in cosmological analyses (e.g. Sullivan et al., 2011b), excluding objects that fall outside of the ranges $0.7 \leq s \leq 1.3$ for stretch, and $-0.25 \leq \mathcal{C} \leq 0.25$ for colour.

Next we ensure a minimum quality of time coverage by requiring that the objects are covered in either $R_{\rm P48}$ or $r_{\rm LT}$: at least one epoch before maximum light, more than twice in a late phase,$10 \leq \tau \leq 50$days, and twice around maximum light, defined as $-5 \leq \tau \leq 10$days. As we wish to ultimately construct a $i_{\rm LT}$ hubble diagram, we require more than two epochs of data in the $i_{\rm LT}$. The effect of these cuts is summarised in Table 6.1. In addition, upon visual inspection

6.2.1.2 Redshift Distribution

The redshift distribution of the sample before and after applying our selection cuts is shown in Figure 6.3. The mean redshift of the final sample, after enforcing $z < 0.09$ is $\bar{z} = 0.064$, and the median $\hat{z} = 0.061$, significantly lower redshift than the PTF parent, which has $\hat{z}_{PTF} = 0.10$.

TABLE 6.1: The Effect of selection cuts on our parent sample, showing the number of SNe lost when imposing each cut, resulting in our multi–band hubble diagram sample. The cuts were done sequentially, from top to bottom as shown in the table; as a result, some SNe would have failed multiple criteria.

	Discarded	Remaining
PTF Parent	-	1258
LT Multicolour Followup	1077	181
Passed Photometric Pipeline	49	132
SiFTO fit success	10	122
$z \leq 0.09$	13	109
$E(B-V)_{MW} \leq 0.2$	1	107
$0.7 \leq s \leq 1.3$	11	96
$-0.25 \leq \mathcal{C} \leq 0.25$	23	73
$N_{\rm r}(\tau \leq 0) \geq 1$	2	71
$N_{\rm r}(10 \leq \tau \leq 50) \geq 2$	2	69
$N_{\rm r}(-5 \leq \tau \leq 10) \geq 2$	6	63
$N_{i_{\rm LT}}(\text{total}) \geq 2$	3	60

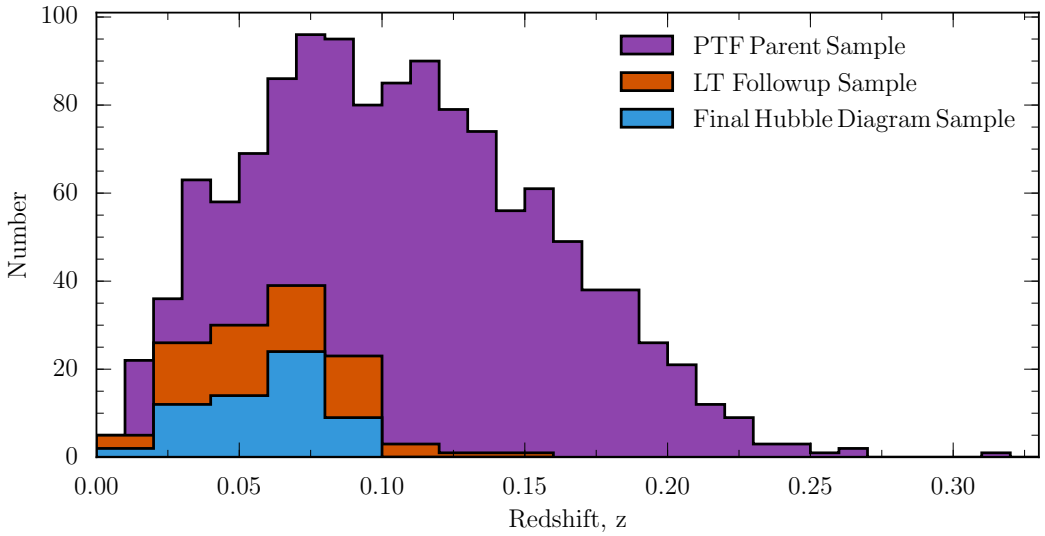

FIGURE 6.3: Histogram showing the redshift distribution of the entire PTF parent sample (purple), the multicolour followup sample that passed the pipeline (red) and fitter, and the redshift distribution of the final sample after applying the remaining cuts outlined in Table 6.1 and Section 6.2.1.1

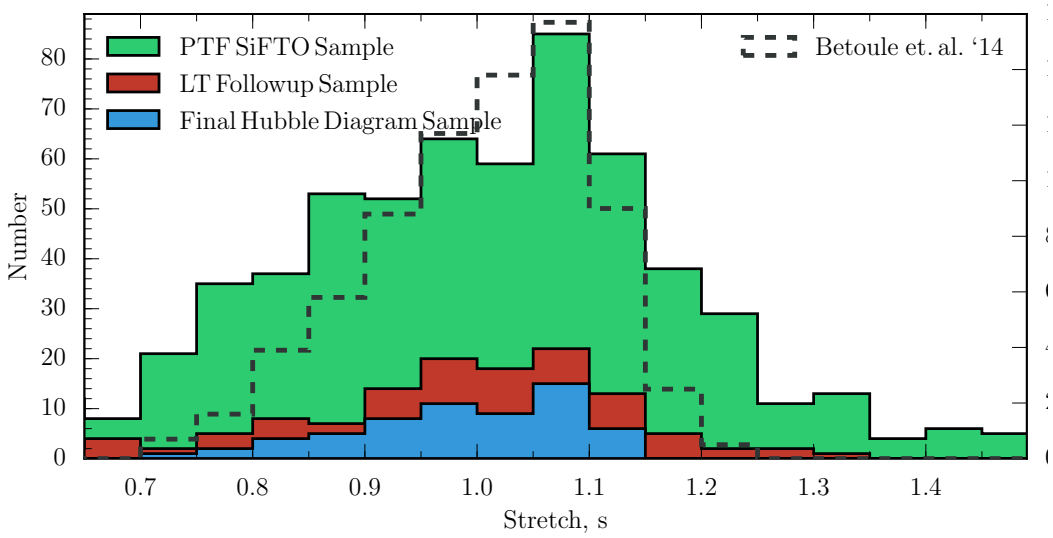

FIGURE 6.4: Histogram showing the stretch distribution of the parent sample (Red) that passed the pipeline and fitter, and the stretch distribution of the final sample after applying the remaining cuts outlined in Table 6.1 and Section 6.2.1.1. The normalised histogram of values from the Betoule et al. (2014) JLA sample is overplotted as a dashed outline.

6.2.1.3 Stretch Distribution

The stretch distribution of the sample before, as described in Section 2.2.1 and 2.1, and after applying our selection cuts, enforcing $0.7 \leq s \leq 1.3$, is shown in Figure 6.3. Before applying our cuts, the LT parent sample has average values of $\bar{s} = 0.97 \pm 0.01$ and $\hat{s} = 0.99$, and a standard deviation $\sigma = 0.16$. The final distribution has both a smaller dispersion than the parent, with a standard deviation $\sigma = 0.10$, and with $\bar{s} = 0.98 \pm 0.01$ and $\hat{s} = 0.99$. Betoule et al. (2014), in their Joint–Lightcurve Analysis (JLA) sample, find a mean stretch (converting from the SALT2 width parameter, x1, using $x1 = 10 \times (s - 1)$) of $\bar{s}_{\rm JLA} = 1.004 \pm 0.004$, consistent with our value within 2.2σ.

6.2.1.4 Colour Distribution

The colour distribution of all of the SNe that we were able to reduce and fit is shown in Figure 6.5 in red, showing significant spread, having a standard deviation $\sigma = 0.6$, and a tail, and separate red population pulling the mean of the distribution to $\bar{\mathcal{C}} = 0.16 \pm 0.06$ and median $\widehat{\mathcal{C}} = 0.03$. After making the redshift, extinction, stretch, colour, coverage and fit quality cuts outlined in Table 6.1 and Section 6.2.1.1, the SNe in the blue histogram remain. They show a much smaller scatter of $\sigma = 0.09$, and the symmetry of the distribution is much improved, with a $\bar{\mathcal{C}} = 0.00 \pm 0.01$ and median $\widehat{\mathcal{C}} = -0.00$. Betoule et al. (2014), in their Joint–Lightcurve Analysis (JLA) sample, find a slightly bluer mean colour, of $\bar{\mathcal{C}} = -0.023 \pm 0.003$, consistent with our value to 2.3σ.

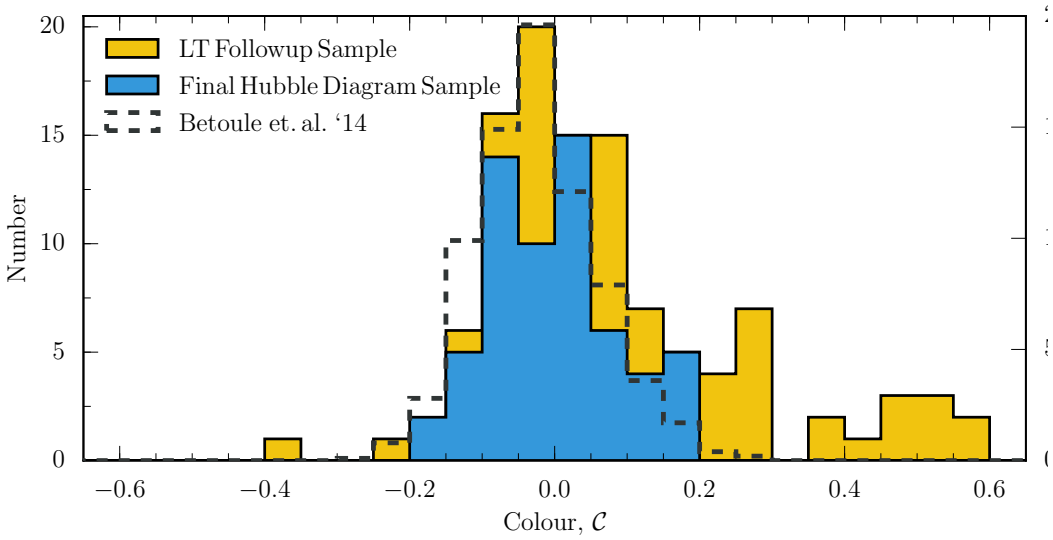

FIGURE 6.5: Histogram showing the colour distribution of the parent sample (Red) that passed the pipeline and fitter, and the colour distribution of the final sample after applying the remaining cuts outlined in Table 6.1 and Section 6.2.1.1. The normalised histogram of values from the Betoule et al. (2014) JLA sample is overplotted as a dashed outline.

6.2.2 Final Sample Summary

In summary, we have a sample of 60 objects with redshift, $z < 0.09$ ($\hat{z} = 0.061$), stretch $0.7 \leq s \leq 1.3$ ($\bar{s} = 0.98 \pm 0.01$), and colour $-0.25 \leq \mathcal{C} \leq 0.25$ ($\bar{\mathcal{C}} = 0.00 \pm 0.01$). Our final total number of SNe compares favourably to existing work (e.g. the 21 $z < 0.09$ CSP SNe Ia used by Freedman et al., 2009) and has the benefits of being an untargeted survey. Figure 6.6 shows stretch versus colour for our sample, and no correlation between these parameters is seen. Now we have defined our sample, we move on to the results of our analysis.

6.3 Results

In this section we present the fit results in all three bands for our free parameters, α, β and $\mathcal{M}$. We also show the resulting Hubble Diagrams and residuals, $\Delta\mu$, from a standard cosmology (Section 6.2), both before correction, with a partial correction for one of $\alpha(s-1)$ and $\beta\mathcal{C}$, and with both corrections applied. We parameterise the degree of variation using the root mean square (RMS) error, the widely used approach in the literature, with a lower RMS value corresponding to a better standard candle. The variation of these values across the optical wavelength regime is also shown. Throughout the following sections we will refer to parameters, x, for each band with the indices x^B for B–band, x^R for $R_{\rm P48}$ and x^i for $i_{\rm LT}$. A table of light–curve parameters can be found in Appendix D; Table D.1.

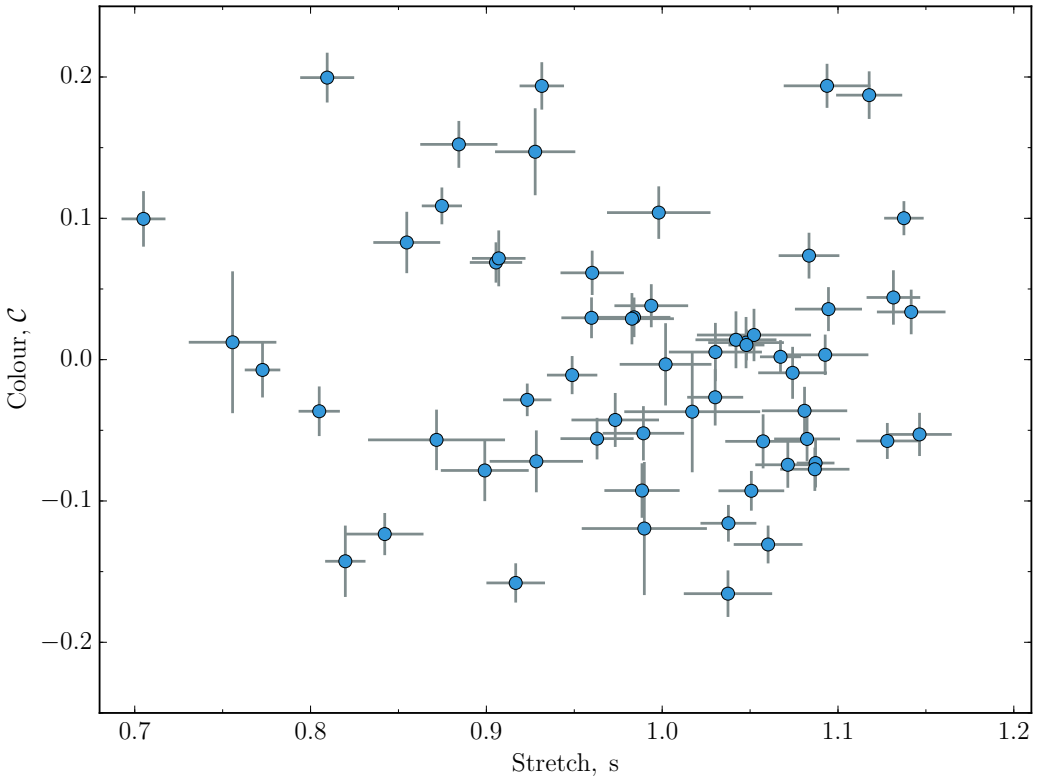

FIGURE 6.6: Colour, $\mathcal{C}$, vs Stretch, s, for Hubble Diagram Sample as described in Section 6.2.1.1

TABLE 6.2: Table of results for B, $R_{\rm P48}$ and $i_{\rm LT}$, showing the best fit correction coefficients α and β, the intrinsic dispersion, $\sigma_{\rm int}$ and absolute magnitude, $\mathcal{M}$. In addition, the root mean square values of the residuals, both before ($\rm RMS_{NoCorr}$), and after (RMS) the correction for stretch and colour are shown.

Band	α	β	$\mathcal{M}$	$\sigma_{\rm int}$ (mag)	$\rm RMS_{NoCorr}$ (mag)	RMS (mag)
B	0.70 ± 0.23	2.65 ± 0.26	-19.05 ± 0.02	0.16	0.301	0.175
$R_{\rm P48}$	0.52 ± 0.21	0.92 ± 0.24	-19.07 ± 0.02	0.15	0.193	0.163
$i_{\rm LT}$	0.18 ± 0.21	0.59 ± 0.24	-18.79 ± 0.02	0.15	0.177	0.167

6.3.1 *B*–band

The Hubble Diagram in B–band can be seen in Figure 6.7, the histogram of the residuals is shown in Figure 6.8 and the best fit parameters can be found in Table 6.2.

Using the method in Section 6.2, we find the best fit stretch correction coefficient $\alpha^B = 0.7 \pm 0.23$, and best fit colour correction coefficient $\beta^B = 2.65 \pm 0.26$. As a comparison, Conley et al. (2011) using an equivalent methodology find $\alpha_{\rm C11} = 1.371^{+0.086}_{-0.084}$ and $\beta_{\rm C11} = 3.18 \pm 0.10$. Our result is only consistent within 2.1σ to this value of β, and there is some tension between the values for α at 2.7σ. Using a larger sample (SNLS+SDSS,

including a re–analysis of the SNLS sample in Conley et al. (2011)) Betoule et al. (2014) find $\alpha_{\rm JLA} = 1.41 \pm 0.06$ and $\beta_{\rm JLA} = 3.101 \pm 0.075$.

One potential explanation for this discrepancy is the deficit of objects at the extreme ends of our colour and stretch distributions, which provide a large degree of leverage within the fitting. However, Kowalski et al. (2008) also find a lower value of $\alpha = 1.07 \pm 0.11$ in their low–redshift ($z < 0.2$) sample, more consistent with our α and a corresponding value of $\beta = 2.23 \pm 0.23$. It should be noted that there is considerable debate in the literature considering the value of β, and that a value of $\beta^B < 3$ is not unusual, for example Astier et al. (2006) find $\beta^B = 1.57 \pm 0.15$, Kowalski et al. (2008) find $\beta^B = 2.23 \pm 0.21$ for their sample and Kessler et al. (2009) find 2.65 ± 0.22 – matching our result (see Section 6.4.2 for further discussion).

Before correction for stretch and colour, the rms scatter around the standard cosmology is $\mathrm{RMS}^B_{\rm NoCorr} = 0.301$ mag, and post–correction $\mathrm{RMS}^B = 0.175$ mag, with an intrinsic dispersion of $\sigma^B_{int} = 0.16$ mag. For the low–redsift sample ($z < 0.1$) Conley et al. (2011) find RMS = 0.153 mag with an intrinsic dispersion of $\sigma_{int} = 0.113$ mag.

The best fit absolute magnitude, $\mathcal{M}^B = -19.05 \pm 0.02$ mag, entirely consistent with the Betoule et al. (2014) JLA value of $\mathcal{M}^B = -19.04 \pm 0.01$ mag.

6.3.2 Other Bands

Having demonstrated that our sample is consistent with current state-of-the-art cosmological samples, we now consider the additional information that is available to us by applying the same method to the peak magnitudes extracted in two other bands: $R_{\rm P48}$ and $i_{\rm LT}$. This will enable us to determine whether we can improve the cosmological utility of these objects, by studying redder wavelengths.

6.3.3 $R_{\rm P48}$–band

The Hubble Diagram in $R_{\rm P48}$ can be seen in Figure 6.9, the histogram of the residuals is shown in Figure 6.10. For the best fit stretch correction coefficient, we find $\alpha^R = 0.52 \pm 0.21$, and the best fit colour correction coefficient $\beta^R = 0.92 \pm 0.24$. Our value of α^R is lower than that found for α^B, but consistent within 1σ, β^R however is inconsistent with β^B. The best fit absolute magnitude, $\mathcal{M}^R = -19.07 \pm 0.02$ mag, is slightly higher than that found for B, but again, is consistant within 1σ uncertainties.

When considering the residuals, it is apparent that the *uncorrected* dispersion, $\mathrm{RMS}^R_{NoCorr} = 0.193$ mag is comparable to the value of the *corrected* B–band, $\mathrm{RMS}^B = 0.175$ mag.

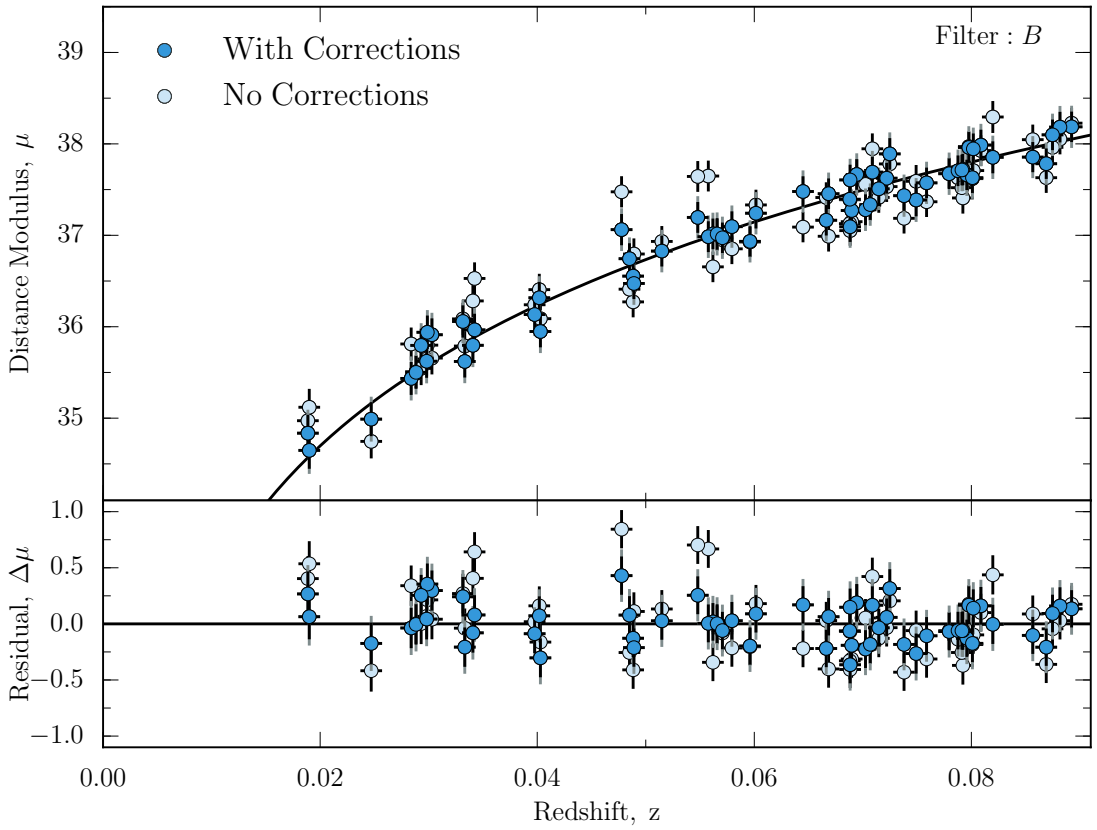

FIGURE 6.7: *Top Panel*: B–band Hubble diagram, where distance moduli calculated without correcting for lightcurve width and colour are shown as light blue, those calculated after applying the best fitting α and β corrections (Table 6.2) are the dark points. *Bottom Panel*: Residuals from the standard cosmology plotted in *Top Panel*. Colour scheme is the same as above. Historgrams of these points are shown in Figure 6.8

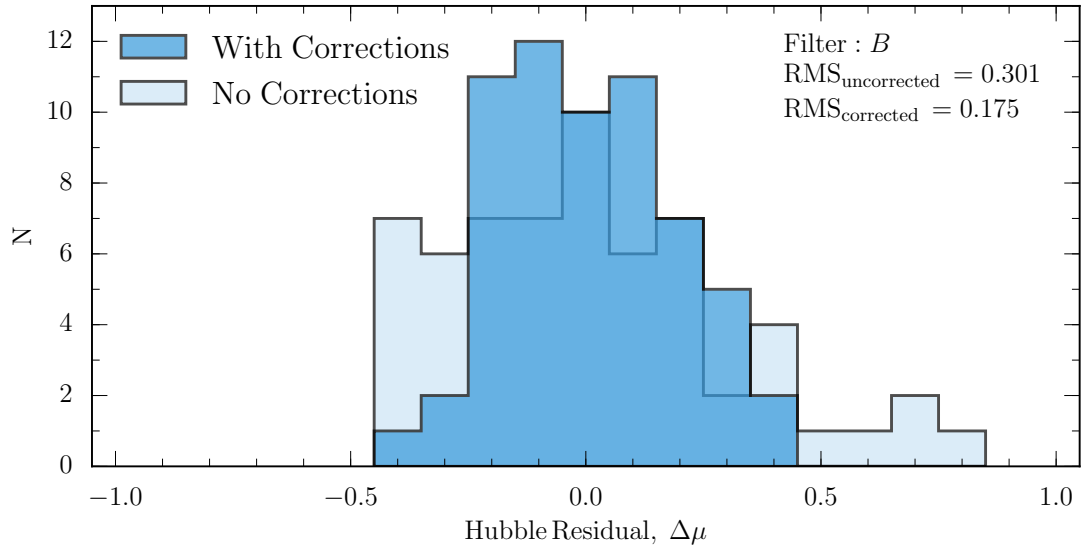

FIGURE 6.8: Histogram of B–band residuals from the Hubble Diagram shown in Figure 6.7. The residuals from standard cosmology (see Section 6.2) for the uncorrected absolute magnitudes are shown in light blue, those calculated after applying an α and β correction (found in Table 6.2) are shown in dark blue.

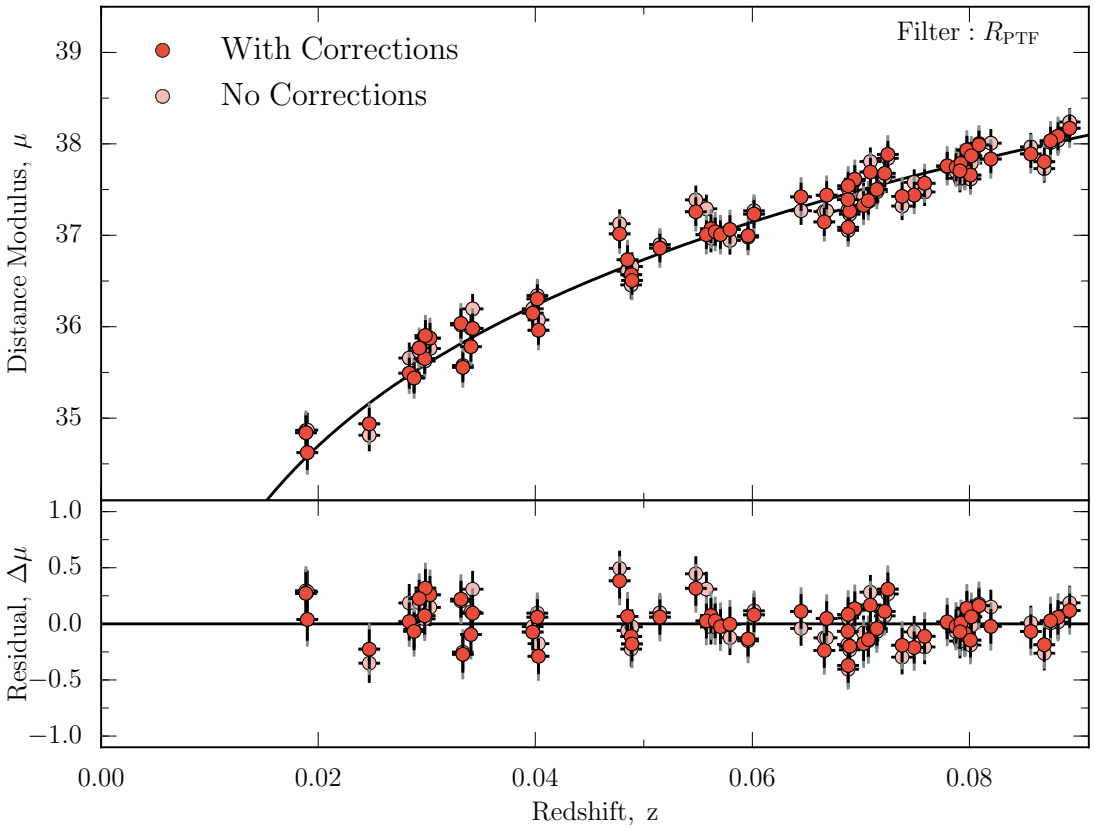

FIGURE 6.9: *Top Panel*: $R_{\rm P48}$ Hubble Diagram, where distance moduli calculated without correcting for lightcurve width and colour are shown as pink, those calculated after applying the best fitting corrections are the red points. *Bottom Panel*: Residuals from the standard cosmology plotted in *Top Panel*. Colour scheme is the same as above. Histograms of these points are shown in Figure 6.10

Post–correction, the rms dispersion in R–band improves to $\mathrm{RMS}^R = 0.163$ mag, with an intrinsic dispersion, $\sigma_{\rm int} = 0.15$ mag. This is a little higher than that found for CSP (Folatelli et al., 2010), which had a RMS = 0.13 mag and $\sigma_{int} = 0.13$ mag.

6.3.4 $i_{\rm LT}$–band

The Hubble Diagram in $i_{\rm LT}$ can be seen in Figure 6.11, the histogram of the residuals is shown in Figure 6.12. For the best fit stretch correction coefficient, we find $\alpha^i = 0.18 \pm 0.21$, for the best fit colour correction coefficient, we find $\beta^{{\rm LT}i} = 0.59 \pm 0.24$, and the best fit absolute magnitude, $\mathcal{M}^i = -18.79 \pm 0.02$. α^i is different from α^B at a level of $> 5\sigma$, and, perhaps more significantly, is consistant with no stretch correction.

Similarly to $R_{\rm P48}$, the initial dispersion is close to that of $\mathrm{RMS}^i_{\rm NoCorr} = 0.177$ is closer to the value of the corrected B–band, $\mathrm{RMS}^B = 0.175$. Post–correction, the rms dispersion improves slightly, to $\mathrm{RMS}^i = 0.167$, with an intrinsic dispersion $\sigma^i_{\rm int} = 0.15$. This RMS value is lower than that found by Nobili et al. (2005) ($\mathrm{RMS}^i = 0.24$), and while Folatelli

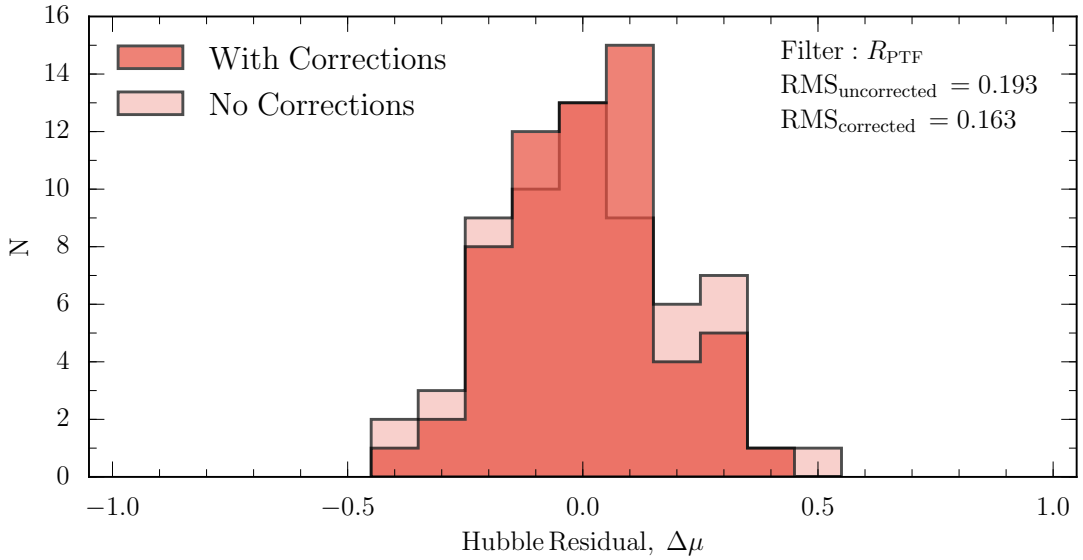

FIGURE 6.10: Histogram of $R_{\rm P48}$–band residuals from the Hubble Diagram shown in Figure 6.7. The residuals from standard cosmology (see Section 6.2) for the uncorrected absolute magnitudes are shown in pink, those calculated after applying an α and β correction (found in Table 6.2) are shown in red.

et al. (2010) do not quote a value of $\rm RMS^{\it i}_{NoCorr}$, they calculate an $\rm RMS^{\it i} = 0.15$, with an intrinsic dispersion of $\sigma_{\rm int} = 0.12$. A value of $\rm RMS^{\it i}_{NoCorr}$ is computed by Freedman et al. (2009), and found to be $\rm RMS^{\it i}_{NoCorr} = 0.17$, comparable with our sample. Once corrected for the effect of colour, Freedman et al. (2009) calculate an impressive $\rm RMS^{\it i} = 0.13$, however, this value only includes SNe Ia with $0.1 < z < 0.7$, so is not directly equivalent to the sample presented in this work.

6.4 Discussion

Our results (Table 6.2) show that a smaller RMS dispersion is attainable in $R_{\rm P48}$ than in B–band, with the two correction parameters, α^R and β^R, smaller than their corresponding values for B. We find that prior to making any corrections for light curve shape and colour, $\rm RMS^{\it i}_{NoCorr} \simeq RMS^{\it B}$, meaning that SNe Ia are intrinsically as uniform in $i_{\rm LT}$ as when corrected in B.

A side–by–side comparison of the uncorrected and corrected hubble residuals is shown in Figure 6.13 as a visual summary. We can see clearly in Figure 6.13 that the low best–fitting α and β mean that the values of the residuals only move a very small amount in $i_{\rm LT}$. This effect is exaggerated by the marked increase shown in both B and $R_{\rm P48}$. In the following section, we examine the results presented in Section 6.3 and compare them to the literature.

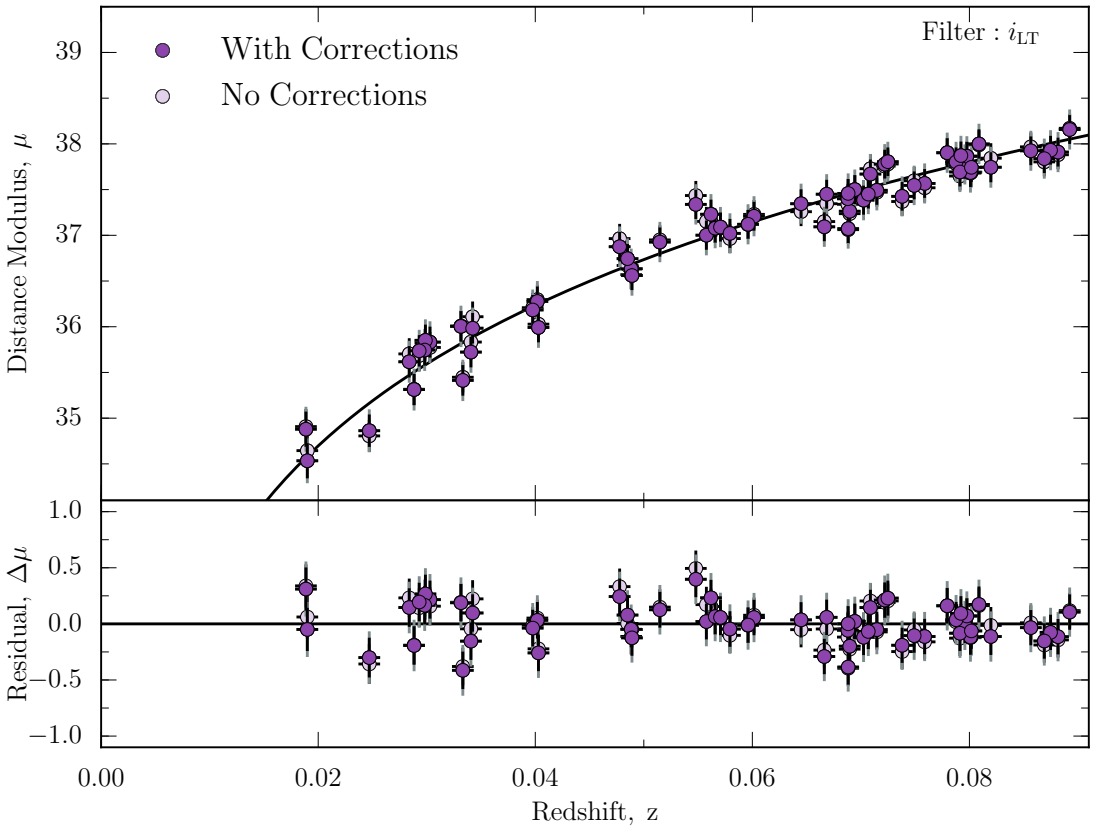

FIGURE 6.11: *Top Panel*: i_{LT} Hubble Diagram, where distance moduli calculated without correcting for lightcurve width and colour are shown as light purple, those calculated after applying the best fitting corrections are the dark purple points. *Bottom Panel*: Residuals from the standard cosmology plotted in *Top Panel*. Colour scheme is the same as above. Histograms of these points are shown in Figure 6.12

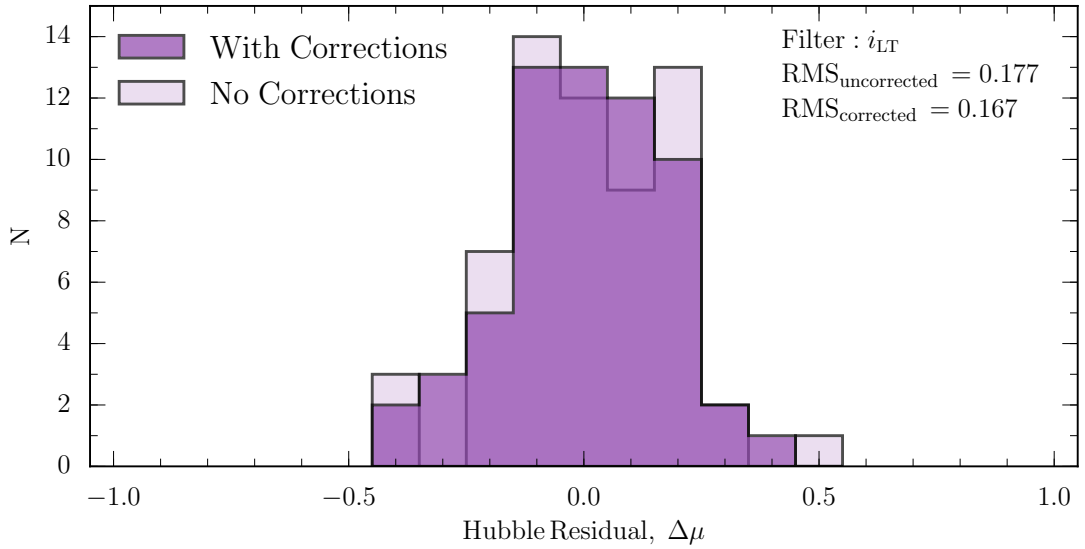

FIGURE 6.12: Histogram of i_{LT}–band residuals from the Hubble Diagram shown in Figure 6.7. The residuals from standard cosmology (see Section 6.2) for the uncorrected absolute magnitudes are shown in mauve, those calculated after applying an α and β correction (found in Table 6.2) are shown in purple.

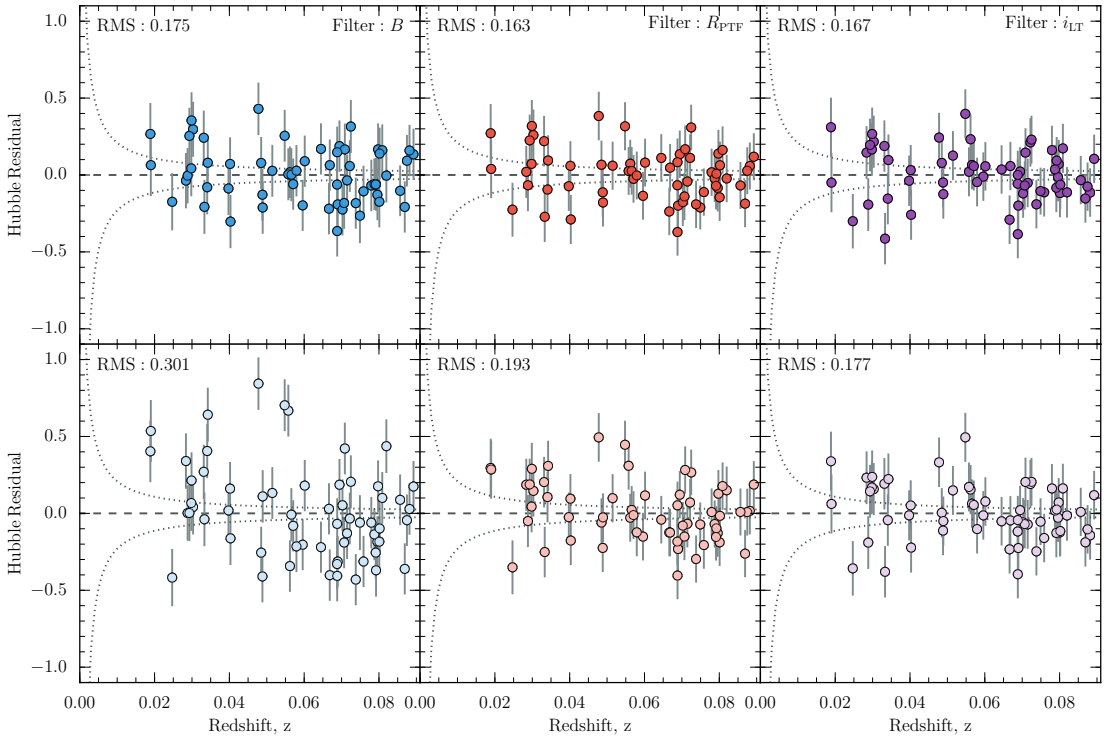

FIGURE 6.13: Hubble Residual vs z before and after stretch and colour correction, in (L-R) B, $R_{\rm P48}$ and $i_{\rm LT}$. Grey lines show the uncertainty due to peculiar velocities of $v_{pec} = 300 {\rm km\,s^{-1}}$. *Top Row*: Residuals against redshift after applying an α correction for stretch and a β correction for colour. *Bottom Row*: Residuals prior to α and β correction.

6.4.1 The Light–Curve Width Correction Parameter, α

Figure 6.14 shows the residuals in each band with a partial correction for colour (as determined by the minimisation described in Section 6.2), $\beta\mathcal{C}$ applied, and the trend with stretch remaining. The change in dependence is clearly illustrated in the lower set of panels, the slope, α goes from being significant at $> 3\sigma$ for B, to consistent with 0 in the case of $i_{\rm LT}$. In their analysis of the CSP DR1 SNe Ia Folatelli et al. (2010) observe a similar change in the correction for their decline rate parameter with wavelength; from a maximum value of $\alpha^B_{\rm CSP} = 1.07 \pm 0.11$ for their gold sample to $\alpha^i_{\rm CSP} = 0.71 \pm 0.13$ in i–band. While the use of a different method stops the direct comparison, the value of their Δm_{15} correction, $\alpha^i_{\rm CSP} = 0.71 \pm 0.13$ is inconsistent with no light–curve width correction. However, in our sample we find a value of $\alpha^i = 0.18 \pm 0.21$; that SNe are a standard candle in i–band, with respect to a stretch correction, analagous to results in J– and H–band (Barone-Nugent et al., 2012).

Betoule et al. (2014) find $\alpha^B_{\rm JLA} = 1.40 \pm 0.06$ for their full sample, double our value of $\alpha^B = 0.70 \pm 0.23$. While the uncertainty is large, this may be a result of our sample

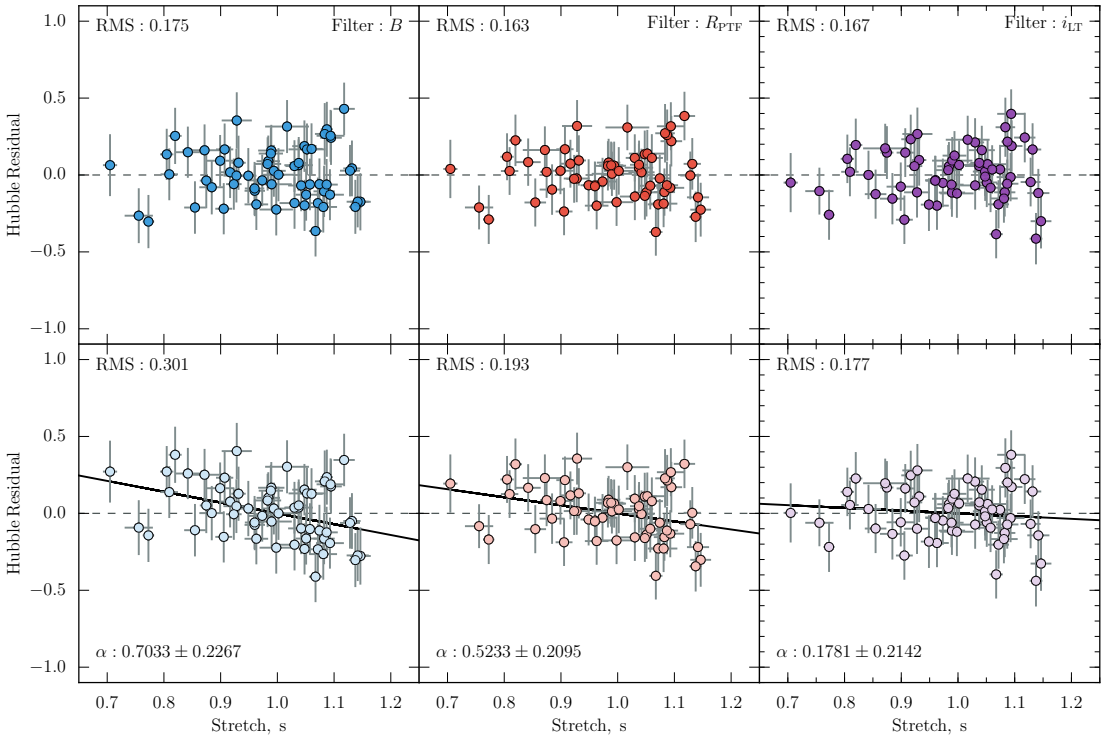

FIGURE 6.14: *Top Row*: Hubble Residuals after correction, for (L-R) B, $R_{\rm P48}$ and $i_{\rm LT}$. *Bottom Row*: Hubble Residuals partially corrected with a $\beta\mathcal{C}$ term showing a stretch dependence, the projected best fit to this relationship is plotted as a solid line with slope α.

lacking objects towards the extreme ends of the colour distribution, that could leverage the fit to higher values.

6.4.2 The Colour Correction Parameter, β

Figure 6.15 shows the residuals in each band with a partial correction for stretch, $\alpha(s-1)$ applied, and the trend with colour remaining. Consistent with our value, of Betoule et al. (2014) find $\beta_{\rm JLA} = 3.139 \pm 0.072$ but report a large degree of variation when re-analysing the sample from Conley et al. (2011), as much as 0.6 on β. They explain this by highlighting the comparable biases that can be imposed on β by changing the colour definition, training method and selection, as explored with SALT2 in Mosher et al. (2014).

Like our values of α, β shows a significant evolution from B to i, both the colour and light–curve width correction become less important as effective wavelength increases (Figure 6.15, Table 6.2). Following the analysis of Conley et al. (2007) (see also Tripp, 1998), because α absorbs the shape-colour relation, β can be considered only to apply to the colour excess of the SNe. As such, in B, if the colour excess is due to dust that behaves according to a Cardelli et al. (1989)–like extinction relation we expect

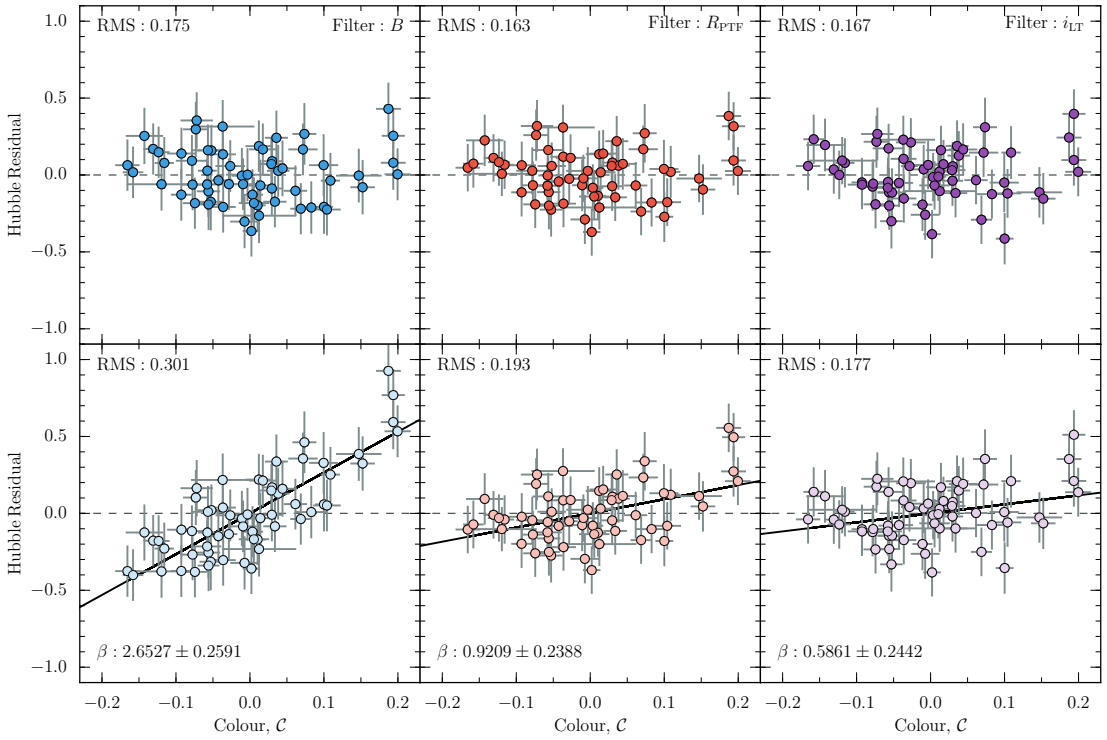

FIGURE 6.15: *Top Row*: Hubble Residuals after correction, for (L-R) B, $R_{\rm P48}$ and $i_{\rm LT}$. *Bottom Row:* Hubble Residuals partially corrected with a αs term showing a $\mathcal{C}$ dependence, the projected best fit to this relationship is plotted as a solid line with slope β.

$\beta^B = R_V + 1$ i.e ~ 4.1. Our value of $\beta^B = 2.65 \pm 0.26$ is not consistent with a SNe Ia colour law that is solely 'MW–like' dust driven at 5.6σ. This is in line with other analyses, for example Burns et al. (2014), who from a sample of 82 CSP SNe Ia find an average value of $R_V = 1.7$, equivalent to $R_B = 2.7$, consistent with our result.

If we do assume a MW–like $R_V = 3.1$, calculating the specific absorption A_λ for the effective wavelengths of $R_{\rm P48}$ and $i_{\rm LT}$ (see Section 2.4.2) predicts $\beta^R_{\rm dust} = 2.51$ and $\beta^i_{\rm dust} = 1.94$ respectively. As in the case of B, our observed β values are less than this in both cases: $\beta^R = 0.92 \pm 0.24$ and $\beta^i = 0.59 \pm 0.24$, discrepant by 6.6σ and 5.6σ respectively.

The total line of sight dust extinction is a sum of the MW, intergalactic medium (IGM), host galaxy extinction and CSM. As such there may be deviations from a MW–like extinction law if the extinction in the IGM, host and CSM is caused by dust with intrinsically different properties. To test this, we fix the dust law, assuming that $R_V = \beta^B - 1 = 1.65$, recalculating the specific absorption in this case gives $\beta^R_{\rm fix} = 1.19$ and $\beta^i_{\rm fix} = 0.78$. Our derived values of β are both lower than the predicted values, β^R is less than $\beta^R_{\rm fix}$ by 1.1σ, while β^i is more consistent, at 0.7σ. However, a value of $R_V = 1.65$ is smaller than that observed for any nearby galaxy (Draine, 2003) implying that extinction

solely due to host galaxy dust cannot adequately explain the observed colour distribution of SNe Ia.

Sullivan et al. (2011b) provide a detailed summary of the possible drivers behind variation in β and note that as well as variation in dust properties, colour variation that does not correlate with light–curve shape (Folatelli et al., 2010) such as viewing angle and SN asymmetry effects (e.g. Kasen et al., 2009; Maeda et al., 2011) as well as host type (Lampeitl et al., 2010). In addition, Sullivan et al. (2010) find that host with low specific star formation rate (sSFR; the star formation rate per unit stellar mass per year, see e.g. Guzmán et al., 1997) of ($\log(\mathrm{sSFR}) < -9.7$ year^{-1}) have a lower β than those with high sSFR ($\log(\mathrm{sSFR}) > -9.7$ year^{-1}). Low values of R_V have also been seen in a range of well studied low–redshift supernovae, notably SN 1999cl ($R_V = 1.55 \pm 0.08$ Krisciunas et al., 2006), SN 2003cg ($R_V = 1.8 \pm 0.19$ Elias-Rosa et al., 2006), SN 2002cv ($R_V = 1.59 \pm 0.07$ Elias-Rosa et al., 2008), SN 2014J ($R_V = 1.4 \pm 0.1$ Amanullah et al., 2015) and a range of values $1.7 < R_V < 3.0$ reported by Amanullah et al. (2014).

From this, we conclude that there is additional intrinsic variations in colour that are not being fully corrected for by MW–like dust, or by a width–colour relationship. This is in line with the findings of Folatelli et al. (2010), where in the CSP data, there is intrinsic dispersion of colour that correlates with peak luminosity, but not light curve width. One possibility is that the dust in the line of sight is significantly different to that in the MW and does not follow the usual law, or that there is additional scattering effects in the local region of the SN (Wang, 2005), which can dramatically decrease the observed R_V depending on the proximity to the SN. Goobar (2008) suggest the low values may be a result of multiple scatterings in dust local to the SN, preferentially attenuating shorter wavelength photons. An alternative possibility is that the SN local environment could have some effect on the intrinsic colour of a given SN, for example, as a result of metallicity variations (Timmes et al., 2003). It should also be considered that the MW, though having a mean value for $R_V = 3.1$, does itself show some degree of diversity with $2.1 < R_V < 5.8$ observed along some sight lines (see review of Draine, 2003, and references therein).

6.4.3 Spectral Features and Other Drivers of Intrinsic Colour Variation

If the colour variation is not due to dust that does not adhere to a 'normal' dust law, then the range of behaviour seen can be interpreted as being driven by the intrinsic variation of the SN itself. As we have seen in Chapter 4 and Chapter 5, the depth and distribution of IPEs throughout the ejecta can change the lightcurve morphology at

very early and post peak phases. Both of these investigations showed that there was additional behaviour that did not correlate well with light curve width. Unfortunately, there is not enough overlap in the data samples to fully investigate any relationship between these behaviours and colours.

The variation seen as a function of host type (Lampeitl et al., 2010; Sullivan et al., 2010, 2011b) if not dust driven, may have a significant contribution from the diversity in the physical charecteristics of the SN. For example, the age or metallicity of the progenitor populations has been suggested to drive the 'mass step' seen in the absolute magnitudes of SNe Ia (Sullivan et al., 2006), and a similar effect on the colour distribution and evolution is not unreasonable to suggest. Coupled with this is the theoretical prediction that signifiant asymmetries in the explosion adds diversity in SN colour (Kasen et al., 2009; Maeda et al., 2011), which as well as varying from event to event, may be more prevalent in some explosion models (Ruiz-Lapuente, 2014).

As shown in Figures 1.2 and 2.1 the dominant spectral features for $R_{\rm P48}$ and $i_{\rm LT}$ are Si λ6150 and Ca II IR triplet respectively. The relatively small corrections for both stretch and colour in these bands indicates that the diversity in these features is relatively small. The presence of additional features that anomalously complicate the line evolution, such as Si II and Ca II HVFs (Childress et al., 2014; Maguire et al., 2014), seem to either be avoided through our cuts, or subdominant to other sources of uncertainty not characterised by stretch and C. It should be noted that in most cases, such features are fade early, before the main peak of the lightcurve, and as such may not be able to strongly effect light curve shape in the region our fitting is most sensative.

Work in measuring the ejecta velocity (of the bulk ejecta, rather than just the HVFs) appears to show that at fixed absolute magnitude, SNe that have higher velocities have redder colours Foley & Kasen (2011). The physical interpretation of this is that the high velocity SNe, defined as those with $v_{SiII}(\tau = 0) > 11,800\text{km s}^{-1}$ suffer enhanced line blanketing at bluer wavelengths. This is due to the rapidly expanding outer layers being cooler than the equivalent mass co-ordinates in low velocity events, resulting in a higher number of optical lines from lowe excitation IPEs. When considering the blue, the magnitude of correction in B–band suggests that there is a deal of spectral diversity, which is well captured by the corrections, raising the possibilty that the dispersion that we see is driven by different spectral features.

6.4.4 RMS Scatter

Our RMS values compare favourably with those in the literature (Kessler et al., 2009; Folatelli et al., 2010; Conley et al., 2011; Freedman et al., 2009), particularly as noted

above, we do not fit for a particular cosmology or apply a Malmquist correction, both of which would act to decrease our RMS. With additional efforts, beyond the scope of this work, further improvements should be possible. For instance, Sullivan et al. (2010) found evidence for a dependence on host galaxy mass – finding SNe Ia of the same stretch and colour to be brighter in more massive hosts ($log(M_{stellar}) > 10M_{\odot}$). As such it is possible to fit two different values of absolute magnitude, $\mathcal{M}_j$, a 'mass–step' luminosity function, when taking into account host galaxy properties (c.f. Sullivan et al., 2010; Childress et al., 2013b). There is a significant overlap in our sample of objects, and the in depth host galaxy analysis of Pan et al. (2014).

Further gains in improving the observed scatter may be found in improving the quality of some light curve fits. SiFTO was not trained on i–band data, and as a result, some of the SN light curve fits have suffered terminal failures in $i_{\rm LT}$ and $R_{\rm P48}$. Examples of such SN fit failures can be seen in Figure 6.16, showing evidence of pathological problems which result in erroneous SN peak magnitude measurements and colours, and the cases shown, removal from our sample. In addition, SiFTO does not provide a treatment of the secondary maximum (see Chapter 5). New templates are needed, and incorporating a functional relationship between the SN properties such as stretch and colour and the secondary maximum require a fundamental shift in how the light curve fitting package operates, and would constitute a significant undertaking.

6.4.5 Using an $R-i$ Colour correction

As the magnitude of the colour correction is small in the case of $i_{\rm LT}$, we explore the possibility that there is a stronger dependence on a different parameter. Additionally, if a correction based on red colours can be made, a significant overhead can be reduced in observations, and in the uncertainty in estimation of rest–frame blue optical colours. To this end, we repeated our methodology using $(R-i)$ colour excess, instead of $\mathcal{C}$, a $(B-V)$ estimator. Essentially, we re-cast Equation 6.1 as

$$m_j^{mod} = 5\log_{10}\mathcal{D}_{\mathcal{L}}(\mathrm{z_{hel}}, \mathrm{z_{cmb}}, \mathrm{w}, \Omega_{\mathrm{m}}, \Omega_{\mathrm{DE}}, \Omega_{\mathrm{k}}) - \alpha_{\mathrm{j}}(\mathrm{s}-1) + \beta_{\mathrm{j}}(\mathrm{R}-\mathrm{i}) + \mathcal{M}_{\mathrm{j}}; \qquad (6.5)$$

the results of this analysis can be seen in Table 6.3.

Figure 6.17 shows the difference in colour correction between using a $\mathcal{C}$ and $(R-i)$ colour parameter for B–band. As we have re–run the analysis, we find different values for α, β and $\mathcal{M}$. The slope of the colour relation β in both methods is positive, but the value of $\beta^B(R-i)$ is less than that of $\beta^B(C)$ by 1.3σ; there is also a greater degree of rms scatter following the $(R-i)$ correction in B. The rms scatter beforehand however, cannot be reliably used between samples because $(R-i)$ colour is not centred around

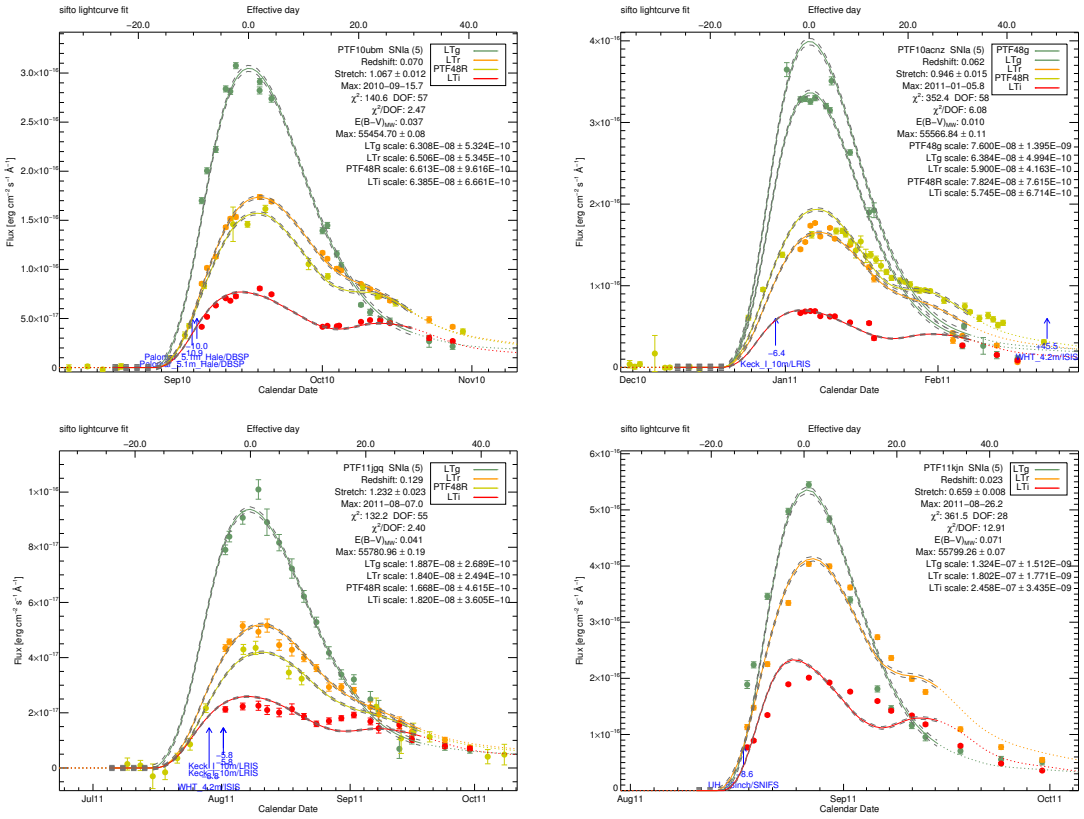

FIGURE 6.16: SiFTO light curve fits of SNe Ia PTF 10ubm, PTF 10acnz, PTF 11jgq and PTF 11kjn. Each of these SNe shows failures in either $R_{\rm P48}$or $i_{\rm LT}$fitting, or both. This is largely a result of the rigid template SiFTO uses for the post maximum behaviour in these bands, and the lack of training in red wavebands.

TABLE 6.3: Table of results for B, $R_{\rm P48}$ and $i_{\rm LT}$, showing the best fit correction coefficients α and β, the intrinsic dispersion, $\sigma_{\rm int}$ and absolute magnitude, $\mathcal{M}$ derived using an $(R-i)$ colour, rather than $\mathcal{C}$ (Equation 6.5). In addition, the root mean square values of the residuals, both before ($\rm RMS_{NoCorr}$), and after (RMS) are shown.

Band	α	β	M	σ_{int} (mag)	$\rm RMS_{NoCorr}$ (Uncorrected)	RMS (Corrected)
B	0.13 ± 0.35	2.03 ± 0.40	-18.47 ± 0.12	0.23	0.635	0.248
$R_{\rm P48}$	0.29 ± 0.24	0.80 ± 0.27	-18.85 ± 0.08	0.16	0.287	0.174
$i_{\rm LT}$	0.40 ± 0.25	-0.40 ± 0.28	-18.90 ± 0.08	0.16	0.216	0.175

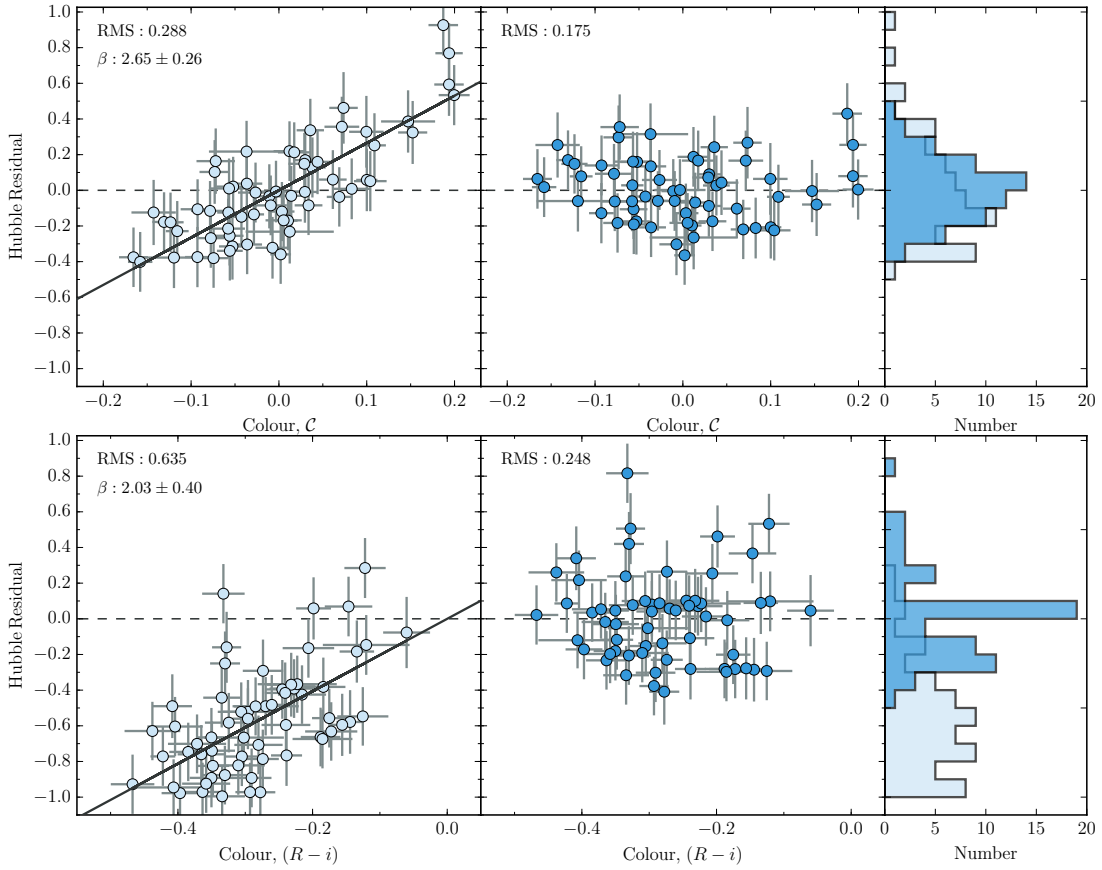

FIGURE 6.17: Residuals Comparing $\mathcal{C}$ vs $R-i$ Colour Corrections for B–band. *left panel*: light points show the residual before making a colour correction. The solid line is not a fit to this data, but is a projection of the plane fitted to the data in colour–stretch space (Section 6.2) to minimise Equation 6.2. *Middle panel*: The dark points show the residual following the colour correction. *Right panel*: Histogram of the residuals shown in the left and middle panels.

zero, like $\mathcal{C}$. We can however compare the Pearsons correllation coefficient, $P^{\mathcal{C}} = 0.78$ and $P^{(R-i)} = 0.4$, demonstrating a weaker relationship. Given that $\mathcal{C}$, as an estimator of $(B-V)$ colour, overlaps with B and as such contains more information about that region in the SED as than $(R-i)$, this may indicate that the diversity seen in B is disctinct from that seen in R and i.

Moving onto R–band, Figure 6.18 exhibits the same behaviour, despite the band being included in the colour measurement. The final RMS is an improvement on the rms scatter in B corrected using $(R-i)$, but still some way short of that found for the same band using $\mathcal{C}$, at $\mathrm{RMS}^{R}_{(R-i)} = 0.174$ compared to $\mathrm{RMS}^{R}_{\mathcal{C}} = 0.163$.

For both B and R_{P48}, the strength of the correction with $(R-i)$ is comparable to that made using $\mathcal{C}$. However, when we consider i_{LT} in Figure 6.19, the correction has changed in sign from negative to positive between the cases $\mathcal{C}$ and $R-i$. This is an unexpected

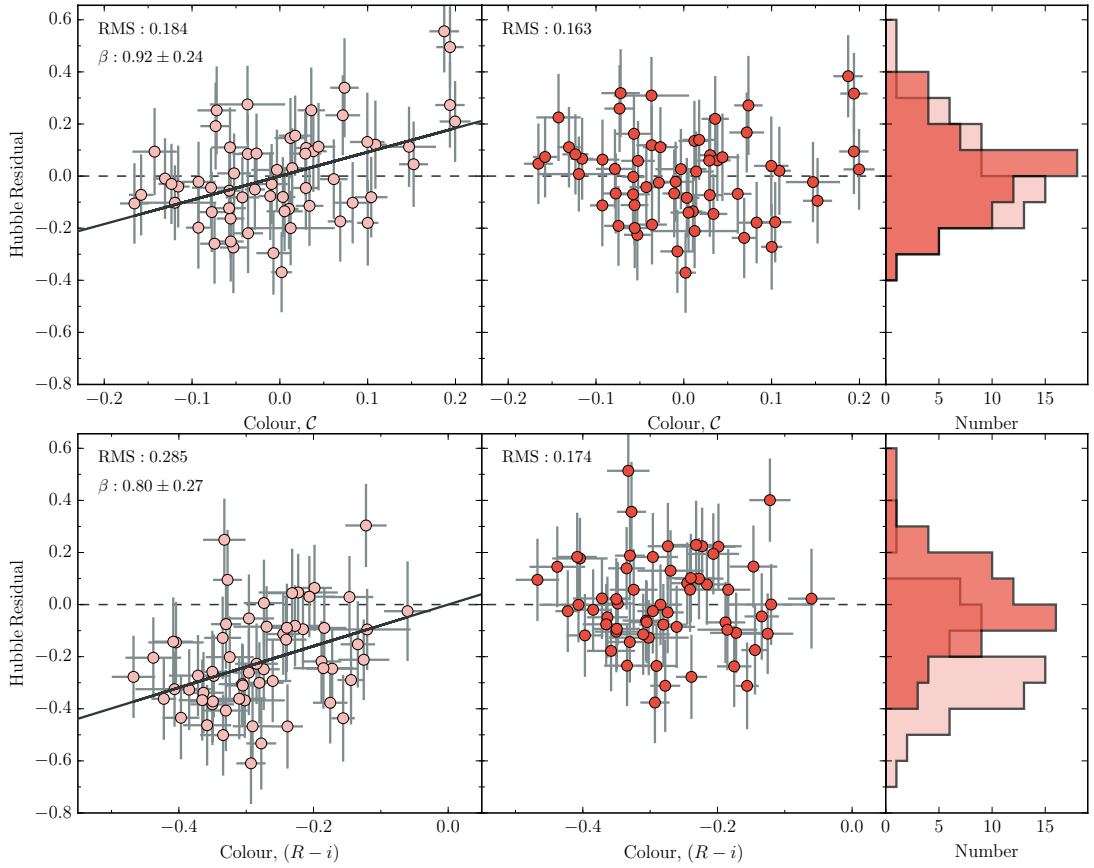

FIGURE 6.18: Residuals Comparing $\mathcal{C}$ vs $R-i$ Colour Corrections for $R_{\rm P48}$. *left panel*: light points show the residual before making a colour correction. The solid line is not a fit to this data, but is a projection of the plane fitted to the data in colour–stretch space (Section 6.2) to minimise Equation 6.2]. *Middle panel*: The dark points show the residual following the colour correction. *Right panel*: Histogram of the residuals shown in the left and middle panels.

result and implies that SNe which have redder $R-i$ colours are more luminous in i–band, the opposite of the standard bluer-brighter relationship. However, it should be noted that the trend only deviates from 0 by 1.4σ, perhaps indicating, as is the case with using $\mathcal{C}$, that no colour correction is required.

6.5 Conclusions

In this chapter we construct a series of Hubble Diagrams, using B, $R_{\rm P48}$and $i_{\rm LT}$from a sub sample of PTF SNe Ia with multicolour followup data from the LT. We find:

- Low values of the light–curve width correction parameter α in all filters, relative to those found in the literature for cosmological samples. However we observe a marked decrease with increased wavelength, as seen in other work. In $i_{\rm LT}$our value

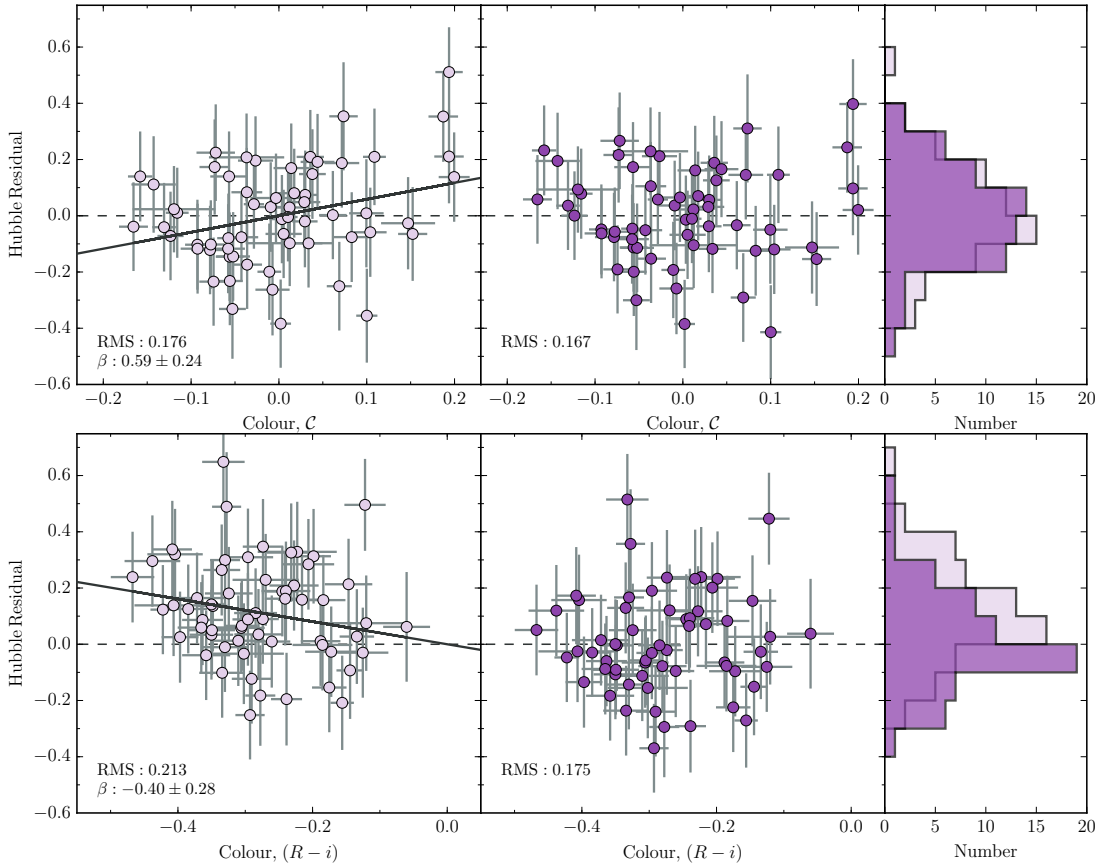

FIGURE 6.19: Residuals Comparing $\mathcal{C}$ vs $R-i$ Colour Corrections for $i_{\rm LT}$. *left panel*: light points show the residual before making a colour correction. The solid line is not a fit to this data, but is a projection of the plane fitted to the data in colour–stretch space (Section 6.2) to minimise Equation 6.2]. *Middle panel*: The dark points show the residual following the colour correction. *Right panel*: Histogram of the residuals shown in the left and middle panels.

of $\alpha_i = 0.18 \pm 0.21$ is constent with zero, making SNe Ia in i–band a standard candle with respect to stretch.

- A value of β^B consistent with the current best measurements. We also obseve a trend of smaller β values with increased effective wavelength.

- Values of β that are not consistent with a Milky–Way–like dust law. Our result of $\beta^B = 2.65 \pm 0.26$ is not consistent with a SNe Ia colour law that is solely 'MW–like' dust ($R_B = 4.1$) at 5.6σ. We find similar deviations of 6.6σ and 5.6σ in $R_{\rm P48}$ and $i_{\rm LT}$respectively.

- For our sample $R_V = 1.65$, is not consistent with literature measurements of dust in the local universe, hinting at additional contributions to the behaviour of observed SNe Ia colour.

- When re–scaling the total–to–selective absorption ratio to $R_V = 1.65$, with a fiducial Cardelli et al. (1989) extinction law we find the wavelength evolution of the law to slightly overestimate β^R at 1.1σ and β^i by 0.7σ.

- We interpret this as additional evidence that either the dominant source of extinction (either in the SN hosts or IGM) follows a profoundly different dust law, or that the variation we see is due to intrinsic SN colour variations. We find it is likely that there is a contribution to the variation is driven both by dust, and intrinsic variation.

- We find some evidence, by using $(R-i)$ colour correction of colour variation that is not encapsulated within a $B-V$ colour correction $\beta\mathcal{C}$. However, correcting using this parameter instead of $\mathcal{C}$ does not improve the degree of standardisation. In i–band, we find evidence of a redder SNe in $R-i$ are brighter than their bluer counterparts, contrary to the relationship seen for $B-V$.

- We find that SNe Ia in i are superior standardardisable candles to the same SNe in B. Even the uncorrected i–band RMS values are comparable to those for B after light–curve width and colour correction. Overall, we find the lowest scatter in $R_{\rm P48}$.

- The minor best fit stretch and colour corrections in i–band imply that SNe Ia are a near–perfect standard candle at these wavelengths.

This concludes our final science chapter, we now move on to conclude the thesis.

Chapter 7

Conclusion

'And so, as we obliterize this star, let us remember those immortal words once spoken by a great man, moi. And I quote; "All good things must come to an end, preferably in a humongous explosion."'

Cpt. Zapp Brannigan, *Futurama, Into The Wild Green Yonder*

7.1 Main Conclusions

In this thesis, we leveraged the properties of the large imaging and spectroscopic astrophysical dataset provided by the Palomar Transient Factory (PTF) to explore the physical processes that underpin Type Ia supernovae (SNe Ia). This work in this thesis has covered the very earliest part of the SN Ia light curve, probing the ejecta structure, the post–maximum light curve, probing the ^{56}Ni distribution, and the utility of SNe Ia as standard candles at different wavelengths. Below we summarise our results.

7.1.1 Rise Times

In Chapter 4 we used 18 type Ia supernovae (SNe Ia) from PTF and the La Silla-QUEST variability survey (LSQ) to measure the rise time ($t_{\rm rise}$) (the time between first light t_0, and maximum light t_{max}) and rise index (n), where $f = (t - t_0)^n$. We find significant diversity at early times, $t < t_{0.5}$, where $t_{0.5}$ is the time at which the SNe reaches half of its maximum. We find:

- The rise index, n, of our sample showed significant variation ($1.48 \leq n \leq 3.70$), with the mean of the distribution $n = 2.44 \pm 0.13$, and $n = 2.5 \pm 0.13$ when

correcting to a pseudo-bolometric value, both inconsistent with a simple fireball model ($n = 2$) at a 3σ level. We found that when the rise index is allowed to vary with time from $n = 2$, $\dot{n}$ is on average positive, with an mean value of $\dot{n} = 0.011 \pm 0.004$ day^{-1}. We find that SN discovered later after first light have, in general a larger value of n, whereas those discovered soonest after t_0 have lower values, supporting the use of a time dependant n.

- The average $t_{\rm rise}$ of our sample is $t_{\rm rise} = 18.98 \pm 0.54$ days, ~ 1 day longer than would ordinarily be found by enforcing $n = 2$, $t_{\rm rise}(n = 2) = 17.86 \pm 0.42$ days. The broadest light curves have a $t_{\rm rise}$ that is faster than that of our stretch-corrected light curve template, which enforces $n = 2$ in its construction. In contrast to current two-stretch fitting methods, which separate the light curve into the pre- and post-maximum sections ($t < t_{max}$ and $t > t_{max}$ respectively), the most significant variation occurs at the very earliest epochs ($t < t_{0.5}$ or phases $\tau < -10$ days).

- We therefore decouple the rise time into two components: t_1 (where $t_1 = t_{0.5} - t_0$) and t_2 (where $t_2 = t_{max} - t_{0.5}$). These time-scales are not correlated with each other; furthermore t_2 is strongly correlated with stretch, whereas t_1 is not. As a result, correcting using a single stretch is ineffective in reducing the dispersion in the earliest portion of the light curve. These two regions are separated by the approximate location of the point at which energy deposition and radiation are equal, meaning that the physical conditions are distinct.

- Using models from Piro & Nakar (2013), we show that potential variation in the shape of the ^{56}Ni distribution within the SN ejecta can explain the measured range of n and $t_{\rm rise}$.

- Considering the prediction of Arnett et al. (2016) that $\dot{n}$ should be negative for early time variation as a result of non-homologous expansion, we conclude that this is not the main source of diversity in our observations, as we find $\dot{n}$ is positive.

- SNe Ia showing evidence of strong interaction with circumstellar material (CSM) have long rise times. However a notable member of this subclass, PTF11kx, has an extremely short rise, $t_{\rm rise} = 14.5 \pm 0.5$ days, when fitted with a fireball model ($n = 2$). This implies that PTF 11kx is not only unusual for a SNe Ia, it is also perculiar within its Ia CSM subclass.

7.1.2 The Post-Maximum Light Curve Diversity in SNe Ia from PTF

In Chapter 5 we used 31 SNe Ia from the PTF to explore the diversity of the post-maximum phases in R–band. Using a modified SiFTO template fit, the secondary

'shoulder' present on the $R_{\rm P48}$ light curve was fitted as an additional gaussian component. To compare to previous work, the mean integrated model flux over two phase ranges $15 \leq \tau \leq 35$ and $20 \leq \tau \leq 40$ for $\langle R_{\rm P48}\rangle_{15-35}$ and $\langle R_{\rm P48}\rangle_{20-40}$ respectively, was calculated. The fitted parameters for the strength F_g, timing τ_g, and duration σ_g of the secondary emission were considered against the light–curve width of the SNe. Are main findings are as follows:

- The correlation between light curve width and mean integrated flux in i-band, $\langle i\rangle_{20-40}$, first found by Krisciunas et al. (2001) was seen in the equivalent parameters $\langle R_{\rm P48}\rangle_{15-35}$ and $\langle R_{\rm P48}\rangle_{20-40}$. However, this was found to be a reflection of the width luminosity relationship.
- The F_g parameter, which quantifies the strength of the feature, has a median value $\hat{F}_g = 0.134$ and a standard deviation $S = 0.031$. Like the stretch corrected $\langle R_{\rm P48}\rangle$ parameters F_g is shown to be greater for narrower, less luminous SNe Ia - the opposite behaviour to that seen in the corresponding NIR secondary maximum.
- The σ_g parameter, which measures the duration of the secondary has a median value $\widehat{\sigma_g} = 5.32$ days and is not found to depend strongly on light curve width. However the timing of the peak in the underlying emission, τ_g *is* found to have a strong correlation ($R = 0.87$) with stretch.
- Measuring the strength of the feature using the area under the gaussian, A_g gives a median value $\hat{A}_g = 1.35$ and standard deviation $S = 0.39$. As with the mean integrated flux, $\langle R_{\rm P48}\rangle$ this does not correlate with light curve shape.

7.1.3 Multi–Colour Low-Redshift Hubble Diagrams From PTF

In Chapter 6 we constructed a series of Hubble Diagrams, using observations of 60 SNe Ia B, $R_{\rm P48}$and $i_{\rm LT}$from a sub sample of PTF SNe with multicolour followup data from the LT. We derived values of the light–curve width correction parameter α and colour correction parameter β in each band, and an effective total–to–selective absorption ratio R_V. Overall, we found:

- Low values of α in all filters, relative to those found in the literature for cosmological samples. We observe a marked decrease with increased wavelength, as seen in other work. In $i_{\rm LT}$ our value of $\alpha_i = 0.18 \pm 0.21$ is constent with zero, making SNe Ia in i–band a standard candle with respect to stretch.
- A value of β^B consistent with the current best measurements. We also obseved a trend of smaller β values with increased effective wavelength. Our values of

β are not consistent with a Milky–Way–like dust law ($R_B = 4.1$); our result of $\beta^B = 2.65 \pm 0.26$ is not consistent with a SNe Ia colour law that is solely 'MW–like' dust at 5.6σ. We found similar deviations of 6.6σ and 5.6σ in $R_{\rm P48}$ and $i_{\rm LT}$respectively.

- For our sample $R_V = 1.65$, is not consistent with literature measurements of dust in the local universe, hinting at additional contributions to the behaviour of observed SNe Ia colour. Even when re–scaling the total–to–selective absorption ratio to $R_V = 1.65$, with a fiducial Cardelli et al. (1989) extinction law we found the wavelength evolution of the law to slightly overestimate β^R at 1.1σ and β^i by 0.7σ. We interpreted this as additional evidence that either the dominant source of extinction (either in the SN hosts or IGM) follows a profoundly different dust law, or that the variation we see is due to intrinsic SN colour variations.

- Some evidence, by using $(R - i)$ colour correction, of colour variation that is not encapsulated within a $B - V$ colour correction $\beta\mathcal{C}$. However, correcting using this parameter instead of $\mathcal{C}$ does not improve the degree of standardisation. In i–band, we found evidence of a redder SNe in $R - i$ are brighter than their bluer counterparts, contrary to the relationship seen for $B - V$.

- That SNe Ia in i are superior standardardisable candles to the same SNe in B. Even the uncorrected i–band RMS values are comparable to those for B after light–curve width and colour correction. Overall, we derive the lowest scatter in $R_{\rm P48}$ but the smaller best fit stretch and colour corrections in i–band imply that SNe Ia are a near–perfect standard candle at these wavelengths.

7.2 Overall Overview and Further Work

In this work we have explored the observed diversity of SNe Ia at early times and after maximum, and extracted physical meaning from our observations. We have also utilised the most well known quality of these objects, their standardisability, to construct low–redshift hubble diagrams, demonstrating that the magnitude of their corrections decrease as a function of wavelength.

Taking this work forwards, ongoing and upcoming high-redshift programs such as the Dark Energy Survey (DES; Flaugher et al., 2015) supernova program (DES-SN)/VISTA Extragalactic IR Legacy Survey (VEILS) and the Wide–Field IR Survey Telescope (WFIRST), will observe IR bands for SNe at $z \sim 0.5 - 1.2$ that correspond to rest–frame i–band, e.g in Y and J with VISTA. Upcoming experiments such as Euclid, LSST, Zwicky Transient Factory (ZTF) and associated followup campaigns will observe

an unprecedented number of SNe with sufficiently high S/N at high cadence to test the findings in this work by constructing samples an order of magnitude larger than those in this work. Dealing with this volume of data in itself will present its own challenge.

Further work analysing the very early time emission of SNe Ia should concentrate on better quantifying the variation, and on which other observable quantities it depends. For this, a large sample of SNe Ia with high quality multicolour photometric and spectroscopic time series data must be assembled. The presence of high velocity features, Si II velocities and colour evolution may all hold valuable information, particularly if the variation at very early times is misunderstood when used for cosmology, for instance when fitting templates. As we have seen, the rising light of a SNe Ia cannot and should not be assumed to follow a fireball model, and as such, any templates used for fitting SNe Ia should not parameterise the early times in this way. Doing so may change the length of the rise by 5%, potentially skewing high redshift cosmological analyses or calculations of SNe Ia rates.

As we consider t_{ex} and t_0 distinct, the use of alternative methods of measuring the time of explosion, such as by fitting a time series of spectral velocities or though full abundance tomography, would enable greater exploration of the 'dark phase' between explosion and first light. This should be closely linked to the ejecta stratification and the distribution of ^{56}Ni - the same factors that are at least partially responsible for the variation we see in n and $t_{\rm rise}$. Building up a statistically meaningful sample of such data would enable significant constraints to be placed on models.

Deviations from a power–law rise, that have been explored in a small number of well observed SNe by fitting broken powerlaws and in this work as a time dependent power–law should continue to be scrutinised. Our finding that on average n is inconsistent with the commonly used fireball model implies that the current understanding of the ^{56}Ni distribution or shock velocity through the ejecta is incomplete, and that more complex physically motivated parameterisations may be needed in future. Development of a self consistent parameterisation that can be used to fit light curves at these epochs, or the use of radiative transfer to make inferences about the very early emission would be tremendously powerful.

Our finding that the behaviour of the secondary in R is inverse to that seen in near-IR implies Si II 6150Å evolution is just as important for the characteristics of the R-band light curve shoulder as the contribution from Fe-peak elements undergoing a ionisation change, particularly for low-stretch objects. However, significant changes to post-maximum morphology can be simulated by changing the metallicity, or the viewing angle. This may be tested by studying supernovae with good very early time coverage, polarimetry, $r - i$ colour evolution and analysis of nebular spectra. A slightly more

immediate, but still involved path may lie in extending our method to our LT i-band sample. As both the behaviour at early times, and post maximum in R is driven in some way by the distribution of IPEs thoughout the ejecta, any combined dataset that can provide both early time data and good multicolour post–maximum coverage *for the same SNe* will have considerable impact on our understanding of ejecta physics.

In our construction of low–redshift hubble diagrams we do not allow our parameters to vary as a function of host galaxy stellar mass (cf. Sullivan et al., 2010) or Si II velocity. Including these corrections in our fitting, as well as making a Malmquist correction should serve to reduce the observed scatter in our diagrams and this is likely to be the subject of further work. As we showed in our analysis of the post–maximum diversity, the SiFTO templates could be improved during the phase of the secondary maximum by taking into account the observed SN–to–SN variation. As well as being physically interesting to examine the characteristics of the secondary as function of other observables, such a discovery woud enable us to further increase the fidelity of our light–curve fitting. Additionally, such corrections will facilitate a full low–redshift cosmological fit. Improving the quality of our low-redshift i–band hubble diagram will allow future, high–redshift restframe i–band observations to be anchored at low redshift, calibrating and combining the samples is likely to present a considerable undertaking.

Appendix A

Late Time Decline Assuming Full Trapping

In this section, using a number of simplifying assumptions, we derive the slope of the SNe Ia radioactive decay tail, γ.

Starting from the decay equation, which gives the number of nuclei, N, at some time t

$$N(t) = N_0 e^{-\frac{t}{\tau}} \tag{A.1}$$

where N_0 is the initial number of nuclei at time $t = 0$, and τ is the mean lifetime, related to the half-life, $t_{1/2}$, and the decay constant λ by

$$\tau = \frac{1}{\lambda} = \frac{t_{1/2}}{\ln(2)}. \tag{A.2}$$

Assuming constant trapping, the luminosity is proportional to the rate of decays

$$L(t) \propto N_0 e^{-\frac{t}{\tau}}. \tag{A.3}$$

If we assume that a single isotope is the dominant source of emission (^{56}Co in this case), which should be a good approximation at times much later than explosion $t >> t_{exp}$, we can take N_0 as constant, such taking the log of both sides, and converting from $\log_e$ to $\log_{10}$ gives

$$log_{10}(L(t)) \propto -\frac{t}{\tau}. \tag{A.4}$$

Magnitudes are defined as

$$m = -2.5\log_{10}(L) + const, \tag{A.5}$$

so substituting in Equation A.4 gives

$$m(t) = 2.5 \times -\frac{t}{\tau} + const. \tag{A.6}$$

for ^{56}Co, $\tau = 111.38$days, so we arrive at

$$\gamma = \frac{2.5}{111.38} = 0.0224\text{mag day}^{-1} \tag{A.7}$$

for an estimate of the linear decline of SNe Ia at late times, assuming constant trapping and that the dominant source of energy is ^{56}Co decay.

Appendix B

PTF SNe Ia Observational Parameters and Samples

In this appendix we present observational parameters, and flags indicating inclusion in subsamples, of all the PTF SNe Ia used in this work and those selected for followup on the Liverpool Telescope, See Table B.1 on the following pages.

TABLE B.1: PTF SNe Ia Observational Parameters and flags for presence in our three samples

SN	Redshift, z	E(B-V), mag	$t_{\max}$ MJD (days)	Stretch, s	$\mathcal{C}$	Rise time	Post Maximum	Hubble Diagram
PTF09alu	0.071 ± 0.001	0.011	55027.59 ± 0.12	0.76 ± 0.02	–	–	Y	–
PTF09aro	0.085 ± 0.001	0.017	55028.20 ± 0.14	1.11 ± 0.01	–	–	Y	–
PTF09cbu	0.056 ± 0.001	0.048	55036.64 ± 0.24	1.06 ± 0.04	–	–	Y	–
PTF09dlc	0.067 ± 0.001	0.054	55073.83 ± 0.11	1.04 ± 0.03	-0.17 ± 0.02	–	–	Y
PTF09dnl	0.019 ± 0.001	0.043	55074.71 ± 0.09	1.08 ± 0.02	0.07 ± 0.02	–	–	Y
PTF09dnp	0.037 ± 0.001	0.018	55070.83 ± 0.17	0.92 ± 0.03	-0.29 ± 0.03	–	–	–
PTF09dsy	0.013 ± 0.001	0.060	55070.41 ± 0.10	0.79 ± 0.01	–	Y	–	–
PTF09fox	0.071 ± 0.001	0.080	55132.51 ± 0.15	1.03 ± 0.03	0.01 ± 0.02	–	–	Y
PTF09foz	0.049 ± 0.001	0.033	55131.64 ± 0.12	0.85 ± 0.02	0.08 ± 0.02	–	–	Y
PTF10aaiw	0.059 ± 0.001	0.123	55517.11 ± 0.15	1.08 ± 0.02	0.50 ± 0.02	–	–	–
PTF10aaju	0.079 ± 0.001	0.032	55510.48 ± 0.24	1.03 ± 0.05	–	–	Y	–
PTF10accd	0.030 ± 0.001	0.129	55555.74 ± 0.10	1.09 ± 0.01	-0.07 ± 0.02	Y	–	Y
PTF10acnz	0.063 ± 0.001	0.012	55566.84 ± 0.11	0.95 ± 0.01	-0.11 ± 0.01	–	Y	–
PTF10bjs	0.030 ± 0.001	0.018	55261.42 ± 0.17	1.12 ± 0.02	-0.15 ± 0.02	–	–	–
PTF10cwm	0.081 ± 0.001	0.019	55271.17 ± 0.89	1.14 ± 0.11	–	–	Y	–
PTF10cxk	0.017 ± 0.001	0.009	55276.12 ± 0.14	0.73 ± 0.02	–	–	Y	–
PTF10duy	0.080 ± 0.001	0.013	55283.19 ± 0.22	1.15 ± 0.03	–	–	Y	–
PTF10duz	0.061 ± 0.001	0.024	55285.03 ± 0.22	0.99 ± 0.05	–	Y	–	–
PTF10gjx	0.077 ± 0.001	0.034	55325.65 ± 0.14	1.01 ± 0.03	–	–	Y	–
PTF10glo	0.076 ± 0.001	0.021	55321.51 ± 0.34	1.22 ± 0.04	–	–	Y	–
PTF10hmc	0.073 ± 0.001	0.020	55341.82 ± 0.28	1.08 ± 0.03	-0.16 ± 0.03	–	–	–
PTF10hml	0.055 ± 0.001	0.014	55352.15 ± 0.11	1.05 ± 0.02	–	Y	Y	–
PTF10hmv	0.033 ± 0.001	0.020	55351.57 ± 0.11	1.16 ± 0.01	-0.05 ± 0.25	–	Y	–
PTF10hyv	0.090 ± 0.001	0.022	55350.93 ± 0.24	1.14 ± 0.03	–	–	Y	–
PTF10iyc	0.055 ± 0.001	0.016	55361.69 ± 0.27	1.12 ± 0.03	–	Y	–	–

PTF10jdw	0.077 ± 0.001	0.014	55365.99 ± 0.25	0.93 ± 0.04	0.65 ± 0.04	–	–	–
PTF10jtp	0.067 ± 0.001	0.055	55363.84 ± 0.20	0.87 ± 0.02	0.04 ± 0.03	–	–	–
PTF10kdg	0.063 ± 0.001	0.019	55369.87 ± 0.12	0.94 ± 0.02	–	–	Y	–
PTF10kiw	0.069 ± 0.001	0.018	55368.66 ± 0.24	1.07 ± 0.04	–	–	Y	–
PTF10lxp	0.088 ± 0.001	0.013	55380.91 ± 0.12	1.01 ± 0.02	–	–	Y	–
PTF10mwb	0.030 ± 0.001	0.030	55390.63 ± 0.17	0.93 ± 0.03	-0.07 ± 0.02	–	–	Y
PTF10nkd	0.069 ± 0.001	0.014	55389.72 ± 0.62	0.90 ± 0.09	–	–	–	–
PTF10ois	0.173 ± 0.001	0.066	55397.34 ± 0.67	1.15 ± 0.08	0.01 ± 0.07	–	–	–
PTF10osn	0.037 ± 0.001	0.042	55397.69 ± 0.42	0.81 ± 0.05	–	–	–	–
PTF10pvi	0.079 ± 0.001	0.054	55409.99 ± 0.20	1.06 ± 0.02	-0.06 ± 0.02	–	–	Y
PTF10qjl	0.058 ± 0.001	0.041	55418.52 ± 0.11	1.13 ± 0.02	-0.06 ± 0.01	–	–	Y
PTF10qjq	0.029 ± 0.001	0.028	55421.03 ± 0.10	0.95 ± 0.01	-0.01 ± 0.01	–	–	Y
PTF10qkf	0.080 ± 0.001	0.048	55413.48 ± 0.27	1.05 ± 0.03	0.02 ± 0.02	–	–	Y
PTF10qkv	0.061 ± 0.001	0.046	55413.69 ± 0.26	0.99 ± 0.03	0.28 ± 0.02	–	–	–
PTF10qky	0.074 ± 0.001	0.097	55420.42 ± 0.11	1.07 ± 0.02	-0.07 ± 0.02	–	–	Y
PTF10qly	0.084 ± 0.001	0.041	55412.12 ± 0.41	1.01 ± 0.04	0.29 ± 0.04	–	–	–
PTF10qny	0.033 ± 0.001	0.111	55418.52 ± 0.21	1.01 ± 0.02	0.05 ± 0.02	–	–	–
PTF10qsc	0.087 ± 0.001	0.044	55422.16 ± 0.27	1.08 ± 0.02	-0.04 ± 0.02	–	–	Y
PTF10qwg	0.070 ± 0.001	0.030	55424.27 ± 0.26	1.00 ± 0.03	0.10 ± 0.02	–	–	Y
PTF10qwm	0.100 ± 0.001	0.112	55424.58 ± 0.37	1.11 ± 0.03	0.04 ± 0.02	–	–	–
PTF10rbc	0.088 ± 0.001	0.054	55425.36 ± 0.26	0.99 ± 0.02	-0.05 ± 0.02	–	–	Y
PTF10rbp	0.078 ± 0.001	0.053	55430.49 ± 0.12	1.04 ± 0.02	0.01 ± 0.02	–	–	Y
PTF10rcg	0.080 ± 0.001	0.073	55430.41 ± 0.13	1.14 ± 0.02	0.03 ± 0.02	–	–	Y
PTF10rgn	0.092 ± 0.001	0.050	55428.86 ± 0.14	1.01 ± 0.02	-0.08 ± 0.02	–	–	–
PTF10rhi	0.084 ± 0.001	0.030	55425.53 ± 0.25	1.01 ± 0.02	0.11 ± 0.02	–	–	–
PTF10tce	0.040 ± 0.001	0.044	55442.80 ± 0.10	0.96 ± 0.02	0.03 ± 0.01	–	–	Y
PTF10trp	0.048 ± 0.001	0.044	55449.70 ± 0.14	1.13 ± 0.02	0.55 ± 0.02	–	–	–
PTF10trs	0.069 ± 0.001	0.054	55441.85 ± 0.24	0.84 ± 0.02	-0.12 ± 0.01	–	–	Y
PTF10twd	0.069 ± 0.001	0.087	55445.09 ± 0.22	1.09 ± 0.02	-0.08 ± 0.02	–	–	Y

PTF10ubm	0.069 ± 0.001	0.043	55454.70 ± 0.08	1.07 ± 0.01	0.00 ± 0.01	–	–	Y
PTF10ucu	0.098 ± 0.001	0.023	–	–	–	–	–	–
PTF10ufj	0.072 ± 0.001	0.116	55456.84 ± 0.09	1.03 ± 0.02	-0.03 ± 0.02	–	–	Y
PTF10umw	0.069 ± 0.001	0.038	55452.18 ± 0.33	0.97 ± 0.03	0.21 ± 0.03	–	–	–
PTF10umy	0.079 ± 0.001	0.035	55460.49 ± 0.13	0.99 ± 0.02	-0.05 ± 0.03	–	–	–
PTF10urj	0.104 ± 0.001	0.052	55458.23 ± 0.11	1.03 ± 0.02	-0.07 ± 0.02	–	–	–
PTF10vfo	0.087 ± 0.001	0.049	55458.64 ± 0.34	0.90 ± 0.02	-0.08 ± 0.02	–	–	Y
PTF10viq	0.030 ± 0.001	0.050	55452.33 ± 0.15	1.13 ± 0.02	0.04 ± 0.02	–	–	Y
PTF10vye	0.046 ± 0.001	0.028	55471.84 ± 0.19	0.92 ± 0.02	3.22 ± 0.04	–	–	–
PTF10wnm	0.064 ± 0.001	0.034	55476.86 ± 0.11	1.06 ± 0.02	-0.13 ± 0.01	–	–	Y
PTF10wnq	0.069 ± 0.001	0.071	55473.15 ± 0.13	0.96 ± 0.02	-0.06 ± 0.01	–	–	Y
PTF10wof	0.051 ± 0.001	0.068	55474.40 ± 0.13	0.99 ± 0.02	0.04 ± 0.02	–	–	Y
PTF10wor	0.055 ± 0.001	0.054	55463.04 ± 0.29	0.50 ± -0.00	–	–	–	–
PTF10wos	0.081 ± 0.001	0.027	55470.03 ± 0.51	0.87 ± 0.04	-0.06 ± 0.02	–	–	Y
PTF10xup	0.061 ± 0.001	0.013	55492.09 ± 0.17	0.97 ± 0.04	–	–	Y	–
PTF10xwg	0.093 ± 0.001	0.050	55484.69 ± 0.46	1.33 ± 0.04	-0.14 ± 0.02	–	–	–
PTF10xyt	0.048 ± 0.001	0.051	55490.63 ± 0.10	1.12 ± 0.02	0.19 ± 0.02	–	–	Y
PTF10yer	0.049 ± 0.001	0.053	55493.39 ± 0.26	1.05 ± 0.03	-0.00 ± 0.02	–	–	–
PTF10ygu	0.026 ± 0.001	0.030	55495.33 ± 0.09	0.95 ± 0.01	0.49 ± 0.02	–	Y	–
PTF10yux	0.056 ± 0.001	0.100	55496.64 ± 0.14	0.81 ± 0.02	0.20 ± 0.02	–	–	Y
PTF10zak	0.041 ± 0.001	0.011	55500.56 ± 0.16	0.82 ± 0.01	–	–	Y	–
PTF10zbk	0.063 ± 0.001	0.144	55497.08 ± 0.74	0.88 ± 0.06	0.23 ± 0.05	–	–	–
PTF10zdk	0.033 ± 0.001	0.097	55516.03 ± 0.17	1.09 ± 0.02	0.04 ± 0.02	–	–	Y
PTF11alo	0.019 ± 0.001	0.094	55599.95 ± 0.08	0.70 ± 0.01	0.10 ± 0.02	–	–	Y
PTF11ao	0.109 ± 0.001	0.067	55582.74 ± 0.25	0.92 ± 0.04	0.24 ± 0.05	–	–	–
PTF11atu	0.085 ± 0.001	0.122	55612.62 ± 0.72	0.82 ± 0.06	-0.14 ± 0.05	–	–	–
PTF11bas	0.086 ± 0.001	0.018	55640.21 ± 0.14	0.96 ± 0.02	0.06 ± 0.02	–	–	Y
PTF11bju	0.033 ± 0.001	0.017	55650.15 ± 0.09	1.14 ± 0.01	0.10 ± 0.01	–	–	Y
PTF11bnx	0.060 ± 0.001	0.050	55652.95 ± 0.09	0.98 ± 0.02	0.03 ± 0.01	–	–	Y

PTF11bpw	0.048 ± 0.001	0.031	55667.93 ± 0.13	0.99 ± 0.02	-0.11 ± 0.05	–	–	–
PTF11bqc	0.082 ± 0.001	0.028	55661.22 ± 0.24	0.93 ± 0.02	0.15 ± 0.03	–	–	Y
PTF11bui	0.029 ± 0.001	0.013	55674.32 ± 0.11	0.97 ± 0.02	–	–	Y	–
PTF11cao	0.040 ± 0.001	0.068	55670.54 ± 0.13	0.98 ± 0.02	0.03 ± 0.02	–	–	Y
PTF11cji	0.089 ± 0.001	0.024	55677.07 ± 0.31	1.06 ± 0.03	–	–	Y	–
PTF11cmw	0.061 ± 0.001	0.018	55687.53 ± 0.15	0.69 ± 0.02	0.33 ± 0.03	–	–	–
PTF11ctn	0.080 ± 0.001	0.009	55685.41 ± 0.35	1.09 ± 0.02	0.00 ± 0.01	–	–	Y
PTF11dif	0.060 ± 0.001	0.012	55702.95 ± 0.07	1.05 ± 0.01	0.01 ± 0.01	–	Y	Y
PTF11drz	0.057 ± 0.001	0.014	55705.38 ± 0.11	0.92 ± 0.01	-0.03 ± 0.01	–	–	Y
PTF11dxu	0.025 ± 0.001	0.051	55713.05 ± 0.20	1.15 ± 0.02	-0.05 ± 0.02	–	–	Y
PTF11ecn	0.062 ± 0.001	0.016	55714.79 ± 0.18	0.64 ± 0.03	0.57 ± 0.02	–	–	–
PTF11eie	0.040 ± 0.001	0.054	55725.03 ± 0.09	1.08 ± 0.02	0.12 ± 0.02	–	–	–
PTF11gdh	0.027 ± 0.001	0.011	55744.10 ± 0.21	1.07 ± 0.04	–	Y	–	–
PTF11gjh	0.039 ± 0.001	0.007	55748.29 ± 0.19	1.06 ± 0.02	0.34 ± 0.02	–	–	–
PTF11htb	0.049 ± 0.001	0.072	55764.79 ± 0.14	1.05 ± 0.02	-0.09 ± 0.01	–	–	Y
PTF11hub	0.029 ± 0.001	0.013	55770.01 ± 0.09	0.82 ± 0.01	-0.14 ± 0.03	Y	–	Y
PTF11icm	0.080 ± 0.001	0.009	55769.85 ± 0.17	1.07 ± 0.03	0.37 ± 0.02	–	–	–
PTF11izs	0.075 ± 0.001	0.059	55775.20 ± 0.26	0.76 ± 0.02	0.01 ± 0.05	–	–	Y
PTF11jfm	0.064 ± 0.001	0.147	55770.58 ± 1.15	1.05 ± 0.06	0.03 ± 0.05	–	–	–
PTF11jgq	0.129 ± 0.001	0.048	55780.96 ± 0.19	1.23 ± 0.02	-0.05 ± 0.02	–	–	–
PTF11kaw	0.079 ± 0.001	0.062	55790.55 ± 0.18	1.07 ± 0.02	-0.01 ± 0.02	–	–	Y
PTF11khk	0.031 ± 0.001	0.035	55784.54 ± 0.20	0.59 ± 0.02	0.29 ± 0.02	–	–	–
PTF11kjn	0.022 ± 0.001	0.082	55799.26 ± 0.07	0.66 ± 0.01	0.23 ± 0.02	–	–	–
PTF11kly	0.001 ± 0.001	0.009	55825.42 ± 0.29	0.52 ± 0.03	–	Y	–	–
PTF11kx	0.046 ± 0.001	0.041	55590.42 ± 0.20	1.07 ± 0.02	–	–	–	–
PTF11lih	0.071 ± 0.001	0.063	55810.98 ± 0.13	0.91 ± 0.02	0.07 ± 0.02	–	–	Y
PTF11mkx	0.054 ± 0.001	0.042	55835.47 ± 0.10	1.07 ± 0.02	0.02 ± 0.01	–	–	–
PTF11mty	0.076 ± 0.001	0.060	55837.31 ± 0.13	1.08 ± 0.02	-0.06 ± 0.02	–	–	Y
PTF11nga	0.072 ± 0.001	0.052	55836.12 ± 0.40	1.02 ± 0.04	-0.04 ± 0.04	–	–	Y

PTF11okh	0.018 ± 0.001	0.102	55849.23 ± 0.09	0.54 ± 0.01	0.55 ± 0.02	–	–	–
PTF11opu	0.069 ± 0.001	0.082	55850.48 ± 0.65	0.98 ± 0.05	0.08 ± 0.04	–	–	–
PTF11owc	0.071 ± 0.001	0.014	55870.27 ± 0.07	0.50 ± -0.00	–	–	–	–
PTF11pbp	0.028 ± 0.001	0.059	55871.02 ± 0.10	1.07 ± 0.01	–	–	–	–
PTF11pdk	0.080 ± 0.001	0.051	55864.88 ± 0.18	0.99 ± 0.02	-0.09 ± 0.02	–	–	Y
PTF11phk	0.072 ± 0.001	0.052	55869.87 ± 0.17	1.00 ± 0.02	0.14 ± 0.02	–	–	–
PTF11qmn	0.079 ± 0.001	0.027	55895.41 ± 0.30	0.99 ± 0.04	-0.12 ± 0.05	–	–	Y
PTF11qmo	0.056 ± 0.001	0.046	55892.28 ± 0.17	0.92 ± 0.02	-0.16 ± 0.01	–	–	Y
PTF11qnr	0.015 ± 0.001	0.065	55902.30 ± 0.10	0.79 ± 0.04	–	Y	–	–
PTF11qri	0.056 ± 0.001	0.024	55893.48 ± 0.37	0.95 ± 0.04	–	–	Y	–
PTF11qzq	0.060 ± 0.001	0.089	55906.07 ± 0.26	0.83 ± 0.02	0.08 ± 0.07	–	–	–
PTF11v	0.040 ± 0.001	0.011	55577.16 ± 0.08	0.77 ± 0.01	-0.01 ± 0.02	–	–	Y
PTF11vl	0.045 ± 0.001	0.049	55580.96 ± 1.22	1.17 ± 0.05	-0.05 ± 0.04	–	–	–
PTF11wv	0.091 ± 0.001	0.041	55596.34 ± 0.24	0.97 ± 0.02	-0.08 ± 0.02	–	–	–
PTF11ya	0.013 ± 0.001	0.690	55594.86 ± 0.38	1.08 ± 0.04	–	–	–	–
PTF12ass	0.039 ± 0.001	0.048	–	–	–	–	–	–
PTF12bok	0.026 ± 0.001	0.018	56014.81 ± 0.14	0.92 ± 0.02	–	–	Y	–
PTF12bsa	0.091 ± 0.001	0.015	56011.73 ± 0.11	1.06 ± 0.02	0.09 ± 0.01	–	–	–
PTF12cks	0.064 ± 0.001	0.021	56028.49 ± 0.16	1.18 ± 0.02	–	–	Y	–
PTF12cnl	0.048 ± 0.001	0.015	56033.86 ± 0.16	1.15 ± 0.02	–	–	Y	–
PTF12csi	0.053 ± 0.001	0.028	56030.57 ± 0.24	1.07 ± 0.04	–	–	Y	–
PTF12dem	0.200 ± 0.001	0.013	56038.85 ± 1.12	1.29 ± 0.10	–	–	–	–
PTF12dhb	0.057 ± 0.001	0.015	56041.38 ± 0.19	1.00 ± 0.03	-0.00 ± 0.03	–	–	Y
PTF12dhl	0.058 ± 0.001	0.012	56040.66 ± 0.22	0.75 ± 0.02	–	–	–	–
PTF12dja	0.166 ± 0.001	0.013	56029.33 ± 0.98	0.77 ± 0.24	–	–	–	–
PTF12dst	0.192 ± 0.001	0.020	56050.72 ± 0.31	1.18 ± 0.03	0.02 ± 0.03	–	–	–
PTF12dwm	0.054 ± 0.001	0.011	56052.12 ± 0.17	0.61 ± 0.02	0.48 ± 0.05	–	–	–
PTF12ecj	0.062 ± 0.001	0.011	56057.55 ± 0.20	0.71 ± 0.02	–	–	–	–
PTF12ecm	0.067 ± 0.001	0.021	56067.17 ± 0.10	0.91 ± 0.01	0.07 ± 0.01	–	–	Y

PTF12ecr	0.069 ± 0.001	0.015	56066.82 ± 0.18	1.05 ± 0.02	0.01 ± 0.02	–	–	Y
PTF12efn	0.062 ± 0.001	0.020	56077.76 ± 1.13	1.22 ± 0.08	–	–	–	–
PTF12emp	0.031 ± 0.001	0.009	56076.26 ± 0.28	0.66 ± 0.02	-0.35 ± 0.03	Y	–	–
PTF12esv	0.033 ± 0.001	0.017	56070.36 ± 0.16	0.69 ± 0.01	0.55 ± 0.02	–	–	–
PTF12eut	0.089 ± 0.001	0.034	56079.04 ± 0.11	0.80 ± 0.01	-0.04 ± 0.02	–	Y	Y
PTF12fjx	0.042 ± 0.001	0.017	56103.40 ± 0.11	1.00 ± 0.02	0.54 ± 0.02	–	–	–
PTF12fkk	0.057 ± 0.001	0.023	56097.17 ± 0.15	0.77 ± 0.02	0.10 ± 0.08	–	Y	–
PTF12fsd	0.070 ± 0.001	0.022	56103.27 ± 0.25	1.01 ± 0.05	–	–	Y	–
PTF12fuu	0.049 ± 0.001	0.052	56111.82 ± 0.09	1.04 ± 0.02	-0.12 ± 0.01	–	–	Y
PTF12fxn	0.051 ± 0.001	0.026	56111.29 ± 0.20	0.92 ± 0.03	–	–	–	–
PTF12gaz	0.071 ± 0.001	0.058	56112.95 ± 0.13	0.97 ± 0.02	-0.04 ± 0.02	–	–	Y
PTF12gco	0.151 ± 0.001	0.031	56112.74 ± 0.39	1.12 ± 0.05	–	–	–	–
PTF12gdq	0.034 ± 0.001	0.040	56115.49 ± 0.17	0.88 ± 0.02	0.15 ± 0.02	Y	–	Y
PTF12ghy	0.034 ± 0.001	0.056	56122.08 ± 0.10	0.93 ± 0.01	0.19 ± 0.02	–	–	Y
PTF12hwb	0.055 ± 0.001	0.068	56170.39 ± 0.16	1.09 ± 0.02	0.19 ± 0.02	–	–	Y
PTF12iiq	0.028 ± 0.001	0.059	56182.21 ± 0.08	0.87 ± 0.01	0.11 ± 0.01	–	–	Y
PTF12lz	0.069 ± 0.001	0.054	55919.62 ± 0.55	0.95 ± 0.05	–	–	–	–
PTF12mj	0.069 ± 0.001	0.067	55943.54 ± 0.13	1.16 ± 0.01	–	–	Y	–

Appendix C

Post–Maximum Fitting Results

This appendix contains the results of the light curve fitting for the Post-Maximum Diversity sample presented in in Chapter 5, see Table C.1 on the following pages.

TABLE C.1: Table of results for the post-maximum fitting in Chapter 5

SN	Redshift, z	$t_{\max}$ MJD (days)	Stretch, s	t_g, days	σ_g, days	F_g	$\langle R_{\rm P48}\rangle_{20-40}$	$\langle R_{\rm P48}\rangle_{15-35}$	χ^2/DOF
PTF09alu	0.071 ± 0.001	55027.89 ± 0.21	0.80 ± 0.03	21.54 ± 0.64	3.99 ± 0.60	0.166 ± 0.047	0.36 ± 0.12	0.28 ± 0.09	1.40
PTF09aro	0.085 ± 0.001	55028.02 ± 0.22	1.05 ± 0.04	29.63 ± 0.64	5.23 ± 0.70	0.139 ± 0.010	0.45 ± 0.07	0.39 ± 0.06	1.33
PTF09cbu	0.057 ± 0.001	55036.69 ± 0.25	1.09 ± 0.08	26.75 ± 1.05	3.62 ± 0.94	0.116 ± 0.009	0.42 ± 0.12	0.36 ± 0.10	1.09
PTF10cwm	0.080 ± 0.001	55271.18 ± 0.79	1.04 ± 0.27	27.67 ± 1.42	7.23 ± 0.86	0.150 ± 0.027	0.48 ± 0.16	0.41 ± 0.14	0.59
PTF10cxk	0.016 ± 0.001	55276.96 ± 0.24	0.86 ± 0.04	18.53 ± 0.40	3.43 ± 0.53	0.115 ± 0.006	0.33 ± 0.06	0.25 ± 0.04	1.45
PTF10duy	0.079 ± 0.001	55283.20 ± 0.27	1.15 ± 0.04	30.49 ± 1.10	5.82 ± 1.19	0.103 ± 0.013	0.46 ± 0.11	0.40 ± 0.10	0.92
PTF10glo	0.075 ± 0.001	55320.49 ± 0.48	1.51 ± 0.07	25.82 ± 0.83	5.12 ± 0.78	0.103 ± 0.009	0.58 ± 0.10	0.48 ± 0.09	1.50
PTF10gjx	0.076 ± 0.001	55325.81 ± 0.20	1.04 ± 0.06	28.15 ± 0.56	6.14 ± 0.64	0.114 ± 0.008	0.44 ± 0.06	0.38 ± 0.05	0.71
PTF10hyv	0.090 ± 0.001	55350.80 ± 0.26	1.10 ± 0.04	29.00 ± 0.65	4.57 ± 0.71	0.167 ± 0.013	0.48 ± 0.08	0.42 ± 0.07	1.02
PTF10hmv	0.032 ± 0.001	55351.71 ± 0.16	1.18 ± 0.02	29.96 ± 0.25	6.15 ± 0.25	0.134 ± 0.004	0.48 ± 0.03	0.42 ± 0.02	4.07
PTF10hml	0.054 ± 0.001	55352.29 ± 0.14	1.07 ± 0.03	27.57 ± 0.20	5.58 ± 0.19	0.136 ± 0.004	0.45 ± 0.02	0.39 ± 0.02	4.12
PTF10kiw	0.069 ± 0.001	55368.37 ± 0.36	1.04 ± 0.07	26.38 ± 2.24	6.79 ± 1.86	0.183 ± 0.021	0.49 ± 0.15	0.42 ± 0.13	0.36
PTF10kdg	0.062 ± 0.001	55369.93 ± 0.16	0.95 ± 0.03	23.71 ± 0.66	4.98 ± 0.65	0.173 ± 0.013	0.43 ± 0.07	0.35 ± 0.05	0.34
PTF10lxp	0.088 ± 0.001	55381.09 ± 0.16	1.04 ± 0.03	27.98 ± 0.59	4.85 ± 0.62	0.130 ± 0.013	0.44 ± 0.07	0.38 ± 0.06	1.02
PTF10xup	0.060 ± 0.001	55492.35 ± 0.29	1.03 ± 0.06	24.56 ± 0.82	4.67 ± 0.68	0.128 ± 0.015	0.42 ± 0.08	0.35 ± 0.07	1.47
PTF10ygu	0.025 ± 0.001	55495.74 ± 0.19	1.07 ± 0.03	25.30 ± 0.39	7.22 ± 0.43	0.184 ± 0.012	0.50 ± 0.05	0.42 ± 0.04	0.97
PTF10zak	0.040 ± 0.001	55500.63 ± 0.19	0.80 ± 0.04	22.41 ± 0.18	4.39 ± 0.19	0.217 ± 0.015	0.39 ± 0.04	0.31 ± 0.03	2.49
PTF10aaju	0.078 ± 0.001	55510.45 ± 0.28	1.02 ± 0.07	27.31 ± 1.44	7.40 ± 1.73	0.125 ± 0.012	0.45 ± 0.12	0.39 ± 0.10	1.49
PTF10acnz	0.062 ± 0.001	55567.57 ± 0.25	1.29 ± 0.04	25.44 ± 0.47	5.23 ± 0.59	0.099 ± 0.011	0.50 ± 0.08	0.42 ± 0.07	1.57
PTF11bui	0.028 ± 0.001	55675.22 ± 0.19	1.09 ± 0.03	27.01 ± 0.19	5.20 ± 0.21	0.172 ± 0.006	0.47 ± 0.03	0.40 ± 0.02	0.75

PTF11cji	0.088 ± 0.001	55676.85 ± 0.47	1.03 ± 0.06	28.14 ± 2.83	6.82 ± 3.52	0.130 ± 0.014	0.46 ± 0.24	0.39 ± 0.21	0.36
PTF11dif	0.059 ± 0.001	55702.99 ± 0.20	1.06 ± 0.03	27.58 ± 0.60	5.15 ± 0.57	0.135 ± 0.007	0.44 ± 0.06	0.38 ± 0.05	1.34
PTF11qri	0.055 ± 0.001	55893.65 ± 0.49	1.00 ± 0.09	25.65 ± 1.77	6.84 ± 1.83	0.120 ± 0.018	0.43 ± 0.14	0.36 ± 0.12	0.62
PTF12mj	0.069 ± 0.001	55943.75 ± 0.21	1.19 ± 0.02	27.21 ± 1.14	7.30 ± 0.91	0.094 ± 0.013	0.48 ± 0.09	0.41 ± 0.08	1.74
PTF12bok	0.025 ± 0.001	56014.98 ± 0.20	0.95 ± 0.04	24.93 ± 0.30	6.13 ± 0.35	0.142 ± 0.005	0.42 ± 0.03	0.35 ± 0.03	0.13
PTF12cks	0.063 ± 0.001	56028.55 ± 0.21	1.20 ± 0.03	27.44 ± 0.54	6.72 ± 0.44	0.113 ± 0.007	0.49 ± 0.05	0.42 ± 0.04	1.22
PTF12csi	0.053 ± 0.001	56031.07 ± 0.37	1.16 ± 0.06	31.46 ± 1.57	6.46 ± 1.94	0.083 ± 0.014	0.44 ± 0.15	0.38 ± 0.13	3.32
PTF12cnl	0.047 ± 0.001	56033.55 ± 0.30	1.10 ± 0.04	30.19 ± 0.33	7.21 ± 0.41	0.152 ± 0.004	0.47 ± 0.03	0.42 ± 0.03	1.16
PTF12eut	0.089 ± 0.001	56079.18 ± 0.24	0.77 ± 0.03	17.19 ± 0.63	4.45 ± 0.73	0.132 ± 0.013	0.32 ± 0.06	0.24 ± 0.05	2.35
PTF12fkk	0.056 ± 0.001	56097.45 ± 0.21	0.79 ± 0.03	20.59 ± 0.54	5.21 ± 0.65	0.136 ± 0.014	0.35 ± 0.06	0.27 ± 0.04	2.64
PTF12fsd	0.069 ± 0.001	56103.10 ± 0.40	0.97 ± 0.08	25.46 ± 0.81	5.32 ± 0.93	0.189 ± 0.018	0.46 ± 0.10	0.38 ± 0.08	0.57

Appendix D

Observational Parameters of Multicolour PTF SNe Ia

This appendix presents the observational parameters of the PTF SNe Ia Hubble Diagram sample used in Chapter 6, see Table D.1 on the following pages.

TABLE D.1: Observational Parameters of Multicolour PTF SNe Ia Hubble Diagram sample from Chapter 6

SN	Redshift, z	m_B (mag)	m_R (mag)	m_i (mag)	Stretch, s	Colour, $\mathcal{C}$	$R-i$	χ^2/DOF
PTF09dlc	0.067 ± 0.001	17.94 ± 0.02	18.19 ± 0.02	18.56 ± 0.03	1.04 ± 0.03	-0.17 ± 0.02	-0.36 ± 0.03	0.77
PTF09dnl	0.019 ± 0.001	15.92 ± 0.02	15.79 ± 0.01	16.12 ± 0.02	1.08 ± 0.02	0.07 ± 0.02	-0.33 ± 0.02	0.84
PTF09fox	0.071 ± 0.001	18.28 ± 0.03	18.30 ± 0.02	18.66 ± 0.03	1.03 ± 0.03	0.01 ± 0.02	-0.37 ± 0.04	1.96
PTF09foz	0.049 ± 0.001	17.75 ± 0.03	17.59 ± 0.01	17.85 ± 0.02	0.85 ± 0.02	0.08 ± 0.02	-0.26 ± 0.03	2.84
PTF10accd	0.030 ± 0.001	16.61 ± 0.05	16.69 ± 0.03	16.99 ± 0.03	1.09 ± 0.01	-0.07 ± 0.02	-0.30 ± 0.04	0.58
PTF10mwb	0.030 ± 0.001	16.75 ± 0.03	16.80 ± 0.02	17.03 ± 0.03	0.93 ± 0.03	-0.07 ± 0.02	-0.23 ± 0.04	0.44
PTF10pvi	0.079 ± 0.001	18.47 ± 0.03	18.55 ± 0.02	18.86 ± 0.03	1.06 ± 0.02	-0.06 ± 0.02	-0.31 ± 0.04	0.42
PTF10qjl	0.058 ± 0.001	17.80 ± 0.02	17.87 ± 0.01	18.18 ± 0.02	1.13 ± 0.02	-0.06 ± 0.01	-0.31 ± 0.02	1.25
PTF10qjq	0.029 ± 0.001	16.46 ± 0.02	16.38 ± 0.01	16.53 ± 0.02	0.95 ± 0.01	-0.01 ± 0.01	-0.14 ± 0.02	2.20
PTF10qkf	0.080 ± 0.001	18.92 ± 0.02	18.85 ± 0.02	19.08 ± 0.03	1.05 ± 0.03	0.02 ± 0.02	-0.23 ± 0.04	1.20
PTF10qky	0.074 ± 0.001	18.14 ± 0.03	18.25 ± 0.02	18.58 ± 0.03	1.07 ± 0.02	-0.07 ± 0.02	-0.33 ± 0.03	0.77
PTF10qsc	0.087 ± 0.001	18.58 ± 0.02	18.66 ± 0.02	19.02 ± 0.03	1.08 ± 0.02	-0.04 ± 0.02	-0.36 ± 0.04	0.90
PTF10qwg	0.070 ± 0.001	18.51 ± 0.02	18.35 ± 0.01	18.66 ± 0.03	1.00 ± 0.03	0.10 ± 0.02	-0.31 ± 0.03	1.72
PTF10rbc	0.088 ± 0.001	19.00 ± 0.02	18.97 ± 0.02	19.09 ± 0.03	0.99 ± 0.02	-0.05 ± 0.02	-0.13 ± 0.04	1.47
PTF10rbp	0.078 ± 0.001	18.63 ± 0.03	18.68 ± 0.02	19.12 ± 0.04	1.04 ± 0.02	0.01 ± 0.02	-0.44 ± 0.04	1.03
PTF10rcg	0.080 ± 0.001	18.57 ± 0.03	18.54 ± 0.02	18.89 ± 0.03	1.14 ± 0.02	0.03 ± 0.02	-0.35 ± 0.03	1.16
PTF10tce	0.040 ± 0.001	17.19 ± 0.02	17.12 ± 0.01	17.42 ± 0.02	0.96 ± 0.02	0.03 ± 0.01	-0.30 ± 0.02	5.25
PTF10trs	0.069 ± 0.001	18.34 ± 0.02	18.44 ± 0.01	18.63 ± 0.03	0.84 ± 0.02	-0.12 ± 0.01	-0.19 ± 0.03	1.54
PTF10twd	0.069 ± 0.001	18.08 ± 0.03	18.20 ± 0.02	18.55 ± 0.03	1.09 ± 0.02	-0.08 ± 0.02	-0.35 ± 0.03	0.58
PTF10ubm	0.069 ± 0.001	18.00 ± 0.02	17.98 ± 0.01	18.27 ± 0.02	1.07 ± 0.01	0.00 ± 0.01	-0.29 ± 0.02	2.47
PTF10ufj	0.072 ± 0.001	18.48 ± 0.04	18.57 ± 0.02	18.97 ± 0.03	1.03 ± 0.02	-0.03 ± 0.02	-0.40 ± 0.04	2.20
PTF10vfo	0.087 ± 0.001	18.91 ± 0.03	18.94 ± 0.02	19.11 ± 0.03	0.90 ± 0.02	-0.08 ± 0.02	-0.17 ± 0.04	3.15
PTF10viq	0.030 ± 0.001	16.60 ± 0.03	16.55 ± 0.02	16.96 ± 0.02	1.13 ± 0.02	0.04 ± 0.02	-0.41 ± 0.03	8.20
PTF10wnm	0.064 ± 0.001	18.04 ± 0.02	18.20 ± 0.01	18.47 ± 0.02	1.06 ± 0.02	-0.13 ± 0.01	-0.27 ± 0.02	0.80
PTF10wnq	0.069 ± 0.001	18.10 ± 0.03	18.16 ± 0.02	18.45 ± 0.02	0.96 ± 0.02	-0.06 ± 0.01	-0.29 ± 0.03	2.12

PTF10wof	0.051 ± 0.001	17.89 ± 0.03	17.83 ± 0.02	18.16 ± 0.02	0.99 ± 0.02	0.04 ± 0.02	-0.33 ± 0.03	0.85
PTF10wos	0.081 ± 0.001	18.88 ± 0.02	18.93 ± 0.02	19.20 ± 0.04	0.87 ± 0.04	-0.06 ± 0.02	-0.27 ± 0.05	1.71
PTF10xyt	0.048 ± 0.001	18.43 ± 0.03	18.05 ± 0.02	18.18 ± 0.03	1.12 ± 0.02	0.19 ± 0.02	-0.12 ± 0.03	4.34
PTF10yux	0.056 ± 0.001	18.60 ± 0.04	18.22 ± 0.02	18.36 ± 0.03	0.81 ± 0.02	0.20 ± 0.02	-0.15 ± 0.04	3.64
PTF10zdk	0.033 ± 0.001	17.04 ± 0.04	16.95 ± 0.02	17.22 ± 0.02	1.09 ± 0.02	0.04 ± 0.02	-0.27 ± 0.03	2.54
PTF11alo	0.019 ± 0.001	16.07 ± 0.04	15.80 ± 0.02	15.86 ± 0.03	0.70 ± 0.01	0.10 ± 0.02	-0.06 ± 0.03	2.03
PTF11bas	0.086 ± 0.001	19.00 ± 0.02	18.90 ± 0.01	19.18 ± 0.03	0.96 ± 0.02	0.06 ± 0.02	-0.28 ± 0.03	1.45
PTF11bju	0.033 ± 0.001	16.74 ± 0.01	16.50 ± 0.01	16.66 ± 0.02	1.14 ± 0.01	0.10 ± 0.01	-0.16 ± 0.02	2.74
PTF11bnx	0.060 ± 0.001	18.28 ± 0.02	18.20 ± 0.01	18.44 ± 0.02	0.98 ± 0.02	0.03 ± 0.01	-0.24 ± 0.02	1.11
PTF11bqc	0.082 ± 0.001	19.25 ± 0.04	18.94 ± 0.03	19.06 ± 0.06	0.93 ± 0.02	0.15 ± 0.03	-0.12 ± 0.06	1.15
PTF11cao	0.040 ± 0.001	17.36 ± 0.03	17.27 ± 0.02	17.51 ± 0.02	0.98 ± 0.02	0.03 ± 0.02	-0.24 ± 0.03	0.68
PTF11ctn	0.080 ± 0.001	18.56 ± 0.01	18.59 ± 0.01	18.97 ± 0.03	1.09 ± 0.02	0.00 ± 0.01	-0.38 ± 0.03	1.18
PTF11dif	0.060 ± 0.001	17.88 ± 0.01	17.91 ± 0.01	18.33 ± 0.02	1.05 ± 0.01	0.01 ± 0.01	-0.42 ± 0.02	2.43
PTF11drz	0.057 ± 0.001	17.90 ± 0.01	17.95 ± 0.01	18.30 ± 0.02	0.92 ± 0.01	-0.03 ± 0.01	-0.35 ± 0.02	2.68
PTF11dxu	0.025 ± 0.001	15.70 ± 0.02	15.74 ± 0.01	16.02 ± 0.02	1.15 ± 0.02	-0.05 ± 0.02	-0.28 ± 0.02	5.19
PTF11htb	0.049 ± 0.001	17.22 ± 0.03	17.39 ± 0.02	17.78 ± 0.02	1.05 ± 0.02	-0.09 ± 0.01	-0.40 ± 0.03	1.02
PTF11hub	0.029 ± 0.001	16.50 ± 0.03	16.66 ± 0.02	16.90 ± 0.03	0.82 ± 0.01	-0.14 ± 0.03	-0.24 ± 0.04	0.75
PTF11izs	0.075 ± 0.001	18.54 ± 0.09	18.51 ± 0.03	18.81 ± 0.05	0.76 ± 0.02	0.01 ± 0.05	-0.30 ± 0.06	1.18
PTF11kaw	0.079 ± 0.001	18.58 ± 0.03	18.62 ± 0.02	19.00 ± 0.04	1.07 ± 0.02	-0.01 ± 0.02	-0.37 ± 0.04	1.21
PTF11lih	0.071 ± 0.001	18.90 ± 0.03	18.73 ± 0.02	18.94 ± 0.03	0.91 ± 0.02	0.07 ± 0.02	-0.21 ± 0.04	1.85
PTF11mty	0.076 ± 0.001	18.32 ± 0.02	18.40 ± 0.02	18.73 ± 0.03	1.08 ± 0.02	-0.06 ± 0.02	-0.33 ± 0.03	1.15
PTF11nga	0.072 ± 0.001	18.73 ± 0.07	18.77 ± 0.03	18.99 ± 0.05	1.02 ± 0.04	-0.04 ± 0.04	-0.22 ± 0.06	2.29
PTF11pdk	0.080 ± 0.001	18.66 ± 0.02	18.72 ± 0.02	18.90 ± 0.04	0.99 ± 0.02	-0.09 ± 0.02	-0.19 ± 0.04	1.59
PTF11qmn	0.079 ± 0.001	18.36 ± 0.08	18.61 ± 0.02	19.02 ± 0.05	0.99 ± 0.04	-0.12 ± 0.05	-0.41 ± 0.06	0.61
PTF11qmo	0.056 ± 0.001	17.61 ± 0.02	17.90 ± 0.01	18.36 ± 0.03	0.92 ± 0.02	-0.16 ± 0.01	-0.47 ± 0.03	3.83
PTF11v	0.040 ± 0.001	17.04 ± 0.02	17.00 ± 0.01	17.24 ± 0.02	0.77 ± 0.01	-0.01 ± 0.02	-0.24 ± 0.02	3.50
PTF12dhb	0.057 ± 0.001	17.96 ± 0.04	17.96 ± 0.02	18.29 ± 0.03	1.00 ± 0.03	-0.00 ± 0.03	-0.32 ± 0.04	1.51
PTF12ecm	0.067 ± 0.001	18.37 ± 0.02	18.19 ± 0.01	18.36 ± 0.02	0.91 ± 0.01	0.07 ± 0.01	-0.18 ± 0.03	3.76
PTF12ecr	0.069 ± 0.001	18.62 ± 0.02	18.53 ± 0.01	18.71 ± 0.03	1.05 ± 0.02	0.01 ± 0.02	-0.18 ± 0.03	6.46

PTF12eut	0.089 ± 0.001	19.18 ± 0.02	19.17 ± 0.01	19.38 ± 0.03	0.80 ± 0.01	-0.04 ± 0.02	-0.22 ± 0.04	10.68
PTF12fuu	0.049 ± 0.001	17.36 ± 0.02	17.53 ± 0.01	17.88 ± 0.02	1.04 ± 0.02	-0.12 ± 0.01	-0.35 ± 0.02	3.86
PTF12gaz	0.071 ± 0.001	18.37 ± 0.03	18.40 ± 0.02	18.68 ± 0.03	0.97 ± 0.02	-0.04 ± 0.02	-0.28 ± 0.04	3.00
PTF12gdq	0.034 ± 0.001	17.23 ± 0.02	16.91 ± 0.01	17.04 ± 0.02	0.88 ± 0.02	0.15 ± 0.02	-0.13 ± 0.03	2.69
PTF12ghy	0.034 ± 0.001	17.48 ± 0.02	17.12 ± 0.01	17.32 ± 0.02	0.93 ± 0.01	0.19 ± 0.02	-0.20 ± 0.03	3.33
PTF12hwb	0.055 ± 0.001	18.60 ± 0.03	18.31 ± 0.02	18.65 ± 0.03	1.09 ± 0.02	0.19 ± 0.02	-0.33 ± 0.03	2.83
PTF12iiq	0.028 ± 0.001	16.76 ± 0.02	16.59 ± 0.01	16.92 ± 0.02	0.87 ± 0.01	0.11 ± 0.01	-0.33 ± 0.02	2.05

Appendix E

SiFTO fits of SNe From PTF with Multicolour LT Followup

In this appendix we present the light curve fits from the light–curve fitter SiFTO, for the sub–sample of objects that have both Palomar Transient Factory (PTF) data and multi–colour followup data from the Liverpool Telesecope (LT). This sample is described in detail in Chapter 2, Section 2.2.1, and in Chapter 6 where it forms the parent sample for our Hubble Diagram sub–sample, as described in Section 6.2.1.

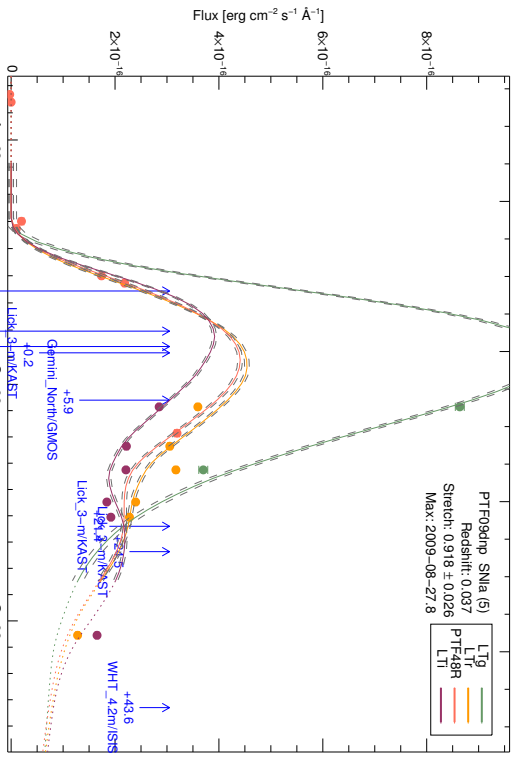

FIGURE E.3: SiFTO light curve fit of PTF09dnp

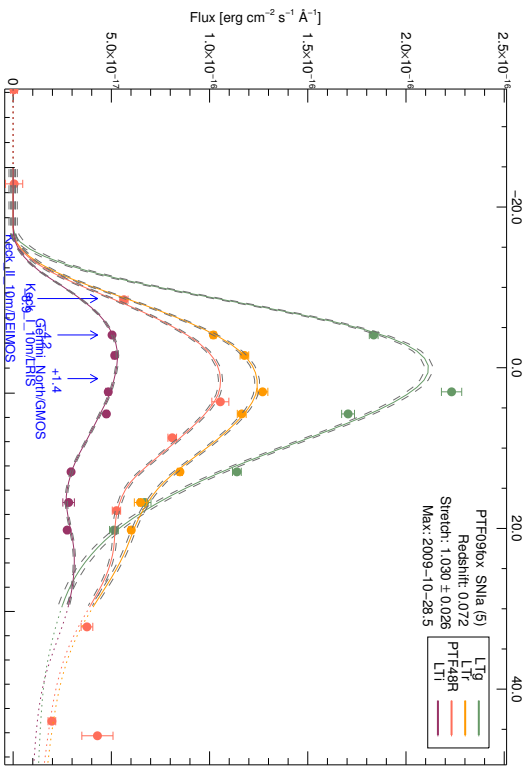

FIGURE E.4: SiFTO light curve fit of PTF09fox

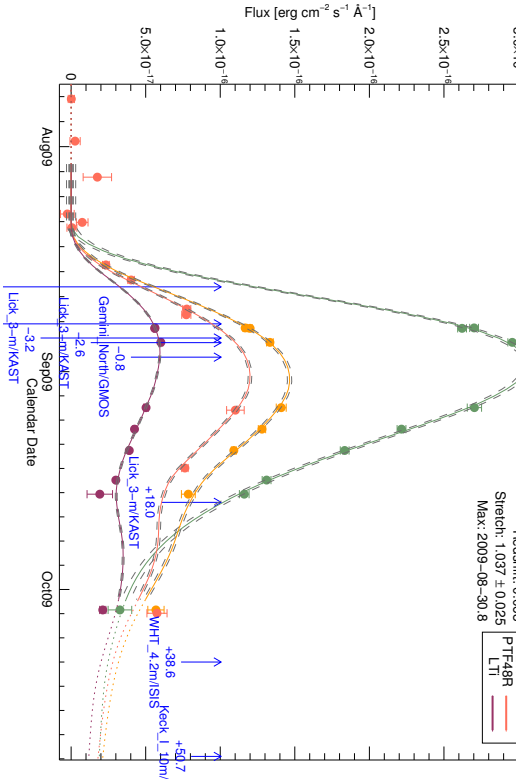

FIGURE E.1: SiFTO light curve fit of PTF09dlc

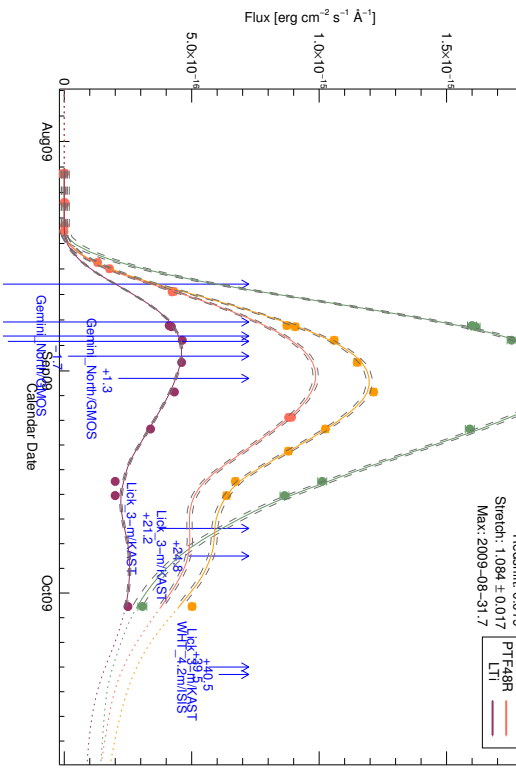

FIGURE E.2: SiFTO light curve fit of PTF09dnl

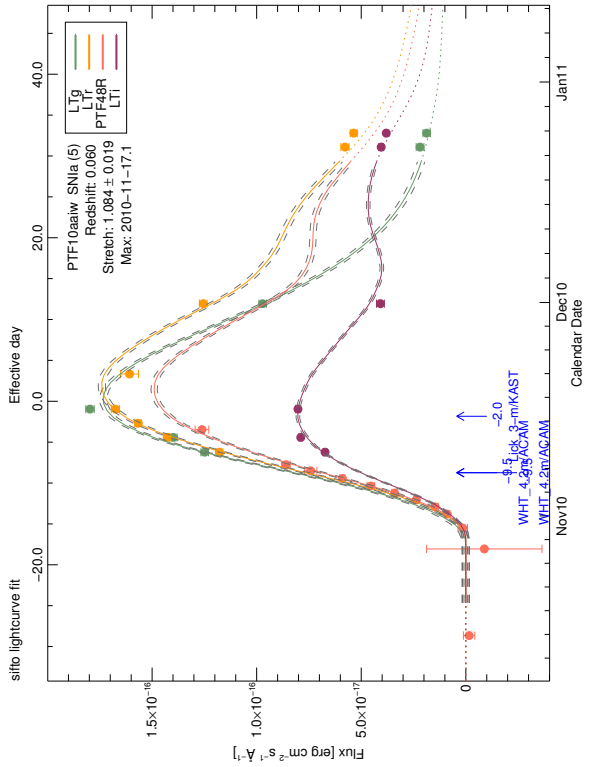

FIGURE E.6: SiFTO light curve fit of PTF10aaiw

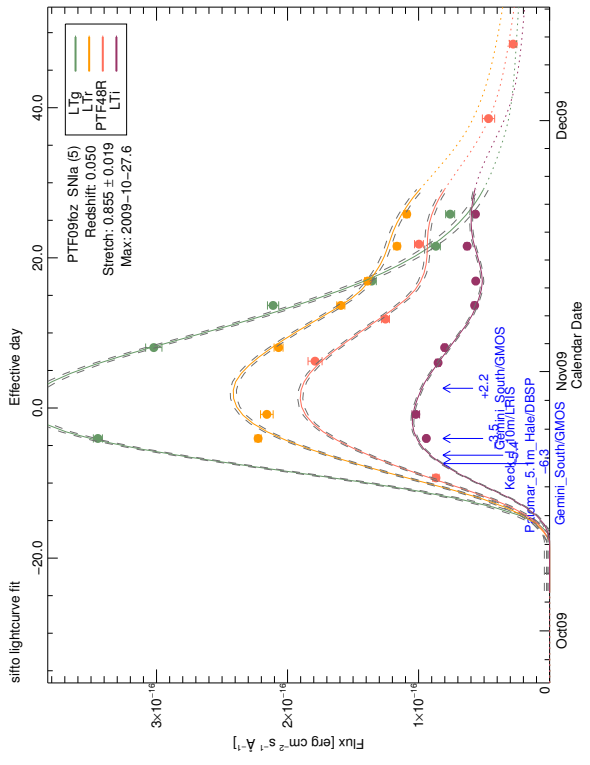

FIGURE E.5: SiFTO light curve fit of PTF09foz

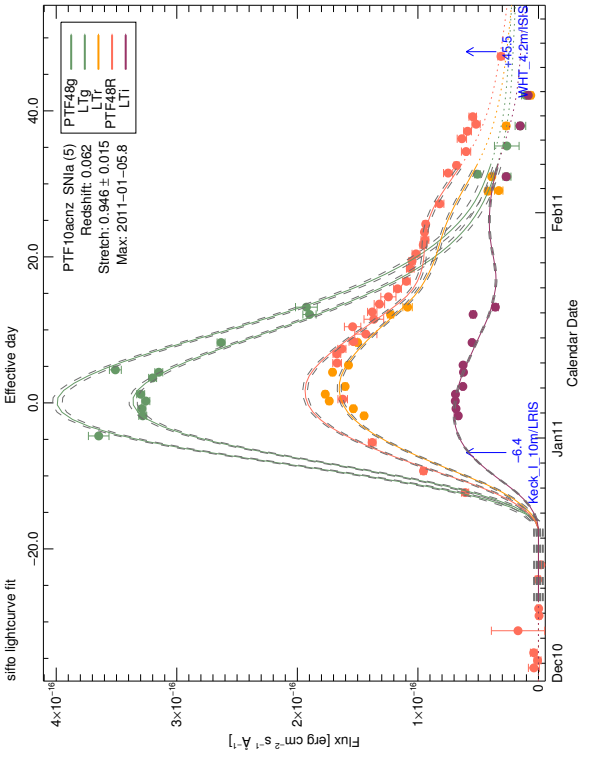

FIGURE E.8: SiFTO light curve fit of PTF10acnz

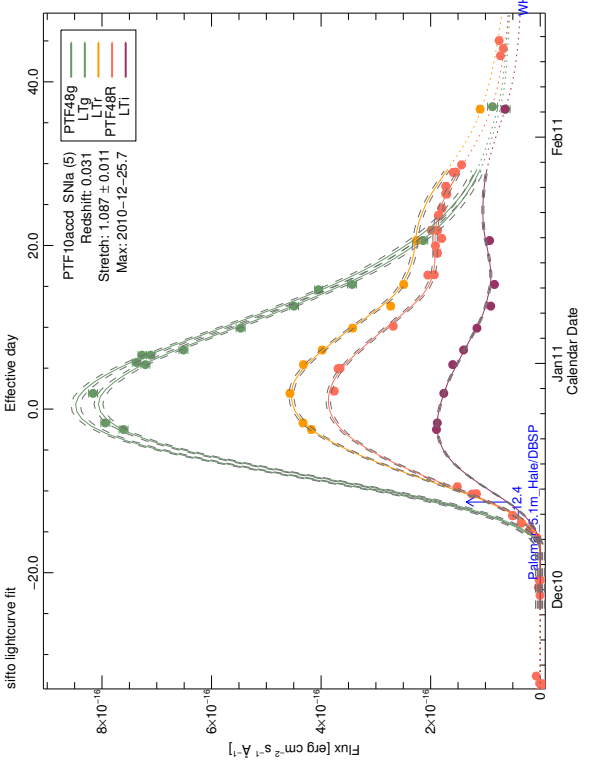

FIGURE E.7: SiFTO light curve fit of PTF10accd

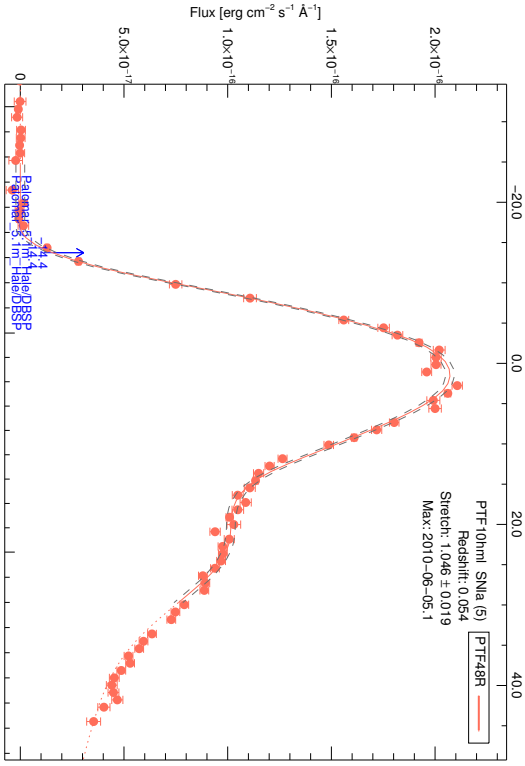

FIGURE E.9: SiFTO light curve fit of PTF10bjs

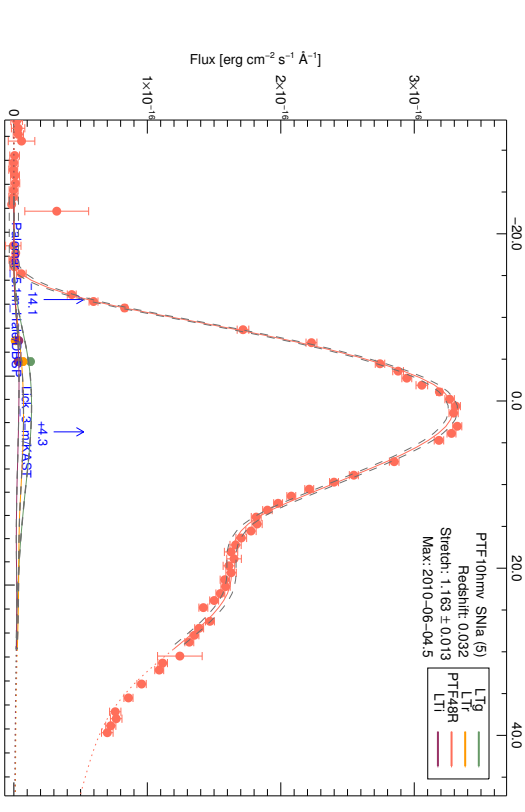

FIGURE E.11: SiFTO light curve fit of PTF10hml

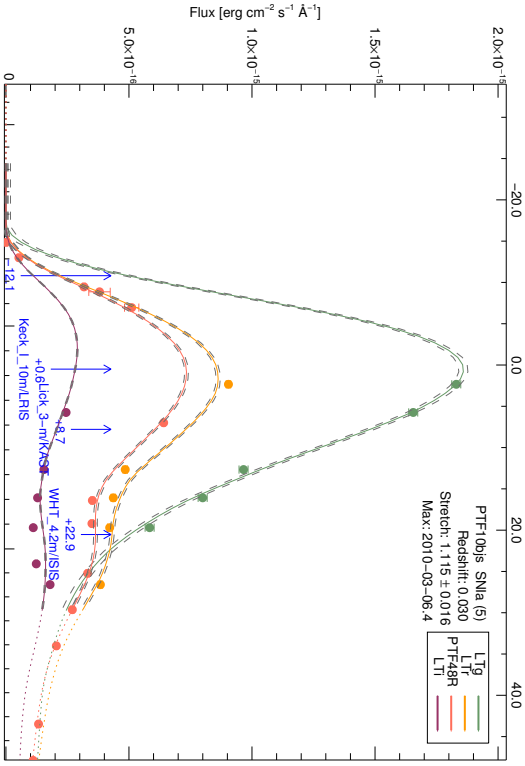

FIGURE E.10: SiFTO light curve fit of PTF10hmc

FIGURE E.12: SiFTO light curve fit of PTF10hmv

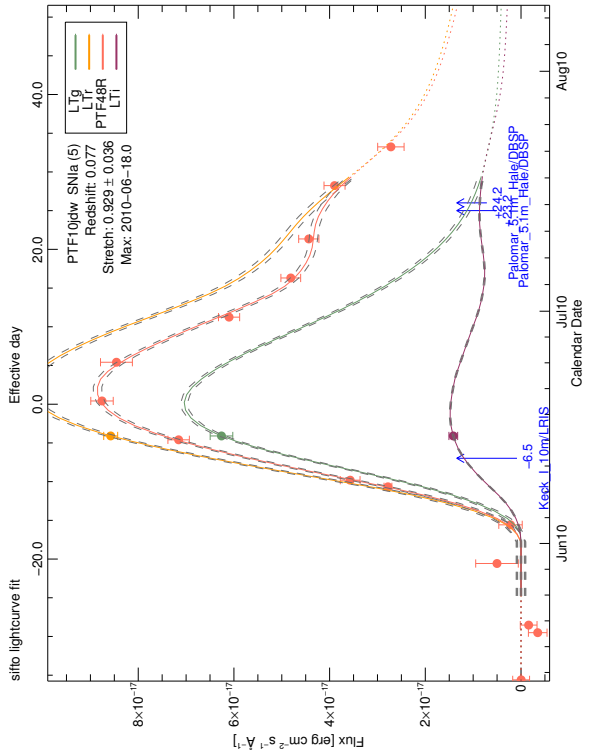

FIGURE E.14: SiFTO light curve fit of PTF10jdw

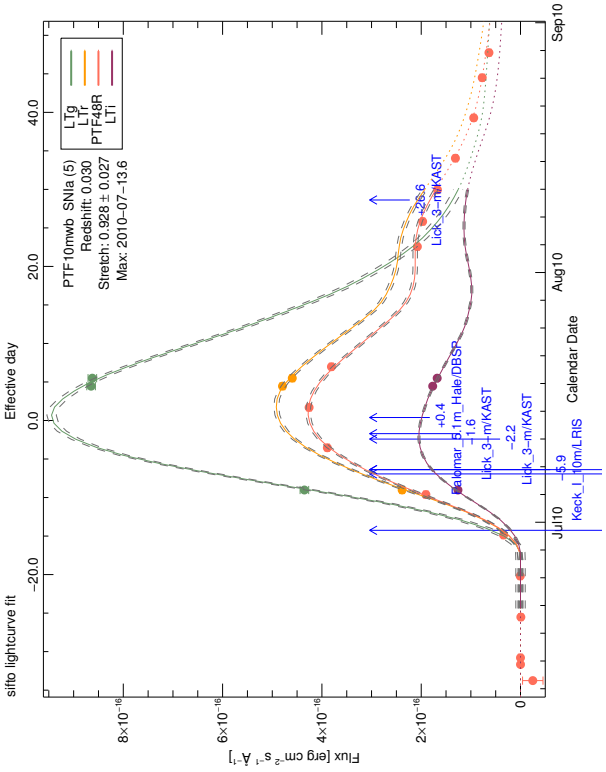

FIGURE E.16: SiFTO light curve fit of PTF10mwb

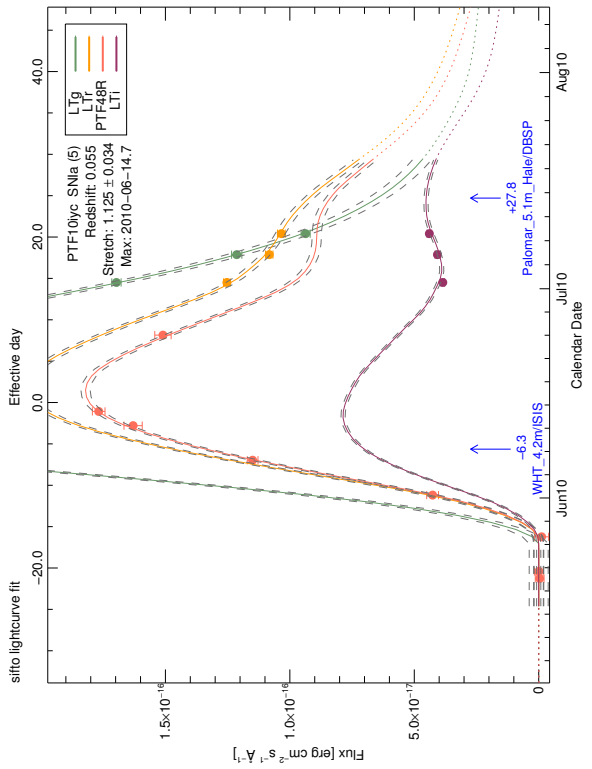

FIGURE E.13: SiFTO light curve fit of PTF10iyc

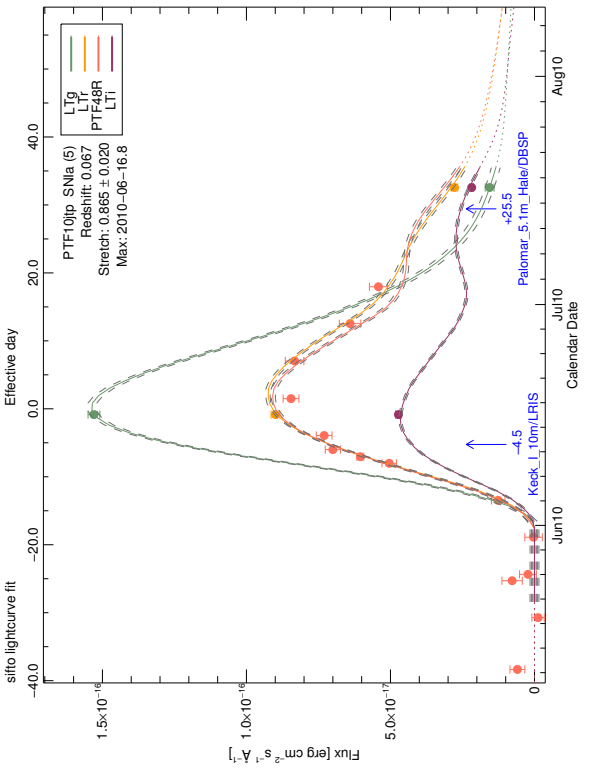

FIGURE E.15: SiFTO light curve fit of PTF10jtp

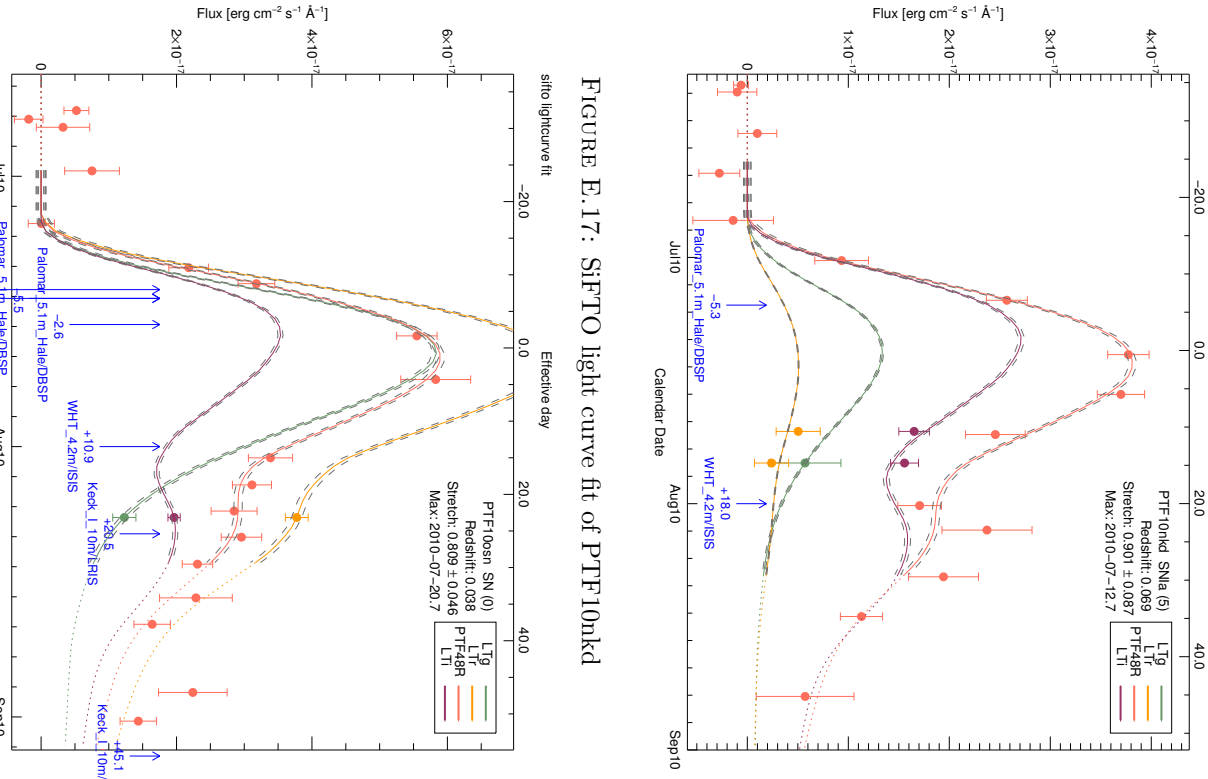

FIGURE E.17: SiFTO light curve fit of PTF10nkd

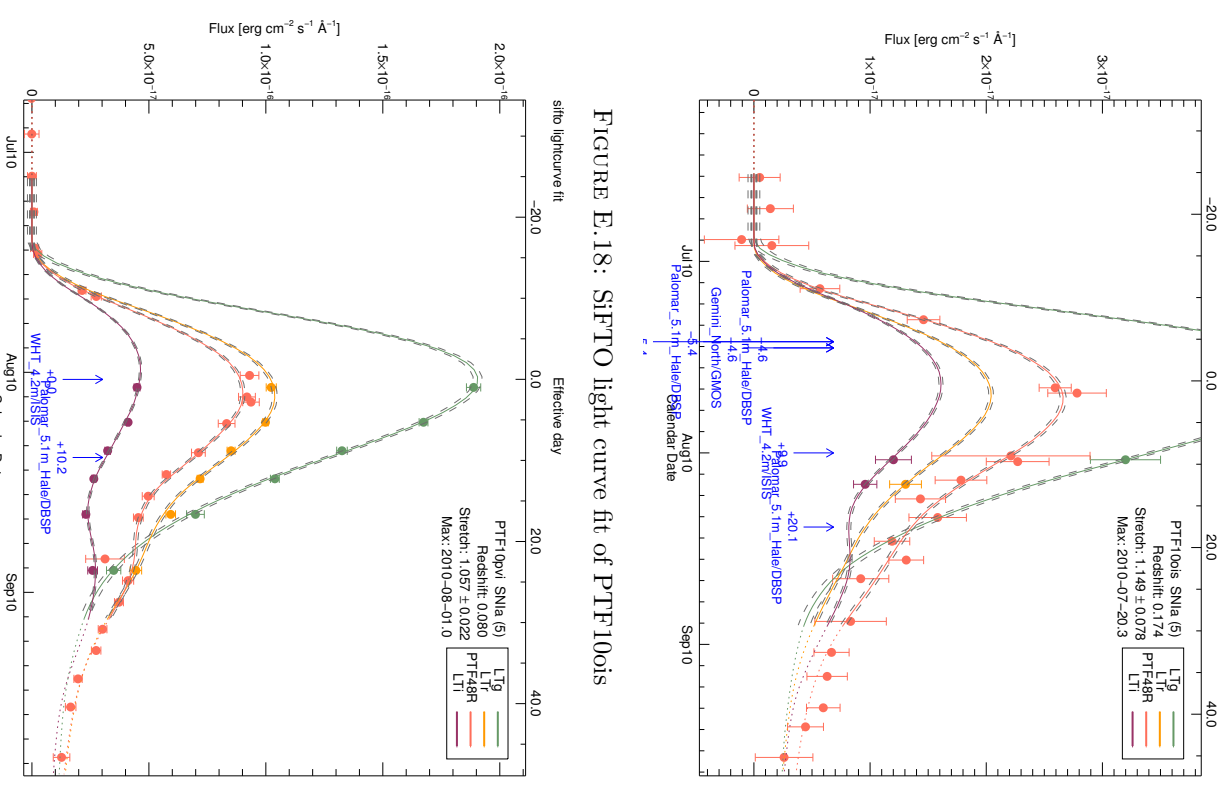

FIGURE E.18: SiFTO light curve fit of PTF10ois

FIGURE E.19: SiFTO light curve fit of PTF10osn

FIGURE E.20: SiFTO light curve fit of PTF10pvi

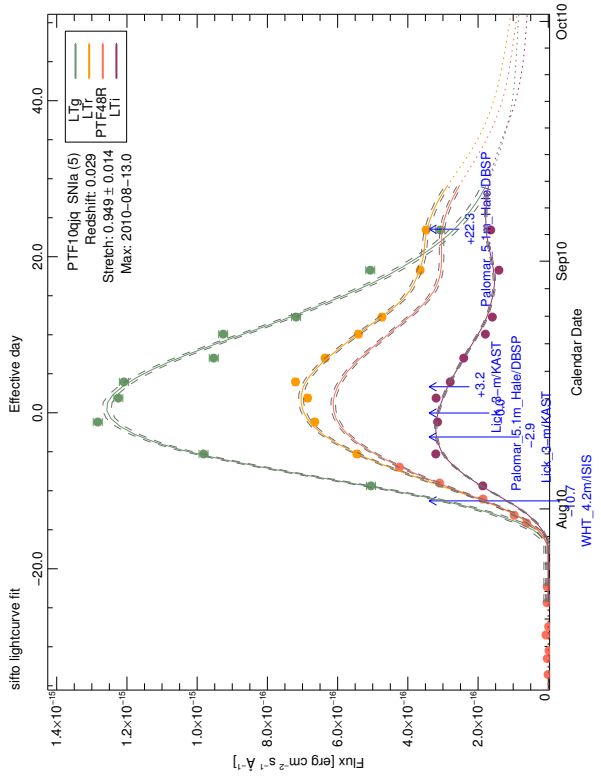

FIGURE E.22: SiFTO light curve fit of PTF10qjq

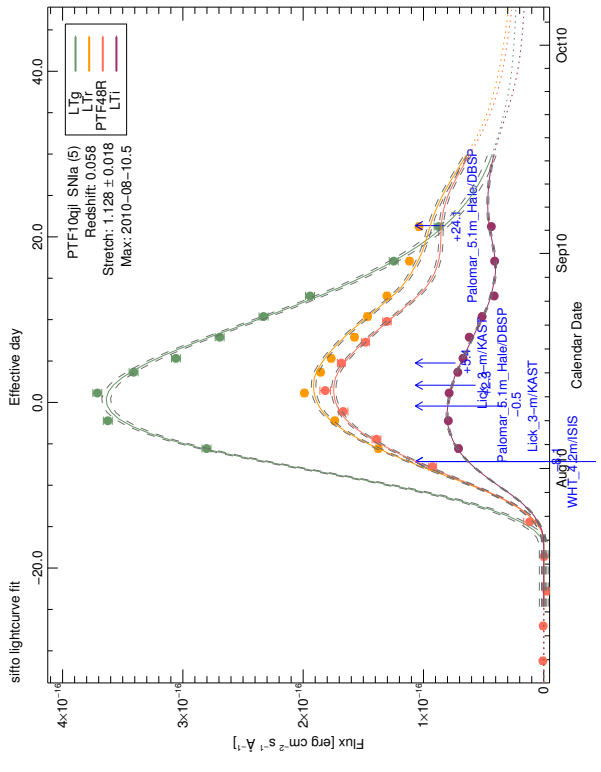

FIGURE E.21: SiFTO light curve fit of PTF10qjl

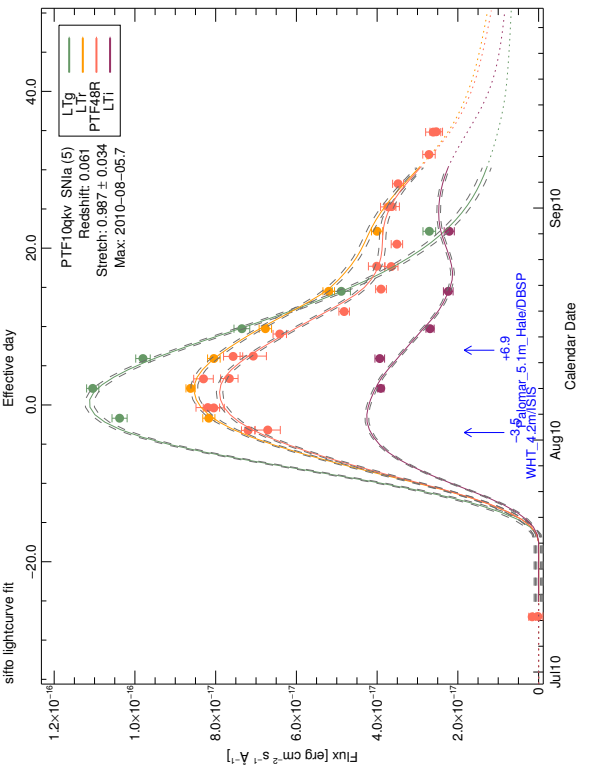

FIGURE E.24: SiFTO light curve fit of PTF10qkv

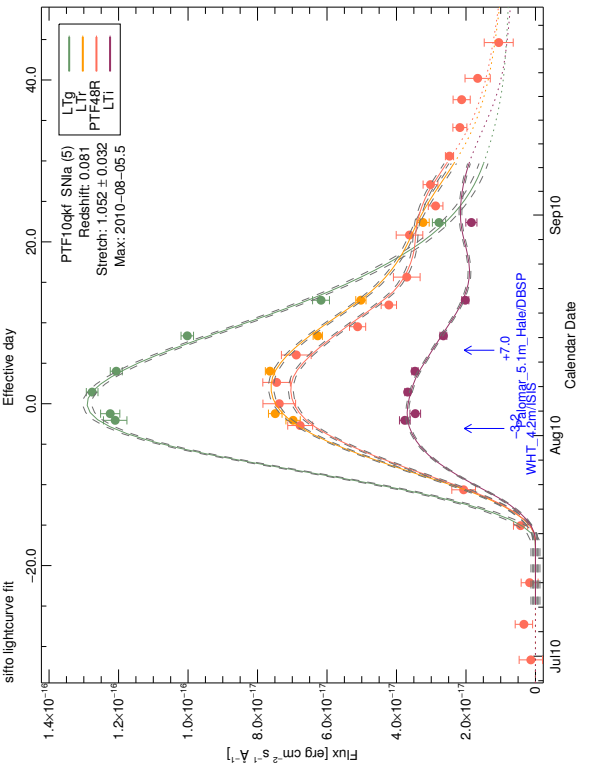

FIGURE E.23: SiFTO light curve fit of PTF10qkf

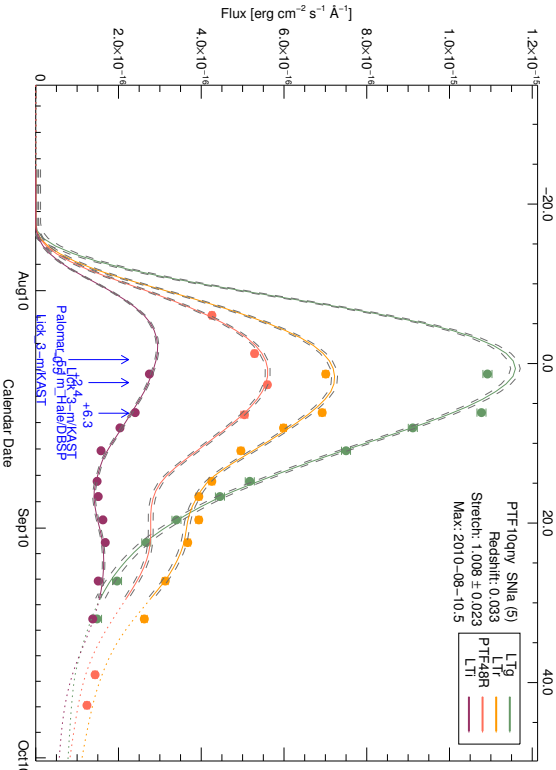

FIGURE E.25: SiFTO light curve fit of PTF10qky

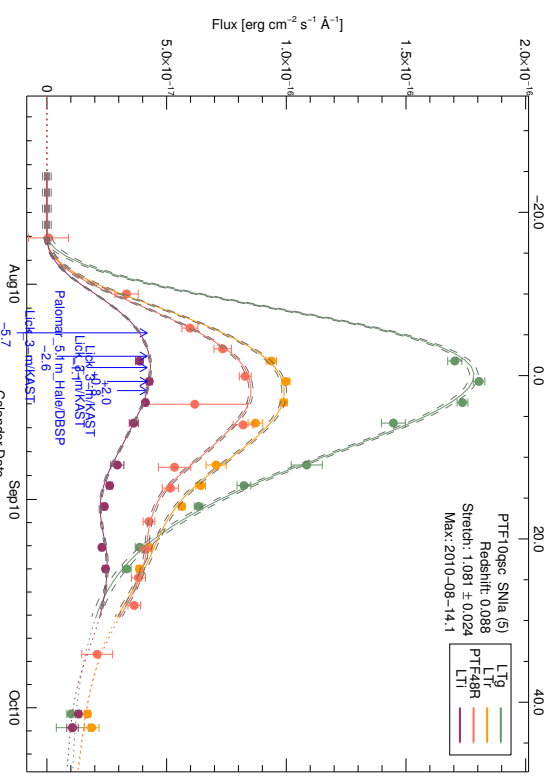

FIGURE E.26: SiFTO light curve fit of PTF10qly

FIGURE E.27: SiFTO light curve fit of PTF10qny

FIGURE E.28: SiFTO light curve fit of PTF10qsc

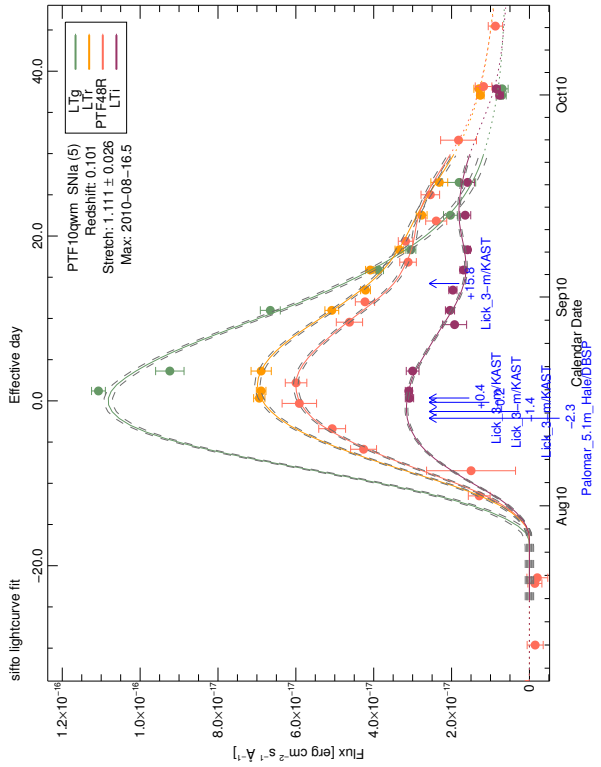

FIGURE E.30: SiFTO light curve fit of PTF10qwm

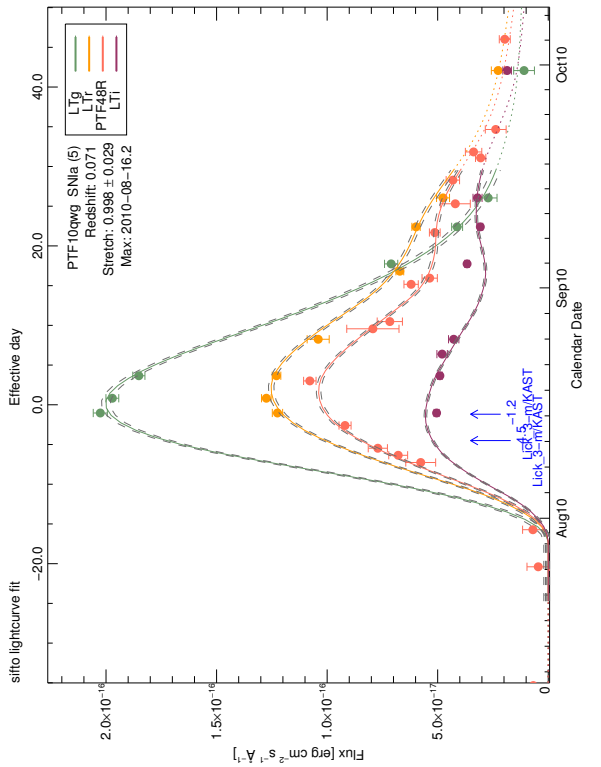

FIGURE E.29: SiFTO light curve fit of PTF10qwg

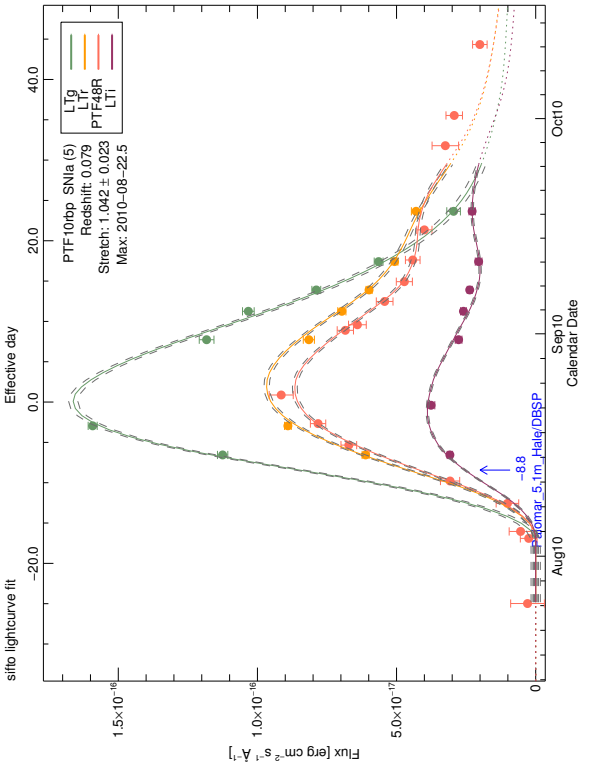

FIGURE E.32: SiFTO light curve fit of PTF10rbp

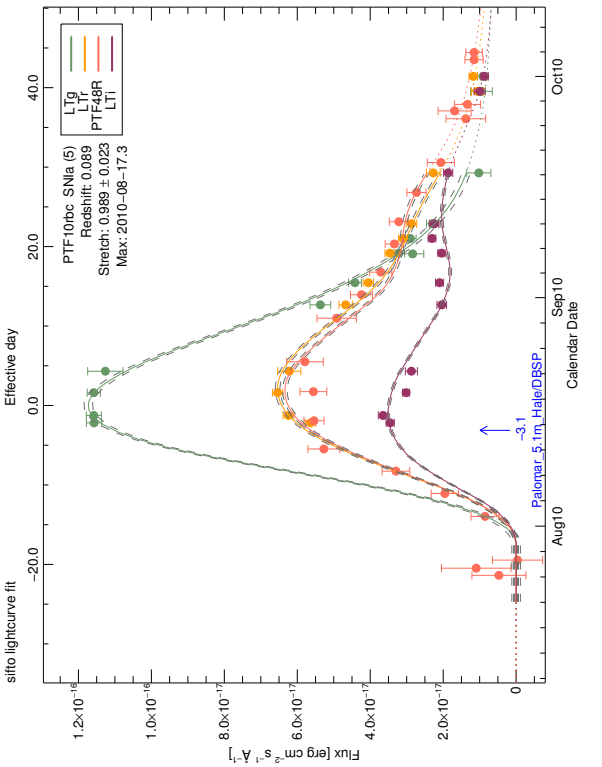

FIGURE E.31: SiFTO light curve fit of PTF10rbc

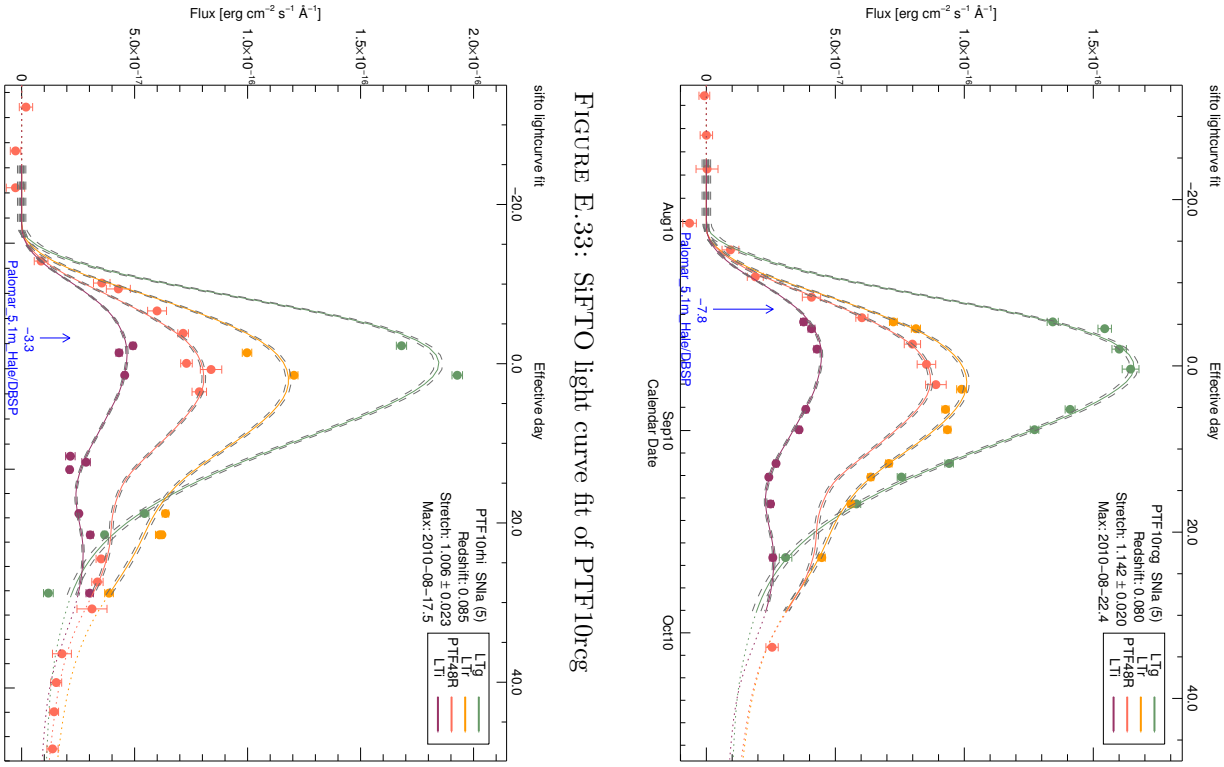

FIGURE E.33: SiFTO light curve fit of PTF10rcg

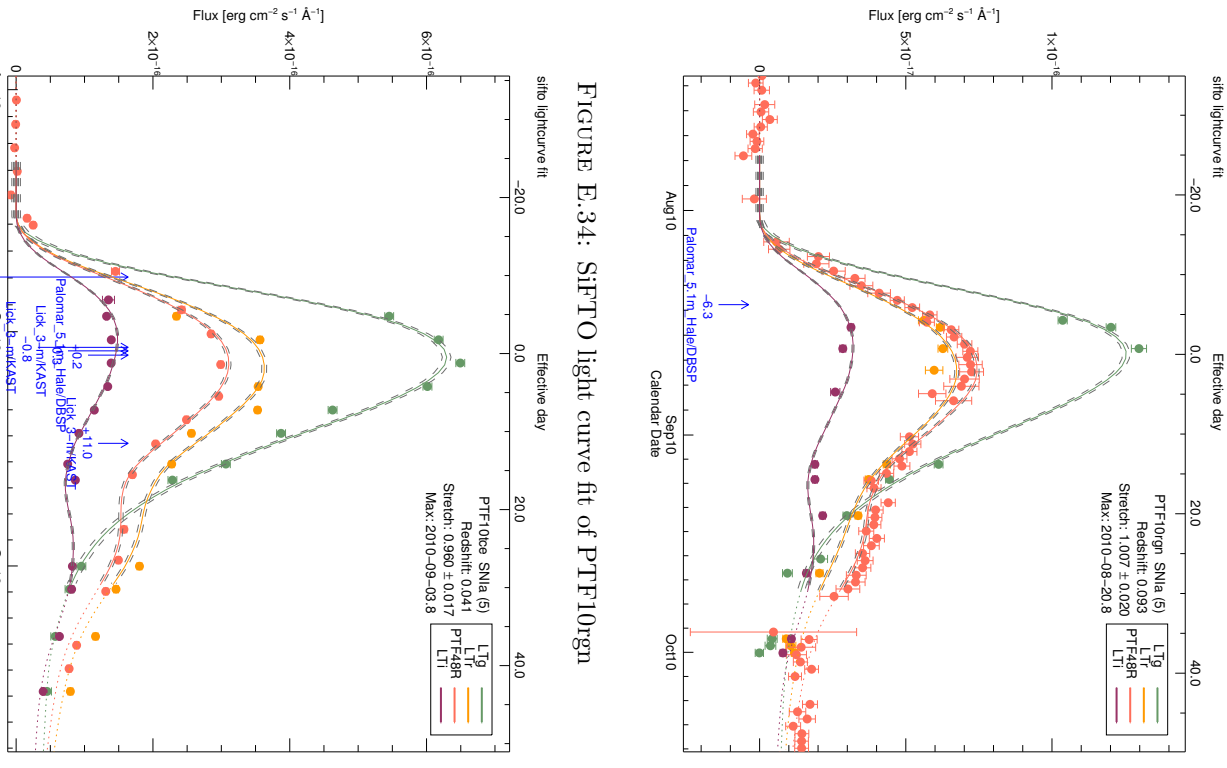

FIGURE E.34: SiFTO light curve fit of PTF10rgn

FIGURE E.35: SiFTO light curve fit of PTF10rhi

FIGURE E.36: SiFTO light curve fit of PTF10tce

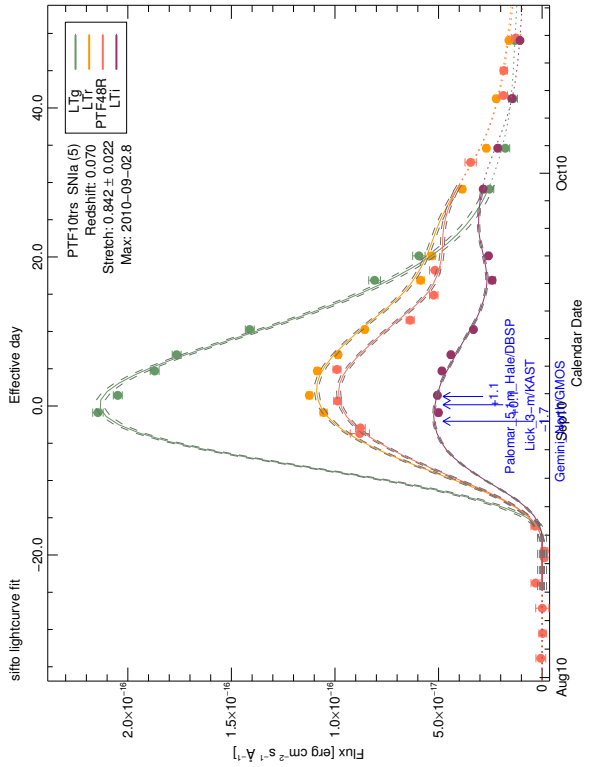

FIGURE E.38: SiFTO light curve fit of PTF10trs

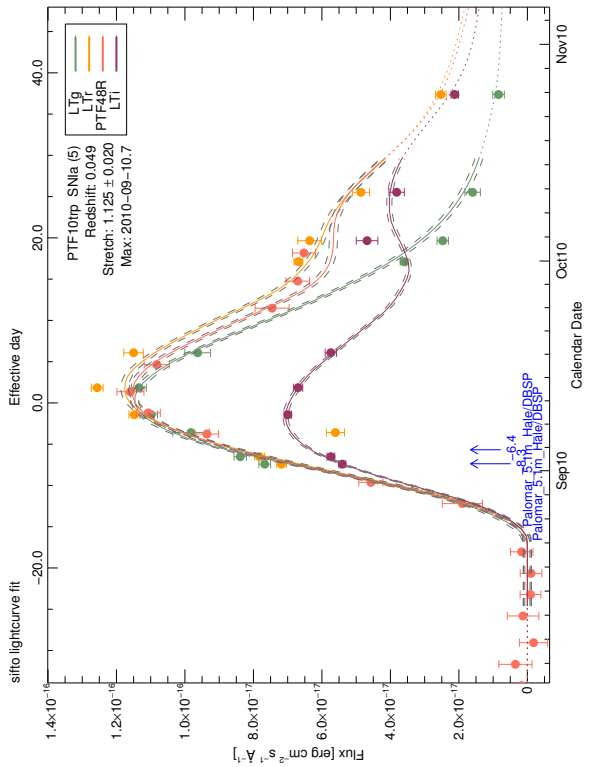

FIGURE E.37: SiFTO light curve fit of PTF10trp

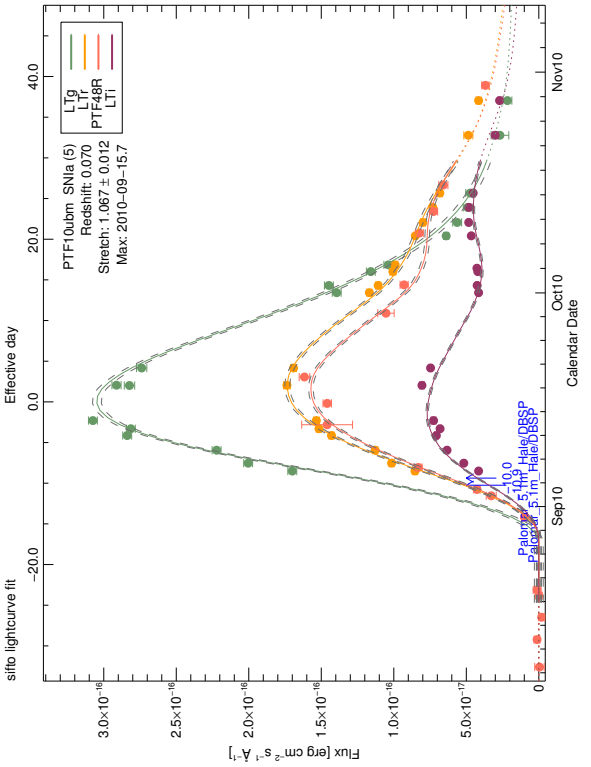

FIGURE E.40: SiFTO light curve fit of PTF10ubm

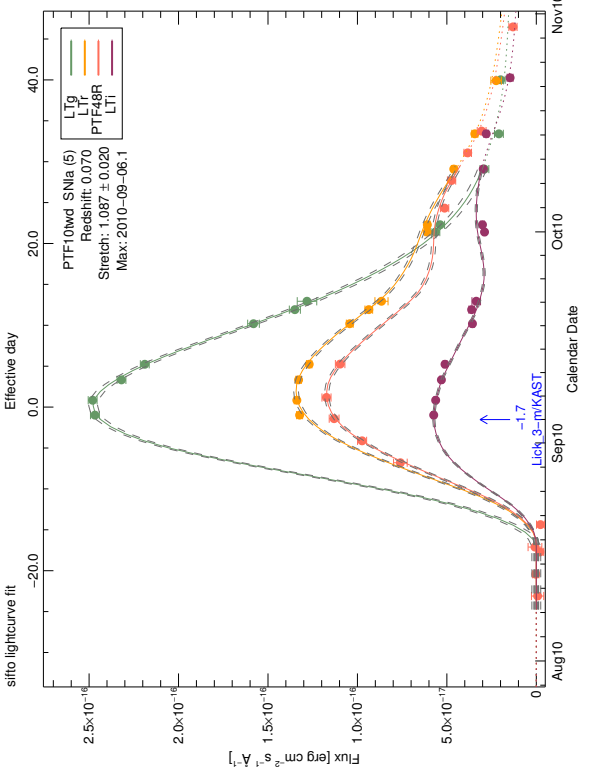

FIGURE E.39: SiFTO light curve fit of PTF10twd

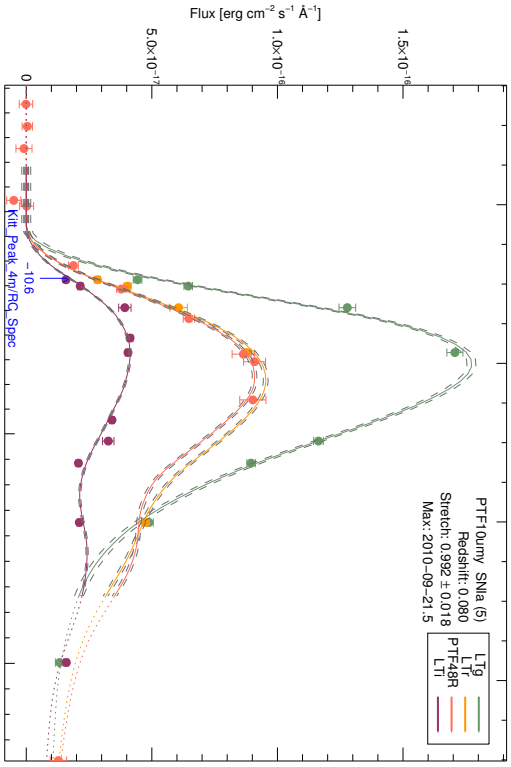

FIGURE E.41: SiFTO light curve fit of PTF10ufj

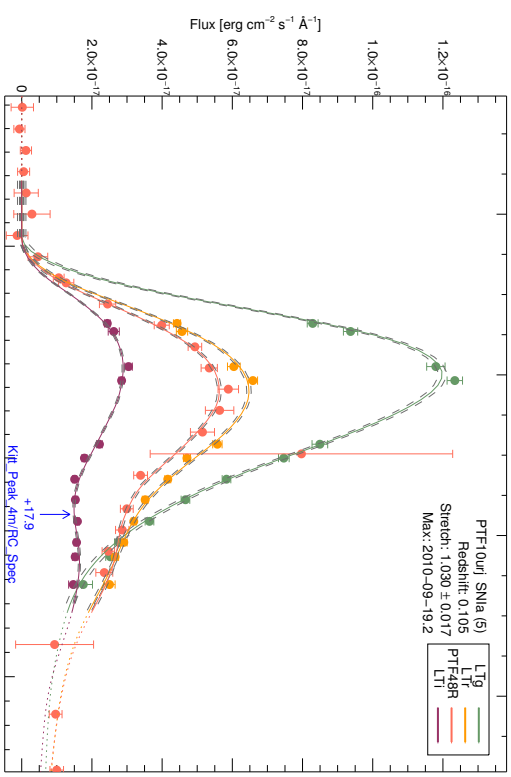

FIGURE E.43: SiFTO light curve fit of PTF10umy

FIGURE E.42: SiFTO light curve fit of PTF10umw

FIGURE E.44: SiFTO light curve fit of PTF10uri

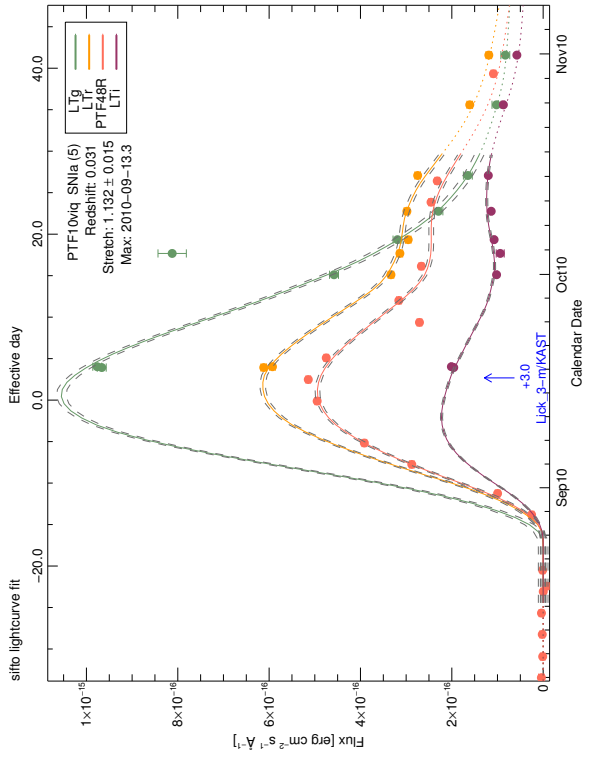

FIGURE E.46: SiFTO light curve fit of PTF10viq

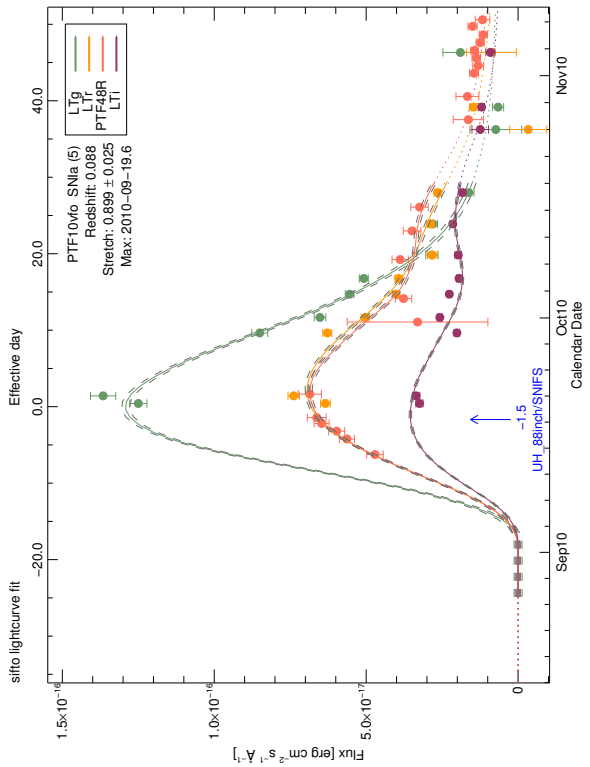

FIGURE E.45: SiFTO light curve fit of PTF10vfo

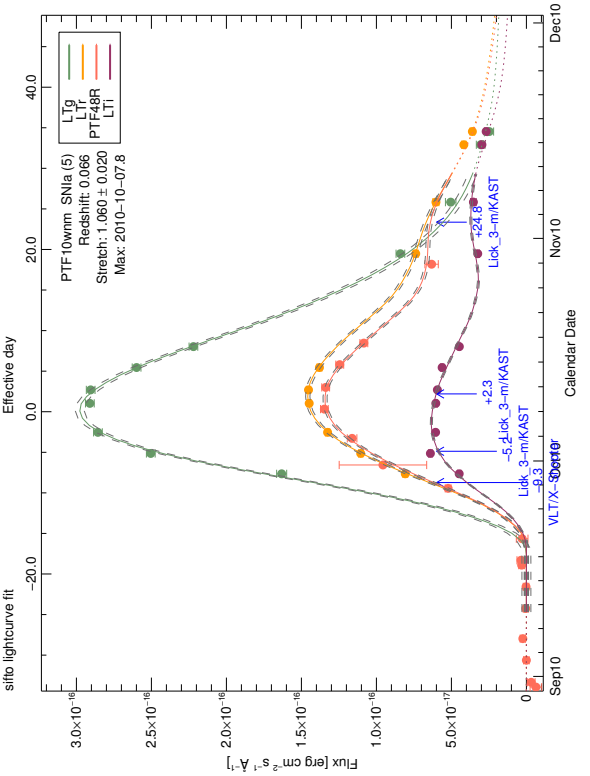

FIGURE E.48: SiFTO light curve fit of PTF10wnm

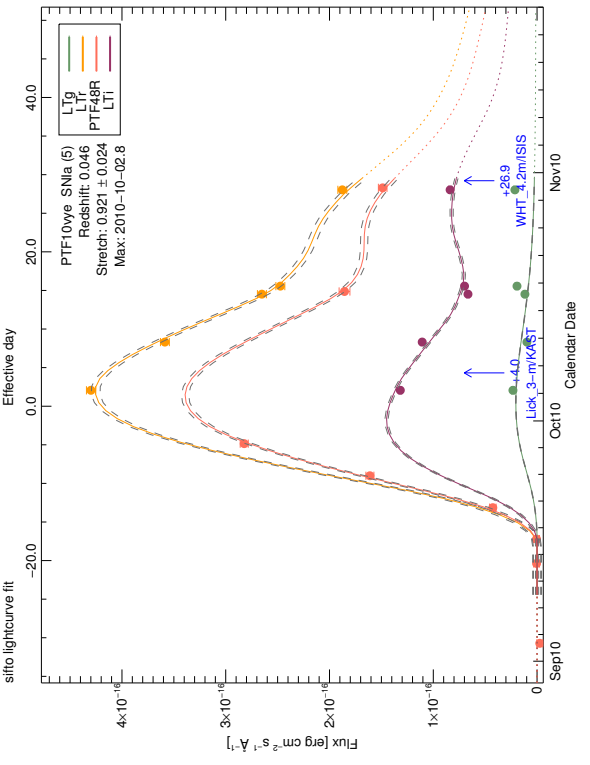

FIGURE E.47: SiFTO light curve fit of PTF10vye

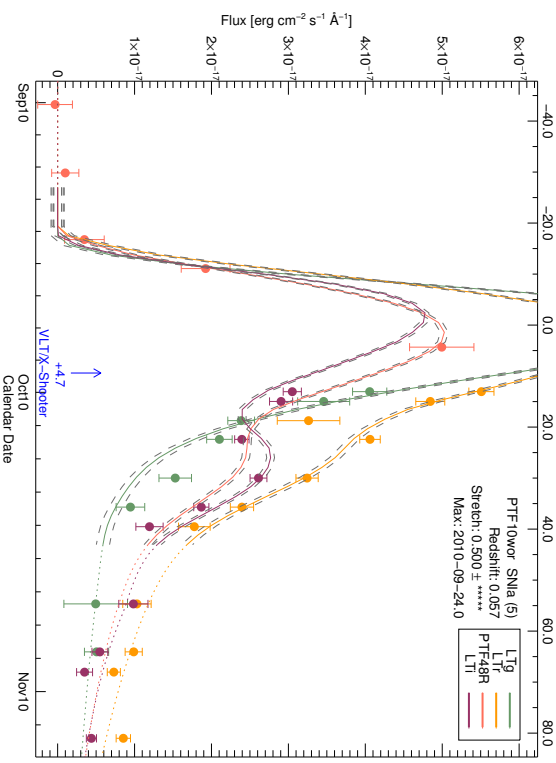

FIGURE E.49: SiFTO light curve fit of PTF10wnq

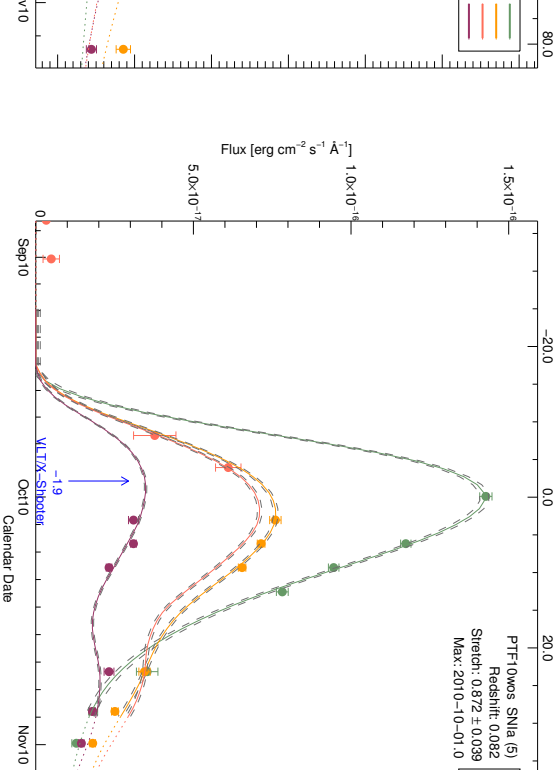

FIGURE E.51: SiFTO light curve fit of PTF10wor

FIGURE E.50: SiFTO light curve fit of PTF10wof

FIGURE E.52: SiFTO light curve fit of PTF10wos

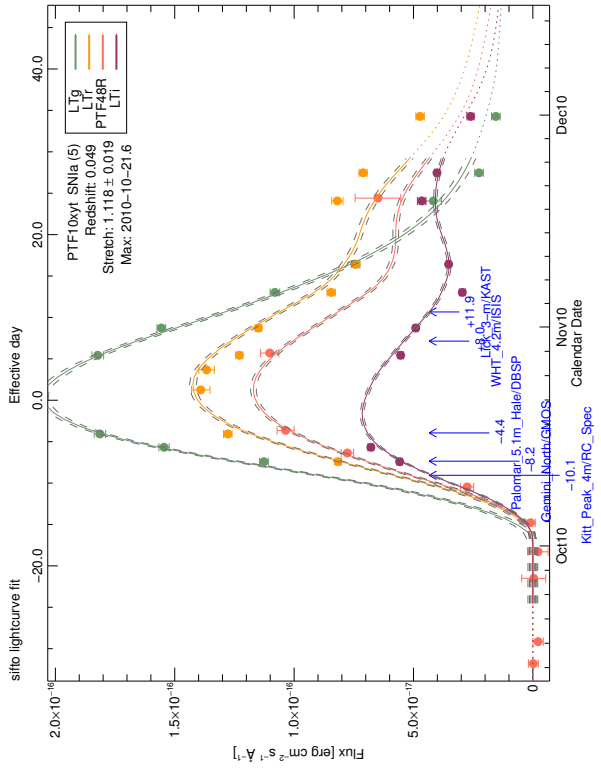

FIGURE E.54: SiFTO light curve fit of PTF10xyt

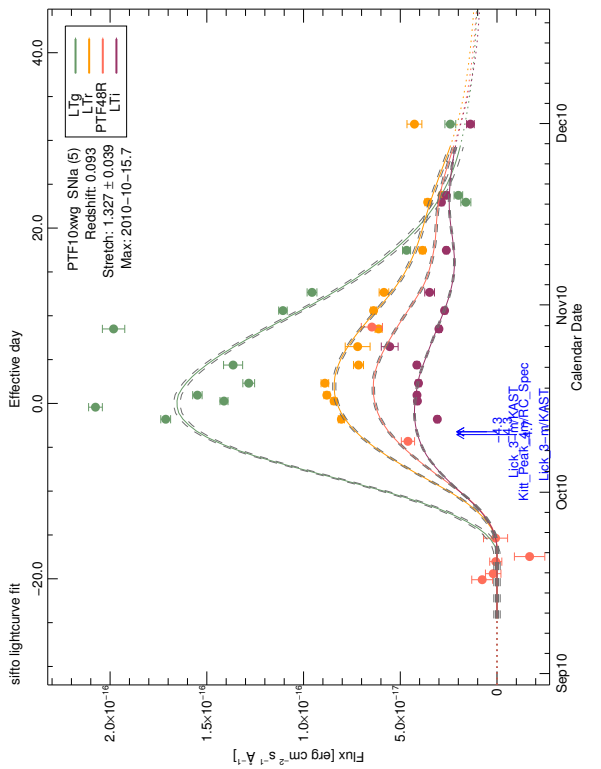

FIGURE E.53: SiFTO light curve fit of PTF10xwg

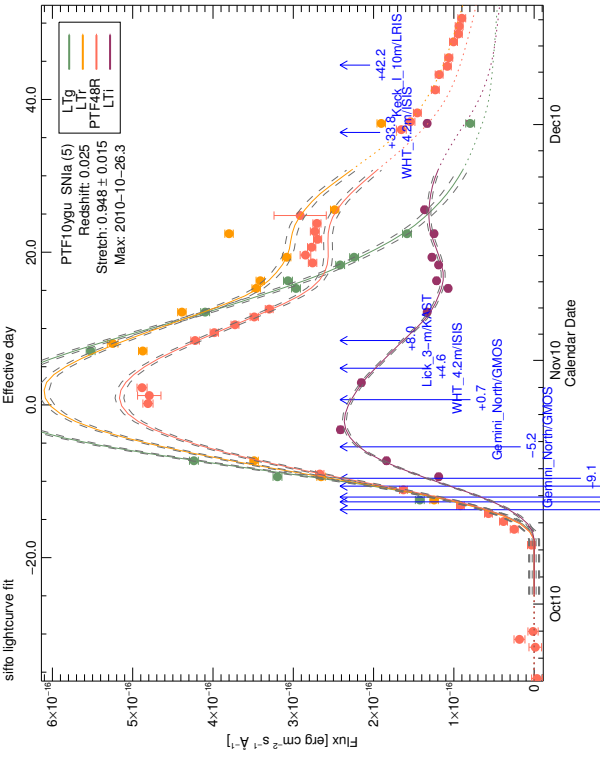

FIGURE E.56: SiFTO light curve fit of PTF10ygu

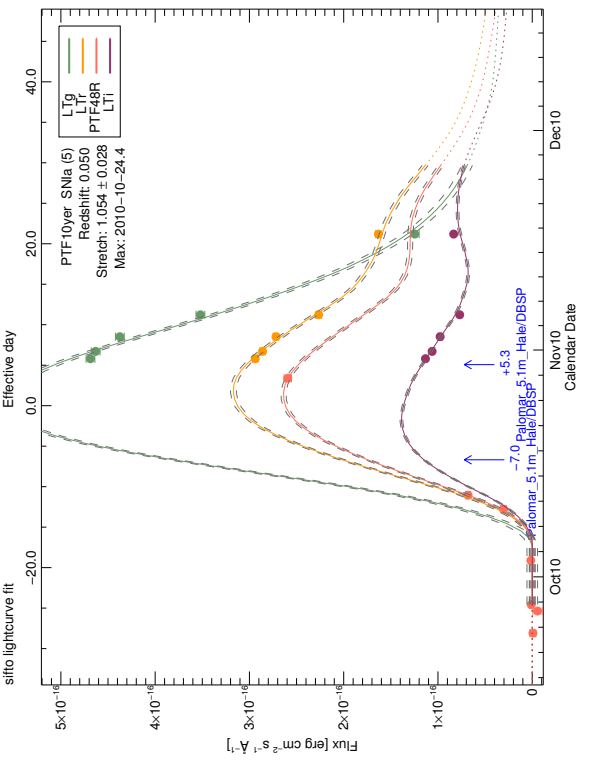

FIGURE E.55: SiFTO light curve fit of PTF10yer

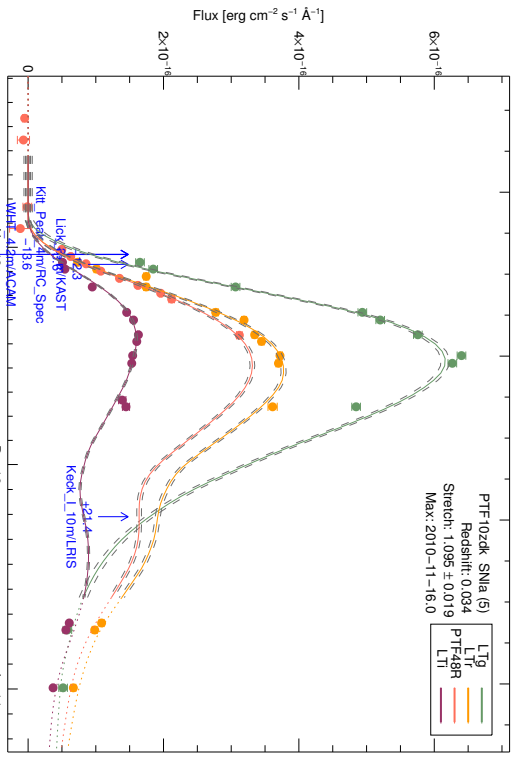

FIGURE E.57: SiFTO light curve fit of PTF10yux

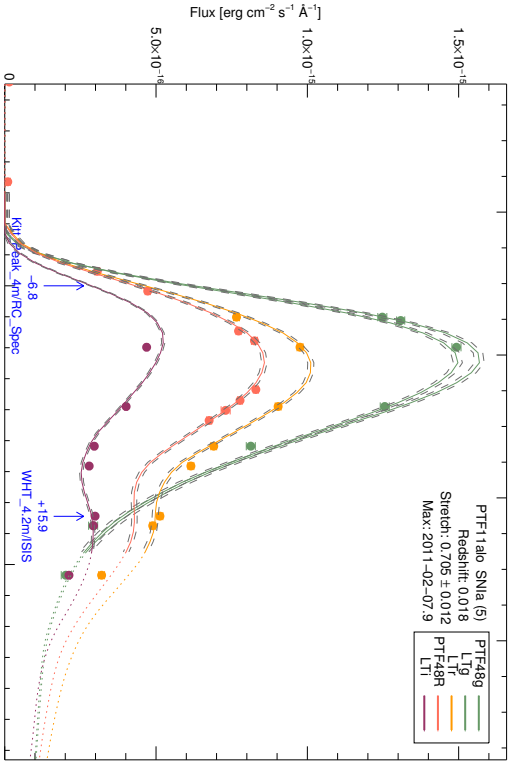

FIGURE E.59: SiFTO light curve fit of PTF10zdk

FIGURE E.58: SiFTO light curve fit of PTF10zbk

FIGURE E.60: SiFTO light curve fit of PTF11alo

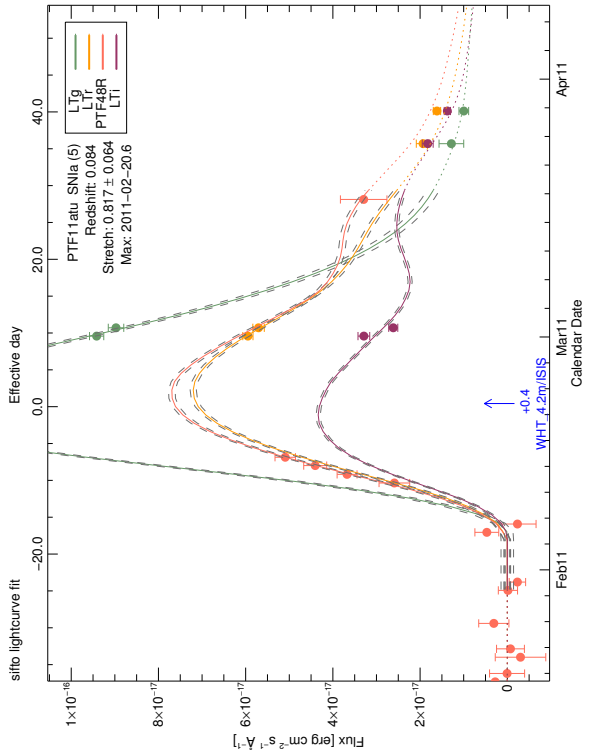

FIGURE E.62: SiFTO light curve fit of PTF11atu

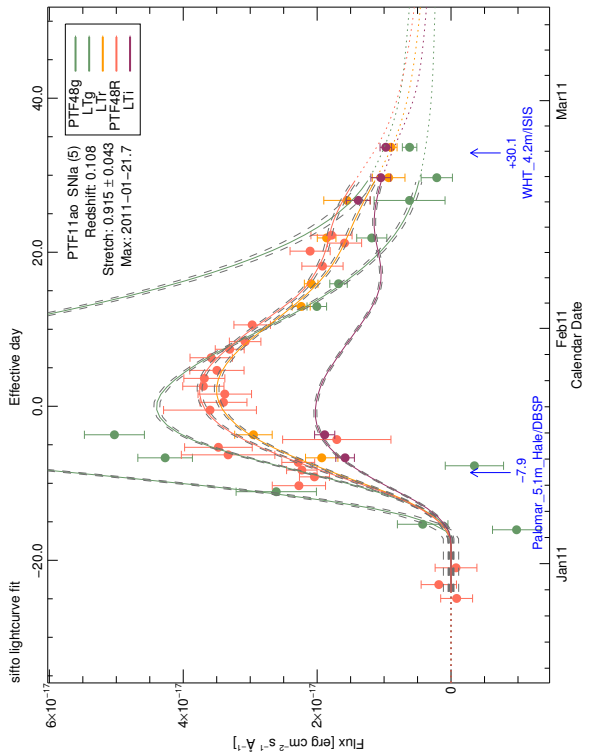

FIGURE E.61: SiFTO light curve fit of PTF11ao

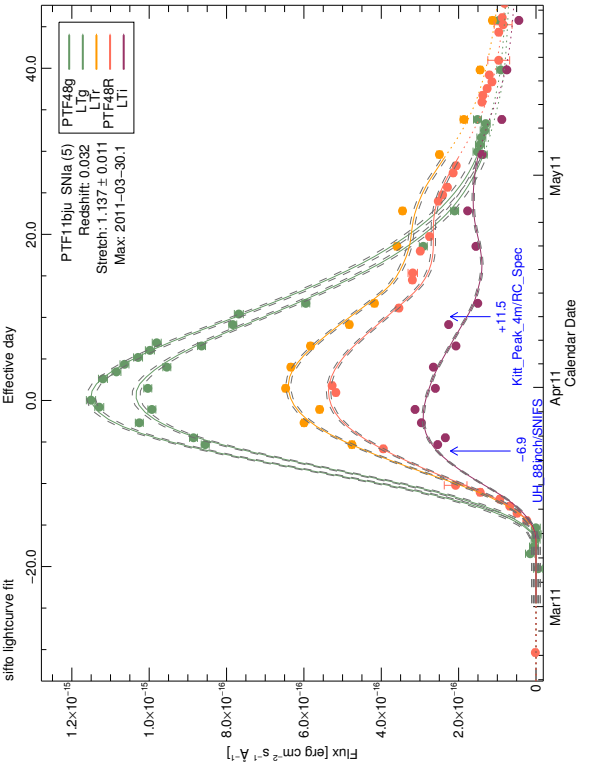

FIGURE E.64: SiFTO light curve fit of PTF11bju

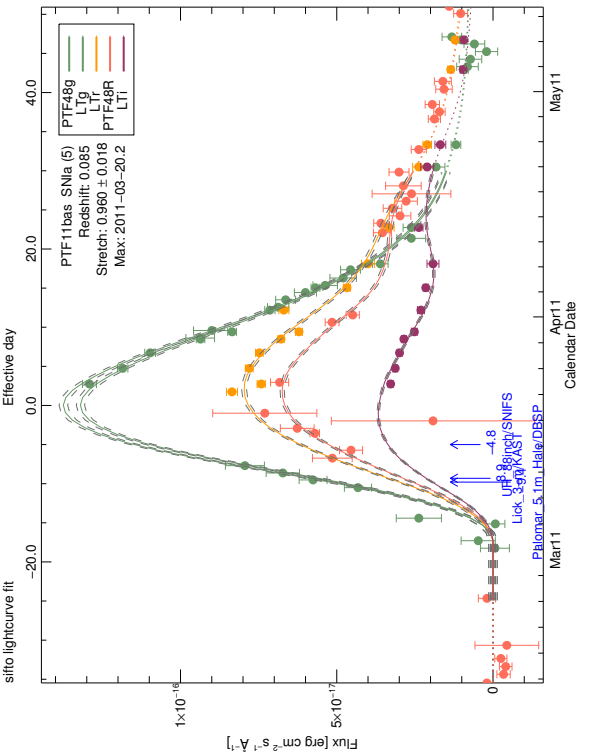

FIGURE E.63: SiFTO light curve fit of PTF11bas

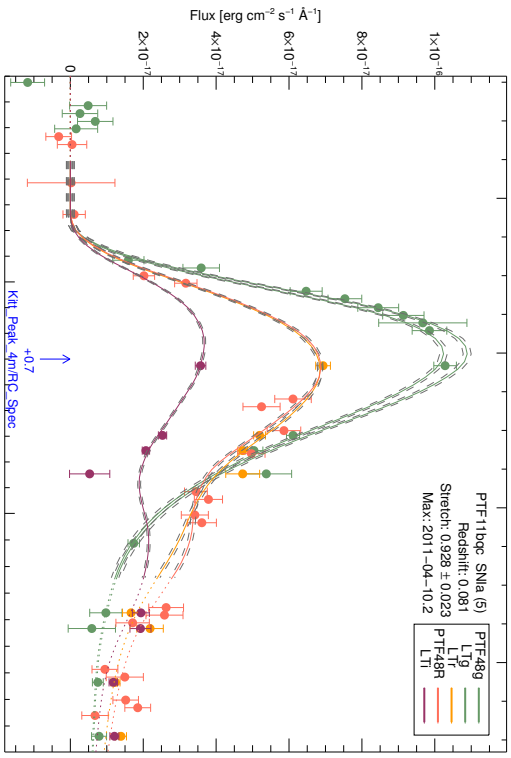

FIGURE E.65: SiFTO light curve fit of PTF11bnx

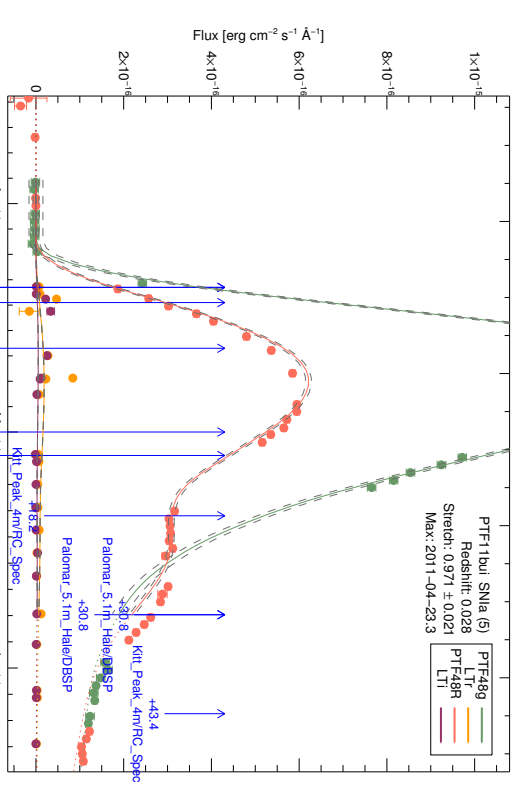

FIGURE E.67: SiFTO light curve fit of PTF11bqc

FIGURE E.66: SiFTO light curve fit of PTF11bpw

FIGURE E.68: SiFTO light curve fit of PTF11bui

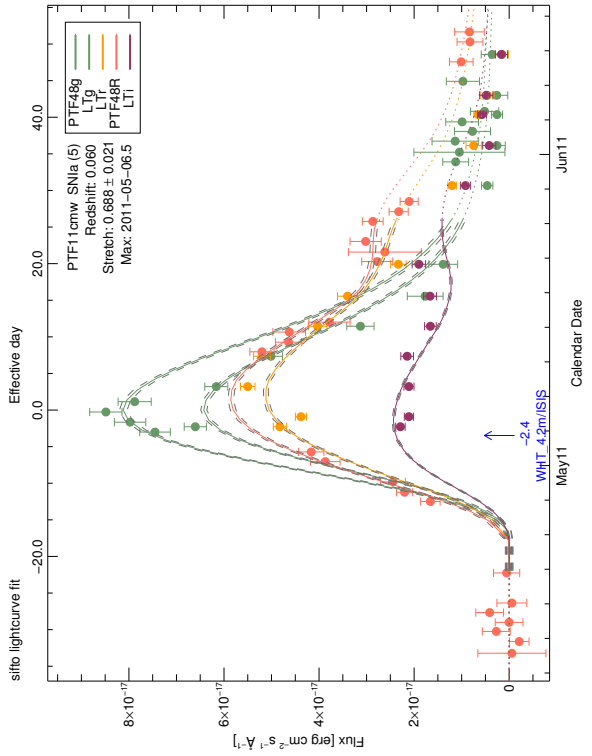

FIGURE E.70: SiFTO light curve fit of PTF11cmw

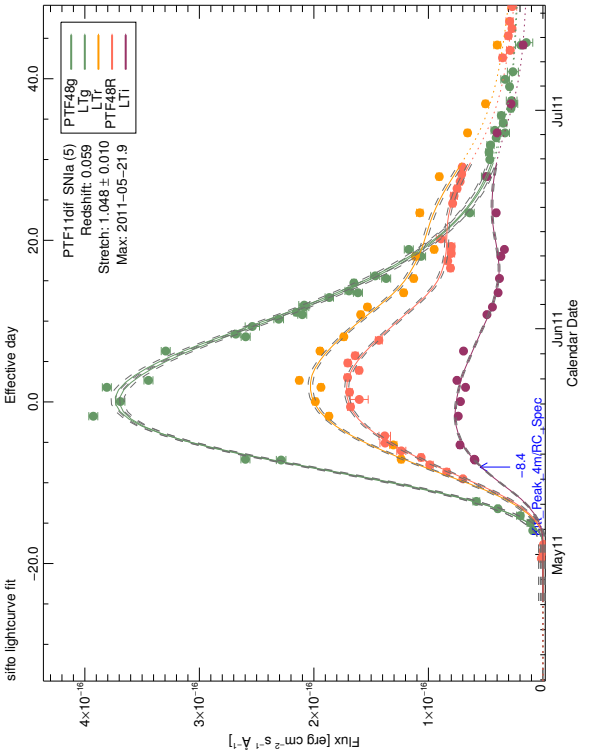

FIGURE E.72: SiFTO light curve fit of PTF11dif

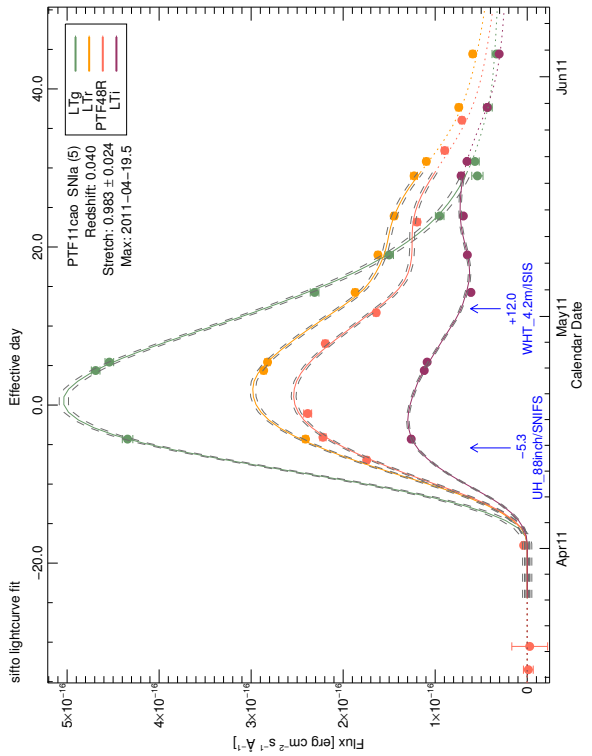

FIGURE E.69: SiFTO light curve fit of PTF11cao

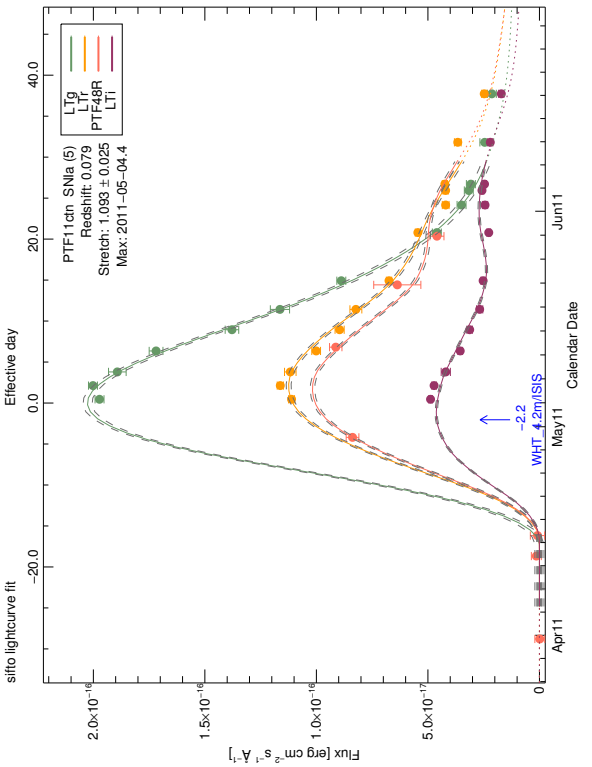

FIGURE E.71: SiFTO light curve fit of PTF11ctn

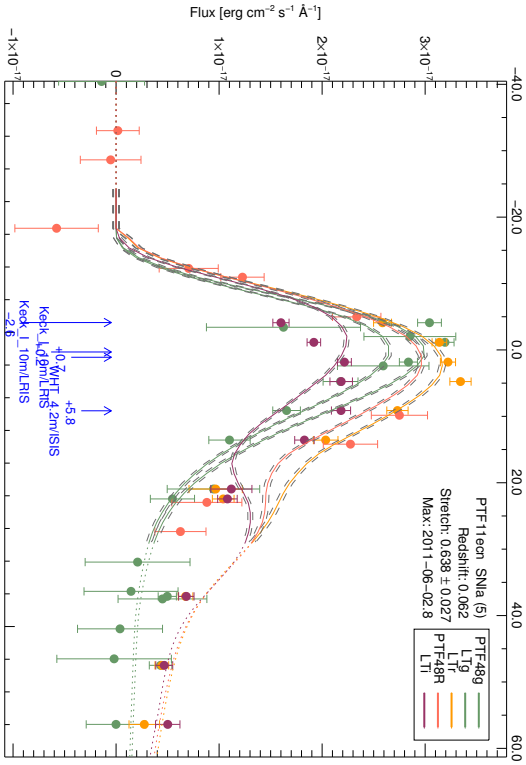

FIGURE E.73: SiFTO light curve fit of PTF11drz

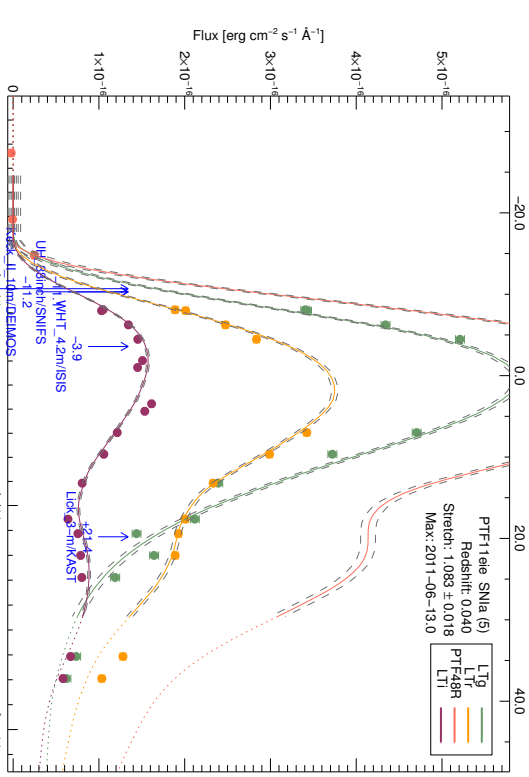

FIGURE E.75: SiFTO light curve fit of PTF11ecn

FIGURE E.74: SiFTO light curve fit of PTF11dxu

FIGURE E.76: SiFTO light curve fit of PTF11eie

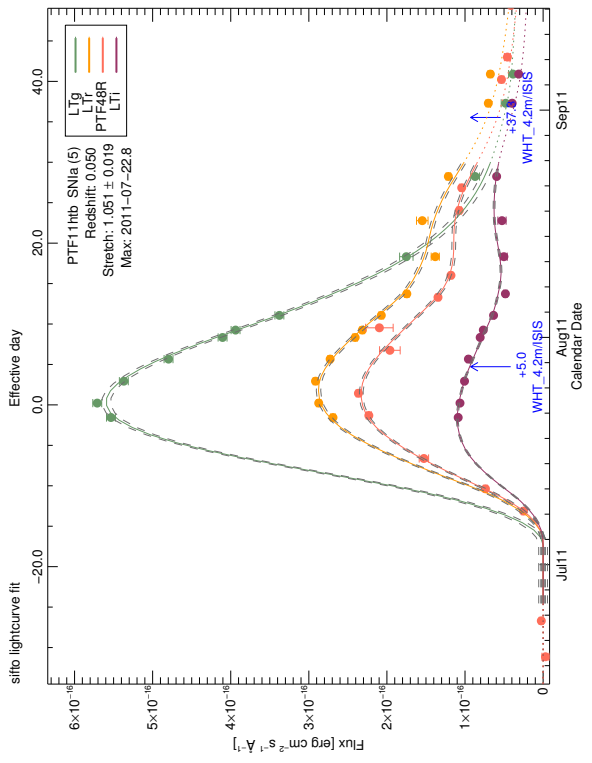

FIGURE E.78: SiFTO light curve fit of PTF11htb

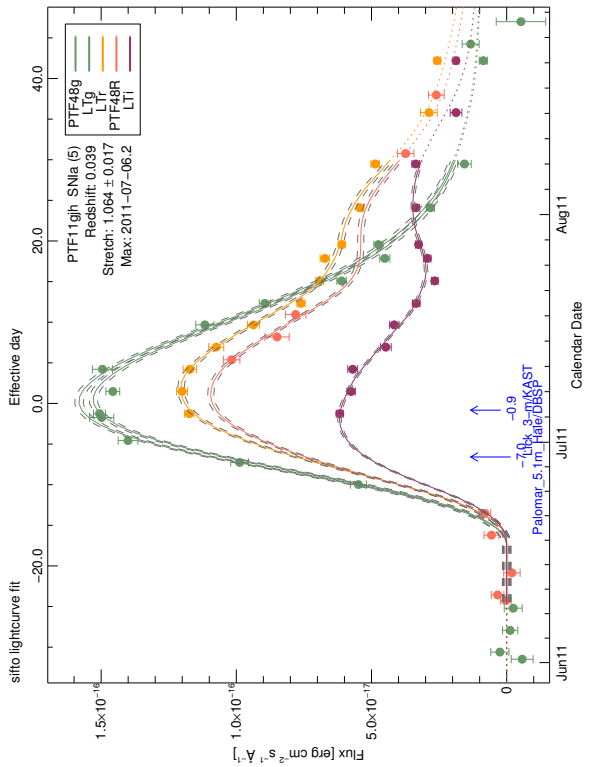

FIGURE E.77: SiFTO light curve fit of PTF11gjh

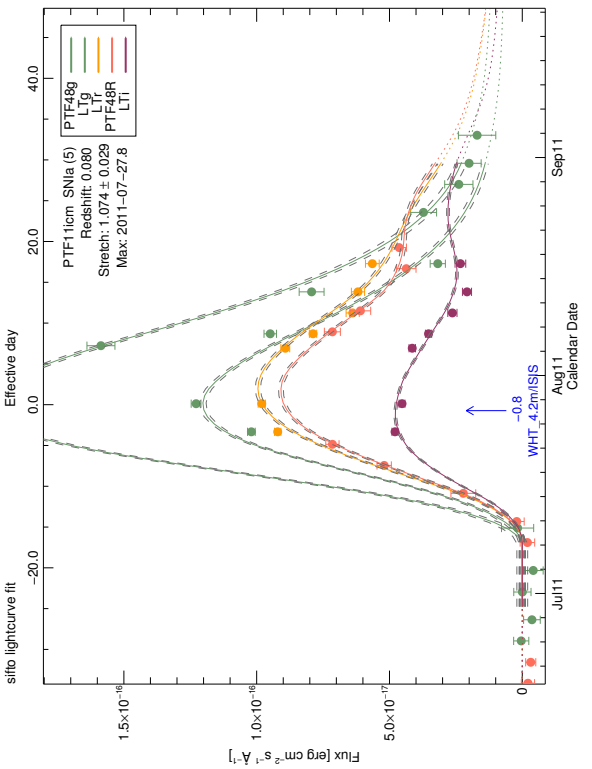

FIGURE E.80: SiFTO light curve fit of PTF11icm

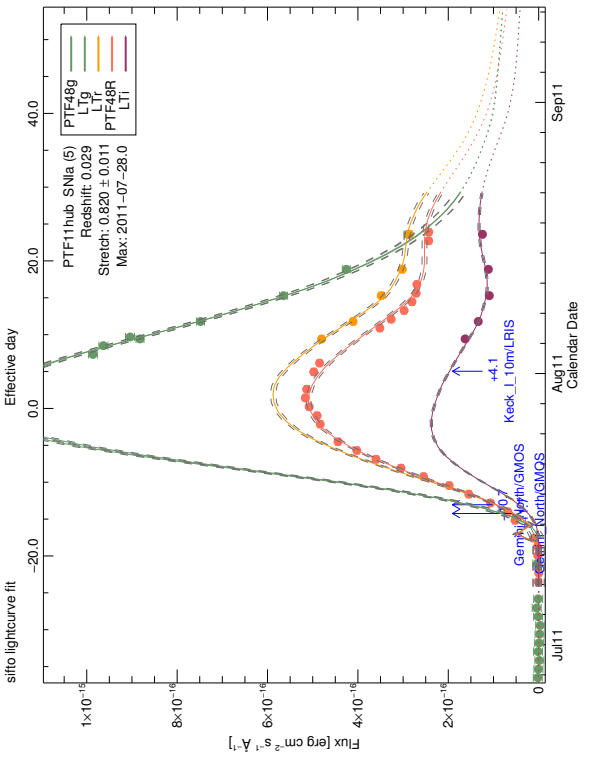

FIGURE E.79: SiFTO light curve fit of PTF11hub

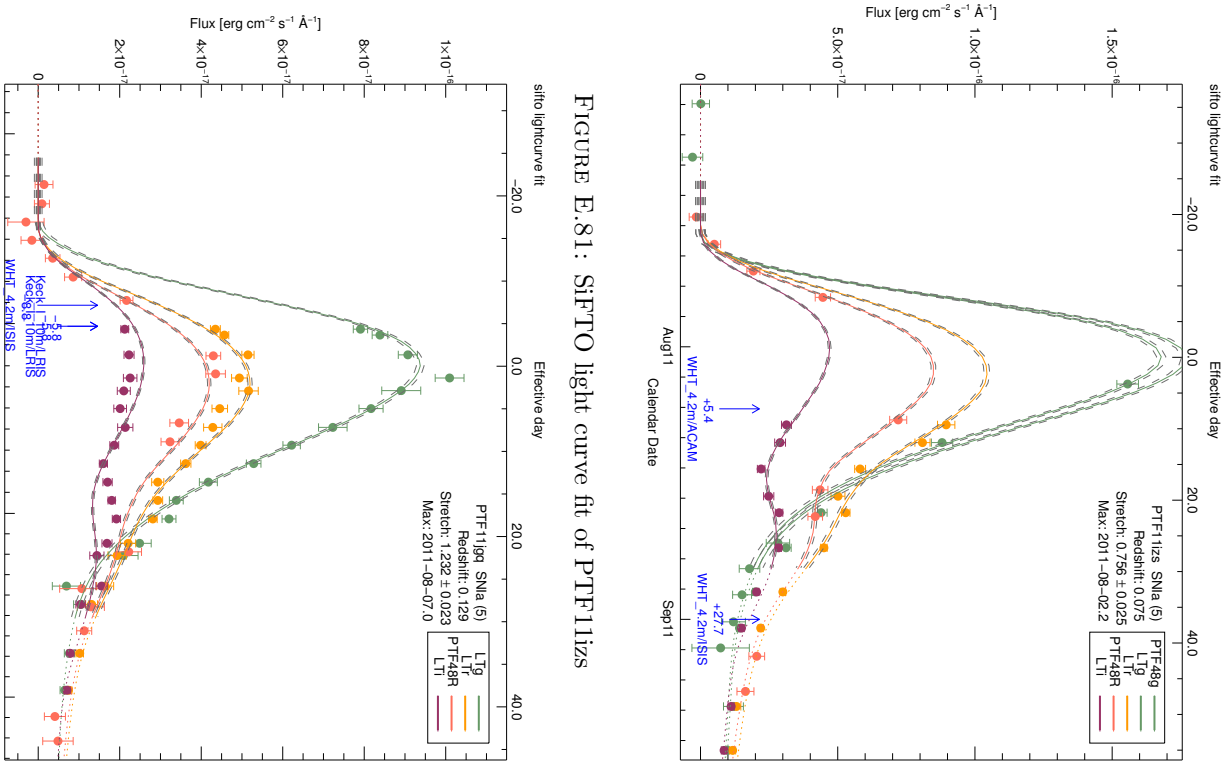

FIGURE E.81: SiFTO light curve fit of PTF11izs

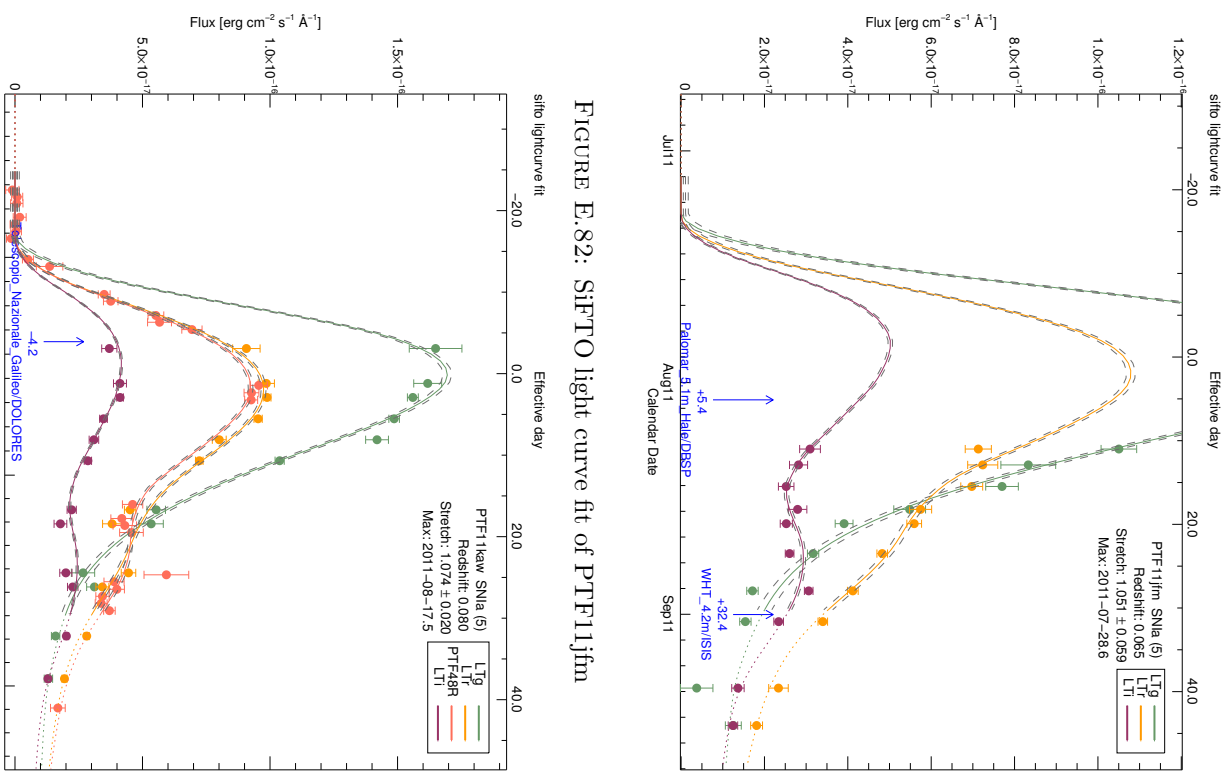

FIGURE E.82: SiFTO light curve fit of PTF11jfm

FIGURE E.83: SiFTO light curve fit of PTF11jgq

FIGURE E.84: SiFTO light curve fit of PTF11kaw

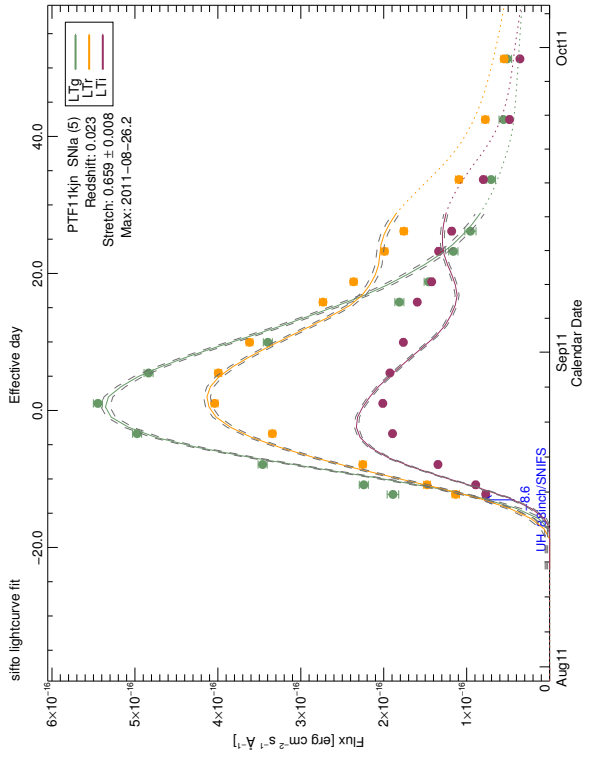

FIGURE E.86: SiFTO light curve fit of PTF11kjn

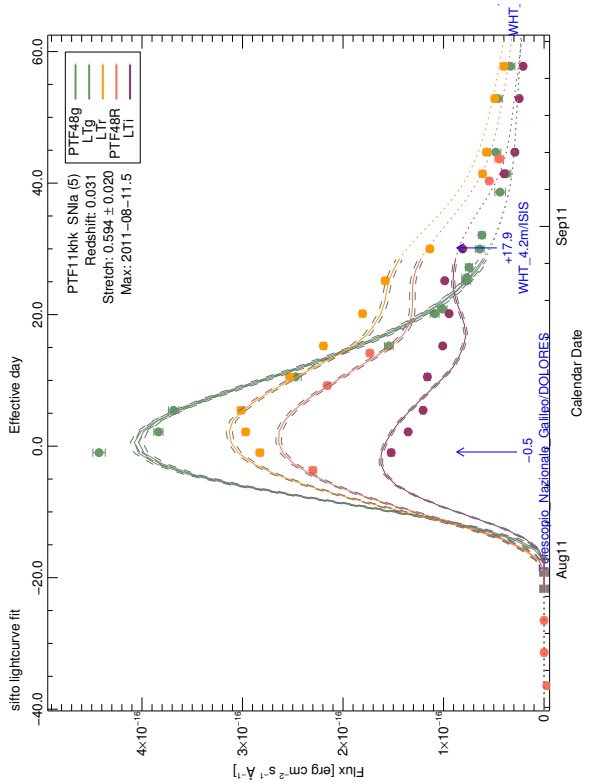

FIGURE E.85: SiFTO light curve fit of PTF11khk

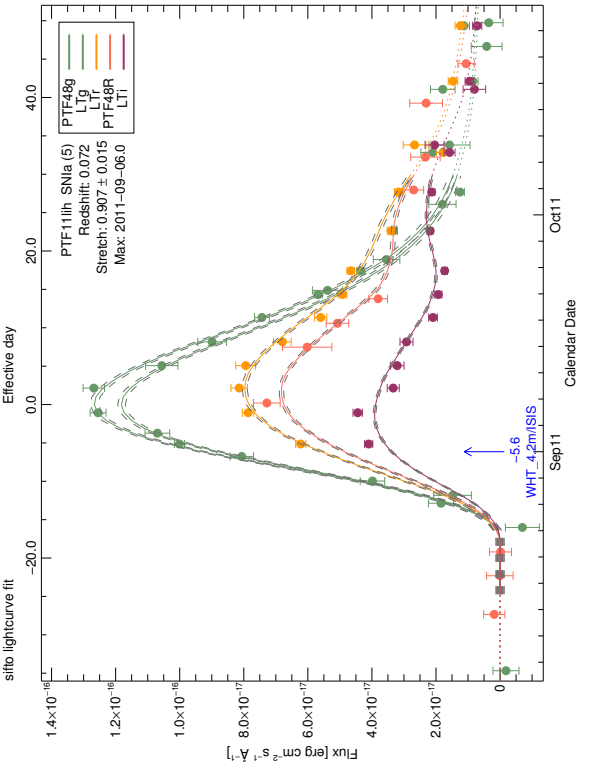

FIGURE E.88: SiFTO light curve fit of PTF11lih

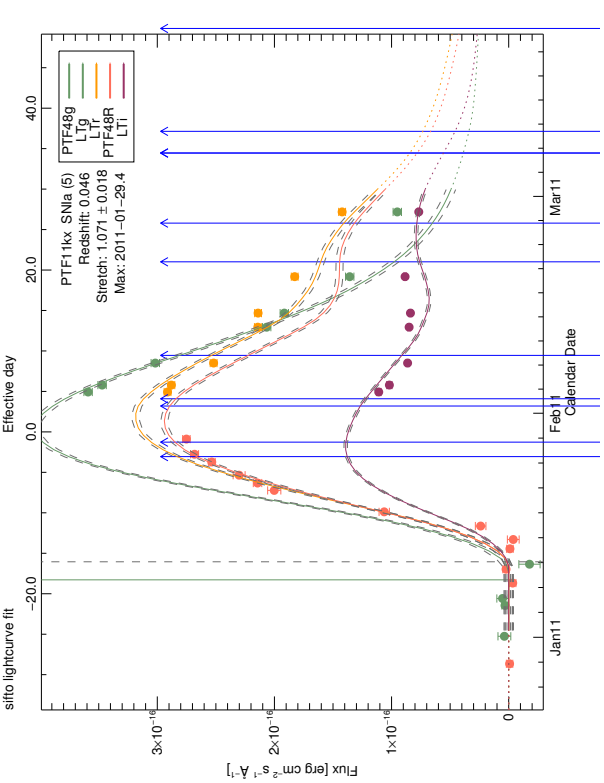

FIGURE E.87: SiFTO light curve fit of PTF11kx

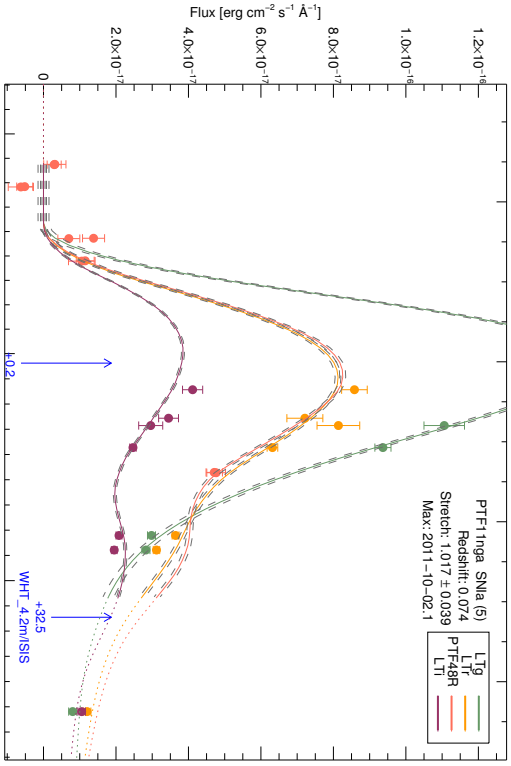

FIGURE E.89: SiFTO light curve fit of PTF11mkx

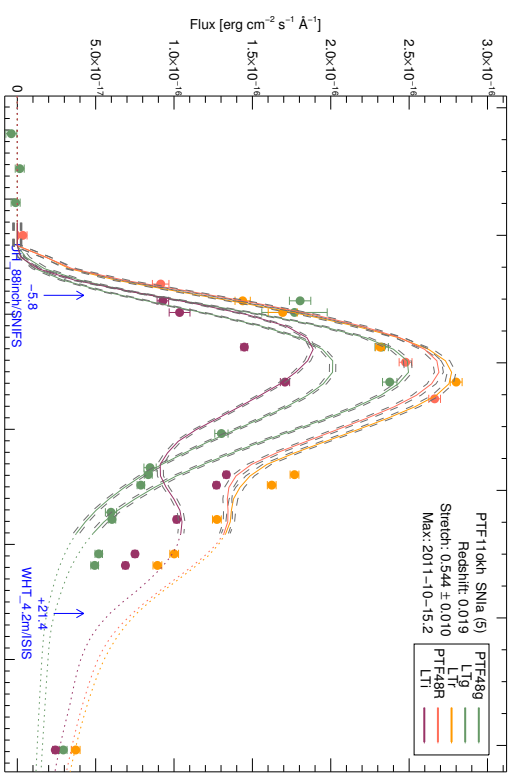

FIGURE E.91: SiFTO light curve fit of PTF11nga

FIGURE E.90: SiFTO light curve fit of PTF11mty

FIGURE E.92: SiFTO light curve fit of PTF11okh

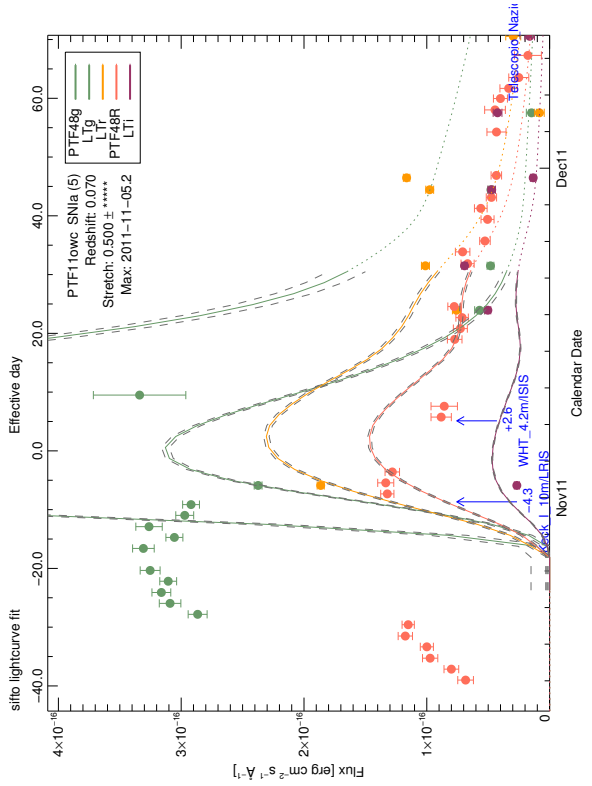

FIGURE E.94: SiFTO light curve fit of PTF11owc

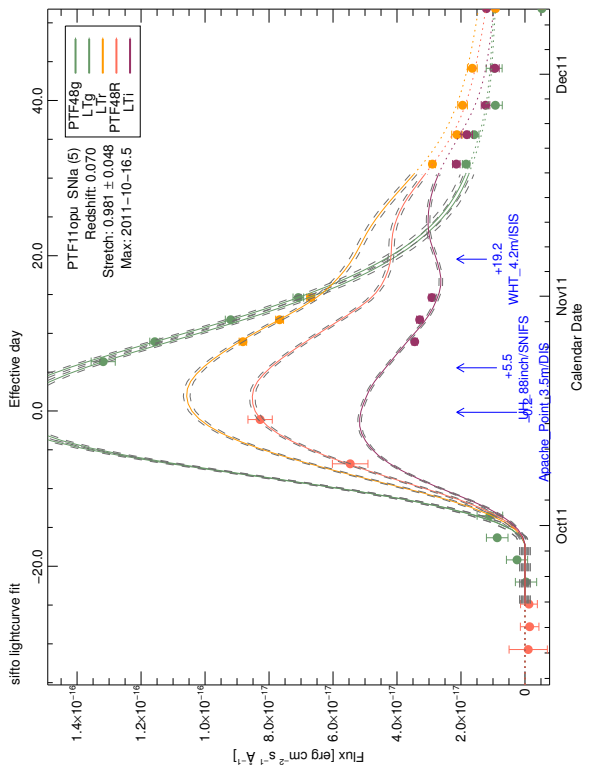

FIGURE E.93: SiFTO light curve fit of PTF11opu

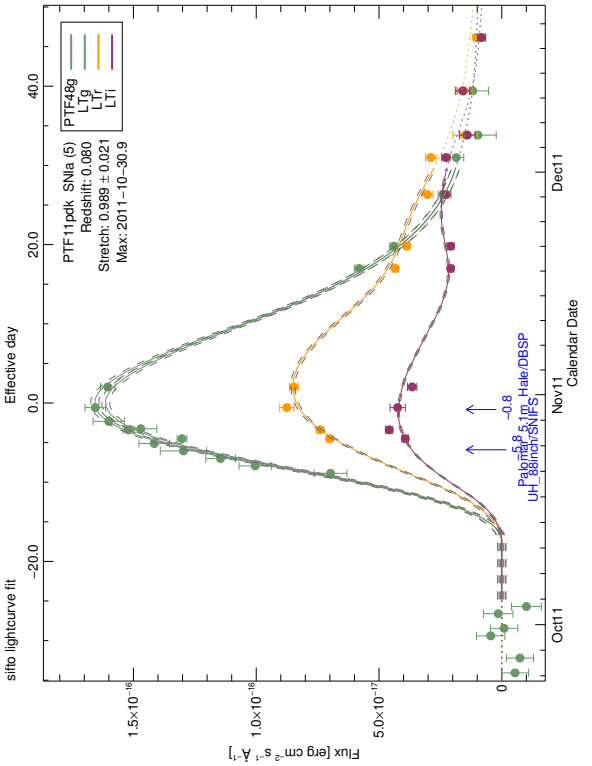

FIGURE E.96: SiFTO light curve fit of PTF11pdk

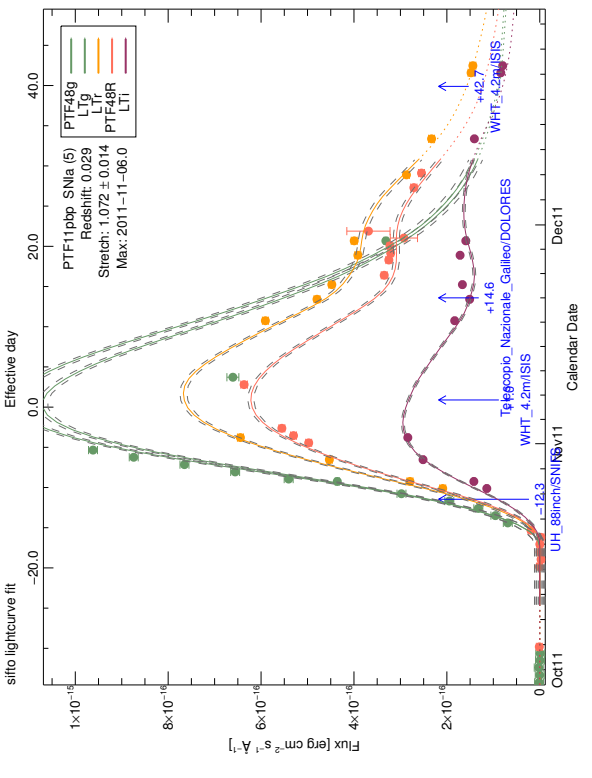

FIGURE E.95: SiFTO light curve fit of PTF11pbp

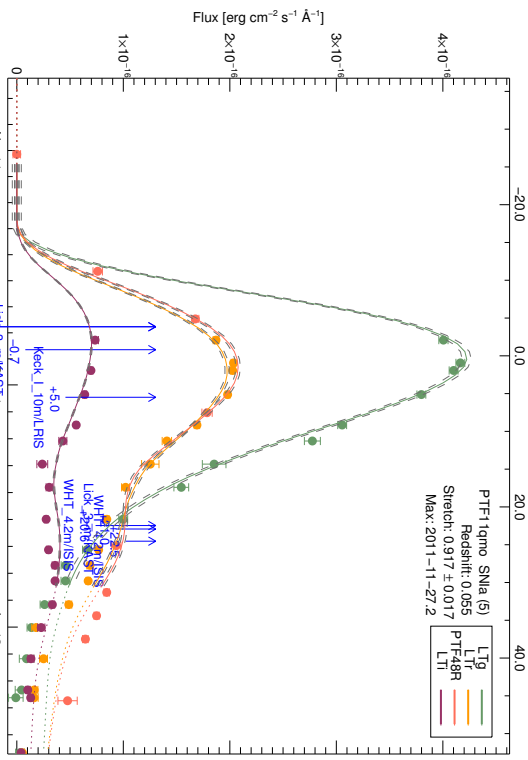

FIGURE E.99: SiFTO light curve fit of PTF11qmo

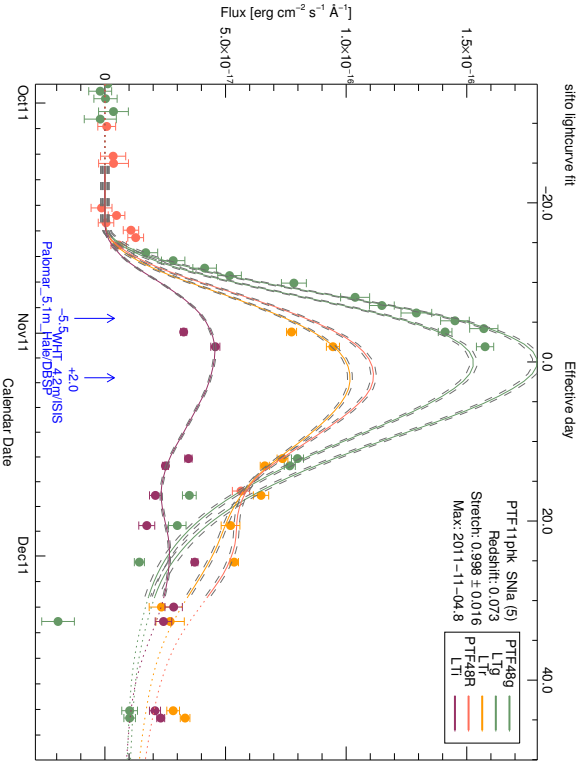

FIGURE E.97: SiFTO light curve fit of PTF11phk

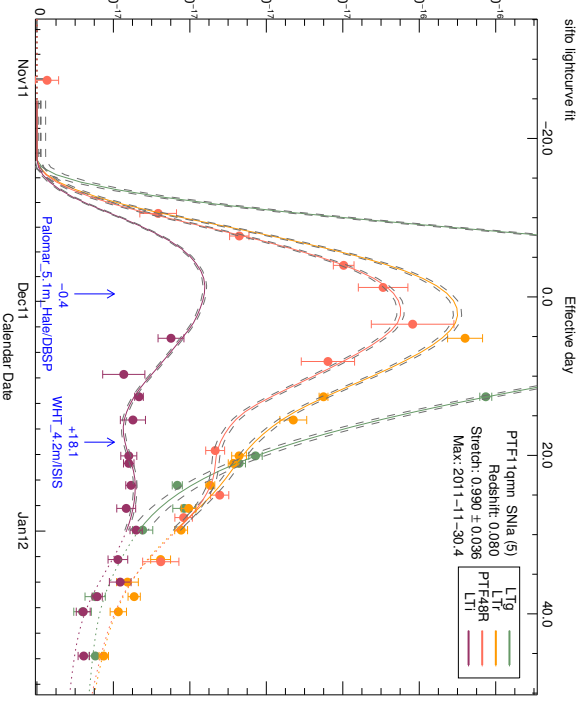

FIGURE E.98: SiFTO light curve fit of PTF11qmn

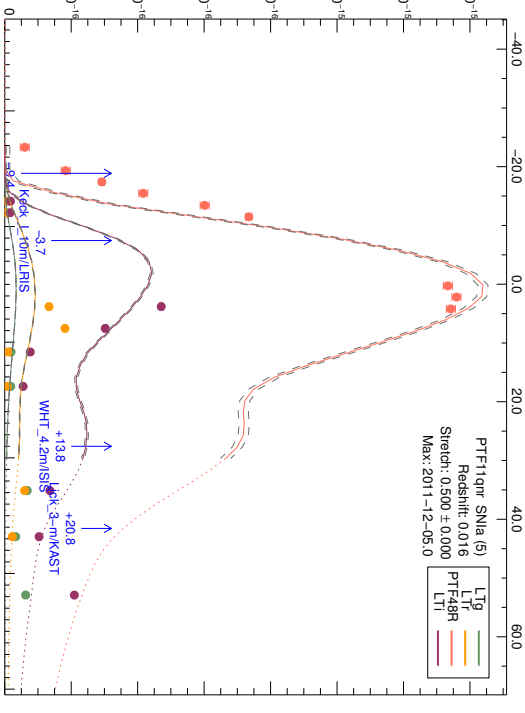

FIGURE E.100: SiFTO light curve fit of PTF11qmr

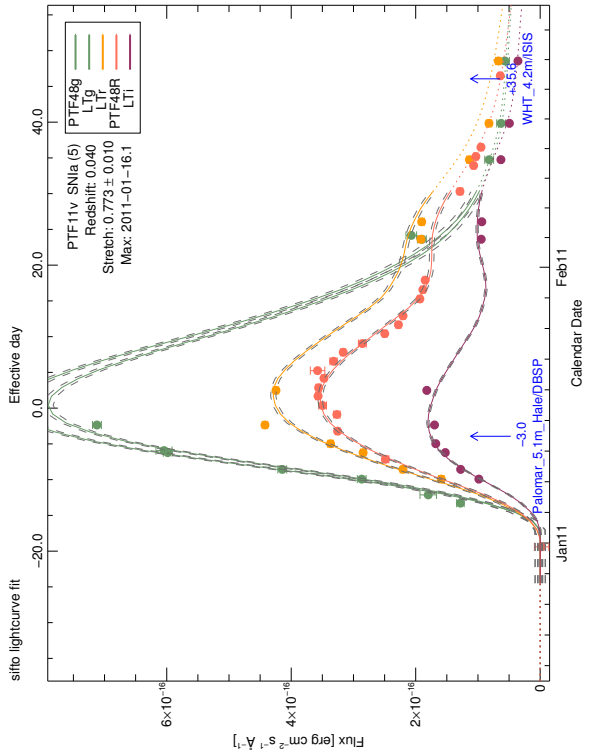

FIGURE E.102: SiFTO light curve fit of PTF11v

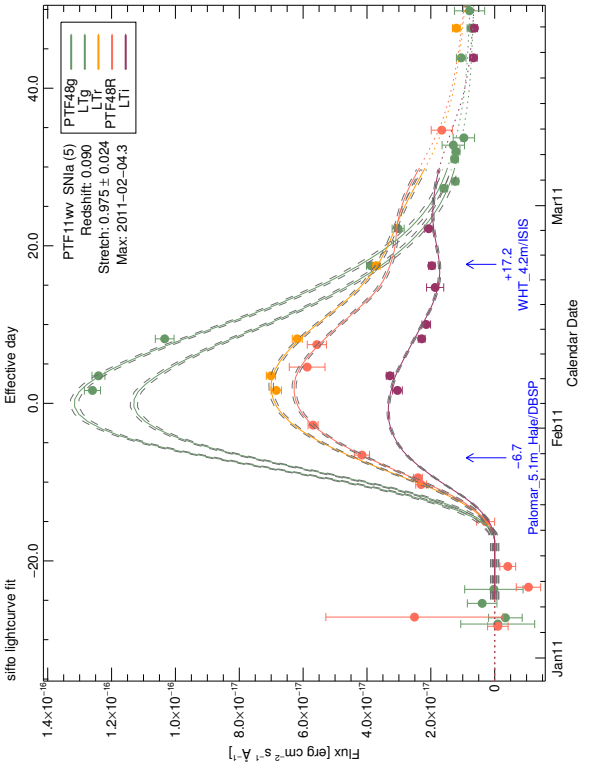

FIGURE E.101: SiFTO light curve fit of PTF11qzq

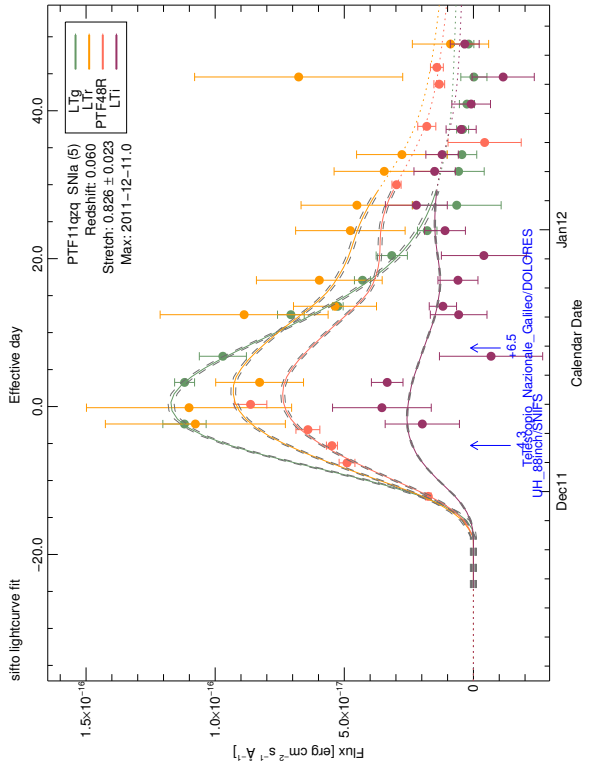

FIGURE E.103: SiFTO light curve fit of PTF11vl

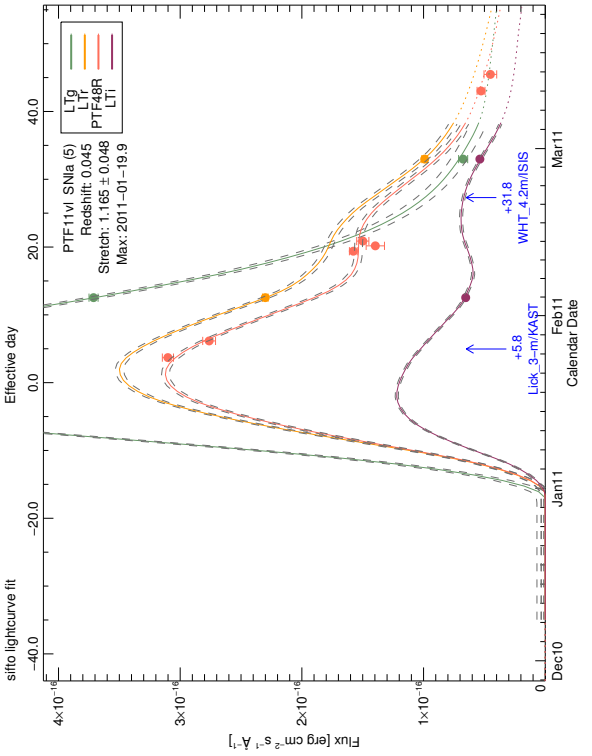

FIGURE E.104: SiFTO light curve fit of PTF11wv

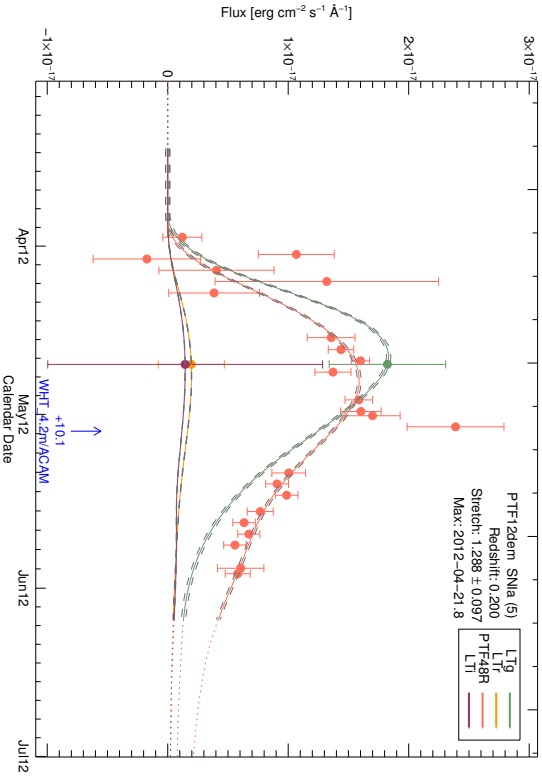

FIGURE E.105: SiFTO light curve fit of PTF11ya

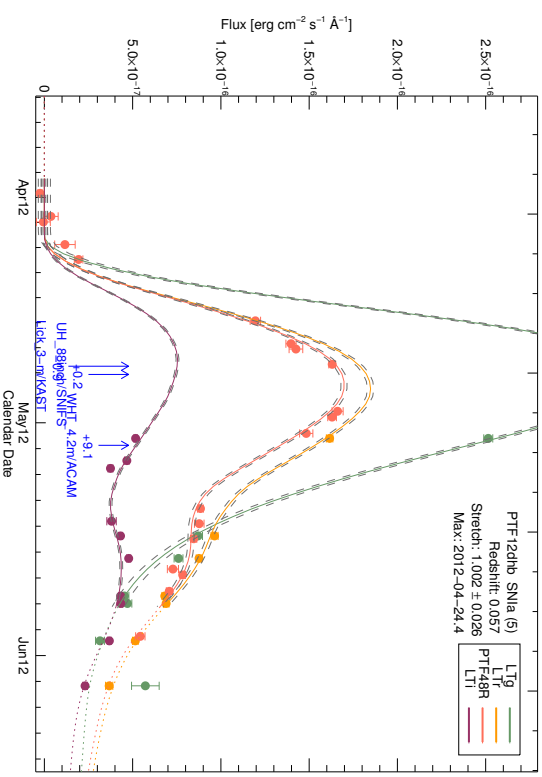

FIGURE E.107: SiFTO light curve fit of PTF12dem

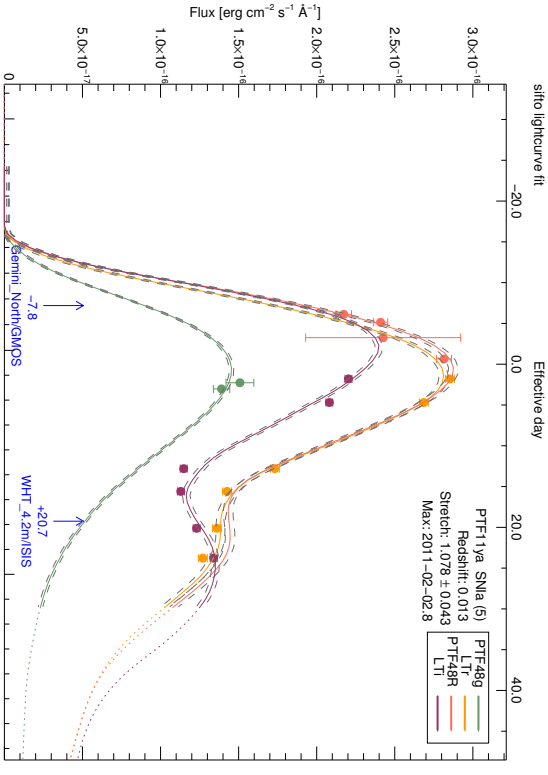

FIGURE E.106: SiFTO light curve fit of PTF12bsa

FIGURE E.108: SiFTO light curve fit of PTF12dhb

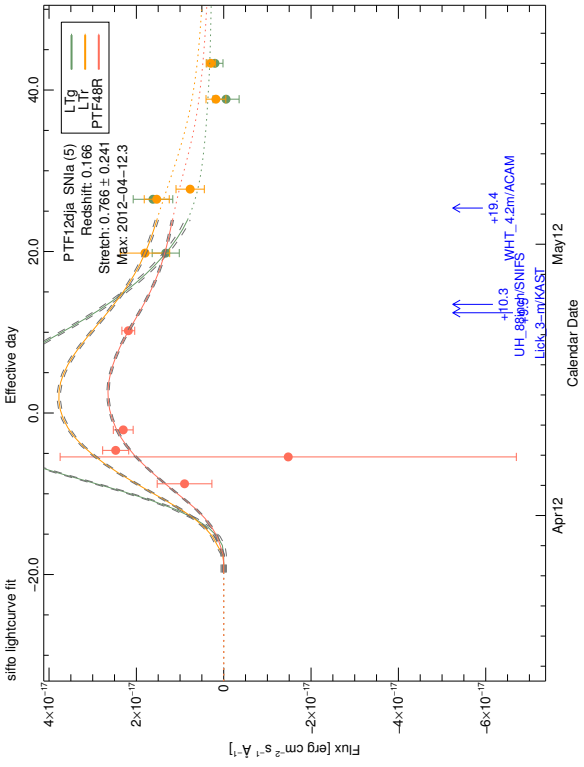

FIGURE E.110: SiFTO light curve fit of PTF12dja

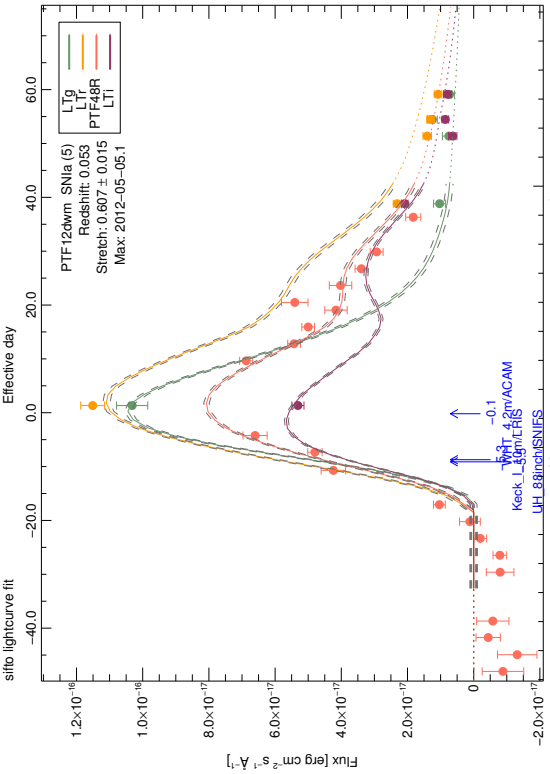

FIGURE E.112: SiFTO light curve fit of PTF12dwm

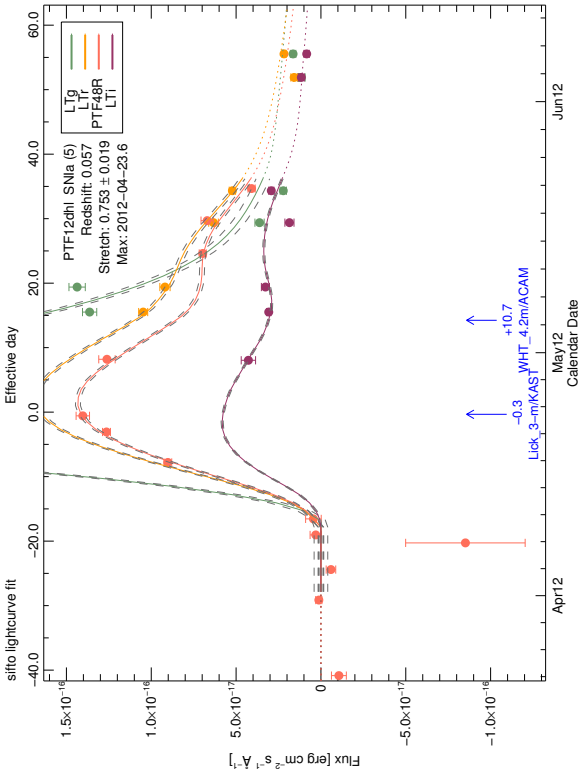

FIGURE E.109: SiFTO light curve fit of PTF12dhl

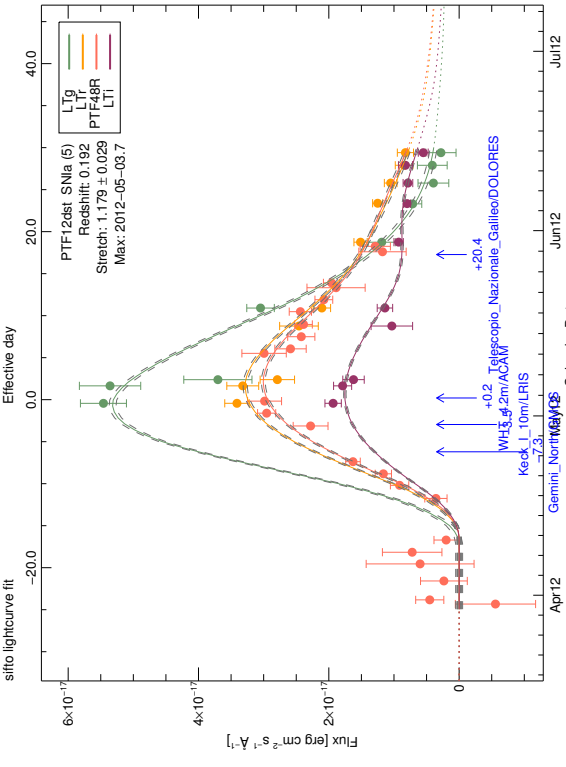

FIGURE E.111: SiFTO light curve fit of PTF12dst

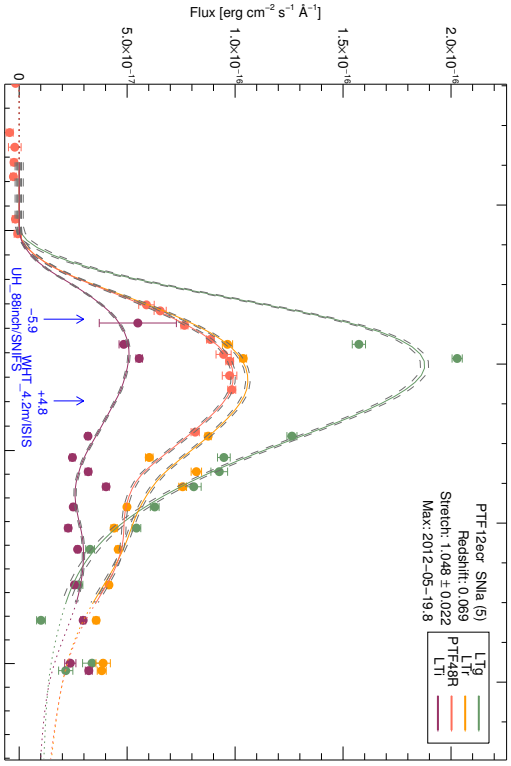

FIGURE E.115: SiFTO light curve fit of PTF12ecr

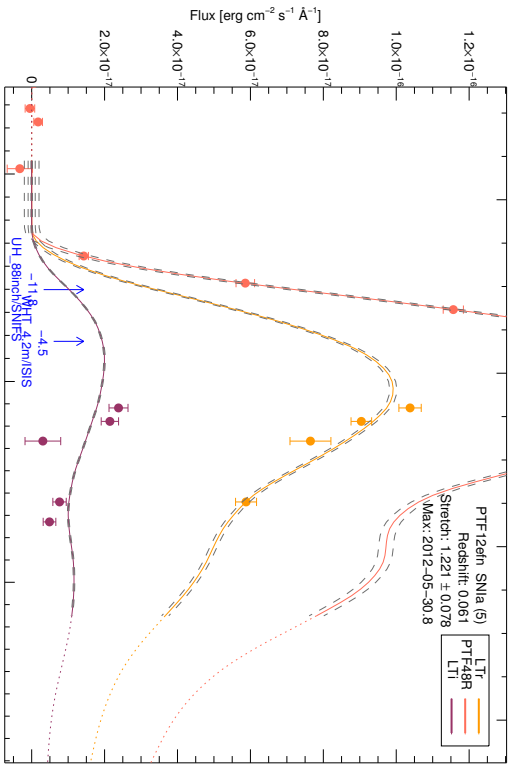

FIGURE E.116: SiFTO light curve fit of PTF12efn

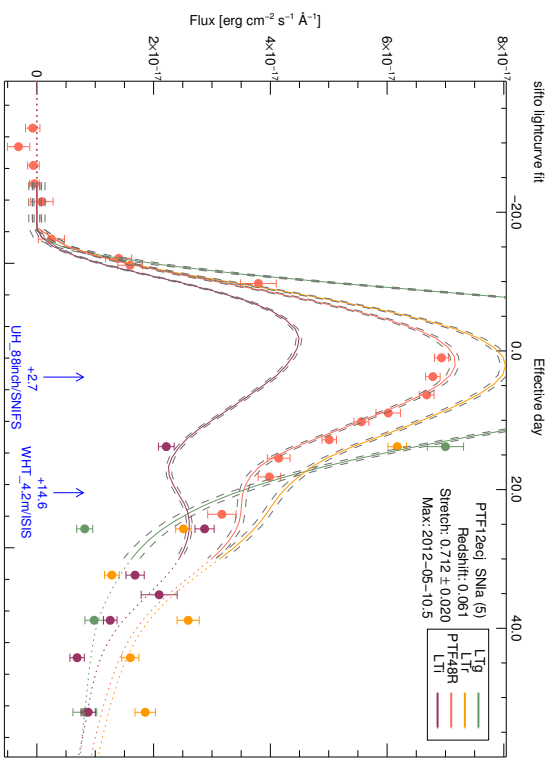

FIGURE E.113: SiFTO light curve fit of PTF12ecj

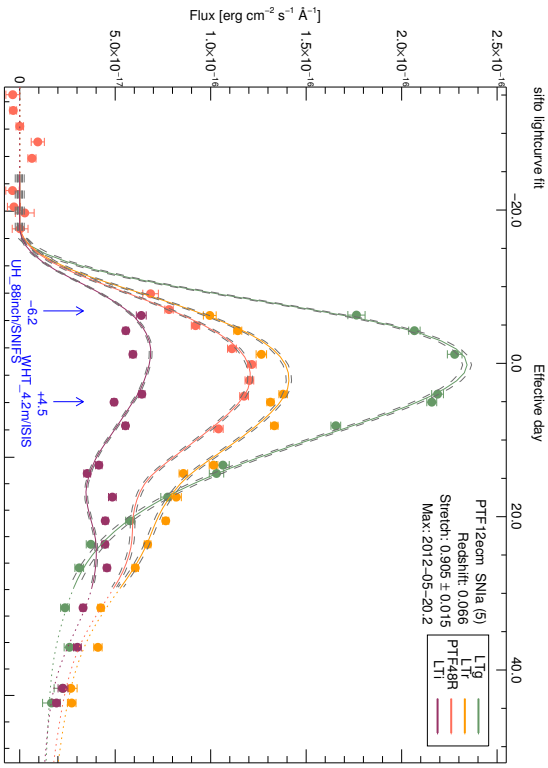

FIGURE E.114: SiFTO light curve fit of PTF12ecm

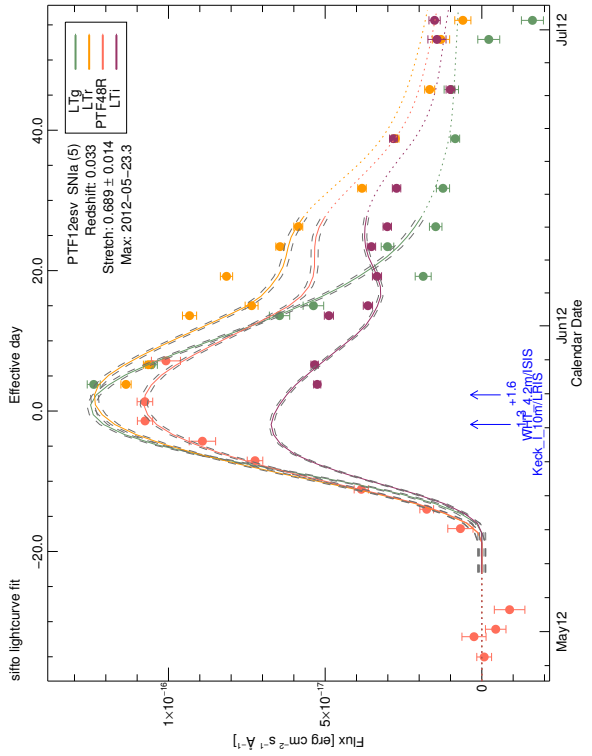

FIGURE E.118: SiFTO light curve fit of PTF12esv

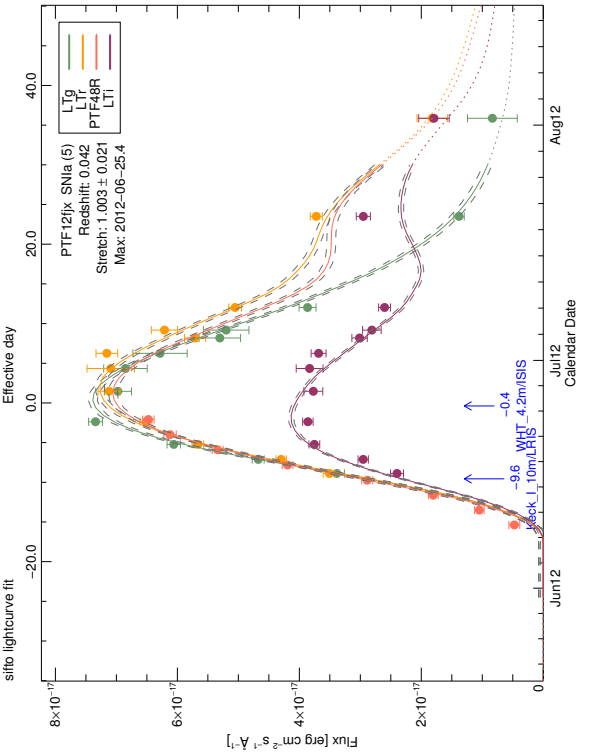

FIGURE E.120: SiFTO light curve fit of PTF12fjx

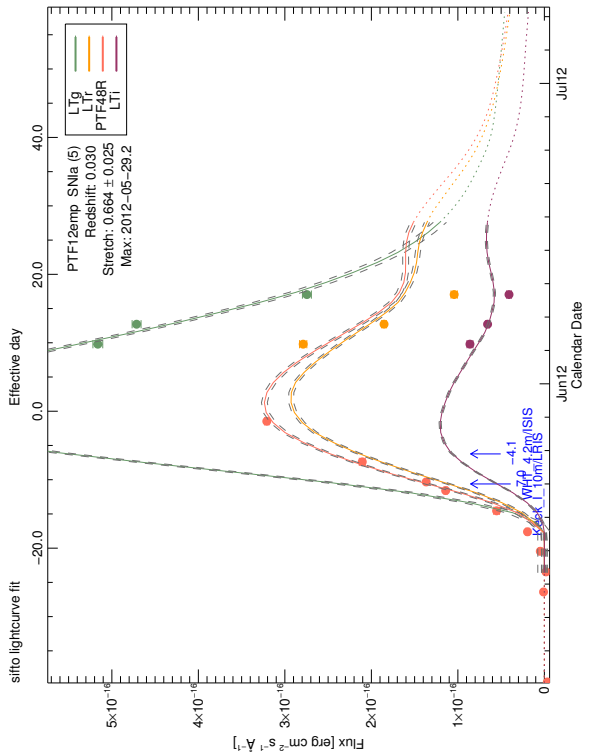

FIGURE E.117: SiFTO light curve fit of PTF12emp

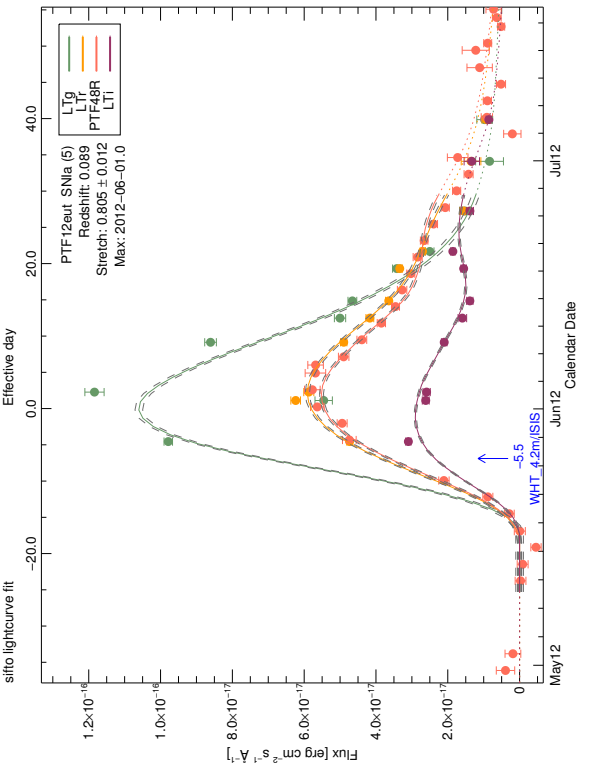

FIGURE E.119: SiFTO light curve fit of PTF12eut

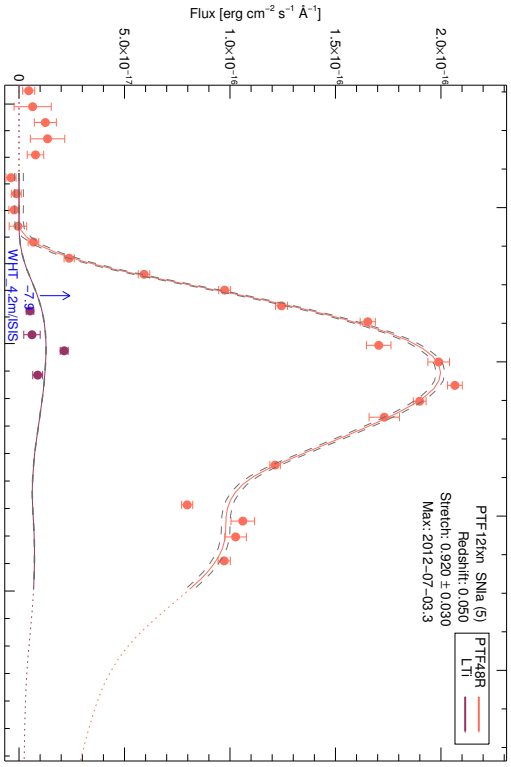

FIGURE E.121: SiFTO light curve fit of PTF12fkk

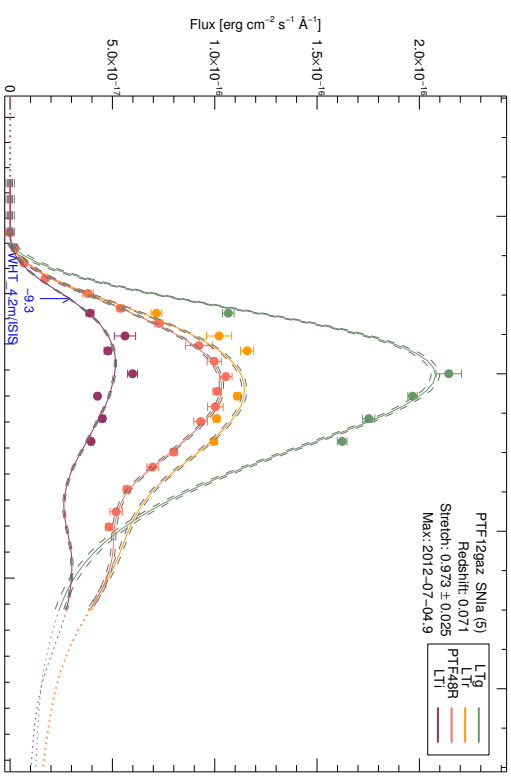

FIGURE E.123: SiFTO light curve fit of PTF12fxn

FIGURE E.122: SiFTO light curve fit of PTF12fuu

FIGURE E.124: SiFTO light curve fit of PTF12gaz

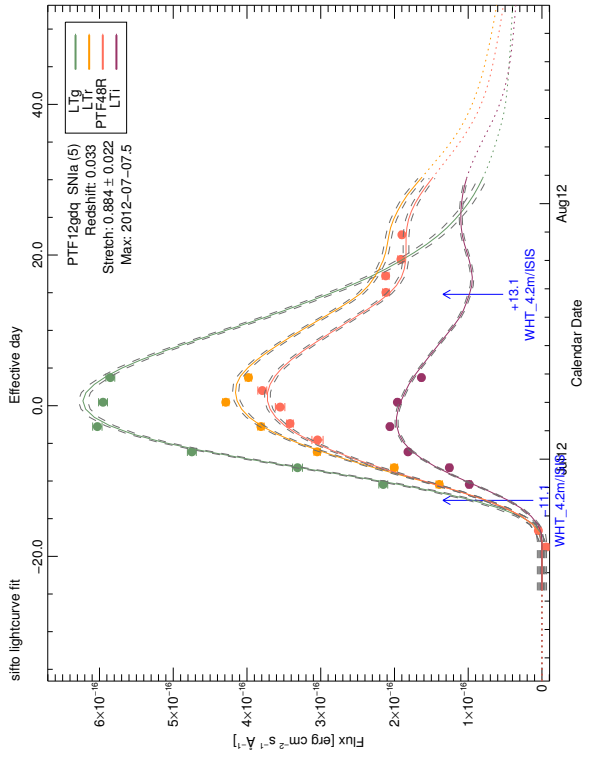

FIGURE E.125: SiFTO light curve fit of PTF12gdq

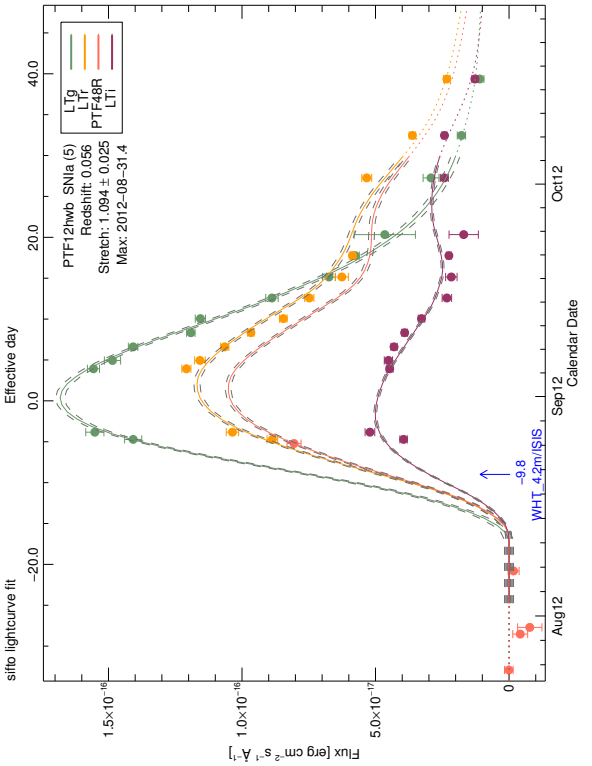

FIGURE E.126: SiFTO light curve fit of PTF12gco

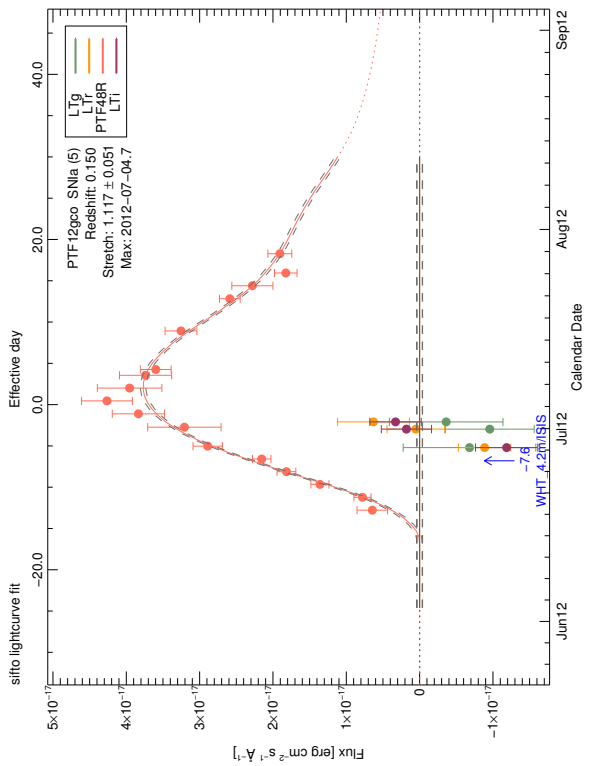

FIGURE E.127: SiFTO light curve fit of PTF12ghy

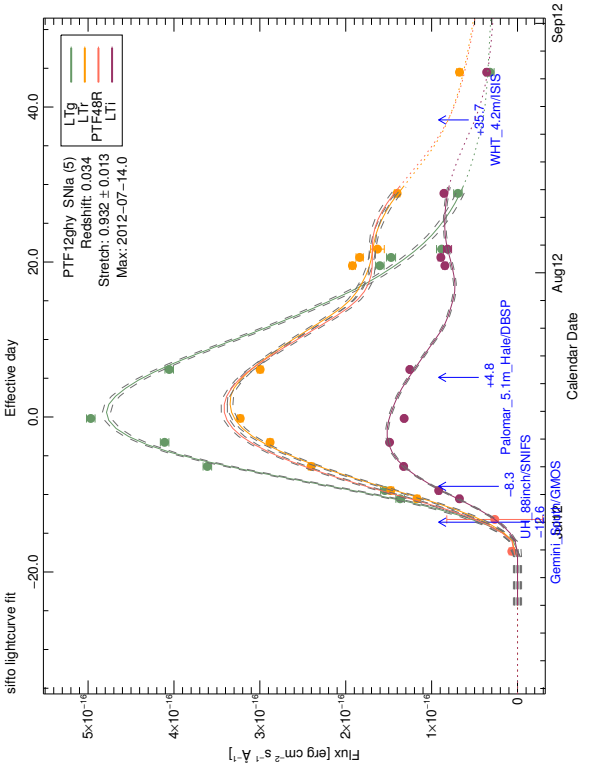

FIGURE E.128: SiFTO light curve fit of PTF12hwb

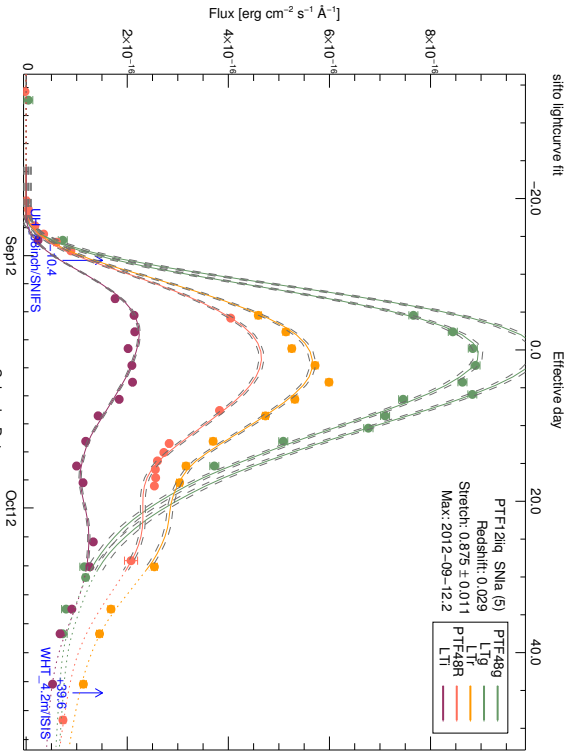

FIGURE E.129: SiFTO light curve fit of PTF12iiq

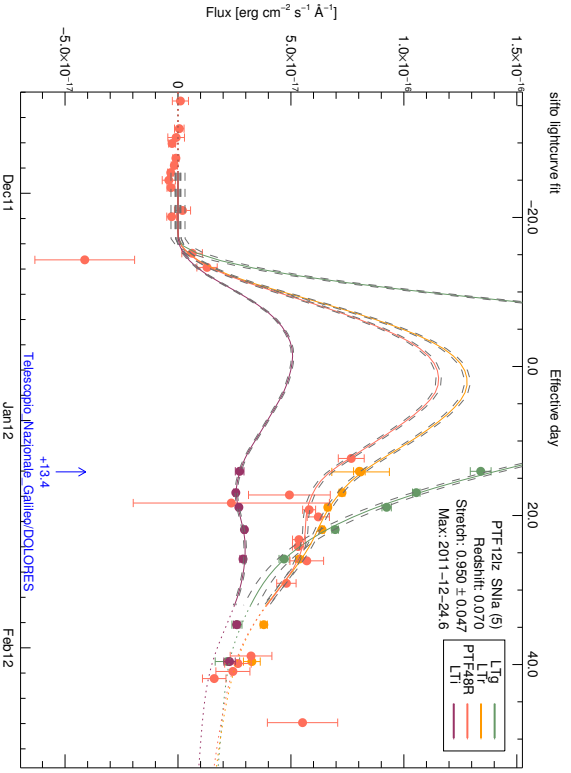

FIGURE E.130: SiFTO light curve fit of PTF12iz

Appendix F

Additional Miscellany

As this thesis aims to encapsulate the work I have done in the last 4 years, in this last appendix, I'd like to inject a little levity, as it hasn't all been quite so serious. Without wanting to be insufferably pretentious (although I admit I am straying awfully close), I've compiled a playlist (https://open.spotify.com/user/berto54/playlist/3rnxjCjqCZiRNmYEDfPcGW) that contains some of the many tracks that I have listened to throughout the last four years, and over the last few months as I tried to cocoon myself in a writing headspace. Whatever that means. I've had some fun with the titles, and, Reader, though I'm not *necessarily* saying that the tracks should align with the preamble, introduction, data chapter, science chapters, conclusions and abstract and you should pair each like a fine wine and good cheese, they totally do, and you absolutely should.

The Birth and Death of the Day – **Explosions in the Sky**, *All of a Sudden I Miss Everyone*

Go! – **Public Service Broadcasting**, *The Race For Space*

Fix the Sky a Little – **65daysofstatic**, *The Fall of Math*

T=0 – **Tall Ships**, *Everything Touching*

Peasantry or 'Light! Inside of Light' – **Godspeed You! Black Emperor**, *Asunder, Sweet and Other Distress*

Red Parallax – **65daysofstatic**, *No Man's Sky: Music For an Infinite Universe*

Colours in Space – **Explosions in the Sky**, *The Wilderness*

Contact – **Daft Punk**, *Random Access Memories*

An Ending (Ascent) – **Brian Eno**, *Apollo*

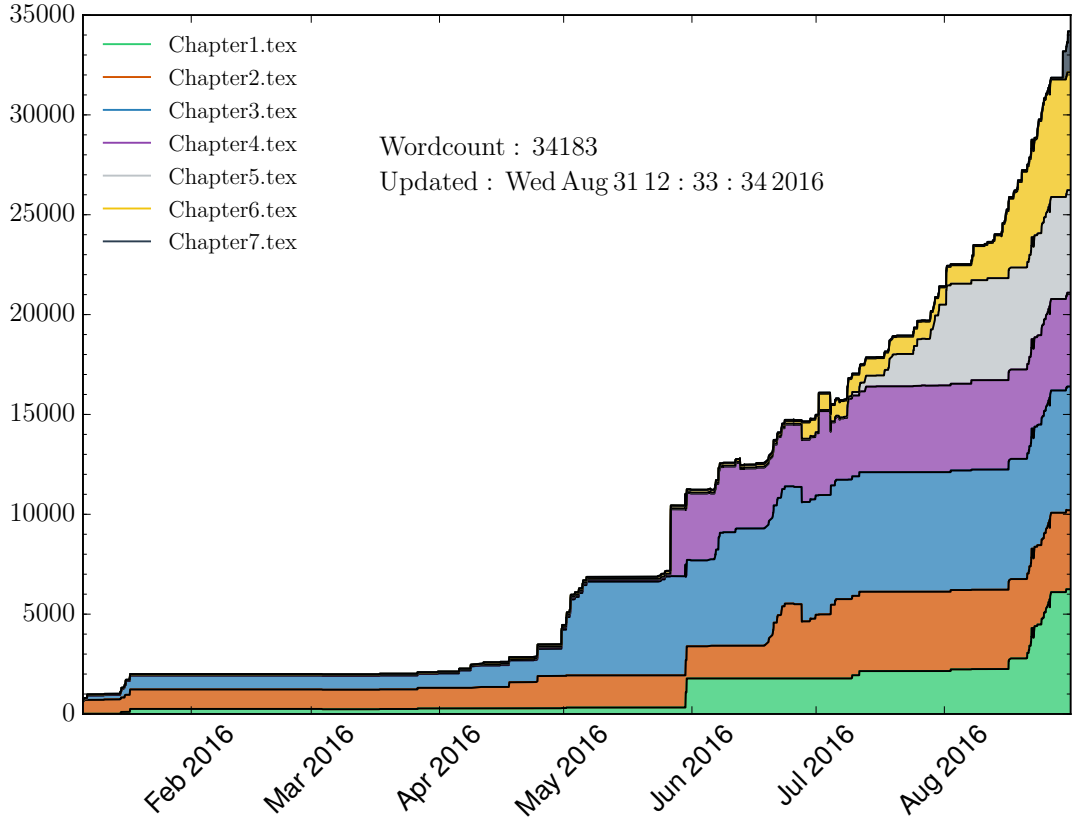

FIGURE F.1: One of the earliest bits of procrastination done on this thesis. The plot shows the wordcount over time, broken by Chapter.

While sat in the control room at La Silla Observatory just after new year 2016, I coded up a script that would record the wordcount of my thesis every hour until it was done. The graph shown in Figure F.1 is the result. The construction of such a plot could have been a bad idea, but for me it helped that every time I had a bad day, or spent what seemed like forever trying to get LaTeXto compile, I could look at it and see that I really was making progress. Whether any of the 34,000 or–so words make any sense however ...

edit: As this is now the *corrected* version of the thesis, I have included the updated wordcount graph, which now totals some 37,000 words, for perspective - Figure F.2. Note the flat section between in September - between submission and Viva, and October - when I couldn't face going back to this thesis.

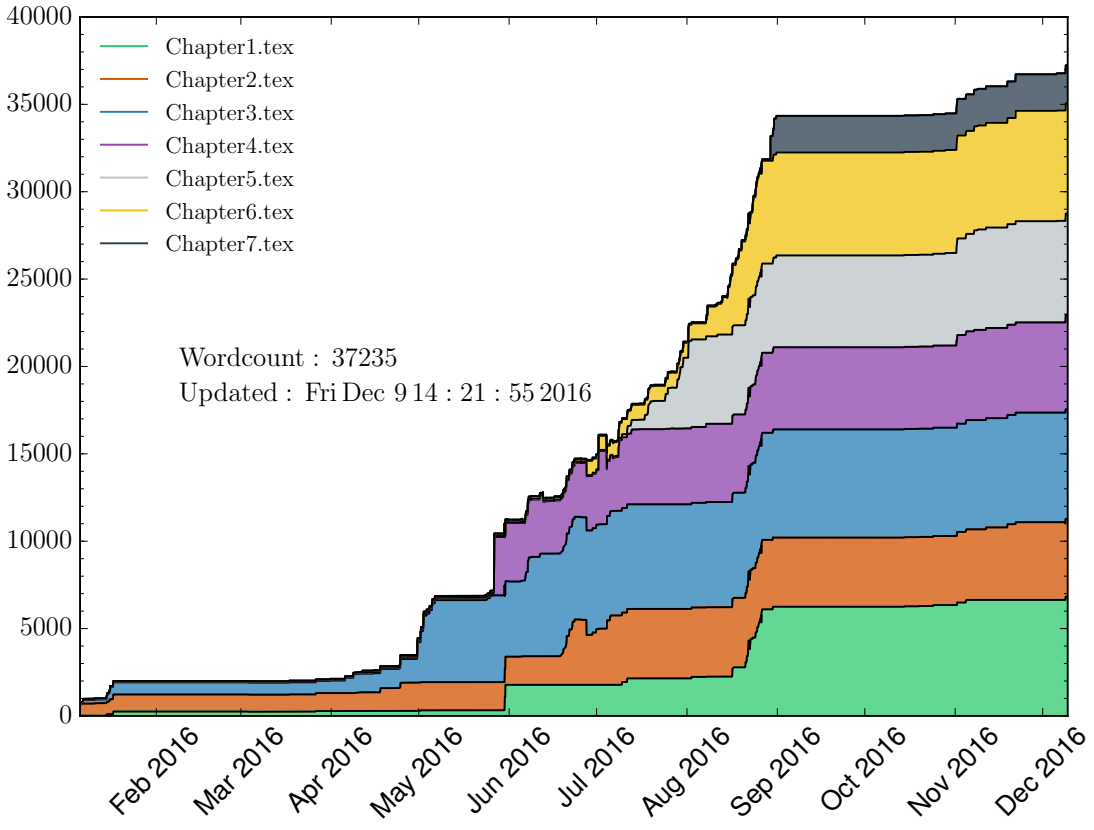

FIGURE F.2: One of the earliest bits of procrastination done on this thesis. The plot shows the wordcount over time, broken by Chapter. Final (!) version, after corrections

Bibliography

Ahn C. P., et al., 2014, ApJS, 211, 17

Aldering G., Knop R., Nugent P., 2000, AJ, 119, 2110

Aldering G., et al., 2002, in Tyson J. A., Wolff S., eds, Proc. SPIEVol. 4836, Survey and Other Telescope Technologies and Discoveries. pp 61–72, doi:10.1117/12.458107

Aldering G., et al., 2006, ApJ, 650, 510

Altavilla G., et al., 2007, A&A, 475, 585

Amanullah R., et al., 2014, ApJ, 788, L21

Amanullah R., et al., 2015, MNRAS, 453, 3300

Anderson J. P., et al., 2014, ApJ, 786, 67

Arnett W. D., 1979, ApJ, 230, L37

Arnett W. D., 1982, ApJ, 253, 785

Arnett D., Livne E., 1994a, ApJ, 427, 315

Arnett D., Livne E., 1994b, ApJ, 427, 330

Arnett W. D., Truran J. W., 1969, ApJ, 157, 339

Arnett W. D., Fryer C. L., Matheson T., 2016, preprint, (arXiv:1611.08746)

Ashall C., Mazzali P., Bersier D., Hachinger S., Phillips M., Percival S., James P., Maguire K., 2014, MNRAS, 445, 4427

Astier P., et al., 2006, A&A, 447, 31

Axelrod T. S., 1980, PhD thesis, California Univ., Santa Cruz.

Baade W., Zwicky F., 1934, Contributions from the Mount Wilson Observatory, vol. 3, pp.73-78, 3, 73

Badenes C., Maoz D., 2012, ApJ, 749, L11

Baltay C., et al., 2007, PASP, 119, 1278

Baltay C., et al., 2013, PASP, 125, 683

Barone-Nugent R. L., et al., 2012, MNRAS, 425, 1007

Benetti S., et al., 2004, MNRAS, 348, 261

Benetti S., et al., 2005, ApJ, 623, 1011

Benetti S., Cappellaro E., Turatto M., Taubenberger S., Harutyunyan A., Valenti S., 2006, ApJ, 653, L129

Betoule M., et al., 2014, A&A, 568, A22

Bianco F., et al., 2011, ApJ, 741, 20

Biscardi I., et al., 2012, A&A, 537, A57

Blondin S., Prieto J. L., Patat F., Challis P., Hicken M., Kirshner R. P., Matheson T., Modjaz M., 2009, ApJ, 693, 207

Blondin S., Dessart L., Hillier D. J., Khokhlov A. M., 2013, MNRAS, 429, 2127

Bloom J. S., et al., 2012a, PASP, 124, 1175

Bloom J. S., et al., 2012b, ApJ, 744, L17

Boisseau J. R., Wheeler J. C., 1991, AJ, 101, 1281

Bramich D. M., 2008, MNRAS, 386, L77

Branch D., Tammann G. A., 1992, ARA&A, 30, 359

Branch D., Fisher A., Nugent P., 1993, AJ, 106, 2383

Branch D., et al., 2004, ApJ, 606, 413

Branch D., et al., 2006, PASP, 118, 560

Burns C. R., et al., 2011, AJ, 141, 19

Burns C. R., et al., 2014, ApJ, 789, 32

Burns C. R., et al., 2015, SNooPy: TypeIa supernovae analysis tools, Astrophysics Source Code Library (ascl:1505.023)

Buzzoni B., et al., 1984, The Messenger, 38, 9

Cao Y., et al., 2015, Nature, 521, 328

Cardelli J. A., Clayton G. C., Mathis J. S., 1989, ApJ, 345, 245

Cartier R., et al., 2014, ApJ, 789, 89

Cartier R., et al., 2016, MNRAS Submitted.

Chan K.-W., Lingenfelter R. E., 1993, ApJ, 405, 614

Chandrasekhar S., 1957, An introduction to the study of stellar structure.. Dover Publications Ltd.

Chevalier R. A., Irwin C. M., 2012, ApJ, 747, L17

Childress M. J., et al., 2013a, ApJ, 770, 29

Childress M., et al., 2013b, ApJ, 770, 108

Childress M. J., Filippenko A. V., Ganeshalingam M., Schmidt B. P., 2014, MNRAS, 437, 338

Childress M. J., et al., 2015, MNRAS, 454, 3816

Chomiuk L., Soderberg A., Simon J., Foley R., 2012, The Astronomer's Telegram, 4453

Chomiuk L., et al., 2016, ApJ, 821, 119

Chotard N., et al., 2011, A&A, 529, L4

Cole S., et al., 2005, MNRAS, 362, 505

Colgate S. A., McKee C., 1969, ApJ, 157, 623

Conley A., et al., 2006b, ApJ, 132, 1707

Conley A., et al., 2006a, AJ, 132, 1707

Conley A., Carlberg R. G., Guy J., Howell D. A., Jha S., Riess A. G., Sullivan M., 2007, ApJ, 664, L13

Conley A., et al., 2008a, ApJ, 681, 482

Conley A., et al., 2008b, ApJ, 681, 482

Conley A., et al., 2011, ApJS, 192, 1

Contardo G., Leibundgut B., Vacca W. D., 2000, A&A, 359, 876

Contreras C., et al., 2010, AJ, 139, 519

Cumming R. J., Lundqvist P., Smith L. J., Pettini M., King D. L., 1996, MNRAS, 283, 1355

Dhawan S., Leibundgut B., Spyromilio J., Maguire K., 2015, MNRAS, 448, 1345

Dhawan S., Leibundgut B., Spyromilio J., Blondin S., 2016, preprint, (arXiv:1601.04874)

Dilday B., et al., 2012, Science, 337, 942

Dimitriadis G., Sullivan M., 2016, in prep.

Dong S., Katz B., Kushnir D., Prieto J. L., 2014, preprint, (arXiv:1401.3347)

Dopita M., et al., 2010, APSS, 327, 245

Draine B. T., 2003, ARA&A, 41, 241

Eisenstein D. J., et al., 2005, ApJ, 633, 560

Elias-Rosa N., et al., 2006, MNRAS, 369, 1880

Elias-Rosa N., et al., 2008, MNRAS, 384, 107

Elias J. H., Frogel J. A., Hackwell J. A., Persson S. E., 1981, ApJ, 251, L13

Elias J. H., Matthews K., Neugebauer G., Persson S. E., 1985, ApJ, 296, 379

Faber S. M., et al., 2003, in Iye M., Moorwood A. F. M., eds, Society of Photo-Optical Instrumentation Engineers (SPIE) Conference Series Vol. 4841, Instrument Design and Performance for Optical/Infrared Ground-based Telescopes. pp 1657–1669, doi:10.1117/12.460346

Falk S. W., Arnett W. D., 1977, ApJS, 33, 515

Filippenko A. V., 1997, ARA&A, 35, 309

Filippenko A. V., et al., 1992a, AJ, 104, 1543

Filippenko A. V., et al., 1992b, ApJ, 384, L15

Fink M., Röpke F. K., Hillebrandt W., Seitenzahl I. R., Sim S. A., Kromer M., 2010, A&A, 514, A53

Fink M., et al., 2014, MNRAS, 438, 1762

Finzi A., Wolf R. A., 1967, ApJ, 150, 115

Firth R. E., et al., 2015, MNRAS, 446, 3895

Fitzpatrick E. L., 1999, PASP, 111, 63

Fitzpatrick E. L., Massa D., 2007, ApJ, 663, 320

Flaugher B., et al., 2015, AJ, 150, 150

Folatelli G., et al., 2010, AJ, 139, 120

Folatelli G., et al., 2012, ApJ, 745, 74

Folatelli G., et al., 2013, ApJ, 773, 53

Foley R. J., Kasen D., 2011, ApJ, 729, 55

Foley R. J., et al., 2012, ApJ, 744, 38

Foley R. J., et al., 2014, MNRAS, 443, 2887

Foley R. J., Jha S. W., Pan Y.-C., Zheng W., Bildsten L., Filippenko A. V., Kasen D., 2016, preprint, (arXiv:1601.05955)

Ford C. H., Herbst W., Richmond M. W., Baker M. L., Filippenko A. V., Treffers R. R., Paik Y., Benson P. J., 1993, AJ, 106, 1101

Fox O. D., et al., 2015, MNRAS, 447, 772

Francis T. ., ed. 1895, Notes on regression and inheritance in the case of two parents No. 58 in Proceedings of the Royal Society of London. Royal Society

Fraser M., et al., 2015, The Astronomer's Telegram, 7209

Freedman W. L., et al., 2009, ApJ, 704, 1036

Frieman J. A., et al., 2008, AJ, 135, 338

Gal-Yam A., 2012, Science, 337, 927

Ganeshalingam M., Li W., Filippenko A., 2011b, MNRAS, 416, 2607

Ganeshalingam M., Li W., Filippenko A. V., 2011a, MNRAS, 416, 2607

Ganeshalingam M., et al., 2012, ApJ, 751, 142

Ganeshalingam M., Li W., Filippenko A. V., 2013, MNRAS, 433, 2240

Garavini G., et al., 2004, AJ, 128, 387

Gerardy C. L., et al., 2004, ApJ, 607, 391

Gilfanov M., Bogdán Á., 2010, Nature, 463, 924

Goldhaber G., et al., 2001, ApJ, 558, 359

González-Gaitán S., et al., 2011, ApJ, 727, 107

González-Gaitán S., et al., 2012, ApJ, 745, 44

González-Gaitán S., et al., 2014, ApJ, 795, 142

Goobar A., 2008, ApJ, 686, L103

Goobar A., et al., 2014, ApJ, 784, L12

Graur O., et al., 2011, MNRAS, 417, 916

Graur O., Zurek D., Shara M. M., Riess A. G., Seitenzahl I. R., Rest A., 2016, ApJ, 819, 31

Groom D. E., 1998, in American Astronomical Society Meeting Abstracts. p. 1419

Gullixson C. A., 1992, in Howell S. B., ed., Astronomical Society of the Pacific Conference Series Vol. 23, Astronomical CCD Observing and Reduction Techniques. p. 130

Guy J., Astier P., Nobili S., Regnault N., Pain R., 2005, A&A, 443, 781

Guy J., et al., 2007, A&A, 466, 11

Guy J., et al., 2010, A&A, 523, A7

Guzmán R., Gallego J., Koo D. C., Phillips A. C., Lowenthal J. D., Faber S. M., Illingworth G. D., Vogt N. P., 1997, ApJ, 489, 559

Hachinger S., Mazzali P. A., Tanaka M., Hillebrandt W., Benetti S., 2008, MNRAS, 389, 1087

Hachinger S., et al., 2013, MNRAS, 429, 2228

Hachisu I., Kato M., Nomoto K., 1996, ApJ, 470, L97

Hachisu I., Kato M., Nomoto K., 2010, ApJ, 724, L212

Hadjiyska E., et al., 2012, in Griffin E., Hanisch R., Seaman R., eds, IAU Symposium Vol. 285, New Horizons in Time Domain Astronomy. pp 324–326 (arXiv:1210.1584), doi:10.1017/S1743921312000944

Hamuy M., Phillips M. M., Maza J., Suntzeff N. B., Schommer R. A., Aviles R., 1995, AJ, 109, 1

Hamuy M., et al., 1996a, AJ, 112, 2408

Hamuy M., Phillips M. M., Suntzeff N. B., Schommer R. A., Maza J., Smith R. C., Lira P., Aviles R., 1996b, AJ, 112, 2438

Hamuy M., et al., 2003, Nature, 424, 651

Hamuy M., et al., 2006, PASP, 118, 2

Harkness R. P., et al., 1987, ApJ, 317, 355

Hayden B., et al., 2010a, ApJ, 712, 350

Hayden B. T., et al., 2010b, ApJ, 722, 1691

Henden A. A., Welch D. L., Terrell D., Levine S. E., 2009, in American Astronomical Society Meeting Abstracts 214. p. 669

Hicken M., et al., 2009, ApJ, 700, 331

Hicken M., et al., 2012, ApJS, 200, 12

Hinshaw G., et al., 2013, ApJS, 208, 19

Hoeflich P., Khokhlov A. M., Wheeler J. C., 1995, ApJ, 444, 831

Höflich P., Gerardy C. L., Nomoto K., Motohara K., Fesen R. A., Maeda K., Ohkubo T., Tominaga N., 2004, ApJ, 617, 1258

Hook I. M., Jørgensen I., Allington-Smith J. R., Davies R. L., Metcalfe N., Murowinski R. G., Crampton D., 2004, PASP, 116, 425

Howell S. B., 2012, PASP, 124, 263

Howell D. A., et al., 2006, Nature, 443, 308

Hoyle F., Fowler W. A., 1960, ApJ, 132, 565

Hsiao E. Y., Conley A., Howell D. A., Sullivan M., Pritchet C. J., Carlberg R. G., Nugent P. E., Phillips M. M., 2007, ApJ, 663, 1187

Hubble E., 1929, Proceedings of the National Academy of Science, 15, 168

Iben Jr. I., Tutukov A. V., 1984, ApJS, 54, 335

Im M., Choi C., Yoon S.-C., Kim J.-W., Ehgamberdiev S. A., Monard L. A. G., Sung H.-I., 2015, ApJS, 221, 22

Isern J., et al., 2016, A&A, 588, A67

Ivanova N., et al., 2013, A&A Rev., 21, 59

Jack D., Baron E., Hauschildt P. H., 2015, MNRAS, 449, 3581

Jha S., et al., 2006, AJ, 131, 527

Kahabka P., van den Heuvel E. P. J., 1997, ARA&A, 35, 69

Kasen D., 2006, ApJ, 649, 939

Kasen D., 2010, ApJ, 708, 1025

Kasen D., Thomas R. C., Nugent P., 2006, ApJ, 651, 366

Kasen D., Röpke F. K., Woosley S. E., 2009, Nature, 460, 869

Kasliwal M. M., 2012, PASA, 29, 482

Kasliwal M. M., et al., 2010, ApJ, 723, L98

Kasliwal M. M., et al., 2011, ApJ, 730, 134

Kasliwal M. M., et al., 2012, ApJ, 755, 161

Katz B., Dong S., 2012, preprint, (arXiv:1211.4584)

Kessler R., et al., 2009, ApJS, 185, 32

Khokhlov A. M., 1991, A&A, 245, 114

Knop R. A., et al., 2003, ApJ, 598, 102

Kowalski M., et al., 2008, ApJ, 686, 749

Krisciunas K., et al., 2001, AJ, 122, 1616

Krisciunas K., et al., 2004a, AJ, 127, 1664

Krisciunas K., Phillips M. M., Suntzeff N. B., 2004b, ApJ, 602, L81

Krisciunas K., Prieto J. L., Garnavich P. M., Riley J.-L. G., Rest A., Stubbs C., McMillan R., 2006, AJ, 131, 1639

Kushnir D., Katz B., Dong S., Livne E., Fernández R., 2013, ApJ, 778, L37

Lair J. C., Leising M. D., Milne P. A., Williams G. G., 2006, AJ, 132, 2024

Lampeitl H., et al., 2010, ApJ, 722, 566

Lantz B., et al., 2004, in Mazuray L., Rogers P. J., Wartmann R., eds, Society of Photo-Optical Instrumentation Engineers (SPIE) Conference Series Vol. 5249, Optical Design and Engineering. pp 146–155, doi:10.1117/12.512493

Law N., et al., 2009, PASP, 121, 1395

Leibundgut B., 1988, PhD thesis, PhD thesis. Univ. Basel.137 pp. , (1988)

Leibundgut B., Pinto P. A., 1992, ApJ, 401, 49

Li W. D., et al., 2000, in Holt S. S., Zhang W. W., eds, American Institute of Physics Conference Series Vol. 522, American Institute of Physics Conference Series. pp 103–106 (arXiv:astro-ph/9912336), doi:10.1063/1.1291702

Li W., et al., 2003, PASP, 115, 453

Li W., et al., 2011, MNRAS, 412, 1441

Liebert J., Bergeron P., Holberg J. B., 2005, ApJS, 156, 47

Lira P., et al., 1998, AJ, 115, 234

Livio M., Truran J. W., 1992, ApJ, 389, 695

Livne E., Arnett D., 1995, ApJ, 452, 62

Lundqvist P., et al., 2013, MNRAS, 435, 329

Lundqvist P., et al., 2015, A&A, 577, A39

Maeda K., et al., 2011, MNRAS, 413, 3075

Magee M. R., et al., 2016, A&A, 589, A89

Maguire K., et al., 2011, MNRAS, 418, 747

Maguire K., et al., 2012, MNRAS, 426, 2359

Maguire K., et al., 2013, MNRAS, 436, 222

Maguire K., et al., 2014, MNRAS, 444, 3258

Maguire K., Taubenberger S., Sullivan M., Mazzali P. A., 2016, MNRAS, 457, 3254

Mandel K. S., Narayan G., Kirshner R. P., 2011, ApJ, 731, 120

Maoz D., Badenes C., 2010, MNRAS, 407, 1314

Maoz D., Mannucci F., Brandt T. D., 2012, MNRAS, 426, 3282

Maoz D., Mannucci F., Nelemans G., 2014, ARA&A, 52, 107

Marietta E., Burrows A., Fryxell B., 2000, ApJS, 128, 615

Marion G. H., et al., 2016, ApJ, 820, 92

Matheson T., et al., 2008, AJ, 135, 1598

Mattila S., Lundqvist P., Sollerman J., Kozma C., Baron E., Fransson C., Leibundgut B., Nomoto K., 2005, A&A, 443, 649

Maund J. R., et al., 2013, MNRAS, 433, L20

Maurer I., Jerkstrand A., Mazzali P. A., Taubenberger S., Hachinger S., Kromer M., Sim S., Hillebrandt W., 2011, MNRAS, 418, 1517

Mazzali P. A., 2000, A&A, 363, 705

Mazzali P. A., Schmidt B. P., 2005, in Lasenby A. N., Wilkinson A., eds, IAU Symposium Vol. 201, New Cosmological Data and the Values of the Fundamental Parameters. p. 241

Mazzali P. A., Benetti S., Stehle M., Branch D., Deng J., Maeda K., Nomoto K., Hamuy M., 2005a, MNRAS, 357, 200

Mazzali P. A., et al., 2005b, ApJ, 623, L37

Mazzali P. A., et al., 2014, MNRAS, 439, 1959

Meikle W. P. S., 2000, MNRAS, 314, 782

Miles B. J., van Rossum D. R., Townsley D. M., Timmes F. X., Jackson A. P., Calder A. C., Brown E. F., 2016, ApJ, 824, 59

Miller J. S., Stone R. P. S., 1994, Technical Report 66, The Kast double spectograph. University of California Observatories/Lick Observatory

Milne P. A., The L.-S., Leising M. D., 2001, ApJ, 559, 1019

Minkowski R., 1941, PASP, 53, 224

Monard L. A. G., et al., 2015, Central Bureau Electronic Telegrams, 4081

Mosher J., et al., 2014, ApJ, 793, 16

Nakar E., Sari R., 2012, ApJ, 747, 88

Napiwotzki R., et al., 2007, in Napiwotzki R., Burleigh M. R., eds, Astronomical Society of the Pacific Conference Series Vol. 372, 15th European Workshop on White Dwarfs. p. 387

Nobili S., et al., 2005, A&A, 437, 789

Nomoto K., 1982, ApJ, 253, 798

Nomoto K., Iben Jr. I., 1985, ApJ, 297, 531

Nomoto K., Thielemann F.-K., Yokoi K., 1984, ApJ, 286, 644

Nugent P. E., et al., 2011, Nature, 480, 344

Nugent P., Cao Y., Kasliwal M., 2015, in Visualization and Data Analysis. pp 939702–939702–7, doi:10.1117/12.2085383, http://dx.doi.org/10.1117/12.2085383

Ofek E. O., et al., 2012, PASP, 124, 854

Ofek E. O., et al., 2013, Nature, 494, 65

Ofek E. O., et al., 2014a, ApJ, 781, 42

Ofek E. O., et al., 2014b, ApJ, 788, 154

Oke J. B., et al., 1995, PASP, 107, 375

Pakmor R., Röpke F. K., Weiss A., Hillebrandt W., 2008, A&A, 489, 943

Pakmor R., Kromer M., Taubenberger S., Sim S. A., Röpke F. K., Hillebrandt W., 2012, ApJ, 747, L10

Pan K.-C., Ricker P. M., Taam R. E., 2012, ApJ, 750, 151

Pan Y.-C., et al., 2014, MNRAS, 438, 1391

Pan Y.-C., Sullivan M., Maguire K., Gal-Yam A., Hook I. M., Howell D. A., Nugent P. E., Mazzali P. A., 2015, MNRAS, 446, 354

Panagia N., Van Dyk S. D., Weiler K. W., Sramek R. A., Stockdale C. J., Murata K. P., 2006, ApJ, 646, 369

Parrent J. T., et al., 2012, ApJ, 752, L26

Parrent J., Friesen B., Parthasarathy M., 2014, APSS, 351, 1

Patat F., Benetti S., Cappellaro E., Danziger I. J., della Valle M., Mazzali P. A., Turatto M., 1996, MNRAS, 278, 111

Patat F., et al., 2007, Science, 317, 924

Patat F., Chugai N. N., Podsiadlowski P., Mason E., Melo C., Pasquini L., 2011, A&A, 530, A63

Percival W. J., et al., 2014, MNRAS, 439, 2531

Pereira R., et al., 2013, A&A, 554, A27

Perlmutter S., et al., 1997a, ApJ, 483, 565

Perlmutter S., et al., 1997b, ApJ, 483, 565

Perlmutter S., et al., 1999, ApJ, 517, 565

Phillips M. M., 1993, ApJ, 413, L105

Phillips M. M., 2012, PASA, 29, 434

Phillips M. M., Lira P., Suntzeff N. B., Schommer R. A., Hamuy M., Maza J., 1999, AJ, 118, 1766

Pignata G., et al., 2008, MNRAS, 388, 971

Pinto P. A., Eastman R. G., 2000a, ApJ, 530, 744

Pinto P. A., Eastman R. G., 2000b, ApJ, 530, 757

Piro A. L., 2012, ApJ, 759, 83

Piro A. L., Nakar E., 2013, ApJ, 769, 67

Piro A. L., Nakar E., 2014, ApJ, 784, 85

Piro A. L., Chang P., Weinberg N. N., 2010, ApJ, 708, 598

Planck Collaboration et al., 2015, preprint, (arXiv:1502.01589)

Postnov K. A., Yungelson L. R., 2014, Living Reviews in Relativity, 17

Prajs S., et al., 2016, preprint, (arXiv:1605.05250)

Prieto J., Garnavich P., Depoy D., Marshall J., Eastman J., Frank S., 2005, IAU Circ., 8633

Pskovskii I. P., 1977, Sov. Astron., 21, 675

Pskovskii Y. P., 1984, Sov. Astron., 28, 658

Quimby R. M., et al., 2011, Nature, 474, 487

Quimby R. M., Yuan F., Akerlof C., Wheeler J. C., 2013, MNRAS, 431, 912

Rabinak I., Livne E., Waxman E., 2012, ApJ, 757, 35

Rahmer G., Smith R., Velur V., Hale D., Law N., Bui K., Petrie H., Dekany R., 2008, in Society of Photo-Optical Instrumentation Engineers (SPIE) Conference Series. , doi:10.1117/12.788086

Rau A., et al., 2009, PASP, 121, 1334

Rest A., et al., 2014, ApJ, 795, 44

Richardson D., Branch D., Casebeer D., Millard J., Thomas R. C., Baron E., 2002, AJ, 123, 745

Richardson D., Jenkins III R. L., Wright J., Maddox L., 2014, AJ, 147, 118

Rieke G. H., Lebofsky M. J., 1985, ApJ, 288, 618

Riess A. G., Press W. H., Kirshner R. P., 1996, ApJ, 473, 88

Riess A. G., et al., 1998, AJ, 116, 1009

Riess A. G., et al., 1999a, AJ, 117, 707

Riess A. G., et al., 1999b, AJ, 118, 2675

Ruiz-Lapuente P., 2014, New A Rev., 62, 15

Saio H., Nomoto K., 1985, A&A, 150, L21

Sako M., et al., 2014, preprint, (arXiv:1401.3317)

Sakurai A., 1960, Communications on Pure and Applied Mathematics, 13, 353

Scalzo R., et al., 2014, MNRAS, 440, 1498

Schaefer B. E., Pagnotta A., 2012, Nature, 481, 164

Schlafly E. F., Finkbeiner D. P., 2011, ApJ, 737, 103

Schlegel D. J., Finkbeiner D. P., Davis M., 1998, ApJ, 500, 525

Schmidt B. P., et al., 1998, ApJ, 507, 46

Schmidt W., Ciaraldi-Schoolmann F., Niemeyer J. C., Röpke F. K., Hillebrandt W., 2010, ApJ, 710, 1683

Seitenzahl I. R., Taubenberger S., Sim S. A., 2009, MNRAS, 400, 531

Seitenzahl I. R., et al., 2013, MNRAS, 429, 1156

Shappee B. J., Stanek K. Z., Pogge R. W., Garnavich P. M., 2013, ApJ, 762, L5

Shappee B. J., et al., 2015, preprint, (arXiv:1507.04257)

Shariff H., Dhawan S., Jiao X., Leibundgut B., Trotta R., van Dyk D. A., 2016, preprint, (arXiv:1605.08064)

Shen K. J., Bildsten L., 2014, ApJ, 785, 61

Silverman J. M., Kong J. J., Filippenko A. V., 2012a, MNRAS, 425, 1819

Silverman J. M., et al., 2012b, ApJ, 756, L7

Silverman J. M., et al., 2013a, ApJS, 207, 3

Silverman J. M., et al., 2013b, ApJS, 207, 3

Silverman J. M., et al., 2013c, ApJ, 772, 125

Sim S. A., et al., 2013, MNRAS, 436, 333

Smartt S. J., et al., 2015, A&A, 579, A40

Soderberg A. M., et al., 2008, Nature, 453, 469

Steele I. A., et al., 2004, in Ground-based Telescopes. pp 679–692, doi:10.1117/12.551456, http://dx.doi.org/10.1117/12.551456

Stehle M., Mazzali P. A., Benetti S., Hillebrandt W., 2005, MNRAS, 360, 1231

Sternberg A., et al., 2011, Science, 333, 856

Stritzinger M., Mazzali P. A., Sollerman J., Benetti S., 2006, A&A, 460, 793

Stritzinger M. D., et al., 2011, AJ, 142, 156

Strovink M., 2007, ApJ, 671, 1084

Sullivan M., et al., 2006, ApJ, 648, 868

Sullivan M., et al., 2010, MNRAS, 406, 782

Sullivan M., et al., 2011a, ApJ, 732, 118

Sullivan M., et al., 2011b, ApJ, 737, 102

Suntzeff N. B., 1996, in Mccray R., Wang Z., eds, Proceedings of the International Astronomical Union Vol. 145, Supernovae and Supernova Remnants. Cambridge University Press, pp 41–48

Suzuki N., et al., 2012, ApJ, 746, 85

Svirski G., Nakar E., Sari R., 2012, ApJ, 759, 108

Tanaka M., et al., 2008a, ApJ, 677, 448

Tanaka M., et al., 2008b, ApJ, 677, 448

Timmes F. X., Brown E. F., Truran J. W., 2003, ApJ, 590, L83

Tripp R., 1998, A&A, 331, 815

Trundle C., Kotak R., Vink J. S., Meikle W. P. S., 2008, A&A, 483, L47

Turatto M., 2003, in Weiler K., ed., Lecture Notes in Physics, Berlin Springer Verlag Vol. 598, Supernovae and Gamma-Ray Bursters. pp 21–36 (arXiv:astro-ph/0301107), doi:10.1007/3-540-45863-8˙3

Tutukov A. V., Yungelson L. R., 1979, Acta Astron., 29, 665

Urata Y., et al., 2009, ApJ, 706, L183

Vacca W. D., Leibundgut B., 1996, ApJ, 471, L37

Vinkó J., et al., 2012, A&A, 546, A12

Wang L., 2005, ApJ, 635, L33

Wang L., et al., 2003, ApJ, 591, 1110

Wang X., et al., 2009, ApJ, 699, L139

Webbink R. F., 1984, ApJ, 277, 355

Wheeler J. C., Hansen C. J., 1971, APSS, 11, 373

Whelan J., Iben Jr. I., 1973a, ApJ, 186, 1007

Whelan J., Iben Jr. I., 1973b, ApJ, 186, 1007

Williams R., Mason E., Della Valle M., Ederoclite A., 2008, ApJ, 685, 451

Wood-Vasey W. M., et al., 2007, ApJ, 666, 694

Woosley S. E., Weaver T. A., 1994, ApJ, 423, 371

Woosley S. E., Kasen D., Blinnikov S., Sorokina E., 2007, ApJ, 662, 487

Woosley S. E., Kerstein A. R., Aspden A. J., 2011, ApJ, 734, 37

Yamanaka M., et al., 2014, ApJ, 782, L35

Yaron O., Gal-Yam A., 2012, PASP, 124, 668

Yoon S.-C., Podsiadlowski P., Rosswog S., 2007, MNRAS, 380, 933

York D. G., et al., 2000, AJ, 120, 1579

Zheng W., et al., 2012, ApJ, 751, 90

Zheng W., et al., 2013, ApJ, 778, L15

Zheng W., et al., 2014, ApJ, 783, L24

van Rossum D. R., 2012, preprint, (arXiv:1208.3781)

van den Heuvel E. P. J., Bhattacharya D., Nomoto K., Rappaport S. A., 1992, A&A, 262, 97

"Space. It seems to go on and on forever. But then you get to the end, and a gorilla starts throwing barrels at you.'

- Philip J. Fry, *Futurama; 'Space Pilot 3000'*